Abstract

The alignment of an optical system plays a fundamental role in its final performances. In the astronomical field, this operation has always been performed using external optical feedback in an iterative process. The aim of this work is to study a different integration procedure devised to reduce the number of iterations needed to reach the required optical quality. The typical design philosophy based on countless alignment screws can be dropped in favour of a more stiffness-oriented mechanical design. The proposed procedures consist in the geometrical measurement of the as-built optical and mechanical elements followed by their integration to the nominal position. To carry out this operation it is necessary to design highly repeatable optomechanical mounts that are easily referenceable to the optical elements, along with a system able to correct the alignment errors. Moreover, an estimation of the reachable accuracy and the damage done on the surfaces while measuring the optical elements is essential.

During this work, the optomechanical mounts and the correction systems have been built, and their performances tested on a dummy system and on an actual instrument (ESPRESSO). The accuracy estimation has been performed with a focus on the Coordinate Measuring Machine (CMM) starting from a series of tests performed on the machine itself. The developed software has the capability to output the expected misalignments in terms of both geometrical values and optical effects. The firsts are useful to estimate the feasibility of this alignment method on a certain system, while the optical effects are used to identify the most critical elements in order to guide the mechanical design. The obtained results have been compared and verified with a dummy system alignment. To estimate the damage on the optical elements due to the measurement operation, the forces applied by different measuring machines (Articulated Arm CMM, CMM, and Laser Tracker) have been evaluated using a strain gauge system. Starting from those data, different optical samples have been tested impinging them with a CMM and measuring the damaged surfaces with a Micro Finishing Topographer. The proposed method allowed the alignment of astronomical instrumentation reducing or even removing external optical feedbacks. Starting from the optical design it is now possible to define the optimal mechanical design and to choose the best alignment strategy matching the requirements in terms of optical quality, throughput loss, and stray light.

Table of Contents

List of figures

List of tables

Introduction

Looking through the optical elements while mounting them has always been the most typical method for the alignment of optical system in the astronomical field. In the past centuries, this was roughly done placing different kind of markers along the optical path. In the last 150 years, the invention of different instruments like the alignment telescope, the autocollimator, and the interferometer strongly improved the accuracy of the alignment allowing for the design of better telescopes and instruments. The introduction of the LASER and the digital imaging systems in the second part of the twentieth century lead us to today's techniques for optical alignment.

In the last decades, astronomical scientists, on the other side, are pushing optical and mechanical engineers towards instruments with higher and higher performances. This is leading to more complex telescopes and instruments with, as a direct consequence, the need of bigger optical elements, more complex instruments, and extremely expensive operational costs.

The evolution of the spectrographs used to discover and study exoplanets with the radial velocity method is a good benchmark to show this evolution. The first one, ELODIE, was built in 1993 in France and could easily be mounted, aligned and verified on a small optical bench. Thirteen years later, the development of ESPRESSO began. ESPRESSO is an ultra-high resolution spectrograph installed in 2017 at the Very Large Telescopes facility and composed by a series of subsystem developed by a consortium of height scientific institutes. Due to its size, this instrument has been mounted and aligned in-situ along an optical path of almost 100 m for each of the four arms.

A typical solution for the alignment of such a system consisted in the visualization of the optical path with a light source and a progressive alignment of all the elements along it using the light source as feedback.

Due to the tight requirements in terms of long-term stability, the typical optomechanical mounts with traditional push-pull systems were not anymore a feasible solution.

The use of stiff optical supports screwed to the optical benches and a full mechanical characterization of the optical elements with respect to mechanical references has been identified as a solution to fulfil all those requirements. As this kind of approach was innovative in the astronomical field, its feasibility had to be studied.

The aim of this thesis is to evaluate the viability of this method proposing a mechanical design and an alignment procedure able to guarantee the desired performances in terms of mechanical stability, optical quality, time needed for in-situ alignment, and mean time to repair.

A first trial has been performed with the ESPRESSO Front End Units (FEU) as their requirements and design made them a perfect test bench for the technique conceived. The mechanical design has been done focusing on long-term stability and fast installation of the whole system. Different alignment methods have been tested using a mix of mechanical and optical measuring systems and have been presented in chapter 1.

All the optical elements and the external interfaces have been characterized and aligned with respect to mechanical references using an Articulated Arm Coordinate Measuring Machine (AACMM) and an optical verification of the optical requirements has been done. The systems reached the expected performances after minor corrections have been applied using the feedbacks coming from the optical verification system.

To remove the need for those corrections and, as a consequence, the need for an optical feedback, decrease the alignment time and improve the predictability of the results a series of upgrades to the original

mechanical design and the alignment strategy have been proposed. Those included a new design of the optomechanical mounts, different references, and the characterization of the optical path of each element starting from the direct acquisition of the optical surface using a Cartesian Coordinate Measuring Machine (CMM).

The mechanical references play a fundamental role during the alignment, the integration, and the maintenance phase as they are used to define the position of the system with respect to the external interfaces and every relevant subsystem with respect to the system. Consequently, a good choice in terms of repeatability, flexibility, and measurement easiness has a direct impact on the optical quality of the system and the Mean Time To Repair. Different references have been tested using a dummy element and measuring it with an AACMM and a CMM to identify the best choice as a function of the chosen alignment strategy.

Once the alignment procedure has been defined the elements must be placed in the correct position via calibrated shims in a reasonable number of trials. To evaluate the practical limitations of this procedure, different repeatability tests of the mounting-dismounting procedure have been performed on the same dummy mount. The obtained results, shown in chapter 2, led to an improved version of the shims and the mounts already used in the ESPRESSO FEU.

Then, to align each optical element with respect to those references it is necessary to acquire a number of points on the optical surfaces and derive its optical characteristics. The reachable accuracy defines the optical quality of the system (e.g. position of the focal planes) and is a function of different inputs like alignment strategy, geometrical characteristics of the element, and environmental conditions. To evaluate if a fully mechanical alignment of the system is feasible, a software based on the actual characteristic of the machine has been developed and shown in chapter 3.

With such a procedure, another constrain to consider during the alignment strategy definition is related to the acceptable level of scratch and digs on the optics. Together with the accuracy, the optical quality of the system is function of the digs generated by the contact between the probing system of the CMM and the optical elements. Those digs could potentially modify the coatings or the substrates decreasing the throughput of the optics and deviate the rays (geometric scattering).

The size, depth, and number of the digs are function of the measuring strategy and the material involved. To quantify those parameters, first a measurement campaign has been performed to estimate the contact force generated by the CMM probing system in different conditions. To have a more general solution, the results obtained have been used to fit a theoretical model of the probing system. The measurements and the model are presented in chapter 4.

Using the obtained values as inputs, different substrates and coatings used in reflective and transmitting optics have been tested and the results are shown in chapter 5. Due to the high variability of the results, no theoretical model has been produced but a procedure has been defined.

To validate the results, a dummy optical system composed by refractive and reflective elements has been designed, built, and aligned with the CMM. The misalignments of the elements foreseen by the accuracy software have been compared to the data obtained with the multiple orientation technique on the CMM and the measurements performed with an interferometer. The obtained results are presented in chapter 6.

The data obtained during this research allowed for a definition of a purely mechanical measurement and alignment strategy of a system starting from its design (mechanical and optical) and requirements (deviation from the nominal optical quality, throughput reduction, and rays deviation).

The obtained results are going to be used in the next years as a guideline for the design and the alignment of the other astronomical instruments like SOXS for the New Technology Telescope (NTT) and the HIRES Front End for the Extremely Large Telescope (ELT).

1 Exoplanets, spectrographs, and the ‘alignment problem’

1.1 Introduction

The construction of an ultra-stable Radial Velocity (RV) machine like ESPRESSO (Echelle SPectrograph for Rocky Exoplanets and Stable Spectroscopic Observations) raise different technological and scientific challenges. The historical path leading to the instrument requirements is presented first. In order to minimize aberrations and, therefore, to reach the expected performances of an optical system like this one, the accurate alignment of all the optical elements is fundamental. The typical alignment methods presented are quite efficient in minimizing them but usually require an optical feedback and a continuous correction until the correct position of the element has been reached.

This can be a fast procedure when using push-pull systems for the alignment but the use of those systems would not have guaranteed the achievement of the very tight stability requirements of ESPRESSO.

For this reason, a fully mechanical alignment method is presented in the last part of the chapter.

1.2 Scientific and technological background

The first confirmed discovery of an exoplanet is dated 1992 when two of them where found around a pulsar (PSR B1257+12) using the Arecibo observatory radio telescope and the pulsar timing method [1.1]. Three years passed before the first exoplanet orbiting around a sun-like star was detected using the RV method [1.2]. This detection was performed with ELODIE, an echelle spectrograph working in the visible range and built in 1993 specifically for exoplanet detection.

As of today, thousands of exoplanets have been confirmed and other methodologies like microlensing, direct imaging, transit photometry, and astrometry have been developed. Most of them have been discovered using the transit photometry and RV methods (see Figure 1.1).

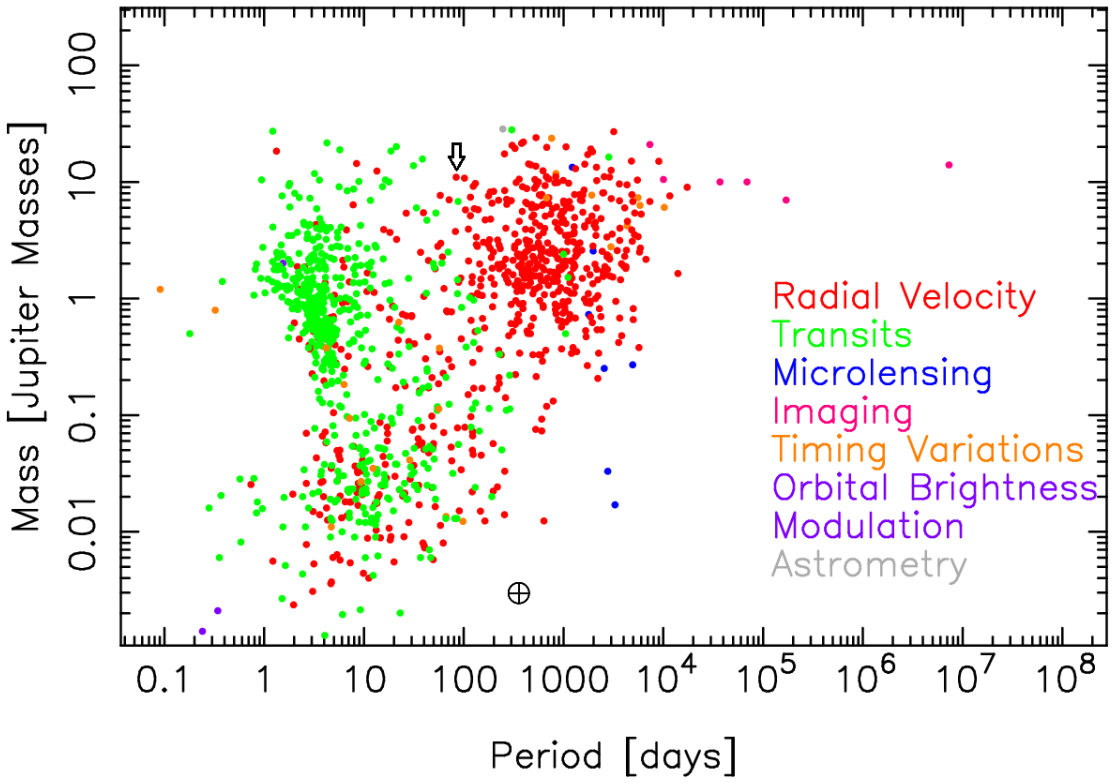

Figure 1.1 Confirmed exoplanets by discovery method as of March 2018. The earth is shown at the bottom as a reference. The arrow points to 51 Pegasi b. Adapted from [1.3].

The first one is done measuring the brightness of the star searching for periodical drops that can be related to a planet crossing between the host star and the observer. As it requires a quasi-perfect alignment between the orbital plane and the observer, only the detection of a little percentage of them can be expected.

The RV method uses the Doppler effect to measure the orbiting of a star around the centre of mass of its stellar system. As the component along the axis between the star and the observer is accounted, this method is only able to estimate the minimum mass of a planet.

The period and amplitude (in m/s) of the sinusoidal RV observed widely vary with the mass of the star and the planet, the distance between them, and the inclination of the planet orbit with respect to the observer line of sight. As an example, the RV of the first exoplanet discovered, 51 Pegasi b indicated by an arrow in Figure 1.1, was equal to 55.9 m/s (see Figure 1.2) while Jupiter and the earth respectively cause a movement of the sun of 12.7 m/s and 0.09 m/s. A longer period orbital can also complicate the RV measurement. Again, the one of 51 Pegasi b was only 4.23 days.

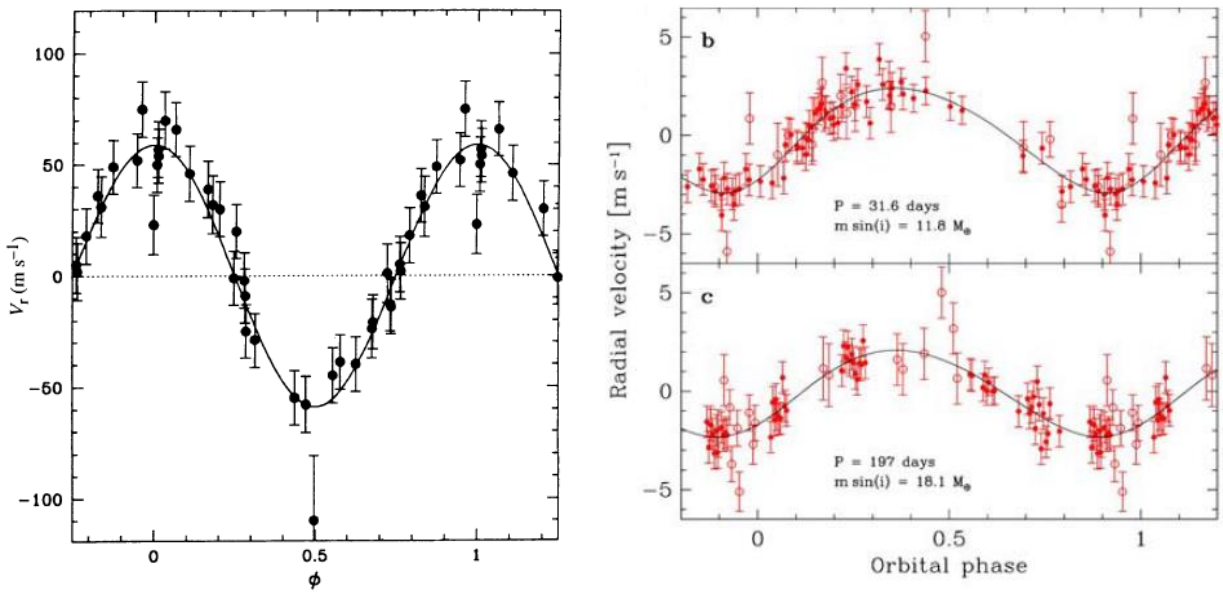

Figure 1.2 Orbital motion detected with the RV method. Left: 51 Pegasi b observed with ELODIE [1.2]. Right: two of the three planets in the HD 69830 system detected with HARPS [1.4].

This method was developed decades before the first discovery of an exoplanet. Instruments like CORAVEL where limited by an accuracy of about 200 m/s. The main disturbance source was the variable illumination of the entrance slit due to guiding, focus, imperfect axis of the telescope and calibration lamp variability [1.5].

In order to reach the 13 m/s accuracy obtained by ELODIE [1.7] different design strategies were introduced in its design: optical fibres to illuminate the spectrograph, fibre scrambling, isothermal environment, simultaneous calibration (with a Thorium-Argon lamp or a Fabry-Perot), sky subtraction, removal of every moving part, and use of an Exposure Meter to correct for earth velocity. Those elements remained a standard for the later RV spectrographs. The instrument is shown in Figure 1.3 (left). As a comparison, the echelle grating is the element shown in foreground and has a size of 408 x 102 mm^2.

In the next years, the instrument has been improved and the accuracy reached a value of 7 m/s but certain disturbances remained and a new RV instrument was developed. HARPS (High Accuracy Radial velocity Planet Searcher) first light in 2003 pushed the limit of RV detection down to a few m/s (see Figure 1.2).

The spectrograph is shown in Figure 1.3 and, even if it appears as a scaled up version of ELODIE (here the grating is a mosaic of two elements with a total size of 800x214 mm^2), it employs different improvements where the most noticeable ones are an operating pressure below 0.01 mbar and a long-term thermal stability around 0.01°C [1.8].

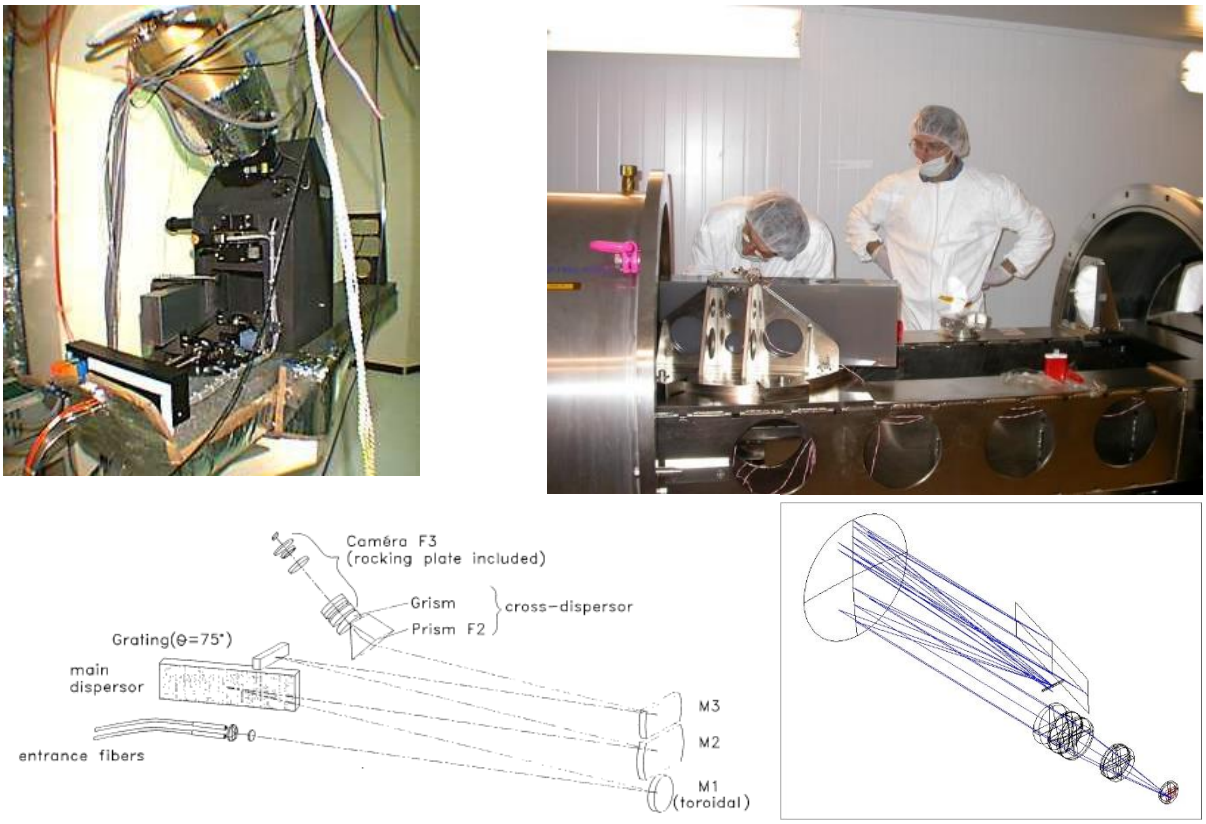

Figure 1.3 Comparison between ELODIE and HARPS. Left: picture and optical design sketch of ELODIE. Right: picture and optical design sketch of HARPS.

Those improvements led to the ability to study the so-called super-Earths, exoplanets with a mass smaller than 10 times the mass of the Earth. The detection of Earth-like planets located into the habitable zone, however, requires an even better accuracy of the instrument (about 0.01 m/s).

For this reason, soon after HARPS started its operations, an evaluation the main error sources begun. Detailed information of the results are shown in [1.4] and included the ThAr calibration lamp, photon noise, guiding noise, stellar oscillation noise and stellar activity-related jitter.

Some of those errors are intrinsic in the observed star like the stellar oscillation (pressure modes with periods ranging between minutes to hours) and stellar jitter (surface magnetic phenomena with time scales of tens of days) or to the finite number of photons collected (photon noise). Those effects must be reduced a posteriori e.g. averaging different observations.

From a more technologically oriented point of view, improvements can be done using a Laser Frequency Comb for the simultaneous calibration, increasing the environmental and mechanical stability, and stabilizing the spectrograph illumination.

All those challenges have been faced by the HARPS successor, ESPRESSO.

1.2.1 ESPRESSO

The ESPRESSO spectrograph has been installed at Paranal (Chile) with the goal to improve the RV precision down to 0.01 m/s.

The overall optical design is more complicated as, in order to guarantee the needed environmental stability, the spectrograph has been placed into the Combined Coudé Lab (CCL) (see Figure 1.4) [1.9]. To fed it, the Coudé Train (CT) [1.10] collects the incoherent light from 1 to 4 UTs (Unit Telescopes) of VLT (Very Large Telescope) sending it to the Front End Units (FEUs).

The FEUs are built around the convergence point (see Figure 1.4) and should inject the light coming from the CT or the Calibration sources into 6 scientific fibres depending on the observation mode chosen [1.11].

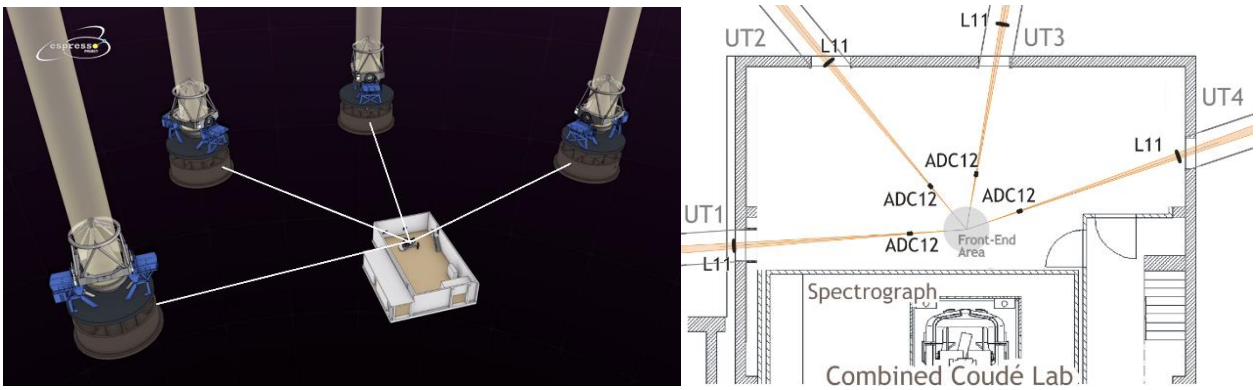

Figure 1.4 Left: view of the 4 UTs and the CCL where the ESPRESSO spectrograph will be installed. Right: CCL detailed view where the positions of the Front End and of the Spectrograph are shown.

The FE is shown in Figure 1.5 and is composed by 5 equal FEUs (4 in operation + 1 spare) used to inject the light beam coming from the star, the sky or the calibration source into the fibres. A toggling system is used for the selection of different operative modes. More details can be found in [1.11] and [1.12].

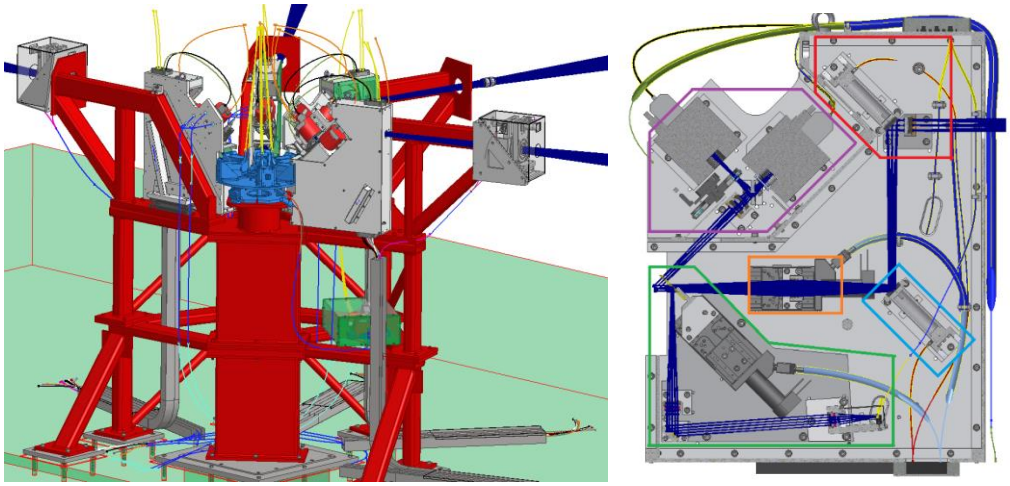

Figure 1.5 Left: overall view of the FE with the FE structure (red), the toggling system (light blue) and the FEUs (grey). Right: detailed view of one FEU. The light goes from top right to centre left.

Each FEU is composed by a calibration part (green box in Figure 1.5, right), a guiding part (purple), and a main path part (rest of the optomechanical elements). The main path consists, from the telescope to the fibre, in a Pupil Lens (PL), a pupil mirror stabilization unit (PSU), a field mirror stabilization unit (FSU) and a refocuser (RL). The guiding part is composed by a field lens mirror (FLM), a group of guiding lenses (GL) and two CCD sensor (TCCD) on the field and pupil plane.

Once the light is injected into the fibre, a scrambler is used to improve the illumination stability as the light goes into the spectrograph shown in Figure 1.6. The spectrograph is similar in concept to the HARPS one,

with two main differences: the light is split in two cameras using a dichroic and the pupil is sliced and superimposed on the grating to reduce its dimensions. Using this solution, coupled to anamorphic compression, the echelle grating dimensions have been reduced from an original size of about 1800x400 mm^2 to the 1270x210 mm^2 element shown in Figure 1.6.

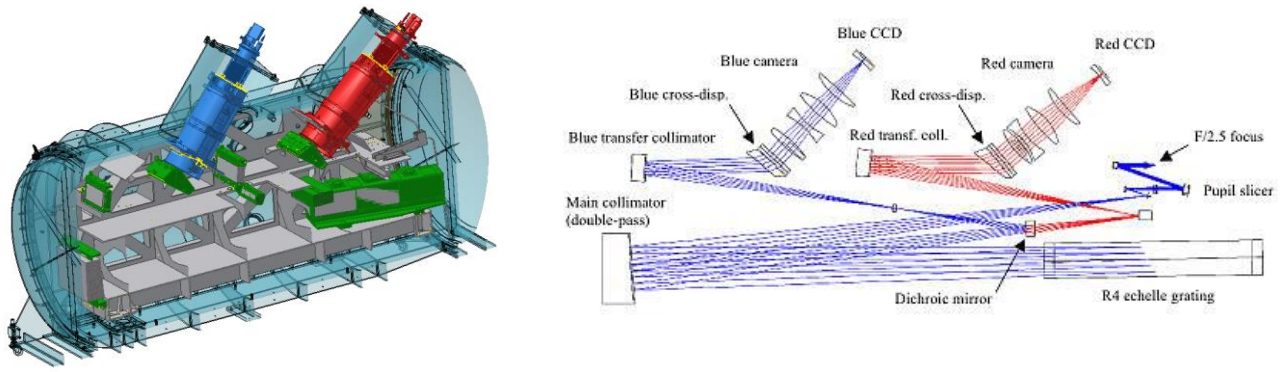

Figure 1.6 ESPRESSO spectrograph. Left: overall view of the mechanical design. Right: optical path.

1.3 Typical alignment and adjustment methods

One thing to keep under control while preparing the optical and mechanical design of an instrument is the alignment procedure. Designing a system without thinking about how to align it can translate in a longer integration process where most of the time is spent searching for the cause of a certain unpredicted behaviour. In the worst case, this can ultimately lead to an instrument with reduced optical performances due to the aberrations introduced, or to the needs of redesigning part of it.

In the followings, those aberrations will be listened and their typical sources put in evidence. Thereafter, different methods typically used to align an optical system and adjust the optomechanical mounts will be shown.

Each of them has it points of force and weakness and they are continuously evolving following the improvements in manufacturing capabilities of optical and mechanical parts, the introduction of new measuring systems, the development of new informatics tools and, last but not least, the requirements derived by the desires of the scientific community.

For this reason, an exhaustive description of all of them is impossible and only the main categories will be presented. It is important to notice that, even inside the framework of a single project, the accuracy and repeatability requirements for different elements can be extremely different. Therefore, when designing the alignment procedure and the adjustment systems of an instrument, a combination of those methodologies and technologies could be applied.

1.3.1 Aberrations in optical systems

No optical system is perfect due to multiple reasons. Those can be traced not only to alignment errors, but also to optical design choices, intrinsic characteristics of the materials used, and manufacturing deviation from the nominal shapes.

A convenient way to separate those errors consists in the use of a wavefront expansion ([1.13], [1.14]), a power series expansion orthogonal to a circular disk. The most common one in the optical field is the Zernike expansion, where the wavefront error can be expressed in polar coordinates as ([1.15])

$$W(r,\theta) = \sum_{n,m} C_n^m R_n^m(r)\cos(m\theta) \;\; for\; m \geq \tag{1.1}$$

$$W(r,\theta) = \sum_{n,m} C_n^m R_n^m(r)\sin(m\theta) \;\; for\; m < 0 \tag{1.2}$$

In this formulation m is the angular frequency, n is the radial order, r is the unit circle, C_n^m denotes the coefficients, and $R_n^m(r)$ is calculated as

$$R_n^m(r) = \sum_{l=0}^{\frac{n-m}{2}} \frac{(-1)^l (n-l)!}{l!\left[\frac{n+m}{2}-l\right]!\left[\frac{n-m}{2}-l\right]!} r^{n-2l} \tag{1.3}$$

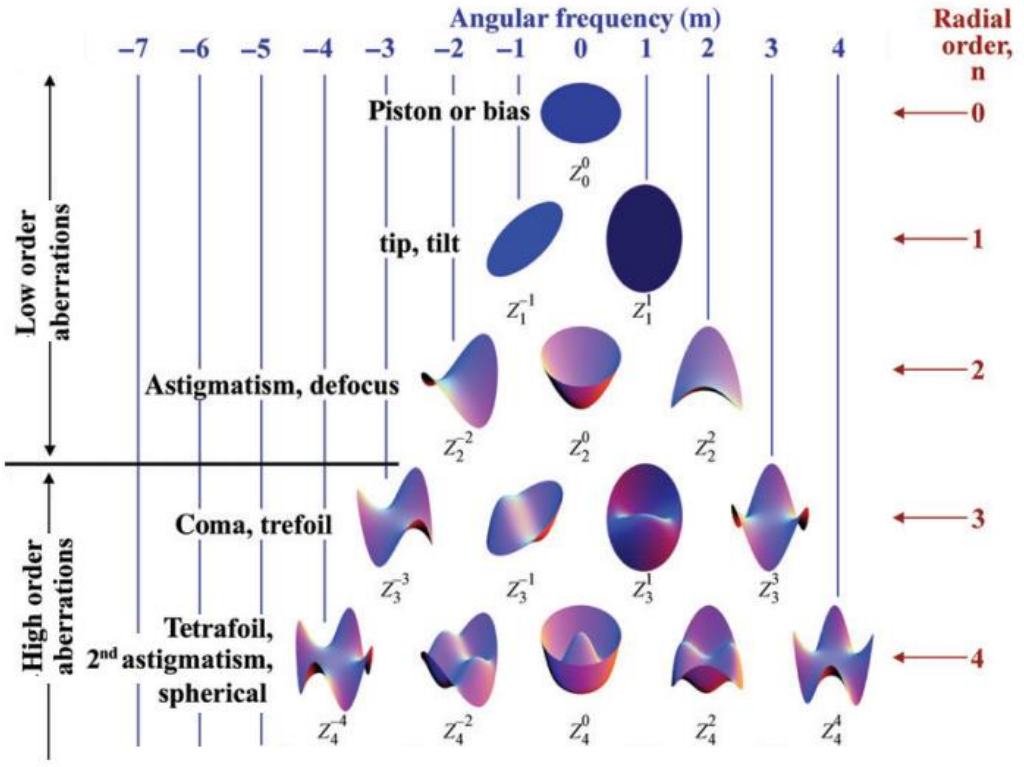

Figure 1.7 Surface plots of the first five orders of Zernike polynomials. Adapted from [1.15].

As seen in Figure 1.7, the low order terms of this expansion are defocus, wavefront tilts, and astigmatism while third and fourth order terms include spherical aberration and coma. Higher order terms have no significant role in the alignment process and will be ignored in this discussion.

Field curvature and image distortion also occur in optical systems and, using the Zernike polynomials, can be expressed as field-dependant defocus and tilt.

1.3.1.1 Defocus

The defocus is the displacement of the actual image plane from the nominal one. An example is shown in Figure 1.8. As the image is contained inside the airy disk, no affect can be noticed for small defocusing. For higher values, instead, the spot size will increase with an effect depending on the f/# of the element, the lens shape, and the resolution required at the image plane.

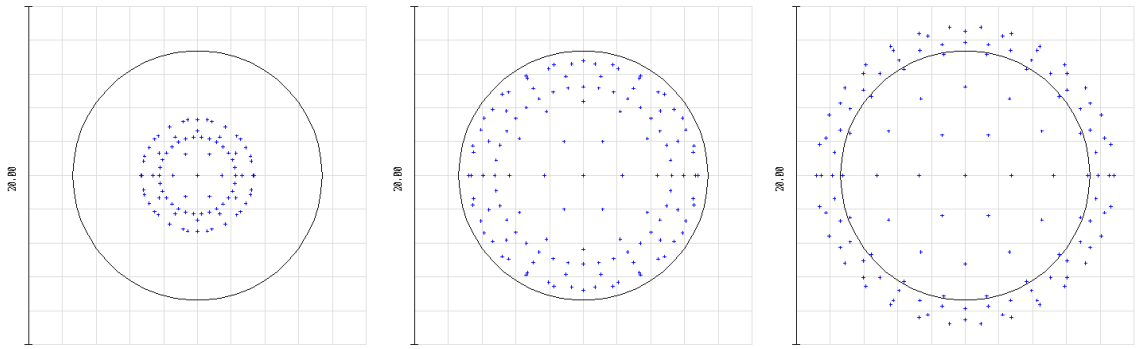

Figure 1.8 Spot size generated by a lens with f/#=8.8. From left to right: best focus, focal plane moved 0.1 mm toward the lens, focal plane moved 0.15 mm in the same direction. The black circle represents the Airy disk.

Displacing in the focal direction of a certain optical element is performed during the operation of the instrument to compensate for environmental variation or during the alignment. In this phase, it is used to compensate for geometrical and optical elements deviations from the design values during manufacturing and to compensate for misalignment of other elements in the optical train. The equations relating optical element and focal plane positions can be found in [1.14] and will be presented in section 3.5.4.2.

1.3.1.2 Wavefront tilt

Another aberration mainly related to the alignment is the wavefront tilt. This effect can arise from the decentring of a refractive element or system like in Figure 1.9, or the tilt of a reflective one.

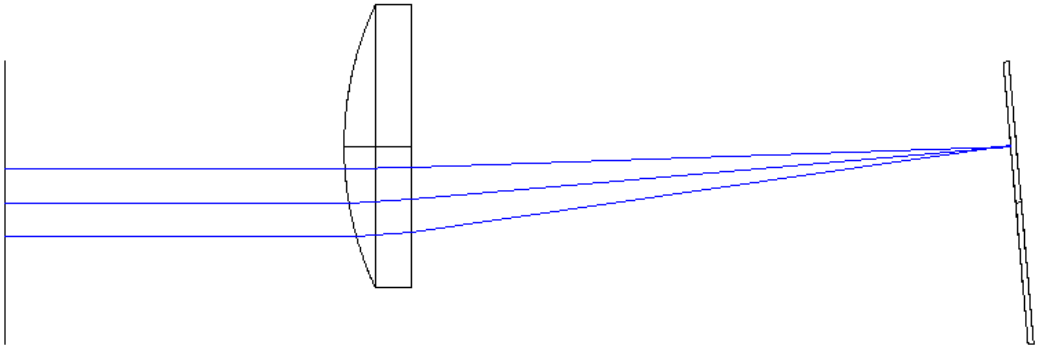

Figure 1.9 Wavefront tilt related to the decentring of a lens.

The equations describing this effect using paraxial approximation can be found in and will be presented in 3.5.4.2.

1.3.1.3 Spherical aberration

In a paraxial model a spherical surface focuses the light on a single point. As the light beam is moved away from the paraxial line, the focus is moved closer to the lens blurring the image crated in the focal plane.

An example of spherical aberration generated by a plano-convex lens is shown in Figure 1.10. This aberration is intrinsic in a certain design and can be reduced using aspherical surfaces instead of spherical ones or decreasing the angle of incidence. The main drawback of the first solution is related to the increase cost of the element while the second one requires more optical elements with smaller power and, therefore, increases the throughput losses due to the bigger number of surfaces in the optical path.

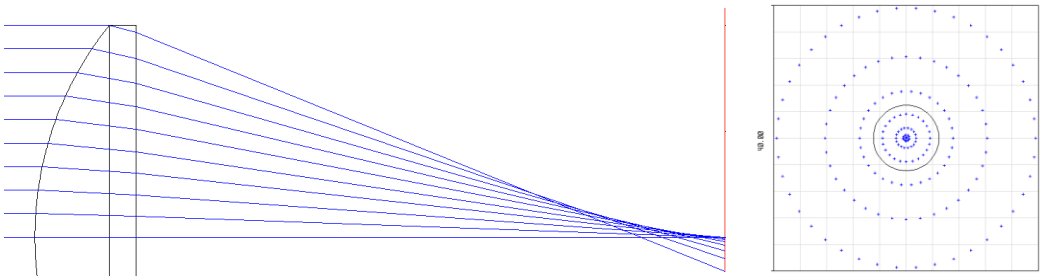

Figure 1.10 Left: spherical aberration. Right: spot diagram in the paraxial focus, the black circle represents the Airy disk.

As the spherical aberration goes with the cube of the maximum distance from the chief ray, while aligning elements with high spherical aberration using optical methods, a reduction of the spherical aberration is usually obtained using a smaller pupil size and, therefore, approaching the results expected by a paraxial calculation.

1.3.1.4 Coma

If the beam enters the optical with an angle different from zero, the magnification varies with the aperture. The spot generated on the focal plane has the typical comet-like shape as shown in Figure 1.11. As in a typical optical system the field of view is finite, a certain degree of come can always be expected. However, a similar effect can also be related to a tilt of the optical element.

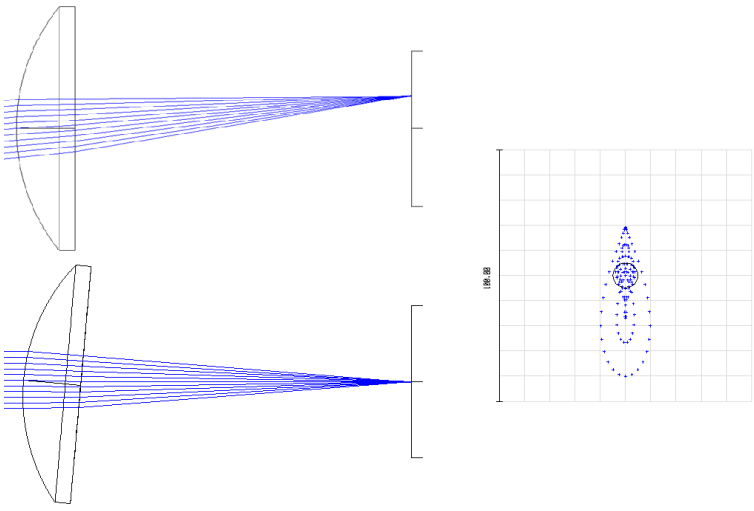

Figure 1.11 Left: coma generated by an off-axis field (top) or a tilted lens (bottom). Right: spot diagram of the 2 cases.

1.3.1.5 Astigmatism

If rays laying on the meridional plane are focused at a different distance than the sagittal ones, a certain amount of astigmatism is present and the image in one of the two foci will have an elongated shape. The overall best focus will be located in an intermediate position of the two and will have a bigger size than the nominal one.

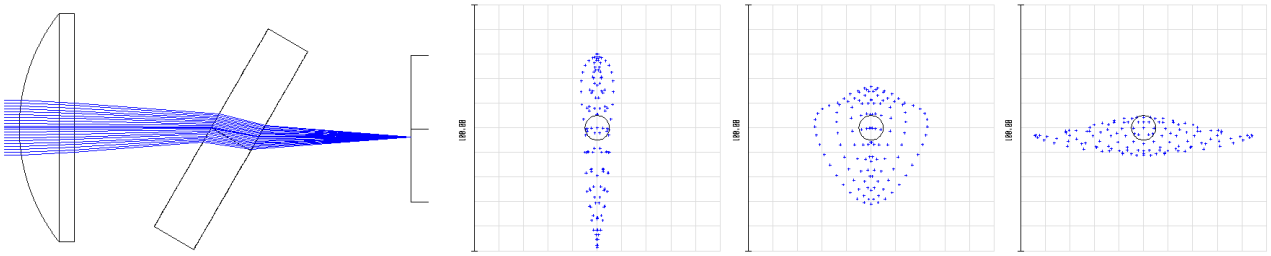

Figure 1.12 Off-axis astigmatic image due to a tilted plane. Right: spot diagrams at different focal positions.

This aberration appears when the slope seen by the tangential rays impinging on a surface is different from the one seen by the sagittal rays and can be seen in in the nominal optical design when an oblique cone of light is incident on an element (see, as an example a tilted plane in Figure 1.12).

Other sources of it can be traced to manufacturing errors (e.g. cylindrical shape of the surface) or misalignments leading to heavily tilted optical beams or surfaces.

1.3.1.6 Field curvature, distortion, and chromatic aberration

A lens forms an image on a curved surface as can be seen in Figure 1.13 (left). This effect is stronger with elements with shorter focal lengths and high refractive index and is corrected by design combining optical elements with positive and negative power: an example is the use of a field lens near the focal plane (Figure 1.13, right).

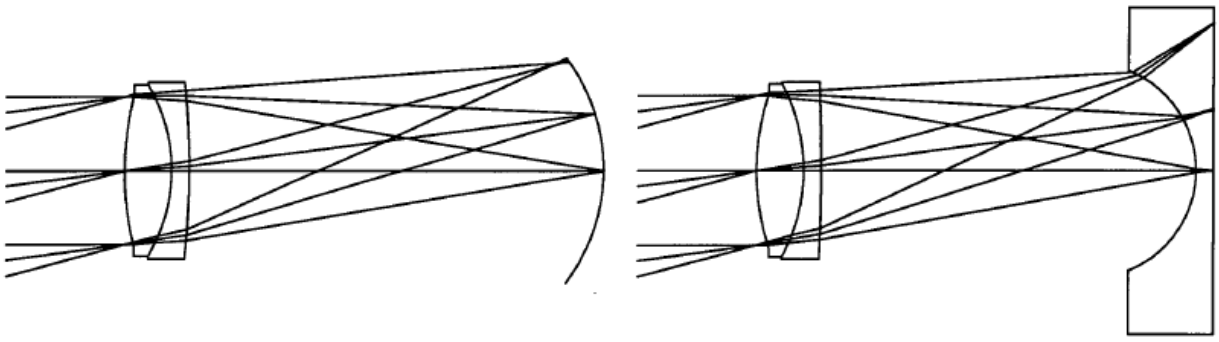

Figure 1.13 Left: curved field. Right: correction using a field lens. Courtesy of [1.1].

Distortion is the change of height in the image plane for different distances from the paraxial condition. It is intrinsic in the optical design and is proportional to the thickness of the lenses, their position with respect to the aperture stop and, in a more general way to the size of the field of view (cubic relationship).

The chromatic aberration is related to variation of the refractive index with the wavelength and it is an unavoidable effect when using refractive elements. The axial colour case (Figure 1.14) can be heavily reduced

using achromatic doublets composed by a crown glass with positive optical power followed by a flint glass element with negative optical power. Lateral colour can also be noticed in large field of view systems and caused, again, by the variation of refractive index.

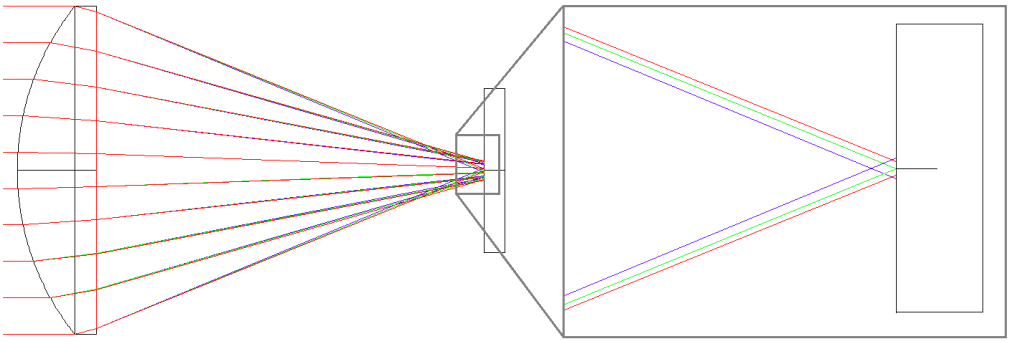

Figure 1.14 Lens focusing lights at 3 different wavelength (411 nm, 522 nm and 633 nm) with a detail on the focal plane.

1.3.1.7 Image displacement

As already seen in Figure 1.12 a titled refractive element introduces astigmatism. Another effect, more important with the small angle errors typical of the alignment phase, is the lateral displacement of the chief ray, the so-called pointing stability. Even if it cannot be properly considered an aberration, this effect is extremely important as it will move the position of the chief ray on the focal plane and will cause an off-axis injection of the light in the subsequent optics, leading to other aberrations like tilt and astigmatism. An example is shown in Figure 1.15 with a tilted window. The formulae describing this effect will be detailed in 3.5.4.2.

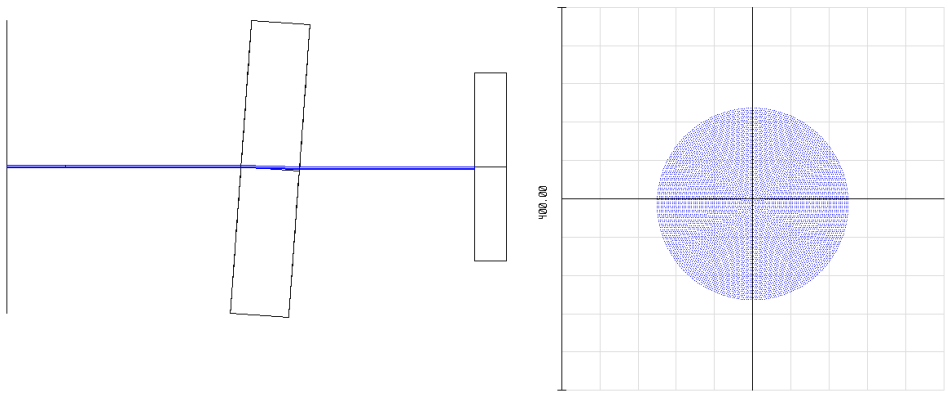

Figure 1.15 Lateral shift due to an optical element tilted of 10 arcminutes. Left: optical system (tilted exaggerated by a factor 25). Right: collimated beam displacement.

1.3.2 Alignment of the optical path

Different techniques can be adopted to align optical systems, trying to have an optical quality and optical planes positions as close as possible to the nominal ones. Those techniques widely vary in terms of complexity, alignment time, required tolerances on the single optical element, and equipment needed. Moreover, some of the techniques can be applied only when certain types of optical elements are involved. The main techniques and instruments are presented here and are the drop-in, the laser, the alignment telescope, the rotary table, the autostigmatic microscope, the interferometer and the Computer Generated

Hologram alignments. As different elements in a system can have different alignment accuracy requirements and sensitivities, a combination of them is usually employed.

The fastest method by far is the '**drop-in**' one [1.17]. It fully relies on the optical and mechanical tolerance analysis and it can be used when the alignment tolerances are not extremely demanding.

This method requires the mechanical references of the optical element to be well defined and, if the tolerances on the mounting interfaces have adequate tolerances, the optical element can be mounted without any mounting correction.

The approach widely varies with the optical element involved. In the lenses case, the element is mounted inside the barrel and subsequently mounted into the system. In addition to the typical mechanical tolerances, the coaxiality of the optical and mechanical axis and the auto centring capabilities of the barrel [1.19] can be limiting factor for this approach.

Another interesting application of this method is applicable for aluminium barrel mounted transmission optics (see [1.20]). Using CNC and a diamond turning machine both the optical surface and the mechanical interfaces are machined together. This leads to mechanical references extremely well characterized with respect to the optical axis.

The clearest advantage of this method is that the alignment time is virtually reduced to zero. However, its application is limited by both the optical and mechanical tolerances obtainable. The limiting factors of tighter optical tolerances are the cost and the interrelation between tolerances [1.21]. If a commercial grade tolerance is sufficient, using best practices is enough to reach them while high precision tolerances require different monitoring and measurements during the production phase, increasing the cost by a factor 2 and the delivery time. Moreover, most of the characteristics like surface power, surface irregularity, centre thickness, and scratch/dig are interrelated and, if none of them can be relaxed, the possible corrections applicable by the optical manufacturer are limited. With only one of them out of specification, it could be necessary to restart the manufacturing from the scratch, again increasing costs and delivery time.

Another critical factor is the mechanical tolerances and is related to goalpost and tolerance stackup. The first one states that, if the manufacturer has to reach a certain tolerance range it will do it until he is confident that, considering the accuracy of the working machine, the obtained value is inside the acceptable value. This operation is done to both save time and allow for subsequent corrections. The consequence is a positive bias in machining and a negative bias in addictive manufacturing that is acceptable for a single element (if the tolerancing is correct) but can be critical when this is applied to all the elements. The same result is related to the intrinsic bias of the machine, e.g. non-squareness of the moving axes or bending of the tool. If the mechanical supports are machined with a similar procedure, this bias will directly translate to the pieces.

One solution is to perform a tolerance analysis with a worst-case approach instead of a statistical one, tightening the tolerances until the manufacturing of the pieces is no longer possible.

The problem of tolerance stackup is obvious considering a series of optical elements mounted in a barrel with high-precision spacers between them. Increasing the number of elements will require tighter and tighter tolerances on manufacturing of spacers and optics with the same problems presented before.

A second solution applicable for a limited number of systems employs the direct installation of the elements on the optical bench using a **laser** and a series of targets. The laser is aligned to the first two targets using a semi-reflective one near it and another one as far away as possible from the first one.

Then, the optical elements are inserted into the system one by one and aligned using subsequent targets. If the system is mainly composed by elements without optical power like mirrors, windows, and dichroic, the alignment can be performed checking for the spot position in different locations with pinholes or crosshairs.

As a last step, the elements with power are inserted into the system and the focus positions are checked with an opaque element or a TCCD/CMOS sensor.

The tilt of the beam is checked placing dummy mirrors in autocollimation and looking at the return of the spot on the first target. Right angles are obtained using pentaprisms with the first surface, again, aligned to the incoming beam in autocollimation [1.22].

This alignment method is typically used when aligning systems in a laboratory and its accuracy is strongly limited by the capability to align the targets and by the need of long arms to be able to see angular misalignments on the first target.

A more rigorous method includes the use of an **alignment telescope**. The alignment telescope is a cylindrical tube containing a series of optical elements, a light source, and two targets well aligned (a few arcseconds in angle and a few microns of concentricity) to the mechanical support [1.22]. A manual focusing system is included to work in retroreflection or autoreflection. In both conditions, one of the two target will be in focus.

The main difference between the two conditions is that retroreflection is insensitive to the rotation of the optical surface while autoreflection is tilt sensitive.

The alignment of a refractive element is performed in an iterative way. The alignment telescope is focused on the two centre of curvature of one of the surfaces of a lens and the lens support is rotated and moved until the image of the bullseye pattern centred in both cases. This condition happens only when both the centres of curvature lie on the line defined by the alignment telescope. Aligning refractive surfaces requires the centration of the only centre of curvature and, if the element is a flat mirror one, the alignment telescope is placed in the so-called autocollimation. In this case, the centration of the element can be performed in autoreflection displacing the element until a fiducial placed near the optical surface is centred to the bullseye pattern.

This alignment procedure is quite straightforward, even if time consuming, for in-line systems while, in case the system has a few folding mirrors, different accessories like pentaprisms and retroreflectors can be used. The same principle can easily applied with different surfaces like rotationally symmetric aspheric elements while for off-axis elements its use becomes more complicated (see [1.23] as an example).

Another drawback of this principle is the low control on the focus position. This condition can be roughly checked with a dummy flat mirror only when the beam is expected to be collimated at the exit of a series of elements.

A fourth method include the use of an **high precision rotary table**, usually an air bearing one, and is widely used by the optical manufacturer for the alignment of single elements inside a support or the creation of multiple element lenses. At first the mechanical support where one of the two optical surfaces will be mounted is centred to the rotation axis of the rotary table with a dial gauge or a similar system. Once this operation has been performed the centre of curvature of the contacting surface will lies on the rotary table axis. The alignment of the second surface is done rotating the table and measuring the height variation with a dial gauge or a similar instrument out of the clear aperture or measuring its slope in the most convenient location with a laser and a CCD/CMOS camera. The objective is to have this value constant during the table rotation and this is obtained rotating the element around the centre of curvature of the first surface. As soon as this is obtained, the centre of curvature of the second surface is located along the rotary table axis and the support can be removed from the machine or another element can be added to the system.

In order to integrate the element or the group of elements into the final system, this method requires a good knowledge of the cell position with respect to the spindle axis. This information can be obtained with a careful design of the external support, a characterization of the table plus the support system or, as usually done by the optical manufacturer, performing a final machining of the support using the rotary table as a lathe.

The position of the element in the rotation axis direction can be obtained measuring the distance between a reference plane placed on the table (or the table itself) and the intersection of the axis with the second surface of the element.

Infinite variations of this method are possible and two of them are presented as an example in Figure 1.16: in the first one, the fringes generated by a laser beam impinging on the two surfaces are used while the second one involves two autocollimators with different refocusing lenses. All of them, however, are based on the principle that the centres of curvature must lay on the rotation axis of the rotary table that, therefore, must have the lowest possible values of wobble and eccentricity.

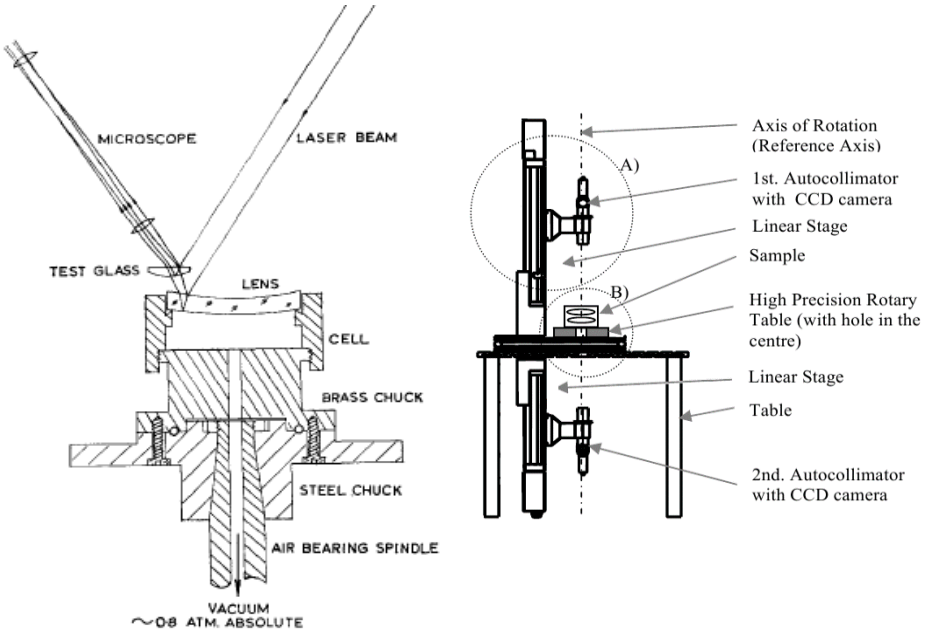

Figure 1.16 Alignment of optical elements with a rotary table. Left: using fringes from the two surfaces and a laser beam. Courtesy of [1.24]. Right: using a point source of light and an external positive lens. Courtesy of [1.25].

The main drawback of this system, apart of the expensiveness of the instruments required, is the capability to align only rotationally symmetric elements or systems. It the overall system is a 2D or 3D one the single elements or group of elements must be characterized with respect to the spindle axis and mounted together using a different method.

An evolution of the previous method, similar to the one presented in [1.25], includes the use of an **autostigmatic microscope**. The Point Source Microscope (PSM) is an example of this instrument and, in addition to a full field sources, includes a point light source conjugated with a CCD camera [1.26]. The point source microscope is a compact system that can be placed on a linear stage and aligned to a rotary stage. Moving the PSM with the linear stage it is possible to record its position and, therefore, obtain the centre of curvature of the two surfaces in autoreflection and, in retroreflection, the surface of the first lens, the optical centre thickness, and the back focal length [1.27].

With those redundant information, it is possible to solve explicitly the equations of the lens and to obtain a better estimation of radius of curvatures, central thickness, and index of refraction of the glass [1.28].

Depending on the optical system to align, it is also possible to insert a relay lens to avoid the use of a second PSM mounted in the opposite direction than the first one

The same result can be obtained using an **interferometer** equipped with a transmission sphere. The only difference is that, as this instrument is usually quite bulky, the optical elements will be moved on the linear stage.

This system has the usual limitation on 2D and 3D system. This problem has been overcome carefully placing a series of sphere in the nominal centre of curvature of all the optical elements foreseen. For each element, one or two PSMs have been positioned is autoreflection on the spheres defining an optical element. Once the PSMs have been placed and the metallic spheres removed, the optical system has been aligned until the PSMs are, again, inn retroreflection with the element itself.

Also in this case different variations must be adopted depending on the optical system design. One example could be the use of dummy concave mirrors to align flat mirrors or the use of coma and astigmatism to find the best alignment condition. All those techniques are shown in [1.29].

A recent development in optical alignment includes the use of **Computer Generated Holograms** (CGHs). A CGH is a diffractive pattern applied to a glass substrate that modifies an incoming beam creating different wavefronts that can be used for different purpose.

Two meaningful examples are shown in Figure 1.17. The one in the left shows a CGH with different separated zones: the external ring and the small rectangle are used to align the CGH itself to the interferometer while the other rectangular parts and the circular spots create reference marks for the centration of the optic to align. The central part, lastly, act as a null lens for the aspheric surface to measure.

The one on the right is based on amplitude dividing multiplexing. The whole surface generates four in-axis diffraction limited spots defining a certain optical axis. One is used to align a TCCD/CMOS sensor in the best focus while the others are used for the alignment. Once each element is inserted in the optical path one of the spots must be in focus with the sensor without aberrations. This information can be used to correct the alignment of the element until the spot is diffraction limited and there are no aberrations. Once this result is obtained, a second optical element is inserted and a third spot is used for the alignment.

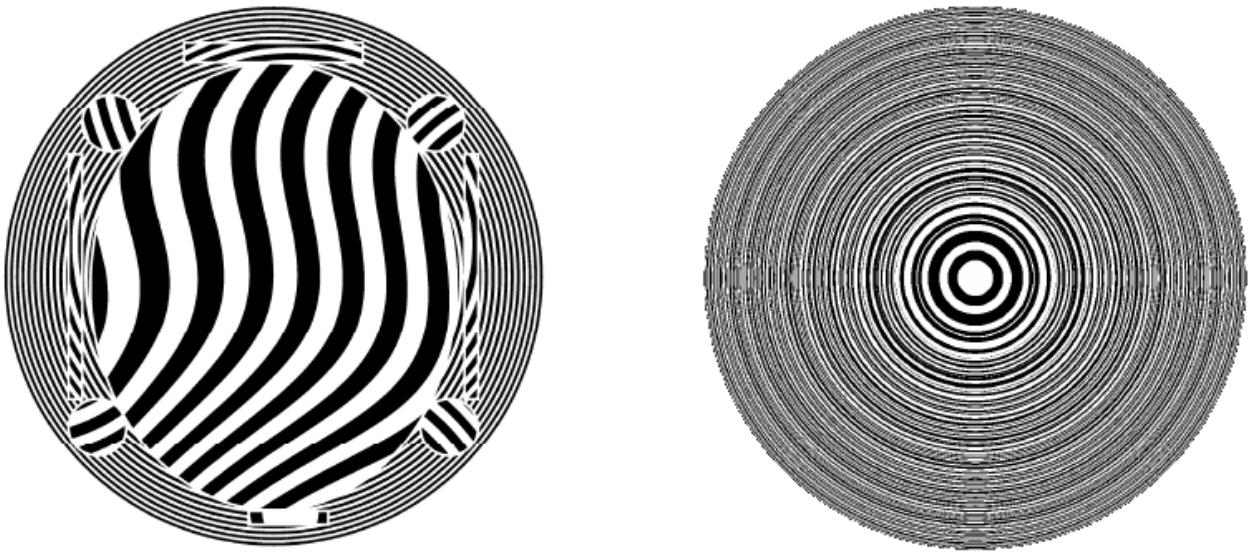

Figure 1.17 CGHs used for alignment. Left: space dividing multiplexing. Right: amplitude dividing multiplexing. Courtesy of [1.30].

The powerfulness of this approach is compensated by the need of one or more CGH specifically designed to align a certain group of lens.

1.3.3 Adjustment systems for optical elements and integration methods

The design of the interfaces between optical elements and the rest of the system and the alignment systems are widely discussed in literature (see [1.17], [1.20], and [1.21]).

Choosing one particular mounting method is dependent on a number of factors. A non-exhaustive list can include environmental conditions, materials choice, optical elements involved, performance requirements, and maintenance plan.

The main environmental conditions to take into consideration are working temperature, temperature variation, working pressure, environmental contamination, vibrations (in operations and during transportation), humidity and, in a broader sense, the direction of the gravity vector. Choosing the materials for the optical elements, their size, and typology is usually done in order to comply with the requirements. The optomechanical mount are then designed to support them limiting the stress and ensuring enough stiffness and stability given the environmental conditions and the performance requirements.

Apart of that, the definition of the maintenance plan pays a fundamental role in the definition of the interfaces. In most of the low-cost commercial applications, the capability to replace effortlessly an optical component due to a failure is of secondary importance.

When designing an optical instrument to be installed on a ground telescope, instead, each optomechanical and optical element must be replaced minimizing the mean time to repair. The possibility to perform this operation by the technicians operating in-situ is a huge step in decreasing the down time of an instrument.

Also in this case countless approaches are possible. The simplest, but quite rare, condition is when the alignment tolerances of an optical element are looser than the manufacturing ones. In this case the element can be directly replaced without further alignment. This is possible if the interface on the instrument is a fixed one and the optical element has, for example, a barrel machined by the manufacturer together with the lens (see 'drop in' case in paragraph 1.3.2). A similar alternative consists in the alignment of a single element inside the optomechanical support and its final bonding. If the whole support must be removed (e.g. if it is mounted on a stage that experience a failure) it is still possible to remount it if proper optical or mechanical references have been established.

Apart of this particular case, the optomechanical mounts can be divided in two big families: adjustable and fixed. The first ones foresee an alignment system permanently mounted on them for all the significant degrees of freedom. During the integration phase, those supports are regulated and locked. If maintenance operations are needed while the instrument is in operation, those systems must then be fully realigned using a mechanical or optical feedback if no hard stops are foreseen.

The main drawbacks are related to the space needed for the alignment systems and its intrinsic mechanical weakness. This can lead to a low stiffness of the support and the related optic, critical for gravity variant systems, and a certain level of drift over time.

Fixed systems overcome those limitations, as they can be extremely compact and stiff. In this case, however, the alignment procedure can be quite complex as no orthogonal real-time alignment systems can be foreseen. Again, using hard stops can simplify the maintenance operations.

Another way to separate the optomechanical mounts typology are between non-kinematic, semi-kinematic, and kinematic systems. The first ones are generally avoided as they usually foresee the contact between large

mounting surfaces. High precision surfaces or systems with one of the two contacting surfaces extremely more flexible than the other are acceptable cases for this mount typology. Another, extremely common, use of non-kinematic systems is the flexures: even if the mounting and dismounting operations have a limited level of repeatability, they are able to compensate most of the environmental variations (e.g. temperature) without stressing the optical element.

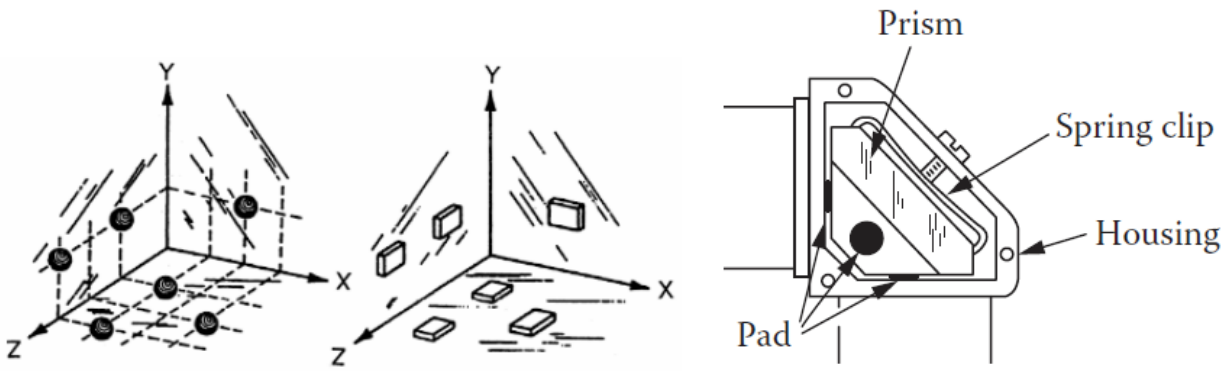

Figure 1.18 Example of prism supports. Left: schematic representation of a kinematic support, from [1.17]. Centre: schematic representation of a semi-kinematic support, from [1.17]. Right: non-kinematic support with flexible compensator, from [1.21].

On the opposite side of the spectrum, there are the kinematic systems where the contact between the optomechanical component and the rest of the system is point based (isostatic). This kind of system is usually more complicated and the contact forces can be critical for large system or if the contact surface is directly the glass of the optical element. The main advantage is the high repeatability and predictability of a movement applied in those points.

The third, intermediate, typology is the semi-kinematic system. The interfaces are small areas instead of points and, if the elements involved are stiff enough and the quality of the surfaces are kept under control, can maintain the same properties of a kinematic system heavily reducing the contact stress.

1.4 Proposed method

In order to design the ESPRESSO mounts and due to the high stability required, the use of adjustable mounts was not possible. A first solution could have been the use of adhesive to fix the elements after the alignment [1.31] but this concept creates a permanent mounting and has a risk of small misalignments during the curing process [1.32]. For those reasons, also this solution has been discarded.

The research activity, then, focused on the design of an optomechanical systems and an alignment procedure with the following characteristics:

- stiffness and stability for high RV precision,
- accurate alignment of the elements for the best optical quality,
- high reproducibility to decrease repair time in case of stages or platform failures,
- compact optomechanical mounts and alignment features for more packed systems,
- minimization of the needs of focal planes uniquely for alignment purposes,

- well known optical axis with respect to the mechanical interfaces.

Those requirements led to a new approach based onto dimensional characterization of optical and/or optomechanical elements and semi-kinematic interface adjustments over the 6 degrees of freedom using calibrated shims.

A preliminary study has been conducted on the ESPRESSO FEUs to exploit different strategies and highlight the most critical points.

The first two methods proposed were the integration by design without any characterization of the elements and the characterization of each optical element with an interferometer.

The 'by design' method consisted in the positioning of the optomechanical elements in their nominal positioning using an Articulated Arm Coordinate Measuring Machine (AACMM) and the subsequent correction moving lenses and mirror until the field was centred and in focus in the required location.

Even if the required corrections were kept as small as possible following the indications of the sensitivity analysis, they remained quite high due to the large number of uncontrolled uncertainty sources, both from the optical and the mechanical side, and the absence of control over systematic manufacturing errors.

The adjustments performed were able to position the focal plane in the correct location but, as this was obtained placing the optical elements in non-nominal positions, piling up all the misalignments resulted in an optical quality well below the requirements and this method has been discarded.

The second method consisted in the characterization of the interferometer beam and the positioning of each optomechanical element in front of it to obtain the desired information (see Figure 1.19).

More in detail the interferometer with a transmission sphere was placed in autoreflection with a reference sphere before replacing the transmission sphere with a transmission flat. A flat mirror was then aligned in autoreflection with the interferometric beam. Each optical element was aligned, then, to the beam until the retroreflection obtained was centred and in focus. As a final step the positions of 6 points were acquired on the mount and referenced to the beam defined by the sphere and the flat mirror.

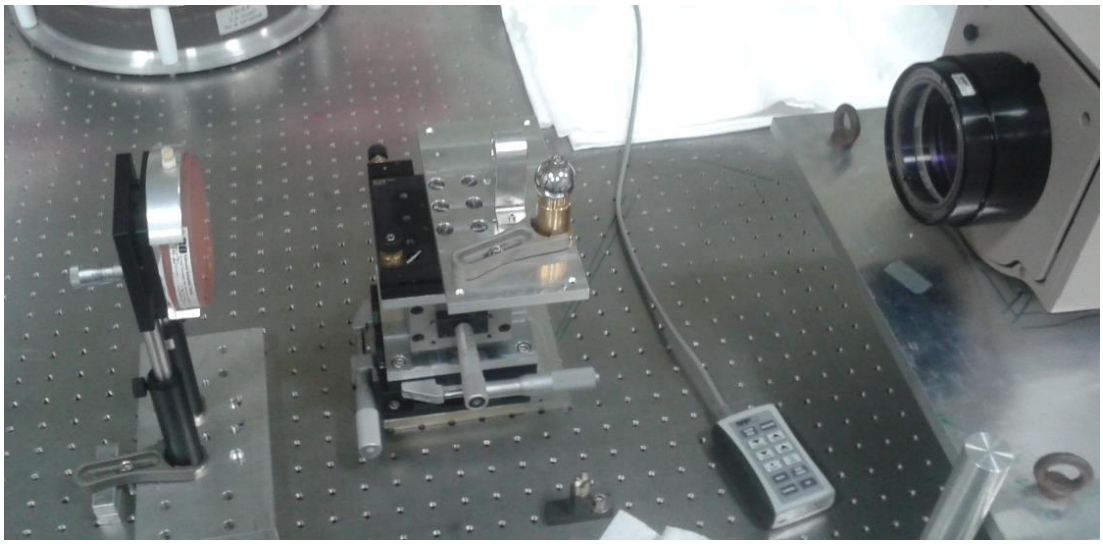

Figure 1.19 Characterization of an optomechanical element with the interferometer. On the right the interferometer and on the left a mirror used for the retroreflection of the beam. In the centre the sphere used for the zero definition and the optomechanical element (in this case a lens with its support).

This method has been also discarded as it was an extremely long process, there was a certain ambiguity between tip-tilt and decentring of the refractive elements, and the accuracy was decreased by the large number of measurements needed.

A third method was an evolution of the first one and consisted in a preliminary characterization of the mounts before the optical elements gluing and the installation on the bench. This allowed for the removal of most of the uncertainties providing sufficient optical quality in the final system. The procedure adopted will be detailed in subchapter 2.1 while the uncertainty analysis performed will be presented in subchapter 3.7.

As will be seen, part of the uncertainties like the ones related to the interface between optic and support and the wedge of the lenses cannot be tackle by this alignment procedure and a different method has been studied.

It consists in the alignment of the optical elements on the system mechanically measuring the optical surfaces and placing them in their nominal positions. A slightly different approach includes the mechanical measurement of the optical surfaces of a single element and their characterization with respect to a number of references followed by the final mechanical alignment on the system.

Both the approaches require the acquisition of the optical surfaces with an automatic CMM as this allows for a control of the contact forces applied.

To have a full understanding of the capabilities and limitations of this method, different tasks have to be completed. The first one is useful for all the methods presented in this section and consists in the repeatability evaluation to compare different types of mechanical references and to improve the practical mechanical capabilities considering different correction systems for the horizontal and vertical degrees of freedom in a fixed optomechanical mount. This part will be presented in chapter 2.

In order to predict the alignment capabilities of this process, the uncertainty of the CMM used plays a fundamental role. Experimental tests to separate the different sources have been performed and a software based on Montecarlo simulations has been developed and presented in chapter 3.

The proposed procedure is based on the contact between a probe and the optical surfaces. This operation is usually discouraged to avoid damages on the substrate or the coating. To have this risk fully under control, the forces applied in every condition must be known (chapter 4) together with their effect on the optics (chapter 5).

Being able to understand the effect of a CMM measurement on the optical elements in terms of accuracy and damage drives the mechanical design and allows for the definition of an optimal measurement and alignment strategy capable to meet all the requirements of the astronomical instrument.

Finally it is important to highlight that, even if it has been thought to be applied in systems requiring high stability like ESPRESSO, due to its flexibility it is advantageous to apply this method also in cramped systems where finding the space for complex optomechanical mountings is difficult.

1.5 References

[1.1] Wolszczan A, Frail DA. A planetary system around the millisecond pulsar PSR1257+ 12. Nature. 1992 Jan;355(6356):145.

[1.2] Mayor M, Queloz D. A Jupiter-mass companion to a solar-type star. Nature. 1995 Nov;378(6555):355.

[1.3] https://exoplanetarchive.ipac.caltech.edu/

[1.4] Lovis C, Pepe F, Bouchy F, Curto GL, Mayor M, Pasquini L, Queloz D, Rupprecht G, Udry S, Zucker S. The exoplanet hunter HARPS: unequalled accuracy and perspectives toward 1 cm s-1 precision. InGround-based and Airborne Instrumentation for Astronomy 2006 Jun 28 (Vol. 6269, p. 62690P). International Society for Optics and Photonics.

[1.5] Griffin R. On the possibility of determining stellar radial velocities to 0.01 km s− 1. Monthly Notices of the Royal Astronomical Society. 1973 Jun 1;162(3):243-53.

[1.6] Duquennoy A, Mayor M. Multiplicity among solar-type stars in the solar neighbourhood. II-Distribution of the orbital elements in an unbiased sample. Astronomy and Astrophysics. 1991 Aug;248:485-524.

[1.7] Baranne A, Queloz D, Mayor M, Adrianzyk G, Knispel G, Kohler D, Lacroix D, Meunier JP, Rimbaud G, Vin A. ELODIE: A spectrograph for accurate radial velocity measurements. Astronomy and Astrophysics Supplement Series. 1996 Oct 1;119(2):373-90.

[1.8] PHASE C. Setting new standards with HARPS. The Messenger. 2003;114:20.

[1.9] Mégevand D, Zerbi FM, Di Marcantonio P, Cabral A, Riva M, Abreu M, Pepe F, Cristiani S, Lopez RR, Santos NC, Dekker H. ESPRESSO: the radial velocity machine for the VLT. In SPIE Astronomical Telescopes+ Instrumentation 2014 Jul 8 (pp. 91471H-91471H). International Society for Optics and Photonics.

[1.10] Cabral A, Abreu M, Coelho J, Gomes R, Monteiro M, Oliveira A, Santos P, Ávila G, Delabre BA, Riva M, Di Marcantonio P. ESPRESSO Coudé-Train: complexities of a simultaneous optical feeding from the four VLT unit telescopes. In SPIE Astronomical Telescopes+ Instrumentation 2014 Jul 28 (pp. 91478Q-91478Q). International Society for Optics and Photonics.

[1.11] Riva M, Aliverti M, Moschetti M, Landoni M, Dell'Agostino S, Pepe F, Mégevand D, Zerbi FM, Cristiani S, Cabral A. ESPRESSO front end: modular opto-mechanical integration for astronomical instrumentation. In SPIE Astronomical Telescopes+ Instrumentation 2014 Aug 6 (pp. 91477G- 91477G). International Society for Optics and Photonics

[1.12] Aliverti M, Pariani G, Moschetti M, Riva M. Integration and alignment through mechanical measurements: the example of the ESPRESSO front-end units. In Ground-based and Airborne Instrumentation for Astronomy VI 2016 Aug 9 (Vol. 9908, p. 99087C). International Society for Optics and Photonics.

[1.13] Greivenkamp JE. Field guide to geometrical optics. Bellingham, WA: SPIE Press; 2004 Jan 20.

[1.14] Wyant JC, Creath K. Basic wavefront aberration theory for optical metrology. Applied optics and optical engineering. 1992 Jan 1;11(part 2):28-39.Schwertz K, Burge JH. Relating axial motion of optical elements to focal shift. InOptical System Alignment, Tolerancing, and Verification IV 2010 Aug 21 (Vol. 7793, p. 779306). International Society for Optics and Photonics.

[1.15] Lakshminarayanan V, Fleck A. Zernike polynomials: a guide. Journal of Modern Optics. 2011 Apr 10;58(7):545-61.

[1.16] Burge JH. An easy way to relate optical element motion to system pointing stability. InCurrent Developments in Lens Design and Optical Engineering VII 2006 Aug 31 (Vol. 6288, p. 62880I). International Society for Optics and Photonics.

[1.17] Yoder PR. Mounting Optics in Optical Instruments, w/CD.

[1.18] Fischer RE, Tadic-Galeb B, Yoder PR, Galeb R, Kress BC, McClain SC, Baur T, Plympton R, Wiederhold B, Bob Grant Alastair J. Optical system design. New York: McGraw Hill; 2000 Jun 30.

[1.19] Baumeister H, Bizenberger P, Bayler-Jones CA, Kovács Z, Röser HJ, Rohloff RR. Cryogenic engineering for OMEGA2000: design and performance. In Instrument Design and Performance for Optical/Infrared Ground-based Telescopes 2003 Mar 7 (Vol. 4841, pp. 343-355). International Society for Optics and Photonics.

[1.20] Kroes G, Kragt J, Navarro R, Elswijk E, Hanenburg H. Opto-mechanical design for transmission optics in cryogenic IR instrumentation. In Advanced Optical and Mechanical Technologies in Telescopes and Instrumentation 2008 Jul 23 (Vol. 7018, p. 70182D). International Society for Optics and Photonics.

[1.21] Ahmad A, editor. Handbook of Optomechanical Engineering. CRC Press; 2017.

[1.22] Dagnall RH, Pearn BS. Optical alignment. Hutchinson; 1967

[1.23] Ruda M. Alignment of off-axis aspheric surfaces. In Optical Alignment I 1980 Dec 31 (Vol. 251, pp. 29-37). International Society for Optics and Photonics.

[1.24] Carnell KH, Kidger MJ, Overill AJ, Reader RW, Reavell FC, Welford WT, Wynne CG. Some experiments on precision lens centring and mounting. Optica Acta: International Journal of Optics. 1974 Aug 1;21(8):615-29.

[1.25] Heinisch J, Dumitrescu E, Krey S. Novel technique for measurement of centration errors of complex completely mounted multi-element objective lenses. In Current Developments in Lens Design and Optical Engineering VII 2006 Sep 1 (Vol. 6288, p. 628810). International Society for Optics and Photonics.

[1.26] Parks RE. Lens centering using the point source microscope. In Optical System Alignment and Tolerancing 2007 Sep 12 (Vol. 6676, p. 667603). International Society for Optics and Photonics.

[1.27] Parks RE. Conjugate selection for precision lens centering. In Optical System Alignment, Tolerancing, and Verification IV 2010 Aug 21 (Vol. 7793, p. 779304). International Society for Optics and Photonics.

[1.28] Parks RE. Measuring the four paraxial lens parameters using an autostigmatic microscope. Applied optics. 2015 Nov 1;54(31):9284-6.

[1.29] Parks RE. Alignment of optical systems. In International Optical Design Conference 2006 Jun 4 (p. MB4). Optical Society of America.

[1.30] Burge JH, Zehnder R, Zhao C. Optical alignment with computer-generated holograms. In Optical System Alignment and Tolerancing 2007 Sep 21 (Vol. 6676, p. 66760C). International Society for Optics and Photonics.

[1.31] Lin WC, Chang ST, Lin YC, Cheng YC, Hsu MY, Huang TM. The alignment of the aerospace Cassegrain telescope primary mirror and iso-static mount by using CMM. In Optical System Alignment, Tolerancing, and Verification V 2011 Sep 13 (Vol. 8131, p. 81310M). International Society for Optics and Photonics.

[1.32] Daly JG, Daly DJ. Structural adhesives for bonding optics to metals: a study of optomechanical stability. In Optomechanical Design and Engineering 2001 2001 Nov 5 (Vol. 4444, pp. 177-185). International Society for Optics and Photonics.

2 Referencing and shimming for Optical Systems mechanical alignment

2.1 Introduction

Several sources of uncertainty can be identified in the searching for extra-solar planets with the RV method. While designing a new ultra-high resolution spectrograph (ESPRESSO [2.2]), the requirement for a lower guiding noise leads to a new concept of mechanical mount design and, therefore, a new alignment procedure.

To align such a system reducing as much as possible the number of iterations a good strategy consists in aligning all the elements with mechanical measurements and using the optical feedbacks only for the final verification of the system.

During the alignment of the ESPRESSO FEUs, the main factors influencing the number of mounting-dismounting iterations and, as a direct consequence, the alignment accuracy of each element has been proven to be the repeatability of the references relating the optical axis to the mechanic and the repeatability in the mounting-dismounting operation itself.

For this reason, after an introduction to the FEUs alignment, different tests carried out to define the best strategy for referencing an optomechanical system and quantify the mounting-dismounting repeatability are presented.

2.2 ESPRESSO Front End alignment

The first extensive use of this philosophy has been done during the design and the alignment phase of the ESPRESSO Front End Units (FEUs). A brief presentation on ESPRESSO and the FEUs has been done in 1.2.1 while a deeper explanation on its design can be found in [2.3] and the detailed alignment procedure is described in [2.4].

In this version of the design, every element was kept in position using 3 screws and 3 pins as shown in Figure 2.1 . Three sets of holed shims have been used to correct the first 3 degrees of freedom (clock, decentring and tilt in one direction) while 3 sets of rectangular shims have been used to correct the other 3 (focus, decentring and tilt in the other direction).

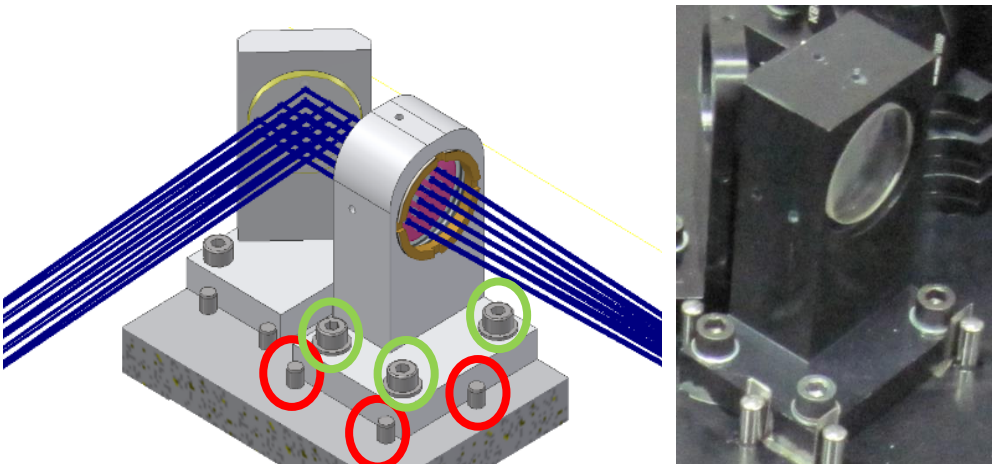

Figure 2.1 Left: CAD view of an optomechanical element with the 3 screws (green circle) and the 3 pins (red) highlighted. Right: the actual element wigh the shims below the screws and between the mount and the pin

As a first step of the alignment process, the optical axis and focus of each element has been defined using the data obtained from a Cartesian CMM.

In case of reflective elements (flat mirrors or dichroics), after gluing the element, several points have been acquired on the plane outside the clear aperture to define the tip-tilt and the focus of the object. The three remaining degrees of freedom have been defined using the external profile of the optical element.

For refractive elements, tip-tilt and decentring have been defined measuring the cylinder of the mount while the focus has been retrieved by the hard stop that will be later used to fix the lens. The clock has been chosen to minimize the difference in thickness between the holed shims. In this case, the optical element has been glued inside the mounting after the characterization of the mount itself.

To reference the geometry of each optical element with the geometry of its corresponding mount in all the degrees of freedom, 6 coordinates coming from 6 reference points have been acquired on the mount itself (see Figure 2.2).

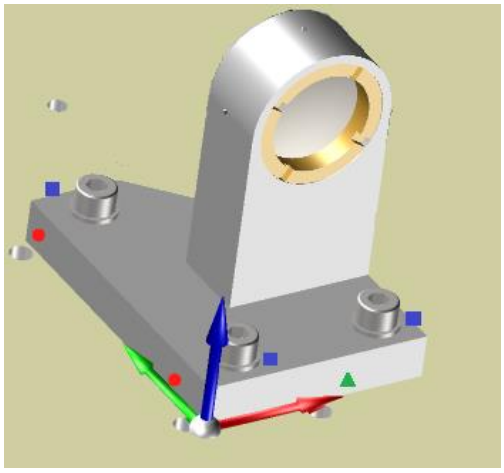

Figure 2.2 An example of a lens mount with the 6 points acquired. The 3 blue squares, the 2 red dots and the green triangle represent those points where only the Z, X and Y coordinates respectively have been used

The second step consisted in the positioning of all the elements in their nominal position measuring the reference points with an AACMM and correcting their location using the holed and the rectangular shims.

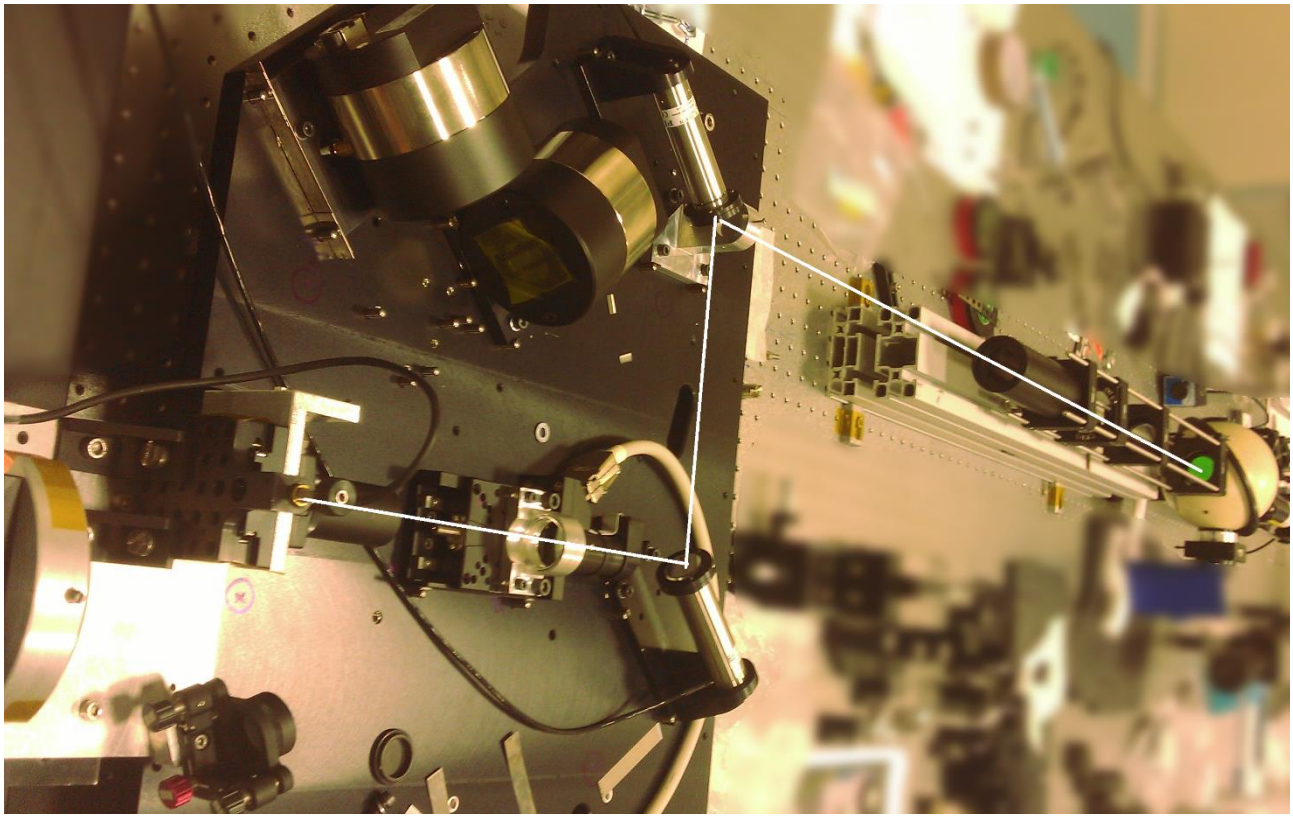

Figure 2.3 FEU during the alignment. On the left the camera used for the exit field verification. On the right, the telescope simulator used to generate the focal plane and the pupil plane in the correct positions. The white line is a sketched version of the optical path.

A picture of one FEU during the alignment is shown in Figure 2.3 together the telescope simulator used to create the field and pupil plane and the camera used for the verification of the output focal plane. The results are summarized in Figure 2.4. On the left, the quality of the alignment as FWHM of the verification spots over the entire field of view is represented.

On the right, the expected position of the field centre is shown in light blue. This is the principal figure of merit of the FEUs and those data have been obtained by the reference points measured on each element while aligning every FEU. Two out of 5 FEUs spots are quite far from the expected centre. This was mainly due to the low repeatability of the shims during the dismounting-remounting process needed during each iteration.

Moreover, the red and green rectangles highlight the uncertainty related to the Maximum Permissible Error (MPE) of the AACMM and to the play between mount and optic for the refractive elements.

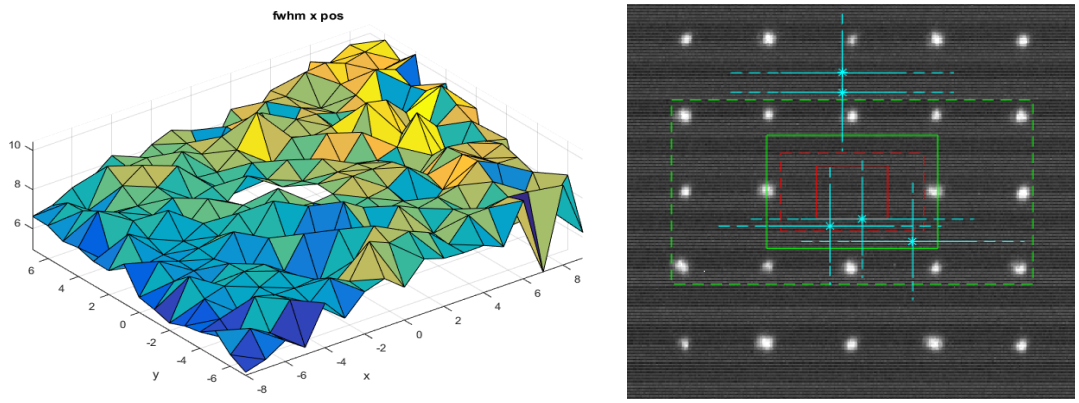

Figure 2.4 Left: FWHM distribution of the spots generated by the telescope simulator on the detector. Right: Expected position of the field centre (light blue cross) on the detector.

During the alignment, the uncertainties related to the repeatability of both the AACMM and the reference points themselves also played an important role.

To quantify and improve the repeatability of both the 'reference point problem' and the 'mounting-dismounting' problem different solutions have been proposed and a series of tests have been performed to verify the results.

2.3 Measuring Machines used

During the tests, 2 different measuring machines have been used: an AACMM and a CMM.

The AACMM is a FARO Edge with 2.7m of measurement range. The ASME B89.4.22 standard [2.5] is used to define the performances of the arm. Per this standard, 3 different tests must be performed:

1. Effective diameter Test, where a reference sphere is measured thrice using nine probing points each time. The maximum difference between the measured and the calibrated diameter is defined as the Effective diameter performance test value.
2. Single Point Articulation Test (SPAT), where 10 points are acquired with the probe fixed in a trihedral seat and the arm is articulated in different positions. The deviations from the average are used to calculate the (maximum-minimum)/2 value. This test is repeated 3 times in different quadrant and with different extensions of the arm and the worst of the 3 values defines the Single Point Articulation performance.
3. Volumetric Performance Test, where calibrated lengths are measured 20 times in different locations and orientations. The maximum deviation obtained from the measures defines the volumetric performance of the arm.

The values from the datasheet and the data obtained from the calibration certificate and from the test performed in-house (19 months after the recertification) are shown in Table 2.1. Generally, the SPAT value is a good representation of the machine repeatability while the Volumetric value represents its accuracy.

Table 2.1 Datasheet and test results for The FARO Edge used for the tests

[mm]	Datasheet	FARO recertification	In-house tests
Effective Diam.	0.0145	0.0068±0.001	0.0052±0.0003
SPAT	0.0290	0.0153	0.0238
Volumetric	±0.041	±0.024	N/A

The CMM is a Coord3 Universal 15.09.08 which can measure inside a volume of about 1500*900*800 mm. This machine is equipped with a Renishaw system composed by a PH10MQ head and a TP200 probe. The performances are defined per the ISO 10360 standards series and the 2 tests are used to evaluate:

1. Length measurement error with zero ram axis stylus tip offset (ISO 10360-2, [2.6]), where 5 calibrated bars of different lengths are placed in 7 different positions and orientations. Their lengths are measured thrice and all the 105 measurement errors must stay inside the Maximum Permissible Error of length measurement ($E_{0, MPE}$) defined as $E_{0, MPE}=\pm(A+L/K)$ where A and K are constant values defined by the manufacturer.
2. Repeatability range of the length measurement error (ISO 10360-2, [2.6]), where for each set of three repeated measurements acquired in the previous test the maximum range is recorded. All the 35 ranges values must stay inside the Maximum Permissible Limit of repeatability range ($R_{0, MPL}$).
3. Single stylus form error (ISO 10360-5, [2.7]), where 25 points are measured along one hemisphere of a calibrated sphere. The difference between the maximum and the minimum distance between each point and the centre of the Gaussian associated sphere must be lower than the maximum permissible single-stylus form error ($P_{FTU, MPE}$).

The values from the datasheet and the data obtained from the calibration certificate are shown in Table 2.2 and have been obtained using a stylus 20mm long with a 4mm diameter ruby sphere. The $P_{FTU, MPE}$ and $R_{0, MPL}$ are a good representation of the machine repeatability while the $E_{0, MPE}$ represents its accuracy.

Table 2.2 Datasheet and certification results for The Coord3 Universal used for the tests

[µm]	Datasheet	Coord3 calibration
$E_{0, MPE}$	± (1.8+L/333)	± (1.8+L/333)
$R_{0, MPL}$	N/A	2.0
$P_{FTU, MPE}$	1.8	1.7±0.1

2.4 Reference repeatability

In a fully mechanical alignment approach, the choice of the references is fundamental. Those references must be placed on the bench/main structure and periodically acquired to realign the system to the measuring machine and, eventually, on each element to check its alignment with respect to the bench/main structure.

Low values of repeatability and reproducibility of the references can have different effects:

- If it is a problem of the ones located on each element directly decrease the quality of the alignment due to the larger uncertainty of the measurement.
- If it is related to the ones used to reference the main structure, a bias between the elements aligned at different times could lead to a tedious and difficult realignment of part of the system once the first alignment is done.

Different kind of references have been studied and tested to quantify their repeatability:

1. three dowel pins fitted into bored holes,
2. six points acquired over 3 surfaces mutually perpendicular,
3. three countersunk holes,
4. three spheres glued into countersunk holes.

The first proposal required the measurement of the cylinder and the plane nearby and use the point obtained intersecting the axis of the cylinder with the plane as reference. This method has been discarded for different reasons:

- the acquisition of the cylindrical pin can be done with just 5 or 6 points [2.8] but, due to the low length of the pin, a higher number of points can be needed to reach an acceptable repeatability (see Figure 2.5).
- The acquisition of such a small cylindrical feature can be difficult and, with manual measuring machine, can be dangerous for the optical elements nearby as the contact force is applied horizontally and the probe can slip away from the cylinder.
- The acquisition of the plane nearby is not univocally defined and, if the surface is not sufficiently planar, different intersecting planes can be defined pending on the operator choice.

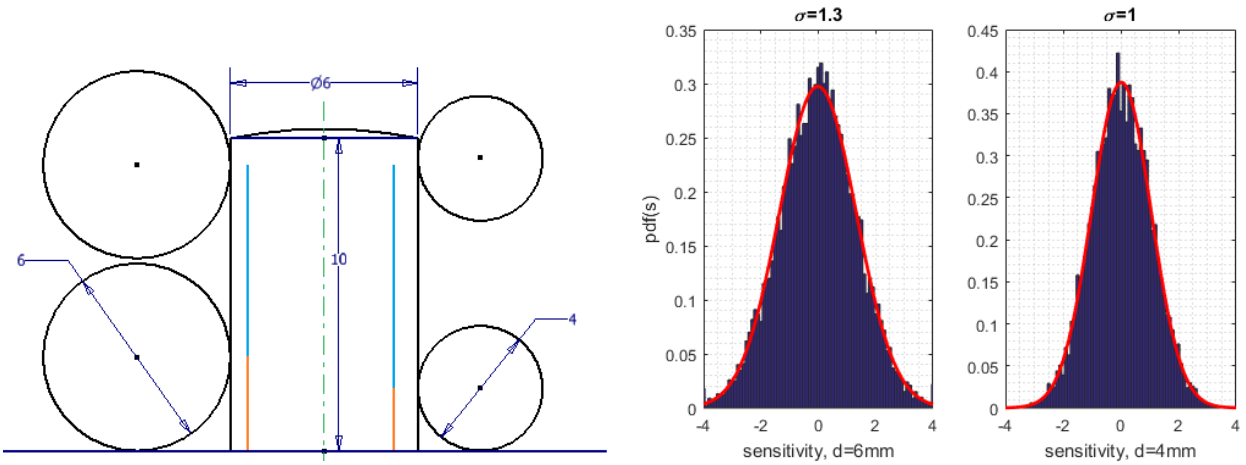

Figure 2.5 Left: Typical dowel pin acquisition with 4 and 6 mm diameter spherical probes. The blue lines represent the length of the measured axis while the orange ones show the projection of the axis on the plane. Right: Horizontal sensitivity coefficient of the points obtained intersecting a perfect plane with the axis of a cylinder probed 6 times (two circle equally spaced at h_1=d/2 and h_2=7mm) with d=6mm and d=4mm probes.

For all the other proposed references a preliminary theoretical study has been performed before comparing the measurement results obtained from a campaign performed with a dummy optical mount.

2.5 References repeatability: theoretical results

2.5.1 Six points over a surface

The simplest way to reference an optomechanical mount consists in acquiring 6 points placed over 3 perpendicular surfaces like in Figure 2.2. In this case, the quality of the results is related to the flatness and the roughness of the surfaces, the elastic deformation due to Hertzian contact and the mutual perpendicularity of the three surfaces.

A typical milled surface has an R_t value spanning between 5 (plane milling) and 10 µm (face milling) with a mean groove spacing (R_{sm}) of 0.1-0.5 mm. As can be seen form Figure 2.6, in most of the cases the R_{sm} value is the dominating factor despite of the spatial filtering of the probes typically used. Those values are critical when measuring with a machine with an automatic trigger like the CMM while can be acceptable if the measurement is performed with a manual trigger machine like the AACMM as the probe tends to go in-between the peaks.

Considering a typical diameter of the circle where the points are probed of about 2mm for manual AACMM and 0.2mm for automatic CMMs, the flatness can be, to a first approximation, ignored. The perpendicularity between the planes, instead, plays an important role in the repeatability of the points acquisition.

In Figure 2.7 (left), the square surface where the tolerance of perpendicularity is applied is shown together with the circular surface where the repeated reacquisition of the reference point takes place. Considering different perpendicularity values and probing zone diameter the dispersion of the probed point can widely vary. More in detail, for an automatic machine the value is in the order of the micron while in a manual machine, where the points are more spatially spread, if can typically span between 4 to 20 microns.

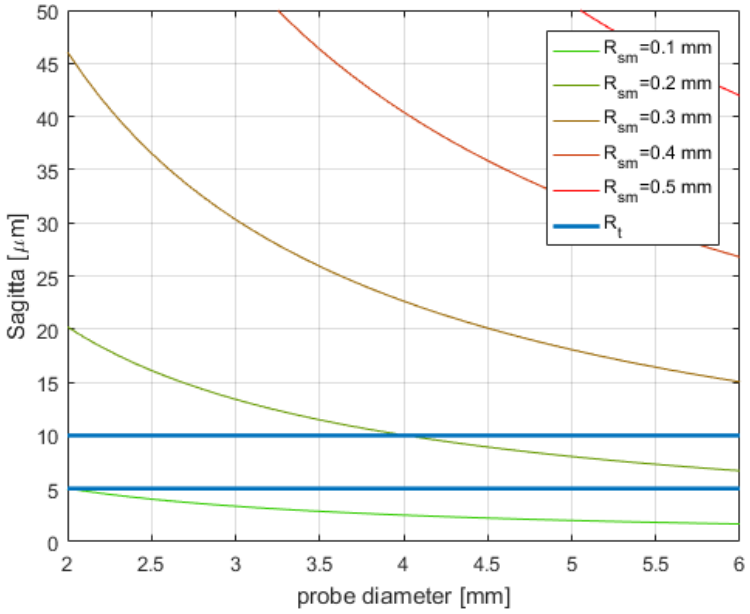

Figure 2.6 Maximum Sagitta for different mean groove spacing (R_{sm}) and typical R_t values.

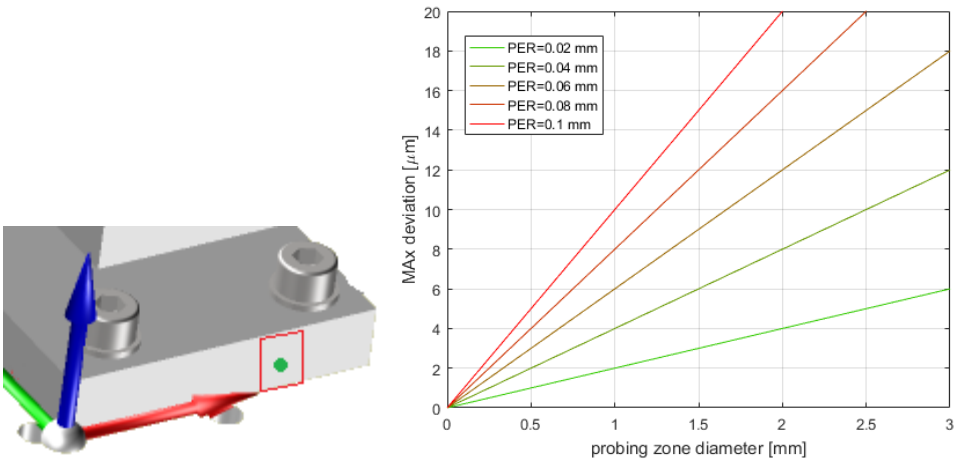

Figure 2.7 Left: detail of Figure 2.2 with a red square showing the surface with a perpendicularity tolerance and a green spot showing the dispersion zone where the points are typically acquired. Right: maximum deviations due to perpendicularity of the surface and sizes of the probing circle.

The elastic deformations due to the Hertzian stress have been computed considering conservative inputs. In both the cases under study, AACMM with ~10N of contact force and CMM with ~1N of contact force, the deformations were at least one order of magnitude smaller than the other sources of uncertainty considered.

2.5.2 Three countersunk holes

The second option foresees the use of three countersunk holes. The probe is placed in the conical cave and the three coordinates of each point are recorded and referenced to the element. This approach can be applied only when considering the alignment with manual trigger measuring machines. In this case, no theoretical uncertainties can be found due to the geometry of the reference. The only risk is related to bi-stable conditions when the cone is machined: in case of imperfect drilling a little burr in the cone like the one shown in Figure 2.8 can lead to two different stable points that can be probed alternatively.

This risk can be removed or strongly reduced with accurate machining of the cone and checking the relative positions between the three reference points acquired during the alignment.

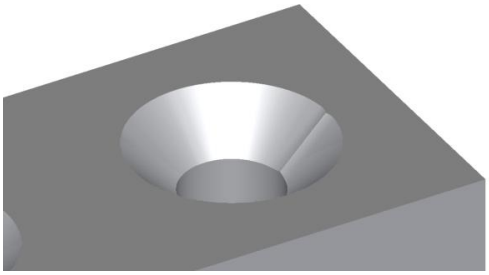

Figure 2.8 Imperfect countersunk with burr.

2.5.3 Three spheres

The last method consists in the measurement of three steel spheres glued in three countersunk. The measuring machine is used to reference the centre of the spheres with respect to the element. In this case the uncertainty is function of the deviation from the spherical form (described in [2.9]) of those spheres. This value is called ΔR_{sw} and ranges between 0.25 and 0.7 µm but its effect strongly depends to the sampling strategy chosen.

The centre point and radius sensitivity coefficient of a circle fitting sampled with 3 points can be calculated in a closed form as demonstrated in [2.10] using the following formulae:

$$S_R = \sqrt{\frac{1+2\cos^2\theta}{2(1-\cos\theta)^2}}; \qquad S_x = \frac{1}{\sqrt{2}\sin\theta}; \qquad S_y = \sqrt{\frac{3}{2(1-\cos\theta)^2}} \tag{2.1}$$

The results are shown in Figure 2.9 (left) together with the reference system considered. With some simple geometrical consideration, it is possible to extend the calculations in the case of a fitted sphere probed with 5 points (one on the pole and four equally spaced at a certain altitude angle (see Figure 2.9, right).

In this case, to have a good sensitivity coefficient value with a small number of points it is important to be able to probe the points below the altitude angle, ideally at -30° where the sensitivity coefficient is equal to $\sqrt{2/3}$. This goal can be reached using a reference sphere with a diameter 3 times bigger than the one of the foreseen measuring probe.

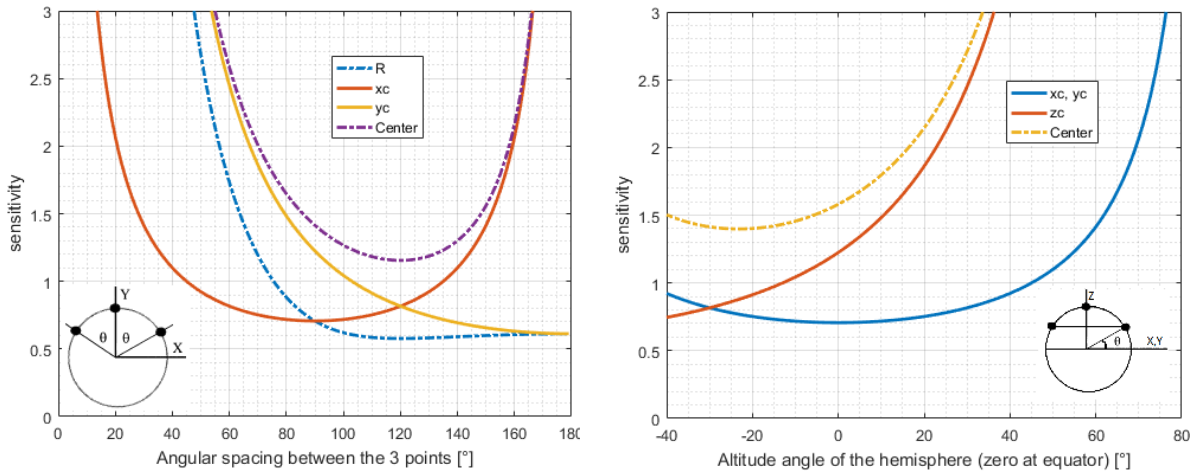

Figure 2.9 Left: Fitting a circle with 3 points, sensitivity coefficient and reference system. Right: Fitting a sphere with 5 points, sensitivity coefficient and reference system.

The sensitivity coefficient values obtained can be used to estimate the uncertainty due to deviation from the spherical form and the one related to the machine uncertainty.

The sensitivity coefficient values can be easily improved with a higher number of points: as an example a Montecarlo analysis shown a 1σ sensitivity coefficient of 0.58 in horizontal direction (-18% w.r.t. the 5 points case with θ=0°) and 0.85 in vertical direction (-29%).

2.5.4 Theoretical results comparison

The results obtained in the theoretical analysis are summarized in Table 2.3.

For the AACMM case, the feature related repeatabilities have been calculated in the following way:

1. Points: acquisition of the point in a circle with 2mm of diameter on a 10x10mm plane with 0.05mm perpendicularity (values from Figure 2.7 divided by $\sqrt{12}$).
2. Countersunk: no repeatability error due to the geometrical feature.
3. Sphere: acquisition of 5 points, one on the pole and 4 equally spaced at θ=-30° on a sphere with ΔR_{sw}=0.7µm (sensitivity coefficient values from Figure 2.9(right) divided by $\sqrt{3}$)).

The machine uncertainty related repeatabilities have been calculated in the following way:

1. Point and countersunk: SPAT value from the last test (see Table 2.1) divided by $\sqrt{3}$.
2. Sphere: SPAT value from the last test (see Table 2.1) multiplied by the sensitivity coefficient (see Figure 2.9 (right)) and divided by $\sqrt{3}$.

For the CMM case, the feature related repeatabilities have been calculated in the following way:

1. Points: acquisition of the point on a plane with R_t=5µm. The value is divided by $\sqrt{3}$ and the less-than sign is due to the spatial filtering effect.
2. Sphere: acquisition of 5 points, one on the pole and 4 equally spaced at θ=-30° on a sphere with ΔR_{sw}=0.7µm (sensitivity coefficient values from Figure 2.9(right) divided by $\sqrt{3}$)).

The machine uncertainty related repeatabilities have been calculated in the following way:

1. Point: $P_{FTU, MPE}$ value from the datasheet (see Table 2.2) divided by $\sqrt{3}$.
2. Sphere: $P_{FTU, MPE}$ value from the datasheet (see Table 2.2) multiplied by the sensitivity coefficient (see Figure 2.9(right)) and divided by $\sqrt{3}$.

Table 2.3 Estimated repeatability of the 3 methods proposed using the AACMM and the CMM (1σ value with normal distribution).

[µm]	AACMM			CMM		
	Feature	Machine uncertainty	TOTAL	Feature	Machine uncertainty	TOTAL
Point on plane	6	14	**17**	<3	1	**3**
Countersunk	-	14	**14**	N/A		
Sphere	0.3	11	**11**	0.3	0.8	**0.9**

2.6 Reference repeatability: tests and results

To measure the repeatability of the references a dummy mount of a typical lens support has been machined (see Figure 2.10). The bottom plate is used to define the reference system and is connected to the optical table using three screws and six spherical washers to minimize the deformations. The three references marked as A-B-C are used to align the system at the beginning of each measurement campaign. The top plate simulates the lens support of a small optical bench and it is fixed to the bottom part via three M4 screws with flat washer and safety lock washers (DIN 9250). The references marked as D-E-F are the ones used to test the repeatability for the three countersunk and the three 7 mm spheres while for the six points case the points are acquired 3 near those points (D-E-F) and 3 near the dowel pins (G-H-I).

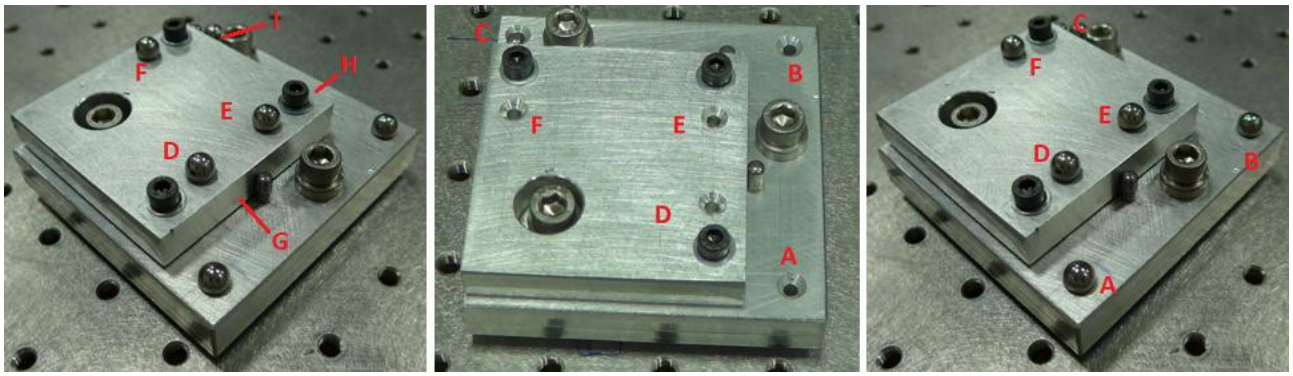

Figure 2.10 Dummy system for repeatability analysis. Left: the one used for 6 points method (the spheres are not used). Centre: the same one with the chamfers highlighted. Right: the same one after gluing the reference spheres to be used as references.

The reference system is defined as centred in B with the X-axis in C-B direction and the Z-axis defined by the A-B-C plane.

The references have been acquired first with the AACMM:

a. measuring the six reference points on the support,
b. measuring each countersunk with a single point,
c. measuring each sphere with a low number of points (4),
d. measuring each sphere with a high number of points (10).

The second series of test has been performed with the CMM:

a. measuring each sphere with a low number of points (4),
b. measuring each sphere with a low number of points (4) with a nominal centre shifted by 0.2mm,
c. measuring each sphere with a low number of points (4) with a nominal centre shifted by 0.5mm.

Considering the results obtained by the first three tests on the CMM, no further analysis with higher number of points has been performed. Neither the six reference point test has been performed as the results would be a simple measure of the flatness of the surface.

Note that each measurement campaign has been performed in a short amount of time (<20 minutes) and, in case of AACMM, without homing the instrument during all the repetitions.

The average values of the positions in each direction have been subtracted, as we were only interested in the standard deviation of each set of measures rather than the compatibility between the different sets. The only exception has been done for the CMM measures with shifted nominal centre where the average values have been used to evaluate the bias on the sphere centre calculation.

2.6.1 1a six reference points with AACMM

The six reference points have been acquired 10 times and the standard deviations of the coordinates in the direction normal to the surfaces have been considered. Those are the Z direction for D, E, and F, the X direction for G and the Y direction for H and I. The results can be seen in Figure 2.11 and can be divided in groups: the points in Z direction and the ones in X and Y direction.

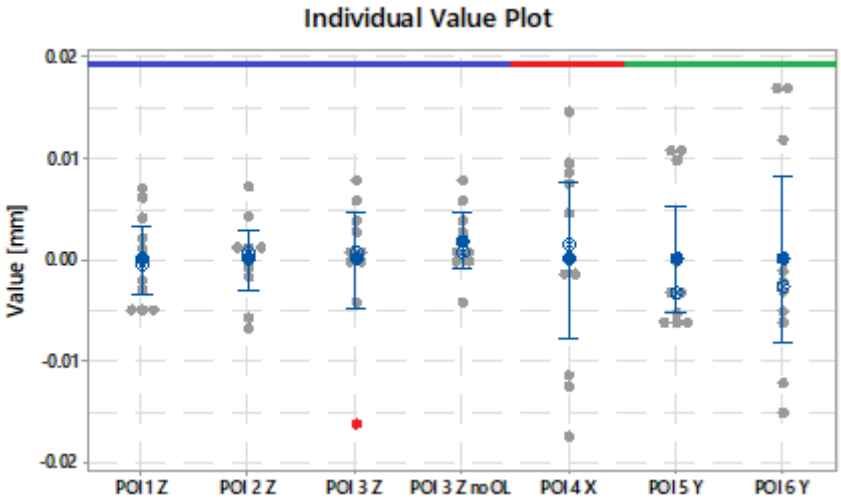

Figure 2.11 Individual value plot for the 6 points acquired with the AACMM. The first four columns show the values acquired on the large plane while the last 3 show the ones acquired on the side of the support. The bars show the standard deviations and the empty blue circles the medians.

The first ones are characterized by low standard deviation ranging between 4.2 and 6.7 µm due to the good flatness of the surface (obtained with a rough polishing with sand paper made on a surface plate). The third point has an outlier (according to the Grubb' test [2.11]) that could be related to a small dip in the plane. Once this point is removed, the standard deviation is reduced to 3.6 µm. Anyway, in order to recognize an outlier multiple measurements must be performed on every alignment cycle. The points in X and Y direction have a higher standard deviation ranging between 7.4 and 11.4 µm due to the worst surface quality obtained with a single pass coarse milling.

2.6.2 1b three countersunk with AACMM

The three reference points have been acquired 10 times placing the probe into the cone and the standard deviations of D, E, and F in the three Cartesian directions have been calculated. The results can be seen in Figure 2.12. In this case, no outlier at the 5% level of significance has been found. According to the Levene's test ([2.12]) all the samples have equal variances with a value ranging between 1.4 and 4.6 µm with the higher values obtained in the Z direction, along the countersunk axes. One explanation of this behaviour can be related to the presence of a small burr due to the machining. This burr can be elastically deformed of a different amount pending on the force applied and, being the countersunk a 90° one, the displacement will be the same in vertical and horizontal direction. While the vertical part will increase the Z standard deviation, the horizontal part will be split between the X and the Y value in proportions pending on the tangential position of the burr.

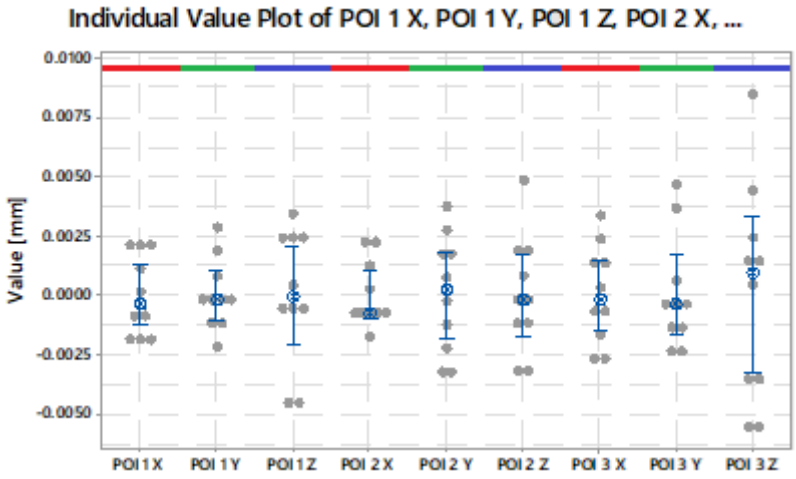

Figure 2.12 Individual value plot for the 3 points acquired with the AACMM. The bars show the standard deviations and the empty blue circles the medians.

2.6.3 1c-d three spheres with AACMM acquired with 4 and 10 points

After the gluing, the three spheres have been acquired 10 times with two different probing strategies:

c. 4 points: one near the pole and 3 approximately 120° spaced along the equator
d. 10 points randomly acquired around the accessible hemisphere.

In the 4 points case the dispersion of the sphere centre in the Z direction was expected to be about 1.5 times the ones in the X and Y directions. This value can be calculated considering that the 3 base points are taken about 120° apart (sensitivity coefficient 0.67 from Figure 2.9) while the points used to define the Z are, in a first approximation, taken about 90° apart (sensitivity coefficient 1 from Figure 2.9).

The results obtained shown, anyway, a value strongly dependent on the sphere (see Figure 2.13): the vertical standard deviation was equal to the horizontal ones in the first sphere (D), and between 2 and 3.5 times higher in the 2 other spheres.

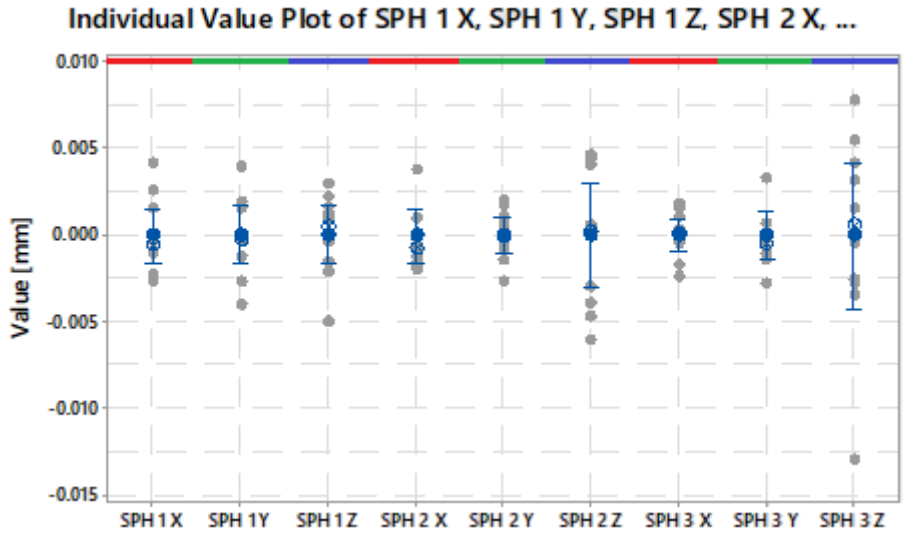

Figure 2.13 Individual value plot the three spheres acquired with the AACMM and 4 points. The bars show the standard deviations and the empty blue circles the medians.

The 10 points case showed an even bigger difference (see Figure 2.14): the vertical standard deviation was 2.5 to 3.5 times higher than horizontal ones except in the third sphere (F) where the σ_Z/σ_Y value was equal to 7.5.

As a general rule, the horizontal standard deviations were better than the vertical ones and less dependent from the number of sampling points. This result can be easily explained by the fact that the points acquired along the equator, and defining the horizontal components of the centre, can be easily acquired in an evenly spaced manner. Unlike them, the ones acquired on the top part of the sphere (including the one on the pole), and mainly defining the vertical position of the centre, will be acquired with a more random distribution.

The non-even distribution will decrease the repeatability of the sphere generated from a Least Square Fit in case the pattern of this distribution vary from one repetition to the other. This fact explains both why the measured $\sigma_Z/\sigma_{Horizontal}$ ratio is higher than the theoretical one and why the 10-points sampling give worse results than the 4-points one.

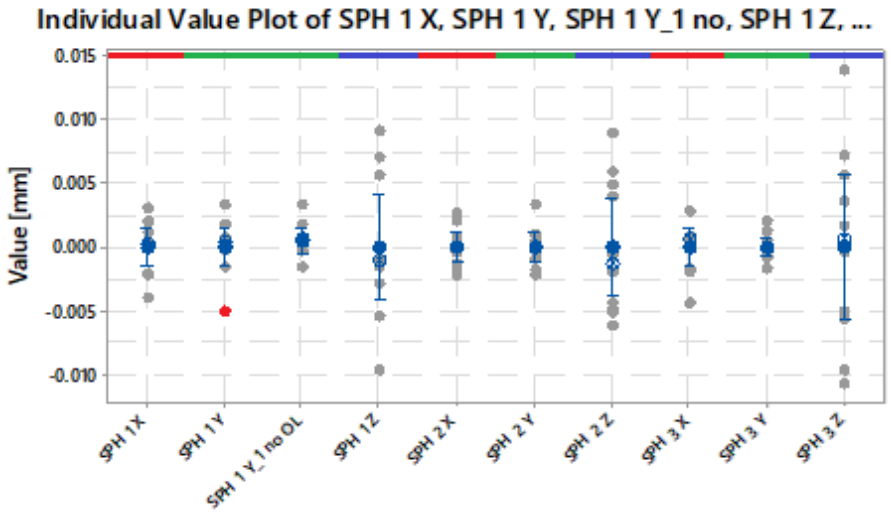

Figure 2.14 Individual value plot the three spheres acquired with the AACMM and 10 points. The bars show the standard deviations and the empty blue circles the medians.

2.6.4 2a-b-c three spheres with CMM (5 points sampling and different offsets)

The three spheres have been acquired again using the CMM. As shown in Figure 2.15 a third plate has been added to mount the system onto the granite plate. The acquisition has been performed with a Renishaw TP200 standard force probe and a 20 mm long stylus equipped with a 4 mm diameter ruby sphere.

Figure 2.15 CMM during the acquisition of one of the spheres.

The 5 points have been acquired with 1 point on the pole and 4 along the equator with 90° spacing. In this case, the dispersion of the sphere centre in the Z direction was expected to be about 80% higher the ones in the X and Y directions (see sensitivity coefficients from Figure 2.9).

The measures have been done first in a zero position meaning that the measurement direction was pointing to the centre of each sphere.

In order to understand if, after a macroscopic alignment correction, a procedure of re-centring of the sphere's nominal values was needed, the measurements have been repeated modifying the nominal values in +x, +y and +z direction of 0.2 mm (overall 3D offset 0.35 mm) and 0.5 mm (overall 3D offset 0.87 mm) to simulate the shimming operation.

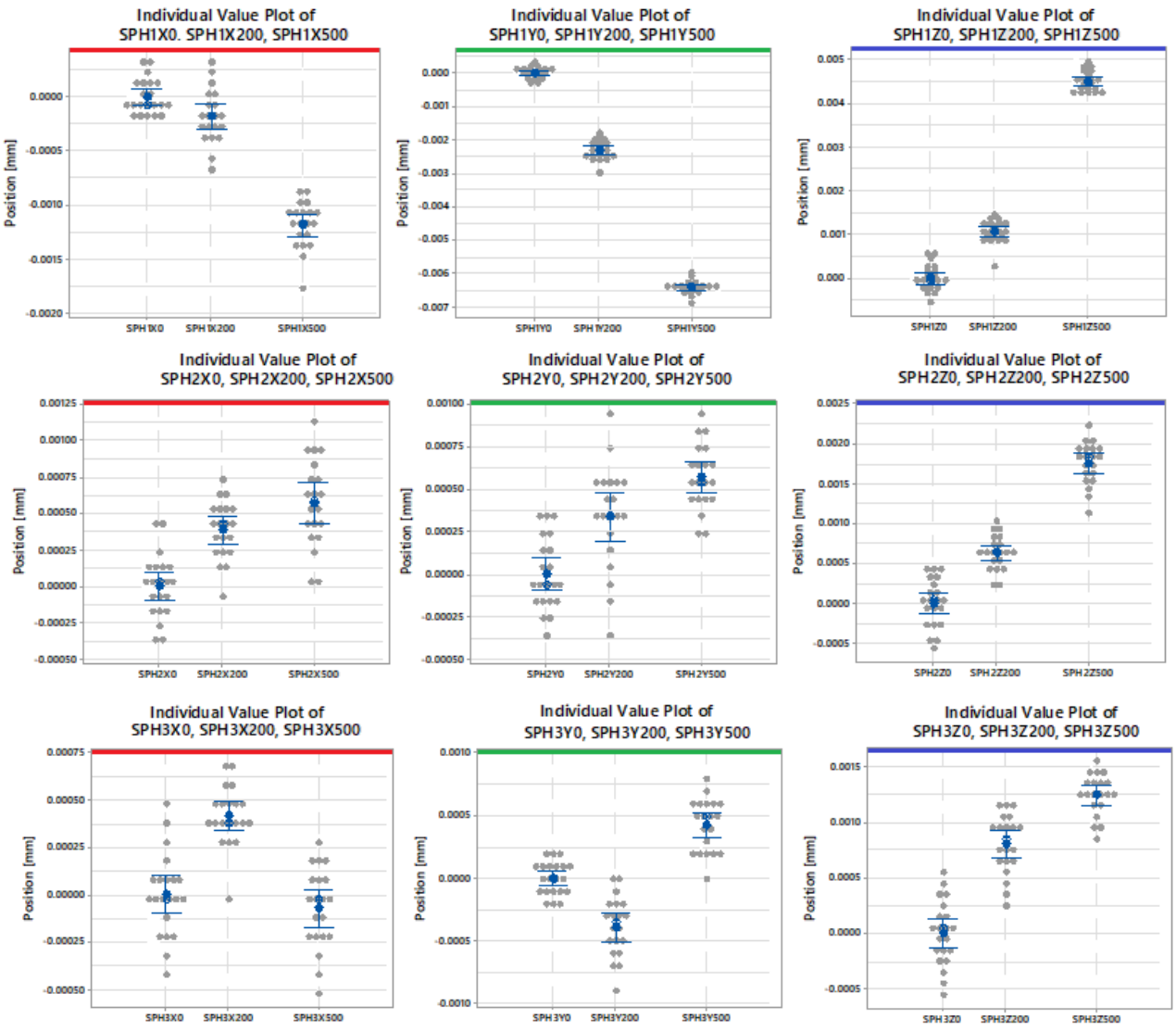

Figure 2.16 Individual value plot the 3 spheres acquired with the CMM. The bars show the standard deviations and the full blue circles the average.

The results of the 20 repetitions are shown in Figure 2.16. The repetitions are always well described by a normal distribution with a standard deviation well below the micron level. In some case, even the resolution of the exported points (0.1 µm) starts playing a significant role.

Moreover, despite some outlier, the distributions of the centre in Z direction is usually bigger that the ones in X and Y direction of 30-80%. In some case, those outliers can be detected and a simple automatic re-measurement of the feature triggered by the roundness of the fitted sphere can be implemented to reduce this risk.

No exact rule relating the offset of the measurements with the calculated centre can be derived. In some cases, no variation can be observed while in others this effect can displace the calculated centre of some micron. Bias of this order of magnitude, anyway, can be neglected as they will show up during the first iterations, when the measured and the nominal sphere are far away and they will disappear in the last iterations, when the actual sphere will almost match the nominal one.

No tests with 10 points have been performed because the 5 points acquisition repeatability is already more than an order of magnitude better the practical alignment capabilities connected to this mechanical alignment method.

2.7 Final results and considerations

The results are presented in Table 2.4. In this case, the six points method, as foreseen for the AACMM, give the worst result while the countersunk method is the one with the best repeatability. Good results can also be obtained using the sphere; this solution is also the only acceptable one in case both the instrument must be used for the alignment. This case can occur with small optical elements to be mounted on a large bench: the elements will be characterized with the CMM and the whole system will be aligned with the AACMM.

Table 2.4 Standard deviation of each repeatability test.

[µm]	Case	X	Y	Z	X	Y	Z	X	Y	Z	mean	st.dev
6 points AACMM	1a	10.8	7.4	4.6		11.4	4.2			6.7	7.5	3.0
Countersunk AACMM	1b	1.7	1.5	2.8	1.4	2.5	2.4	2.1	2.4	4.6	2.4	1.0
Sphere 4pts AACMM	1c	2.2	2.4	2.4	2.2	1.4	4.2	1.3	2.0	5.9	2.7	1.5
Sphere 10pts AACMM	1d	2.2	2.2	5.8	1.6	1.6	5.5	2.2	1.0	7.8	3.3	2.4
Sphere 0 offset CMM	2a	0.16	0.17	0.30	0.22	0.21	0.31	0.22	0.13	0.29	0.22	0.06
Sphere 0.2 offset CMM	2b	0.25	0.30	0.27	0.20	0.31	0.22	0.16	0.24	0.27	0.24	0.05
Sphere 0.5 offset CMM	2c	0.22	0.20	0.23	0.30	0.19	0.26	0.21	0.21	0.18	0.22	0.04

The comparison between the theoretical predictions with the experimental data is shown in Table 2.5 for the AACMM.
In all the cases, the theoretical results were conservative with respect to the results obtained. This discrepancy can be justified by the fact that the SPAT test requires a full rotation of the arm while the tests have been performed trying to maintain the same movements during the repetitions, as it is the best practice while measuring with an AACMM.

Table 2.5 Estimated repeatability of the 3 methods proposed using the AACMM compared with the experimental data (1σ value)

[µm]	AACMM theory			AACMM measures
	Feature	Machine uncertainty	TOTAL	TOTAL
Point on plane	6	14	**17**	**7.5±3.0**
Countersunk	-	14	**14**	**2.4±1.0**
Sphere (4 points)	0.3	11	**11**	**1.9±0.4 (X,Y)** **4.2±1.8 (Z)**
Sphere (10 points)	0.3	11	**11**	**1.8±0.5 (X,Y)** **6.3±1.3 (Z)**

The comparison between the theoretical predictions with the experimental data is shown in Table 2.6 for the CMM.
Also with this machine, the theoretical results were quite conservative with respect to the experimental results obtained. The difference can be explained from one side with lower measured roundness due to the low number of probing points. In addition, the machine uncertainty is at least four time smaller than expected probably due to the measurement direction. During the machine reverification (see [2.7]), 25 points are acquired along the reference sphere with different altitudes and are affected by the 3D anisotropy of the probe while the measurements on the test sphere are only affected by the 2D anisotropy along the equator and on the pole. This difference is directly proportional to the stylus length due to the bending of the stem.

Table 2.6 Estimated repeatability of the 3 methods proposed using the CMM compared with the experimental data (1σ value)

[µm]	CMM theory			CMM measures
	Feature	Machine uncertainty	TOTAL	TOTAL
Sphere	0.3	0.8	**0.9**	**0.22±0.05 (X,Y)** **0.26±0.04 (Z)**

2.8 Positioning repeatability

In the previous section, a study about the repeatability of the references has been performed. Once the reference type has been chosen, it becomes critical to be able to place the elements in the correct position. To do so for all the 6 degrees of freedom, calibrated steel shims will be placed below each of the 3 screws, constraining Z, Rx and Ry (according to the reference system defined in Figure 2.2) and between the mount and the dowel pins, constraining X, Y and Rz.

The typical procedure is shown in the chart in Figure 2.17. The points 3 and 7 have already been covered in the previous section while the first point will be discussed in the next chapter. The remaining critical part is the one related to the points 5 and 6.

If the repeatability during the dismounting and mounting procedure is low, an up to infinite number of repetitions could be necessary to reach the alignment targets defined by the sensitivity analysis. On the other hand, if this repeatability is well below the target values, experience shown that it is possible to align the system with just three measurements: an initial one without shims, a second one with the first set of shims and a third one for the final corrections.

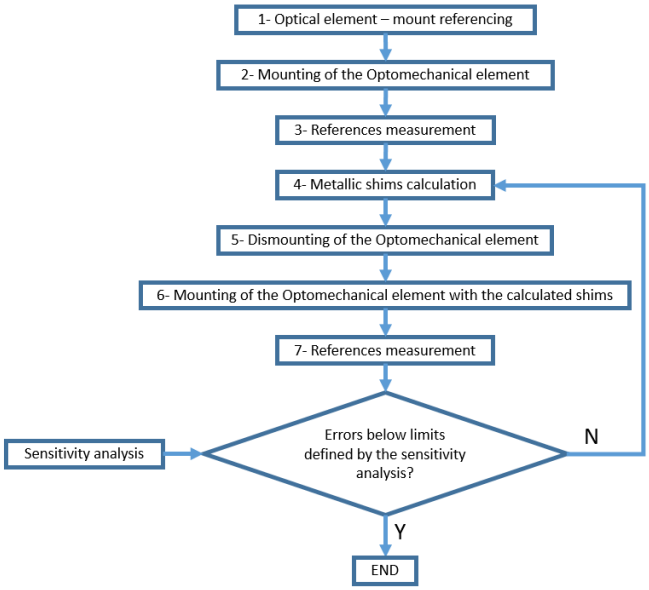

Figure 2.17 Alignment procedure of a single optomechanical element.

To quantify the repeatability of during the mount-dismount operation a series of test has been performed using the same dummy as before. The top part has been mounted and dismounted 20 times and, between every iteration, the three spheres (marked as S1, S2 and S3 in Figure 2.18) have been acquired with the CMM.

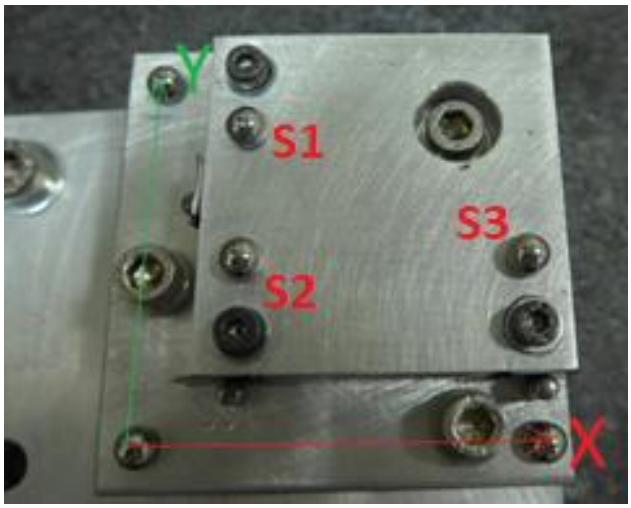

Figure 2.18 Dummy system with the reference system and the spheres names.

To evaluate the effect of different shimming methods a first test without any shimming has been performed. The results obtained represent the maximum obtainable repeatability for this kind of mounting system. The results from the subsequent tests have been divided in 2 different parts:

1. horizontal displacements, defined by the 3 dowel pins, and
2. vertical displacements, defined by the 3 screws.

The horizontal repeatability has been tested with and without shims placed freely between the mount and the dowel pin and with and without shims placed between an L shaped spacer and the mount. The vertical

repeatability has been tested without shims and with commercial, etched, punched and commercial + etched shims.

2.8.1 Positioning repeatability: shims construction

Three options can be exploited for the construction of shims: a monolithic element machined with the correct thickness, laminated shims, and a stack of calibrated shims.

The use of milled monolithic shims has been exploited for the alignment of the ESPRESSO spectrograph optical mounts [2.13] and its main advantage is that its repeatability is equal to the one of the no shim case. However, to use this strategy a first measurements of all the elements mounted is needed followed by a machining of 6 shims for each element with an accuracy better than the alignment target defined by the sensitivity analysis. This procedure can be applied but can be time consuming in case subsequent corrections are needed.

The laminated shims are similar to the monolithic shims with the advantage of being composed by a series of laminated sheets glued together. One or more of those sheets, with a typical minimum thickness of 0.01 mm, can be removed from the stack to obtain the correct thickness of the whole shim. Due to the cost, this option was thought as a backup solution is case the calibrated shims could not guarantee enough repeatability.

Those calibrated shims are usually sold in stripes or foils made of carbon steel 1.1274 or stainless steel and washers made of Steel St 2K50 or spring steel with different thickness. The list of the commercially available thicknesses for those shims is shown in Table 2.7.

Table 2.7 Typical values of thickness and tolerances for commecially available shims. The bold ones can be practically used for this kind of alignment.

Thickness [mm]	Foil/strip tolerances [mm]	Washer thickness (DIN988) [mm]
0.005	**±0.001**	NA
0.01 0.02 0.025 0.03	**±0.002**	NA
0.04 0.05 0.06	**±0.003**	NA
0.07 0.075 0.08 0.09	**±0.004**	NA
0.1	**±0.004**	**+0/-0.03**
0.2	**±0.006**	**+0/-0.04**
0.3	±0.007	**+0/-0.05**
0.5	±0.010	**+0/-0.05**
1.0	±0.017	**+0/-0.05**

For the horizontal alignment the strip shims will be used manually cutting them in pieces of about 5 x 12.7 mm. For thickness higher than 0.2mm their flexural stiffness will decrease the repeatability to unacceptable values (at least in a free shim condition like the one presented in chapter 2.8.3) and an integral milled shim will be necessary to compensate this error.

The vertical alignment will be performed with the washers but, unfortunately, the thicknesses between 0.005 and 0.09 mm are not available on the market. To cover this range of corrections different solutions have been studied: water jet cut washers, laser cut washers, punched washers and chemically etched washers.

Water jet cut and laser cut washers have been manufactured trapping the foil in-between two wooden layers to keep them in position after the cut. Despite this technique, the water jet proved to be an unfeasible

technology for small pieces. **Laser cut** could be an interesting alternative but most of the workshops are able to cut high thickness elements using the continuous wave technology and, as a result, most of the shims with lower thickness were characterized by an unacceptable amount of burrs.

Figure 2.19 shows the results obtained: the burr thickness is negligible in the 0.3 and 0.5mm cases while it has a value between 0.03 and 0.05 mm in the other cases. This is critical not only because it changes the nominal thickness of the shim but also because it decreases the repeatability due to the burrs plasticization and the displacements of the shims during the alignment cycles.

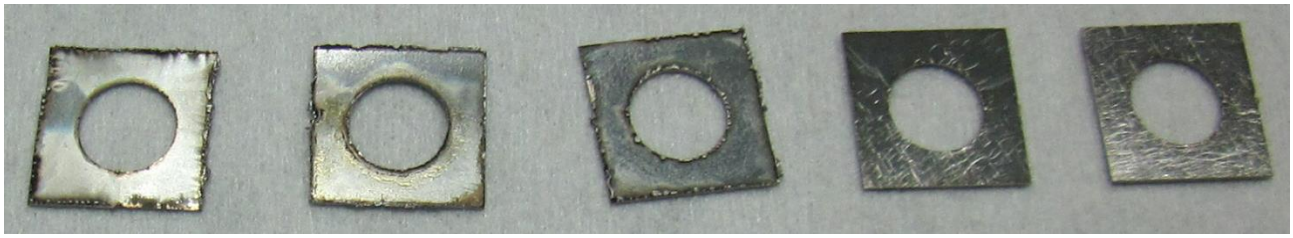

Figure 2.19. Shims obtained with laser cut. From left to right 0.05, 0.1, 0.2, 0.3 and 0.5 mm thicknesses.

Another alternative is to **punch** the hole inside every square shim. The main advantage of this process is the low production time and the capability to produce those holed shims online during the alignment with the desired diameter and without any need of external workshops.

One of the puncher designed is shown in Figure 2.20 (right): two screws are tightened to press the strip centred via two small walls. Each system is made of steel and has three holes in it with different sizes and every time one is used, in the remaining ones two dowel pins are inserted to guarantee the alignment of the two rectangular parts. The hole is made hammering an HSS puncher with a sharp, tilted head.

A series of shims obtained are shown in Figure 2.20 (left) and no burr can by noticed at any specimen thickness. Two criticality emerged from the test: the first appears with shims thicknesses above 0.2 mm and is related to the excessive wear of the puncher that must be regenerated with a grinder every 10-20 holes. The second problem can be seen in Figure 2.20 (left) and appeared with thicknesses below 0.05 mm. While punching those shims a series of wrinkles appear around the hole. This makes the 0.005 and 0.01 mm thick shims completely unusable, as the final thickness is unpredictable. Also in the 0.02 mm ones, those wrinkles slightly reduce the thickness repeatability between different shims while in the 0.05 mm case the effect is purely cosmetic.

Figure 2.20 Left: Holed shims obtained by punching: from left to right 0.02, 0.05, 0.1 and 0.2 mm. Right: one of the puncher used.

At this point, the shims can be directly purchased off-the-shelf for thicknesses between 0.1 and above while between 0.02 and 0.1 mm the puncher is a good option. To obtain thinner shims a solution using **chemical etching** has been studied.

The procedure followed can be divided in the following steps:

1. A pattern of washers has been printed on a 'Press and peel' blue paper
2. Every oil trace has been carefully removed with acetone from the steel strips or foils.
3. The blue paper has been placed steel element, then heat and pressure have been used to transfer the ink from paper to steel
4. Every imperfection has been corrected with a specific marker
5. The back of the steel surface has been covered with plastic tape or acrylic spray
6. The system has been placed in Ferric Chloride (Iron(III) chloride), stirred and heated for different times pending on the thickness and the chemical composition of the steel
7. The washers have been cleaned with Acetone

The main parameters for steel etching where found to be material composition, Ferric Chloride temperature, and stirring. To investigate those factors a series of test have been performed. One example is shown in Figure 2.21 and, as a general rule, with stirring on and a temperature of 25°C, the removal rate is between 50 and 60 µm/h for high carbon steel and 10 µm/h for stainless steel. It is also noticeable how the high carbon steel degradation is related to the corrosion of the material while the stainless steel is consumed by a pitting-like phenomenon. If the etching is performed at 18°C, the penetration speed is reduced of 20-25% in both cases.

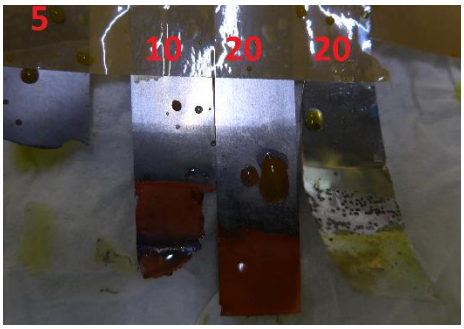

Figure 2.21 Etching speed test performed at 25°C with stirring on with the numbers showing the thicknesses in micron. The 3 specimens on the left are the high carbon steel (1.1274) ones while the forth is made of stainless steel.

This technique allowed the shims manufacturing with thicknesses between 5 and 50 µm with the best results obtained for the thinner ones made of high carbon steel due to the lower etching time. An example can be seen in Figure 2.22.

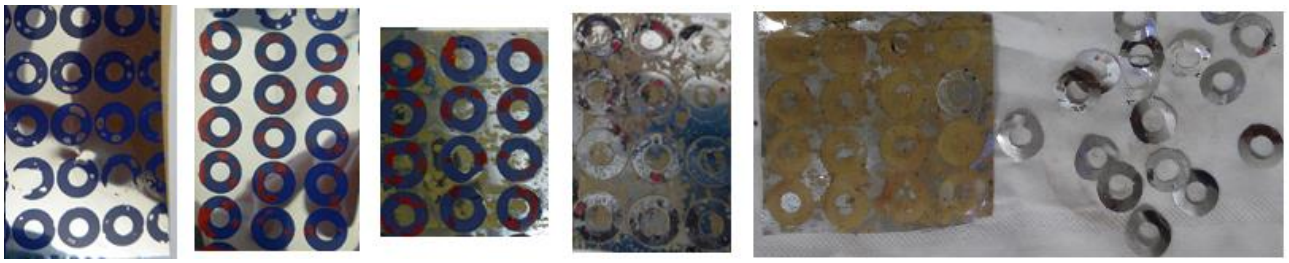

Figure 2.22 Different phases of the shim production with etching. Left to right: print with press and peel paper, correction of the print with a permanent marker, foil after the etching process, removal of the print, final shims after 30 minutes of acetone bath.

Figure 22 summarizes the performances of the three possible technologies for shims production.

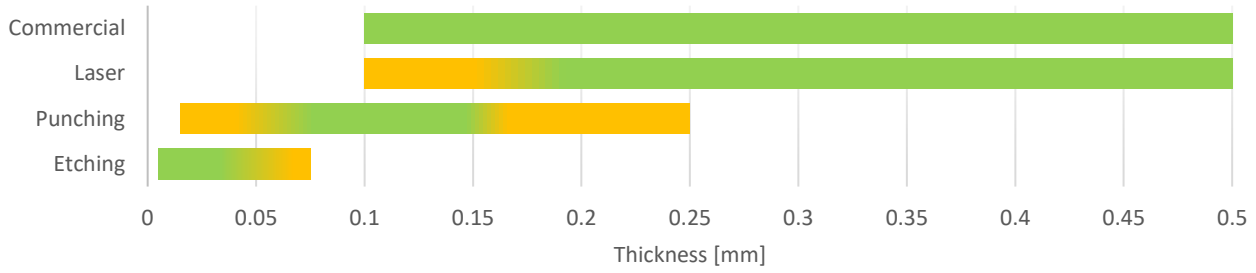

Figure 2.23 Possible technique for shims production. The green colour is where the techinque has the best performances while in the yellow part gives acceptable results.

2.8.2 Positioning repeatability: tests and results in vertical direction

To measure the repeatability of the references during the mounting and dismounting operation the same dummy mount of a typical lens support has been used (see Figure 2.10).

During the ESPRESSO Front End Unit mounting, the alignment in this direction was done exclusively using punched shims with a thickness between 0.02 and 0.1 mm and Laser cut shims with a thickness of 0.2 mm already showing good repeatability values (see [2.4]).

The goal of this test was to understand the repeatability limitations due to the mounting concept itself and related to the different number and type of used shims. To do that the dummy has been dismounted and remounted 20 times recording, for each iteration, the position of the reference spheres.

Five different cases have been studied:

1. No shims
2. Commercial shims, 4 shims with a total thickness of 1.1 mm
3. Etched shims, 4 shims with a total thickness of 0.11 mm
4. Punched shims, 4 shims with a total thickness of 0.36 mm
5. Commercial + etched shims, 8 shims with a total thickness of 1.21 mm.

In Figure 2.24 the first four cases are presented. Even if the performances decrease with respect to the reference condition (no shim case), the repeatability always remains at an acceptable level. Considering that,

the minimum shim thickness is 5 µm the alignment in this direction will always be limited by the thickness of the thinner available shims.

The Boxplot of Figure 2.25 highlight that an increase in the number of shims decreases the repeatability in a nonlinear way (cases 1 and 2 vs 3). This result suggests that a minimization in the number of shims during the alignment in this direction is fundamental.

The standard deviation values are summarized in Table 2.8.

Another effect seen but not presented here is the crosstalk between the horizontal and vertical alignment direction related to the non-perfect parallelism between the reference system and the plane where the shims are placed. In this specific case, the repeatability crosstalk was equal to 4%.

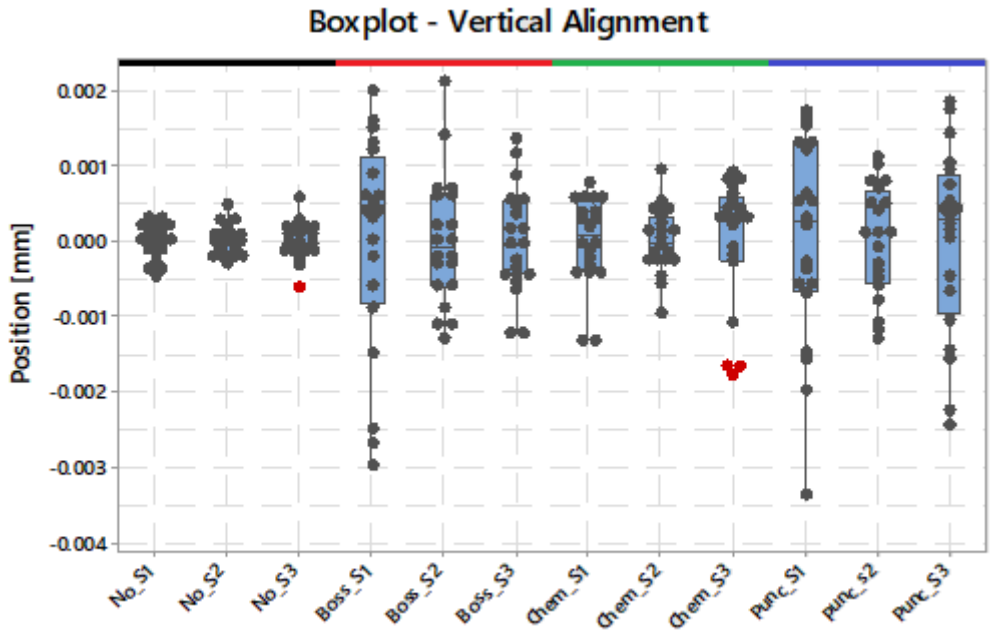

Figure 2.24 Position variation in vertical direction. From left to right: no shim (black line), Commercial shims (red line), Etched shims (green line), and punched shims (blue line). The red spots represent the outliers.

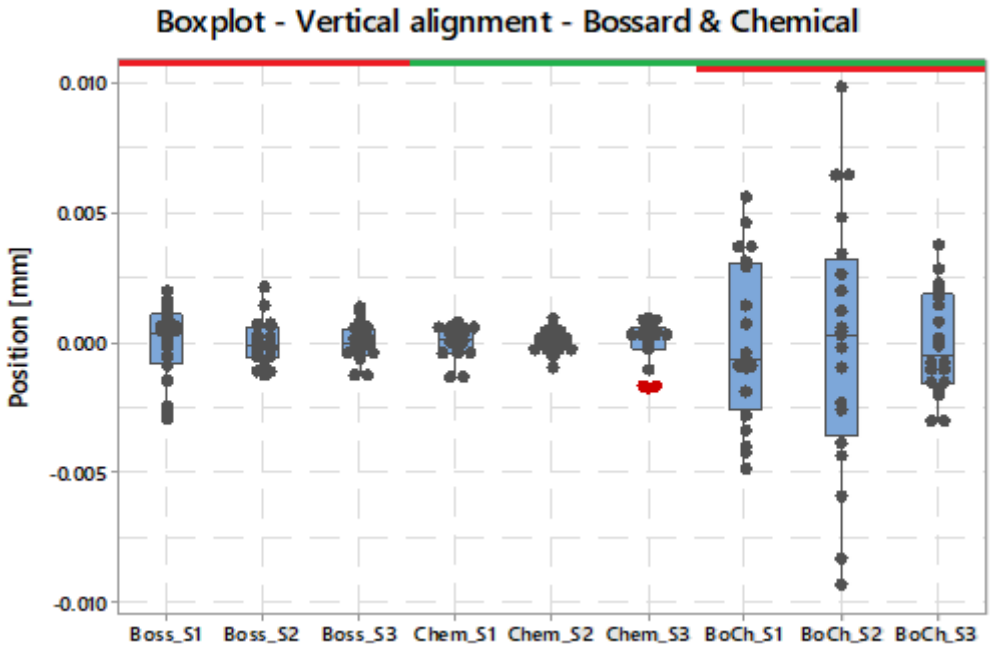

Figure 2.25 Position variation in vertical direction. From left to right: Commercial shims (red line), Etched shims (green line) and commercial and etched shims together (greed and red line). The red spots represent the outliers.

Table 2.8 Standard deviations of the vertical cases. Average [%] shows the variation as percentage of the total shims thickness.

[µm]	Thickness	Z_1	Z_2	Z_3	Average	Average [%]
No shims	0	0.24	0.21	0.25	0.23	-
Etched	110	0.59	0.43	0.87	0.63	0.57%
Punched	360	0.48	0.53	0.81	0.61	0.17%
Commercial	1100	1.45	0.86	0.71	1.01	0.09%
Commercial + Etched	1210	3.12	4.94	1.99	3.35	0.28%

2.8.3 Positioning repeatability: tests and results in horizontal direction

The repeatability of the references in the horizontal direction during the mounting and dismounting operation has been evaluated, again, using the same dummy mount (see Figure 2.26 and Figure 2.10).

During the ESPRESSO Front End Unit mounting, the alignment in this direction was done placing cut strips of shims with a thickness between 0.02 and 0.2 mm as in Figure 2.26 (left) with poor repeatability values (see [2.4]).

As in the vertical case, the goal of this test was to understand the repeatability limitations due to the mounting concept itself and to investigate different solutions. To do that the dummy has been dismounted and remounted 20 times recording, for each iteration, the position of the reference spheres. The repeatability of the shims, for Pin2 and Pin3, was estimated using the centre of the corresponding spheres in the Y direction. For Pin1, placed midway between 2 spheres, their average position in X direction has been considered.

Four different cases have been studied:

1. No shims
2. Free shims, with the shims compressed between the pin and the mount: 4 with a total thickness of 0.18±0.011 mm for Pin1 and 5 with a total thickness of 0.38±0.015 mm for Pin2 and Pin3 (see Figure 2.26, left).
3. L fixed shims, 4 shims with a total thickness of 0.18±0.011 mm placed between the mount and an L shaped aluminium part screwed with a single central screw to the mount itself near Pin2 (see Figure 2.26, right)
4. L fixed shims, 4 shims with a total thickness of 0.18±0.011 mm placed between the mount and an L shaped aluminium part screwed with 2 lateral screws to the mount itself near Pin3.

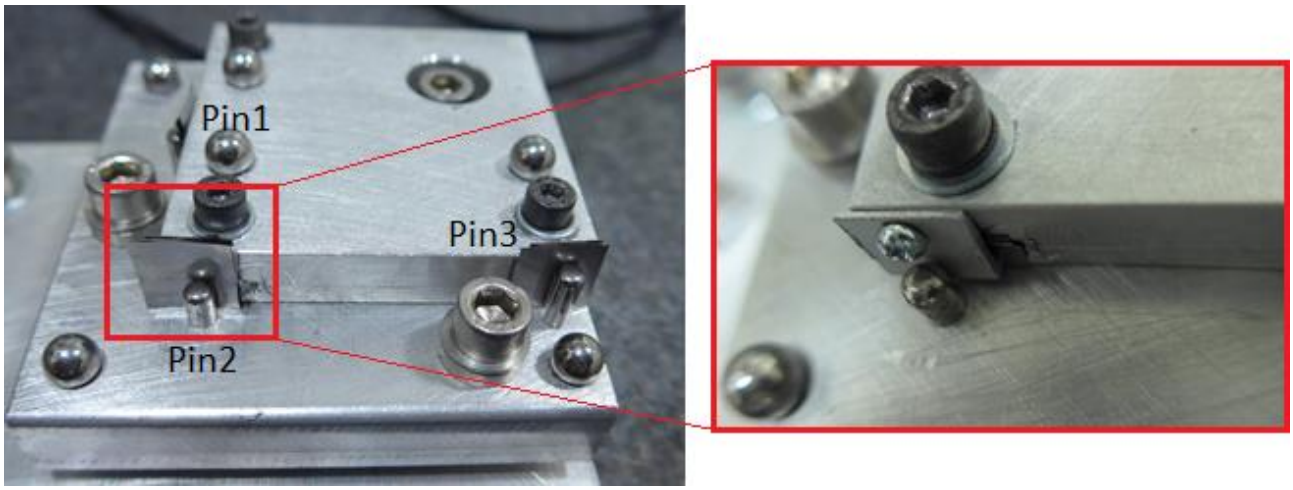

Figure 2.26 Dummy mount used for the horizontal repeatability test. Left: with the shims freely placed. Right: detail of the Pin2 with the L mounted to fix the shims.

The results obtained can be seen in the following graphs: case 1 is shown in Figure 2.27, case 2 in Figure 2.28, case 3 in Figure 2.29 while case 4 is not presented as the bending of the L due to the 2 screws provided extremely low repeatability values even without placing any shim in-between.

The standard deviation values are summarized in Table 2.9.

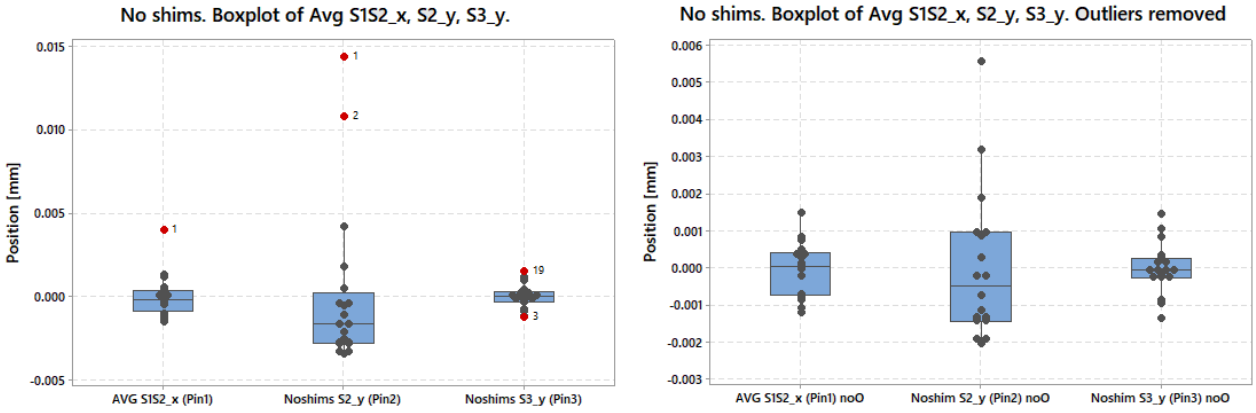

Figure 2.27 Position variation in horizontal direction in the 'no shims' case. Left: all the data. Right: same graph after the removal of the outliers.

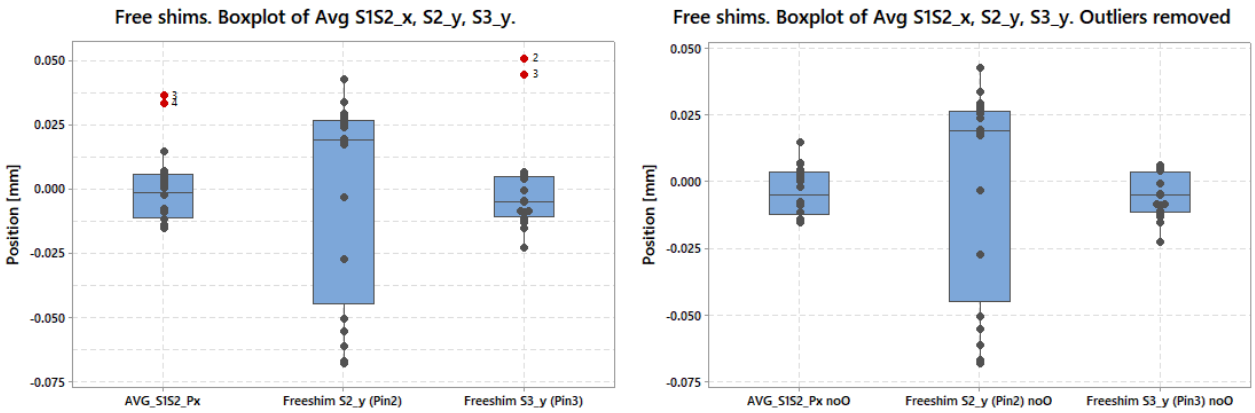

Figure 2.28 Position variation in horizontal direction in the 'free shims' case. Left: all the data. Right: same graph after the removal of the outliers.

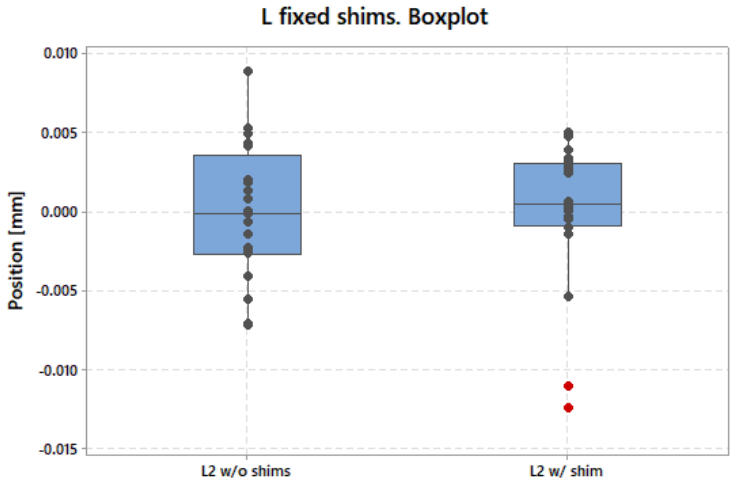

Figure 2.29 Position variation in horizontal direction in the 'L fixed' case. On the left, the first test without any shim and on the right the same test repeated after adding 0.18 mm of shims.

Table 2.9 Standard deviations of the horizontal cases. Average [%] shows the variation as percentage of the total shims thickness.

[µm]	Thickness	Pin 1	Pin 2	Pin 3	Average	Average [%]
No shims	0	1.21	4.74	0.71	2.2	-
No shims – outlier removed	0	0.78	2.01	0.57	1.1	-
Free shims	180 or 380	14.6	38.7	18.0	23.7	4.7 – 10.2
Free shims – outlier removed	180 or 380	9.0	38.7	8.3	18.6	2.2 – 10.2
L support without shims	0		4.3		4.3	-
L support with shims	180		4.7		4.7	2.6

Without placing any shim for the mount positioning, the repeatability is worse than the vertical case previously studied but remains below the 5 µm goal. The use of free shims in-between the mount and the pin decreases the repeatability at unacceptable level: with this strategy, an alignment with accuracy of 20-30 µm becomes extremely difficult.

Fixing the shims with a screwed aluminium L as in Figure 2.26 (right) gives performances compatible with the 'no shim' case.

Another test was foreseen with integral shims following this alignment procedure: an aluminium rectangle with a thickness slightly higher than the desired value must be machined and, after a first alignment of the system, must be removed and its thickness carefully corrected to reach the final value.

This procedure is longer than the 'L support' one and, considering the results obtained in this test, cannot give any advantage in terms of repeatability. Therefore, this solution has not been tested even if it could be considered for a first, rough, alignment.

One interesting behaviour of the mount highlighted by this test is related to the position of the screws with respect to the pins and is shown in Figure 2.30 (left). Due to the momentum applied on the mount while tightening the first screw the mount itself moves from the desired position (blue contour) to a rotated position (black contour).

A simple analysis of the forces applied between pins and mounts shows that this effect can be reduced by choosing a certain order while tightening the screws (Figure 2.30, right). With the same analysis, it is possible to define the areas where the screws must be placed to avoid this effect.

A careful design of the mount can improve the repeatability of a factor of five, as shown in Figure 2.27 and Figure 2.28.

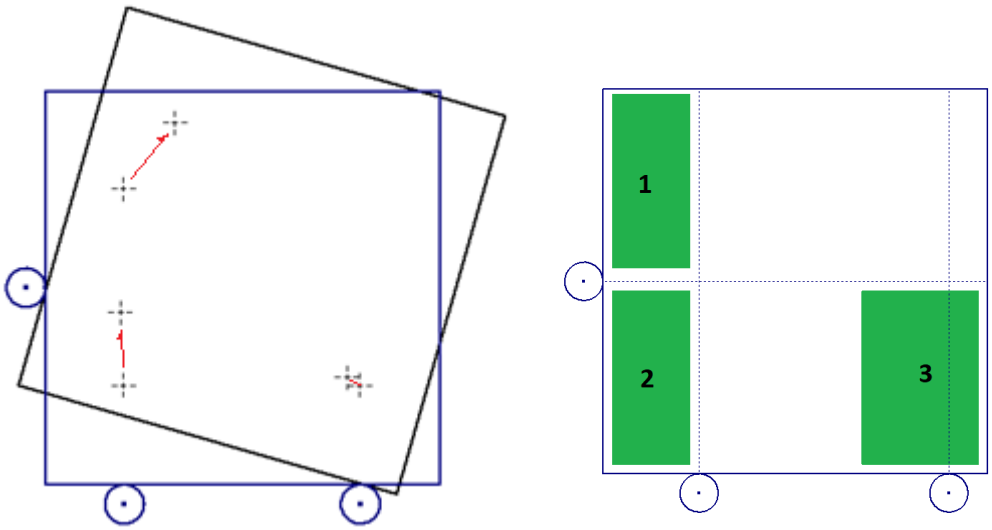

Figure 2.30 Left: typical mount rotation during mounting operation. The red arrows show the displacements of the three reference spheres. Right: best position of the three screws to avoid the mount rotation together with the correct tightening order.

2.9 Conclusions and future improvements

The first part of this chapter was dedicated to a brief introduction of the ESPRESSO Front End alignment procedure and the machines available for the foreseen tests. The second part was focused on the choice of the best system to reference each optical mount with respect to its optical axis. The analysis was performed first with a theoretical point of view and then with a series of tests with different machines and references.

Once the combination of machine and reference with the best repeatability has been chosen, this system has been used to evaluate the actual repeatability of a single mount with different kind of shims placed below the 3 mounting screws or near the 3 pins.

In this part it has been demonstrated that the alignment in the vertical direction (the three degrees of freedom defined with shims below the screws) is limited by the available thicknesses of the shims (5 µm) once they are manufactured with different techniques.

In the horizontal direction (the three remaining degrees of freedom defined with shims near the pins), the alignment is limited by the repeatability of the mounting-dismounting operation but, with the proper procedures and design, it can be reduced to values that make, again, the available thicknesses the limiting factor.

To validate the results obtained in those tests, a dummy optical system (see Figure 2.31) has been designed and aligned with the CMM and the relative alignment between the optical elements has been verified with an interferometer. The results are presented in chapter 6.

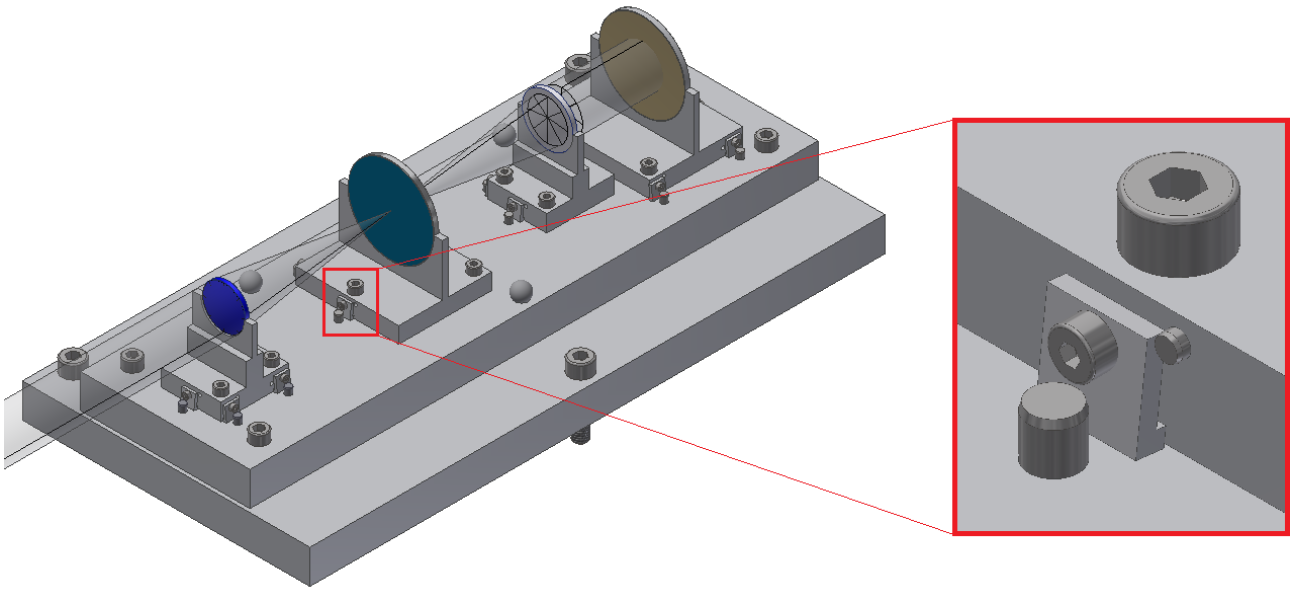

Figure 2.31 Dummy optical system used as a validation of the alignment procedure. In the red rectangle a detail of the horizontal alignment system.

2.10 References

[2.1] Lovis C, Pepe F, Bouchy F, Curto GL, Mayor M, Pasquini L, Queloz D, Rupprecht G, Udry S, Zucker S. The exoplanet hunter HARPS: unequalled accuracy and perspectives toward 1 cm s-1 precision. In SPIE Astronomical Telescopes+ Instrumentation

[2.2] Mégevand D, Zerbi FM, Di Marcantonio P, Cabral A, Riva M, Abreu M, Pepe F, Cristiani S, Lopez RR, Santos NC, Dekker H. ESPRESSO: the radial velocity machine for the VLT. In SPIE Astronomical Telescopes+ Instrumentation 2014 Jul 8 (pp. 91471H-91471H). International Society for Optics and Photonics.

[2.3] Riva M, Aliverti M, Moschetti M, Landoni M, Dell'Agostino S, Pepe F, Mégevand D, Zerbi FM, Cristiani S, Cabral A. ESPRESSO front end: modular opto-mechanical integration for astronomical instrumentation. In SPIE Astronomical Telescopes+ Instrumentation 2014 Aug 6 (pp. 91477G- 91477G). International Society for Optics and Photonics

[2.4] Aliverti M, Pariani G, Moschetti M, Riva M. Integration and alignment through mechanical measurements: the example of the ESPRESSO front-end units. In SPIE Astronomical Telescopes+ Instrumentation 2016 Aug 9 (pp. 99087C-99087C). International Society for Optics and Photonics.

[2.5] ASME B89.4.22. Methods for Performance Evaluation of Articulated Arm Coordinate Measuring Machines (CMM)

[2.6] ISO 10360-2:2009. Geometrical product specifications (GPS) — Acceptance and reverification tests for coordinate measuring machines (CMM) — Part 2: CMMs used for measuring linear dimensions

[2.7] ISO 10360-5:2010. Geometrical product specifications (GPS) — Acceptance and reverification tests for coordinate measuring machines (CMM) — Part 5: CMMs using single and multiple stylus contacting probing systems

[2.8] Lichtblau D. Cylinders through five points: computational algebra and geometry. Journal of Mathematics Research. 2012 Nov 26;4(6):65.

[2.9] ISO 3290-1:2014. Rolling bearings — Balls — Part 1: Steel balls

[2.10] Phillips SD, Borchardt B, Estler WT, Buttress J. The estimation of measurement uncertainty of small circular features measured by coordinate measuring machines. Precision Engineering. 1998 Apr 30;22(2):87-97.

[2.11] Grubbs FE. Sample criteria for testing outlying observations. The Annals of Mathematical Statistics. 1950 Mar 1:27-58.

[2.12] Brown MB, Forsythe AB. Robust tests for the equality of variances. Journal of the American Statistical Association. 1974 Jun 1;69(346):364-7.

[2.13] Tschudi SS, Fragosoa A, Amatea M, Reboloa R, Mégevandb D, Zerbic FM, Pepeb F. Design of the opto-mechanical mounts of the ESPRESSO spectograph. In SPIE Astronomical Telescopes+ Instrumentation 2014 Jul 28 (pp. 915153-915153). International Society for Optics and Photonics.

3 Accuracy estimation of a Coordinate Measuring Machine for optical systems alignment

3.1 Introduction

Thanks to their high flexibility and accuracy, the Coordinate Measuring Machines (CMMs) are nowadays widely used in the industrial field to verify the geometric characteristics (dimensions, orientations, forms, and tolerances) of the mechanical parts.

The typical CMM acquires a series of points on the surface of the workpiece, reconstruct a best fitting surface, and compare the obtained value with the nominal ones. The acquisition can be performed with different type and configurations of contact or non-contact probing systems, in different part of the measuring volume, with the measuring head oriented in different directions. This freedom on one side gives high flexibility in terms of workpieces and characteristics that can be measured while on the other side makes extremely difficult to find a general rule to estimate the uncertainty of a specific measurement.

In the first part, after a brief introduction to some of the Cartesian CMMs and probing system existing on the market, some possible methods to estimate the uncertainty will be presented. In the second part the uncertainty estimation of an AACMM performed while aligning the ESPRESSO FEU will be also presented, followed by a simple method and the relative software developed for the uncertainty estimation of optical system composed by a series of small optical elements aligned with a Cartesian CMM.

3.1.1 Cartesian CMMs and probing systems

Different types of Cartesian CMM can be found on the market and the most common layouts are sketched in Figure 3.1. The configuration of the machine can be chosen depending on different factors but, generally, the horizontal arm is used in the automotive field, the gantry is specific for large structures and parts while most of the remaining market is taken by the moving bridge configuration.

The work presented hereby has been performed using a moving bridge CMM (Coord3 universal 15.9.8) nevertheless the uncertainty estimation can be easily extended to any kind of Cartesian CMM.

The probing system connected to the ram, can also be based on different principles. A first categorization can be done considering contact and non-contact sensors. The first ones (see Figure 3.2) typically have a tip, usually spherical, and a contact detection system used to identify the contact time (digital probes) or to evaluate the force applied between the workpiece and the stylus tip (measuring probes).

The second ones are usually based on 2D or 3D vision systems and are able to measure complex geometries faster than the contact ones but have lower accuracy and the measurement of shiny or transparent elements can be difficult or even impossible.

For this reason, the analysis has been performed using a piezoelectric digital contact probe (Renishaw PH10MQ articulation system and Renishaw TP200 probe). A schematic view is shown in Figure 3.2 on the right: once the contact between the probe and the workpiece has been established according to the silicon strain gauges a first trigger a point is recorded. If the trigger remains activated in a certain time, the point is saved and sent to the software, otherwise it is deleted as it probably comes from external disturbances (e.g.

air, vibrations). The kinematic system shown in Figure 3.2 (right) is only used to protect the stain gauges in case of high contact forces or collisions.

Also a measuring probe like the Renishaw SP25M or a digital probe with mechanical trigger could be used for the alignment of optical system but the first one gave no advantage for this kind of measurements and is more expensive while the second has poorer performances.

The developed software presented at the end of the chapter, even if fed with the data obtained by a specific CMM, can be easily adapted to the accuracy study of different measuring machines and contact probes with a similar analysis of the expected uncertainty sources.

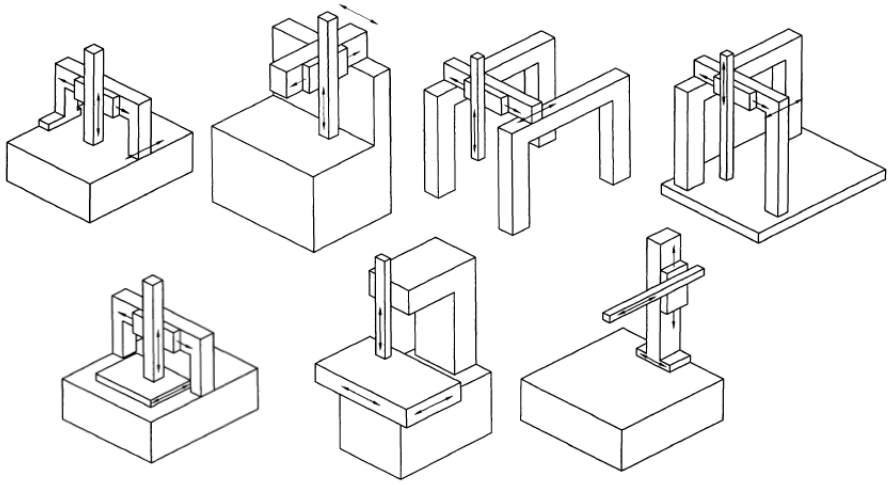

Figure 3.1 Typical CMM configurations according to [3.1]. Top, left to right: moving bridge, fixed table cantilever, gantry, L-shaped bridge. Bottom, left to right: fixed bridge, moving table cantilever, moving ram horizontal-arm.

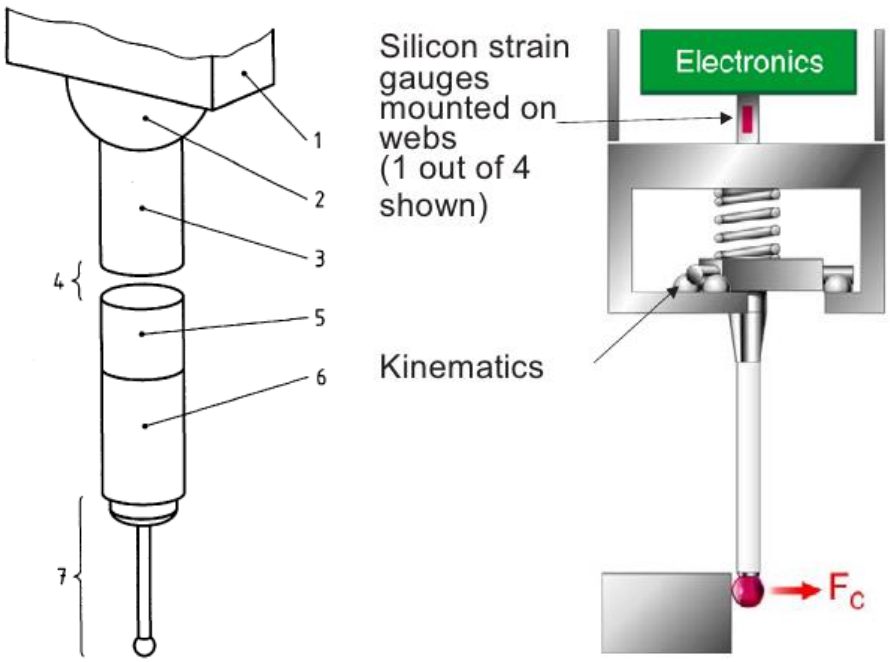

Figure 3.2 Left: articulated probing system according to [3.1]. 1-ram, 2-articulation system, 3- probe extension, 4-probe changing system, 5-probe, 6-stylus extension, 7-stylus. Right: schematic view of the Renishaw TP200 digital probe (Image adapted from [3.3]).

3.1.2 CMMs error compensation and performance evaluation

For a typical CMM the measurement uncertainty of a certain piece usually comes from the geometrical errors of the machine, environmental factors, probe system errors, feature form errors, sampling strategy and fitting algorithms.

Most of the CMMs relay on a quasi-rigid body model to compensate for the systematic geometrical errors and the slow temperature variations while an appropriate machine and environment design are fundamental to reduce the environmental factors like the faster temperature variation or the vibrations.

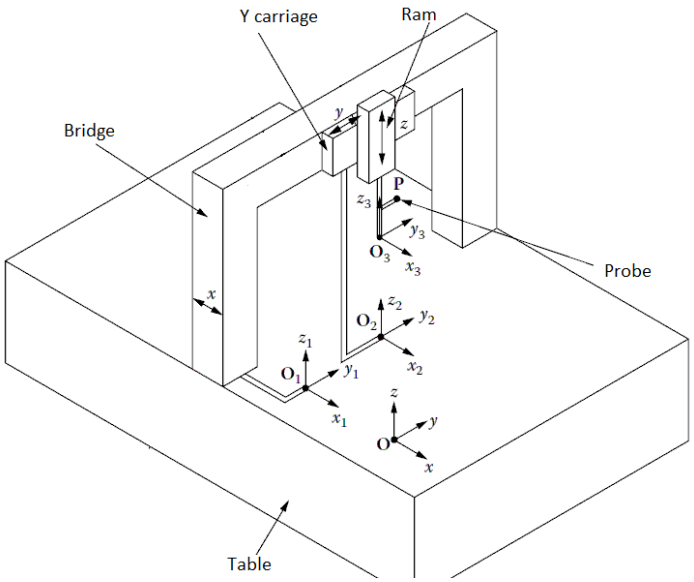

Figure 3.3 Coordinate system of a bridge type CMM (Redrawn from [3.4]).

For the geometrical compensation, according to [3.4] the deviation from a perfect machine can be calculated as difference between the nominal and the actual position of P (see Figure 3.3).

Considering a quasi-rigid body model, its position can be calculated solving the equation

$$\boldsymbol{P} = \boldsymbol{X} - \boldsymbol{R}^{-1}(x)\{Y + \boldsymbol{R}^{-1}(y)[\boldsymbol{Z} + \boldsymbol{R}^{-1}(z)P_3]\} \tag{3.1}$$

where

$$\boldsymbol{X} = \begin{pmatrix} X + \delta_x(X) \\ \delta_y(X) \\ \delta_z(X) \end{pmatrix} \qquad \boldsymbol{R}(x) = \begin{bmatrix} 1 & \epsilon_z(X) & -\epsilon_y(X) \\ -\epsilon_z(X) & 1 & \epsilon_x(X) \\ \epsilon_y(X) & -\epsilon_x(X) & 1 \end{bmatrix} \tag{3.2}$$

$$\boldsymbol{Y} = \begin{pmatrix} \delta_x(Y) - Y\alpha_{xy} \\ Y + \delta_y(Y) \\ \delta_z(Y) \end{pmatrix} \qquad \boldsymbol{R}(y) = \begin{bmatrix} 1 & \epsilon_z(Y) & -\epsilon_y(Y) \\ -\epsilon_z(Y) & 1 & \epsilon_x(Y) \\ \epsilon_y(Y) & -\epsilon_x(Y) & 1 \end{bmatrix} \tag{3.3}$$

$$\boldsymbol{Z} = \begin{pmatrix} \delta_x(Z) - Z\alpha_{xz} \\ \delta_y(Z) - Z\alpha_{yz} \\ Z + \delta_z(Z) \end{pmatrix} \qquad \boldsymbol{R}(z) = \begin{bmatrix} 1 & \epsilon_z(Z) & -\epsilon_y(Z) \\ -\epsilon_z(Z) & 1 & \epsilon_x(Z) \\ \epsilon_y(Z) & -\epsilon_x(Z) & 1 \end{bmatrix} \tag{3.4}$$

The volumetric error, then, can be expressed as follow

$$\Delta X = \delta_x(X) + \delta_x(Y) + \delta_x(Z) - Y\alpha_{xy} - Z\alpha_{xz} - Y\epsilon_z(X) + Z\left[\epsilon_y(X) + \epsilon_y(Y)\right] + \\ -Y_{P3}[\epsilon_z(X) + \epsilon_z(Y) + \epsilon_z(Z)] + Z_{P3}\left[\epsilon_y(X) + \epsilon_y(Y) + \epsilon_y(Z)\right] \quad (3.5)$$

$$\Delta Y = \delta_y(X) + \delta_y(Y) + \delta_y(Z) - Z\alpha_{yz} - Z[\epsilon_x(X) + \epsilon_x(Y)] + X_{P3}[\epsilon_z(X) + \epsilon_z(Y) + \epsilon_z(Z)] + \\ -Z_{P3}[\epsilon_x(X) + \epsilon_x(Y) + \epsilon_x(Z)] \quad (3.6)$$

$$\Delta Z = \delta_z(X) + \delta_z(Y) + \delta_z(Z) + Y\epsilon_x(X) - X_{P3}\left[\epsilon_y(X) + \epsilon_y(Y) + \epsilon_y(Z)\right] + \\ +Y_{P3}[\epsilon_x(X) + \epsilon_x(Y) + \epsilon_x(Z)] \quad (3.7)$$

where the δ representing the linear displacement and straightness errors and the ε representing the angular errors are part of the kinematic errors and α is the squareness error between two axes.

Those parameters are calculated in different part of the measuring volume using a laser interferometer to remove most of the systematic geometrical error.

The slow thermal variations are usually compensated supposing a uniform temperature of each axis and applying a length correction on the same axis based on the equivalent CTE of the axis itself.

The residual errors are the ones not captured by the model used, the ones related to the uncertainty of the model's parameters evaluation and the random ones.

To quantify them during the acceptance and reverification phase, the ISO 10360 standards are usually used.

In this particular case, following the ISO10360-2 [3.5] standard, 5 gauge blocks with different lengths are acquired with the machine under test along 7 directions and the measurement is repeated 3 times for a total of 105 deviations from the gauge block lengths. All those points must be included in the two lines defined by the maximum permissible error of length measurement $E_{0,MPE} = \pm\left(a + \frac{L}{K}\right)$ where L is the length in mm. Moreover, the maximum permissible limit of the repeatability range ($R_{0,MPL}$) is calculated as the maximum

range value between all the 3 repetitions sets. Those values are a good benchmark of all the error associated while measuring with the CMM.

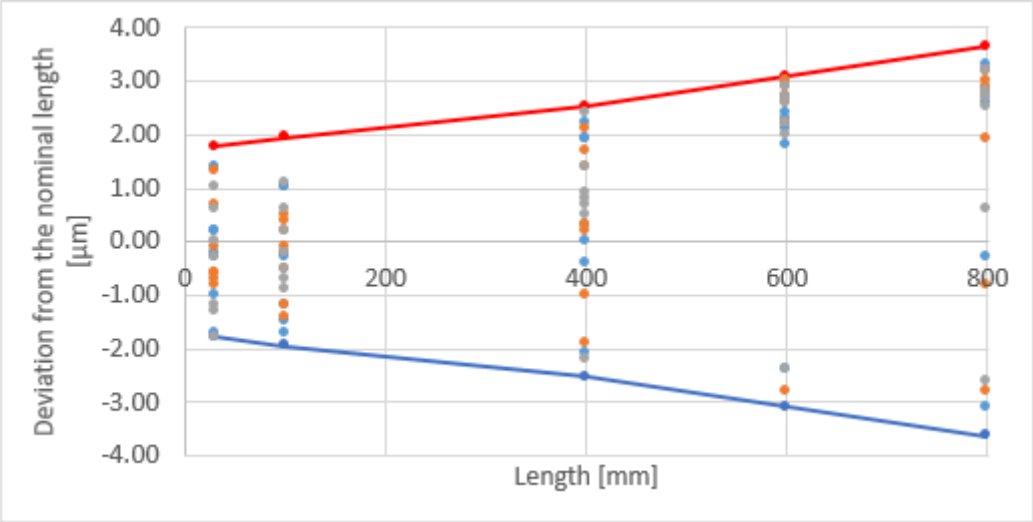

Figure 3.4 Results of the reverification tests performed on the machine according to ISO 10360-2. The lines represents the $E_{0,MPE}$ value once the uncertainty of the calibration gauges has been removed.

The ISO 10360-5 [3.6] defines the maximum permissible single-stylus form error ($P_{FTU,MPE}$) as the maximum radial error of 25 points acquired on a reference sphere and fitted with a Gaussian algorithm. This value is used to highlight the uncertainty in the measurement of small volumes and is mainly related to the accuracy of the probing system.

The machine used for the test has $P_{FTU,MPE}$ of 1.8 µm, $E_{0,MPE} = \pm\left(1.8 + \frac{L}{333}\right)$ (see Figure 3.4) and $R_{0,MPE}$=2.0 µm according to the last recertification.

3.1.3 Uncertainty estimation with CMMs

The standard ISO/TS 14253-2 [3.7] contains a Procedure for Uncertainty MAnagement (PUMA) method (see Figure 3.5) and is the reference document for the uncertainty estimation of geometrical products.

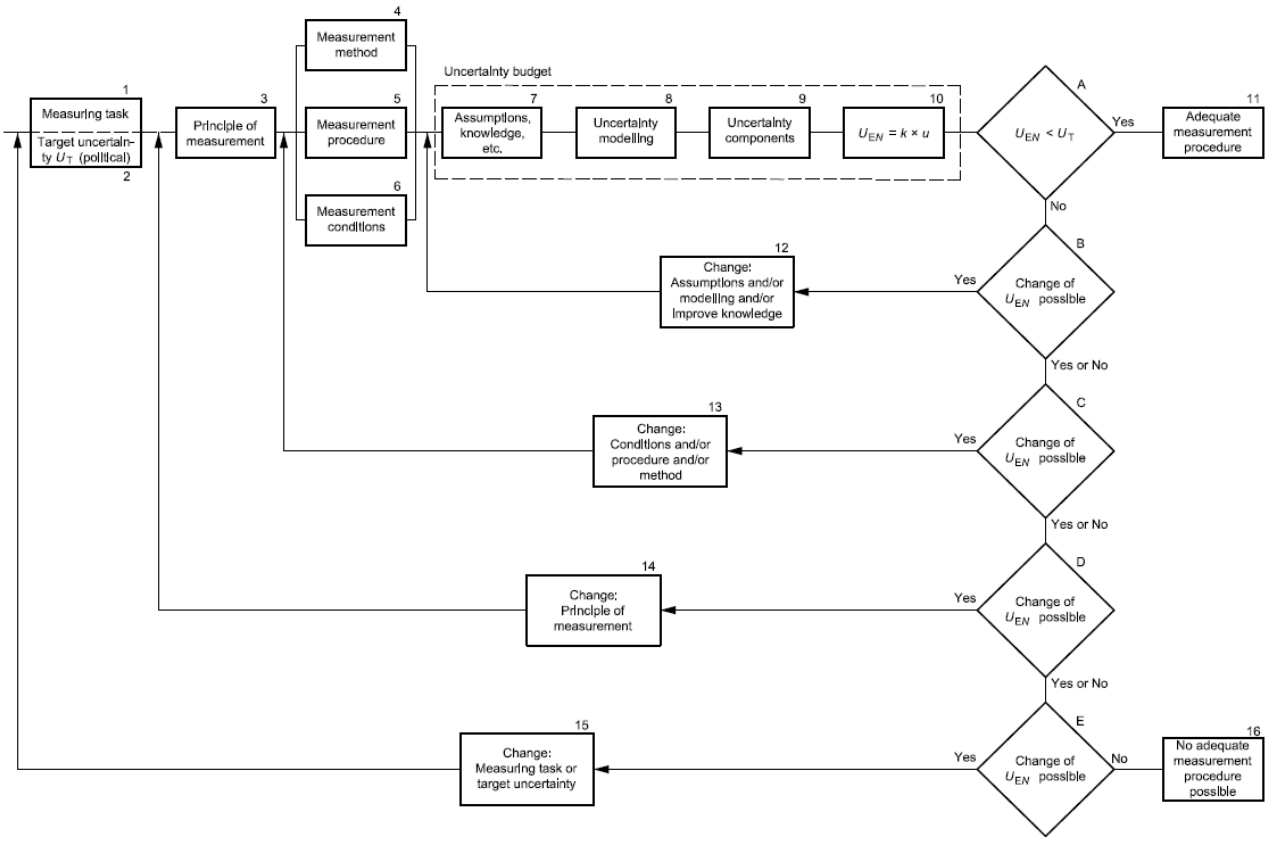

Figure 3.5 Procedure for uncertainty of measurement management for a measurement process/procedure [3.7].

In the case of CMM measurements its application has been shown in [3.2] where 4 uncertainty sources have been taken into account: machine, sampling, temperature and datum.

The expanded uncertainty is then equal to $= k\sqrt{u_{machine}^2 + u_{sampling}^2 + u_{temperature}^2 + u_{datum}^2}$.

The machine uncertainty considered is the one coming from the ISO 10360-2 certification $E_{0,MPE} = a + \frac{L}{K}$ where L is the bigger value between the maximum length to be evaluated and the largest distance to a datum.

The sampling uncertainty is calculated as $u_{sampling} = \frac{\sigma_{pc}}{\sqrt{n-x}}$ where n is the number of points probed to define the feature and x is the minimum number of points needed. The point coordinate error σ_{pc} is calculated as the square root of the quadratic sum of the probing error $P_{FTU,MPE}$ as from 10360-5 and the additional probing error due to the stylus. This additional error is needed because the ISO 10360 tests are performed with a specific stylus (in case of digital probe a 20 mm long stylus with a 4 mm diameter ruby sphere is typically used) while the actual measurement of the workpiece could involve different styli. This value can be obtained from the probe qualification routine performed at the beginning of each measurement.

The uncertainty due to the temperature is calculated, according to [3.8], as $u_T = \sqrt{UNE_S^2 + UNE_W^2 + LUTM_S^2 + LUTM_W^2}$ where W stand for workpiece, S for Scale of the machine, UNE is the uncertainty of the nominal thermal expansion and LUTM is the length uncertainty due to the temperature measurement.

The UNE values are calculated as $UNE_x = \sqrt{L^2 \times u_{\alpha x}^2 \times \left(T_{x,avg-20}\right)^2}$ where $u_{\alpha x}$ is calculated multiplying the CTE of the scale or the workpiece by a coefficient called C_D and tied to the temperature distribution (0.5 for normal, 0.6 for rectangular) and by 0.1 (consider that the CTE coefficients have a ±10% variation).

The LUTM values are calculated as $LUTM_x = \sqrt{(L^2 \times u_x^2 \times u_{TX1}^2) + (L^2 \times u_x^2 \times u_{TX2}^2)}$ where u_{TX1} is the uncertainty due to the temperature variation ($u_{TX1}=(T_{Xmax}-T_{Xmin})xC_D$) and u_{TX2} is due to the uncertainty of the temperature-measuring device.

If the feature to be measured in associated to a datum, alto its uncertainty must be evaluated. The proposed formula is $u_{datum} = \sqrt{\frac{3}{6}u_{primary}^2 + \frac{2}{6}u_{secondary}^2 + \frac{1}{6}u_{tertiary}^2}$ where the uncertainties are calculated with the previous formulae.

The two main limitations of this method are related to the direct use of the ISO 10360 values which are synthetic number representing the range of a small number of measures and the thermal uncertainty that doesn't take into account the compensation performed by the CMM.

Due do the difficult application of the PUMA method on CMM measures the ISO 15530 series has been developed. The first of those standards [3.9] provide an overview of the proposed methods.

The ISO 15530-3 [3.11] foresees the use of a calibrated master to evaluate the measurement uncertainty due to the instrumentation, the measurement plan and many of the extrinsic sources. The main limitation of this method is the need of a calibrated workpiece, which make its use unfeasible for single piece production like in most of the cases of interest.

The ISO/TS 15530-4 [3.12] consider the use of a Montecarlo simulation to capture complex interaction between the different uncertainty sources. The Uncertainty Evaluation Software (UES) must then be validated with different techniques:

- physical test on an individual CMM,
- computer-aided verification and evaluation,
- comparison with specific reference results,
- statistical long term investigations

The ISO/DTS 15530-2 [3.10], still under development, consider multiple measurements of the workpiece in different position and orientations and will be used as a first verification of the dummy optical system built to validate the Uncertainty Evaluation Software proposed in chapter 3.3.

3.2 ESPRESSO Front End alignment with an AACMM

A first, simple, uncertainty evaluation has been done during the alignment of the ESPRESSO Front End Units (FEUs).

To keep under control the image quality and the spatial repeatability of the five FEUs beam an on-line analysis of the elements positions has been performed.

The first step consisted in a sensitivity analysis performed with a raytracing software like Zemax. The results are shown in Table 3.1, Table 3.2 and Table 3.3. The x direction is the axis exiting the optical plane, the z

direction is the optical path for the lenses, or the normal to the surface for the reflecting elements, and the y direction is the remaining axis in a left-handed reference system.

Table 3.1 Central spot displacement on the output focal plane for an element displacement of 1 mm or a rotation of 1 arcminute.

		PL	PSU	FSU	RL	FLM	GL	TCCD
Displacement x	[µm/mm]	-50	-	-	1550			
Displacement y	[µm/mm]	-50	-	-	1550			
Displacement z	[µm/mm]	-	-800	800	-			
Rotation x	[µm/arcmin]	1	2	-80	1			
Rotation y	[µm/arcmin]	-1	-2	55	-1			

Table 3.2 Central spot displacement on the Field TCCD focal plane for an element displacement of 1 mm or a rotation of 1 arcminute.

		PL	PSU	FSU	RL	FLM	GL	TCCD
Displacement x	[µm/mm]	30	-	-	-1000	-	1650	1000
Displacement y	[µm/mm]	30	-	-	-1000	-	1650	1000
Displacement z	[µm/mm]	-	500	-500	-	500	-	-
Rotation x	[µm/arcmin]	0	-2	80	0	0	-1	-
Rotation y	[µm/arcmin]	0	1	-35	0	0	1	-

Table 3.3 Central spot displacement on the Pupil focal plane for an element displacement of 1 mm or a rotation of 1 arcminute.

		PL	PSU	FSU	RL	FLM	GL	TCCD
Displacement x	[µm/mm]	-600	-	-	450	-	1000	1000
Displacement y	[µm/mm]	-650	-	-	500	-	1000	1000
Displacement z	[µm/mm]	-	-700	700	-	-10	-	-
Rotation x	[µm/arcmin]	0	-67	-1	1	40	0	-
Rotation y	[µm/arcmin]	0	45	-1	-1	-35	0	-

The alignment has been performed following the scheme presented in Figure 3.6 in order to have the injection of the light into the fibre minimizing the stroke of the FSU piezo motor.

The nominal decentring due to the misalignment of each element has been calculated considering the displacement of the reference points acquired on the mount while the uncertainty comes from the play between the mount and the optical element and the uncertainty of the AACMM itself.

The effect of the play has been calculated considering the geometrical characteristics of the optical and mechanical elements like cilindricity tolerances of the relative interfaces, diameter differences, and length of the lenses.

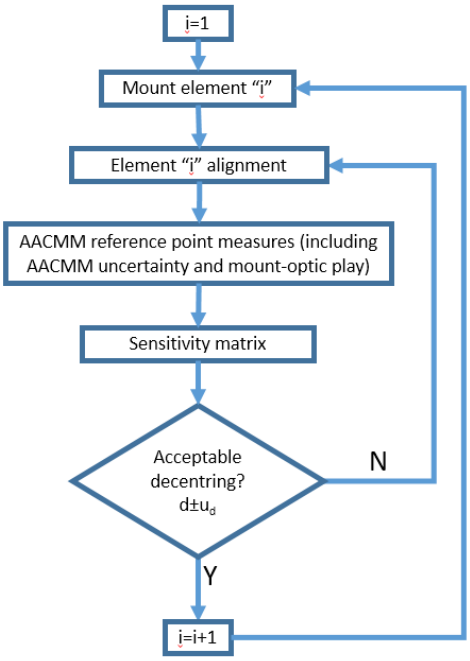

Figure 3.6 Flowchart of a FEU alignment. Each element is aligned one after the other keepeing track of the nominal value and the uncertainty of the misalignments.

For the measurement uncertainty, the Volumetric Performance Test value of the AACMM (see [3.13]) has been used. In this case, it was 0.041 mm.

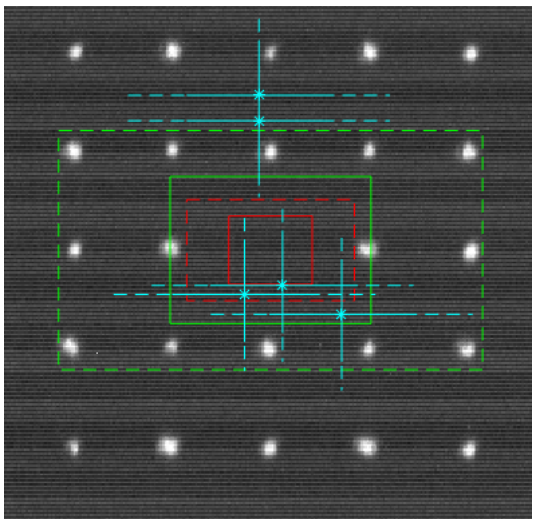

Figure 3.7 Expected decentring at the Fibre Link injection for the 5 FEUs.

The final results are shown in Figure 3.7. The green rectangles delimit the area where the centre of the optical beam should fall considering the uncertainty of the AACMM and the possible misalignments between the optical axis and the axis of the cylinder of each mechanical mounts while the red rectangles have been calculated considering only the play between the elements.

The light blue points represent the 5 FEUs expected position considering the remaining misalignment errors over the 6 degrees of freedom due to the imperfect alignment with the calibrated steel shims while the bands highlight the uncertainty of the AACMM. The full lines have been calculated with a statistical approach (2σ values) while the dashed lines ones with a worst-case approach.

The light blue points obtained from this simulation are compatible with the centres positions seen with the CMOS camera (data not shown here) proving that the procedure is reliable and can be used to check the expected results.

The Worst Case approach has a better match with the real system. This is related to bias in both the AACMM measurements and the lens-optomechanical elements mounts (e.g. all the elements tilted or decentred in the same direction during the gluing procedure).

Three different approaches can be considered in order to improve the alignment:

1. the use of a different strategy for optical mounts characterization (reduces the size of the red and the green box),
2. the improvement of the semi-kinematic mounts repeatability for a faster alignment (moves the light blue spots to the centre of the image),
3. the use of a more accurate measuring instrument like a Cartesian CMM (reduces the length of the blue lines of at least one order of magnitude).

This chapter will focus on point 3. In particular, a software developed to estimate the uncertainty of a Cartesian CMM based on experimental data would be described.

3.3 Uncertainty evaluation for small lenses systems

Multiple software packages with the aim of predicting the accuracy of features acquired with a CMM have been developed over the time. The usual approach consists in the generation of single, perturbed, measuring points followed by the comparison of the computed substitute geometric elements with the nominal ones. The differences arise from the model used to generate those points.

Different approaches to obtain this model have been investigated in the past [3.14] but the most interesting ones are called the Virtual CMM and the simulation by constraints, both based on Montecarlo simulations.

The simulation by constraints is presented in [3.15]. With this method, the nominal points to be acquired during the actual measurement are randomly perturbed. If the point cloud generated, representing a “parametric state of the CMM”, does not respects the constrains defined by, for example, the calibration certificate, the parametric state is discharged. Once an adequate number of parametric states is recorded, the uncertainty of each point is calculated.

The Virtual CMM instead, uses as an input for the generation of the perturbed points a number of measured or estimated influencing factors usually coming from the machine geometry, the probing, and the environment.

Both those approaches can be extremely different in terms of time, equipment, and complexity pending on the number of sources considered and how general the desired solution is. Two extreme examples from this point of view are the Virtual CMMs presented in [3.16], where the uncertainty of a small circular feature is estimated with a simple procedure and [3.17], where the whole volume of a machine has been characterized using a laser tracer.

The activity presented here focused on the uncertainty estimation of system composed by small optical elements distributed on a large bench trying to keep the evaluation as simple and inexpensive as possible.

3.4 Uncertainty evaluation for small lenses systems, parameters estimations

Six categories of the main CMM influence factors are considered in the ISO 15530-4 standard and are shown in Figure 3.8. In [3.18] a detailed discussion of those elements can be found:

- Workpiece factors
  - form error
  - fixturing
- Probing (sensor system)
  - probe type
  - stylus configuration
  - calibration strategy
  - stylus bending
  - approach velocity
  - probe repeatability
  - lobing
  - indexable head repeatability
  - scanning force and speed
  - filtering
- Evaluation (data analysis)
  - Fitting algorithm choice
- CMM Geometry
  - rigid body errors
  - quasi static errors
  - dynamic errors
  - scale resolution
- Scales/environment
  - thermal effects
  - external vibration
  - humidity
  - atmospheric pressure
  - utility variations
  - lightning/ventilation system
- Strategy
  - number and location of sampling points

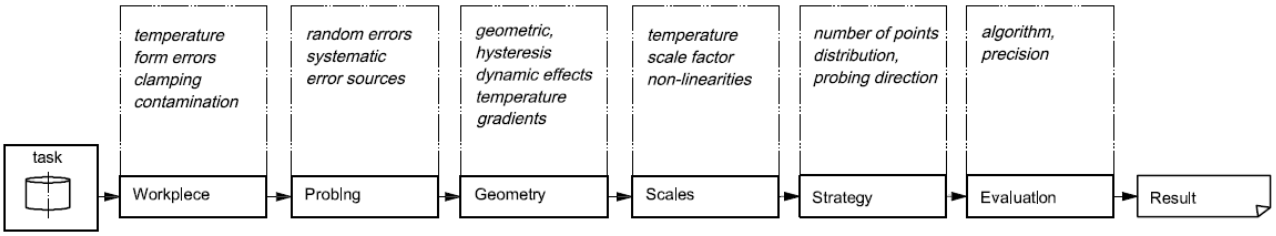

Figure 3.8 Categories of influence factors in a CMM according to [3.12].

The workpiece factors in this case can be removed from the analysis as the elements measured have a form error more than 2 order of magnitude smaller than the CMM accuracy and the fixturing is always done with isostatic systems to avoid undesired deformations.

The fitting algorithm choice also has a negligible effect. Due to the high quality of the surfaces and the consequent small deviations of the measured points from the substitute geometry, the use of different fit objectives or different mathematical implementation of the fits leads to the same substitute geometry.

The number and location of the sampling point will be considered when the points will be used to create the substitute geometry.

The remaining factors, then, are related to the probing system, the CMM geometry, and the environment.

In order to simplify the software the following assumptions are considered:

- The probing system uncertainty is responsible for the random errors in small measuring volumes. The probe error is then directly related to 'a' in the $E_{0,MPE}$ formula. With this simplification, the probe lobing is considered a secondary effect while the index head repeatability is considered as a CMM geometry error.
- The CMM geometry parameters presented at the beginning of chapter 3.1.2 have a low spatial frequency (see Figure 3.9). This error is then directly related to 'K' in the $E_{0,MPE}$ formula.
- The drift of the machine is related to the environmental conditions and has negligible effects in the short time needed to measure a single surface.

The three factors will be evaluated in the next sections.

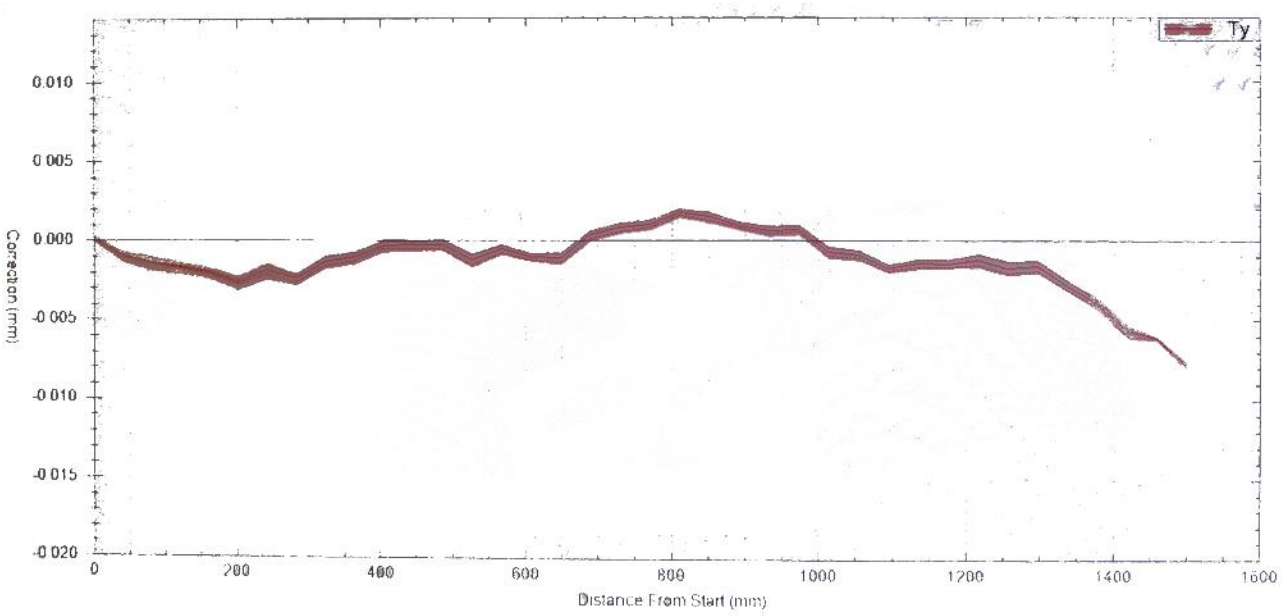

Figure 3.9 One of the CMM geometrical errors evaluated with a laser interferometer. The graph has been obtained during the periodical CMM recalibration and the error is measured back and forth with a spatial resolution of 40 mm.

3.4.1 Probe Error (repeatability)

Some of the factors included in the 'sensor system' part are not applicable for a digital probe like the Renishaw TP200 while the importance of some other has to be evaluated.

Four factors have been evaluated first to understand if they have some effect on the measurement uncertainty of the probe: the measurement time, the measurement speed, the head altitude, and the probe type.

3.4.1.1 Measuring time

he measuring time for a digital probe is defined at the time between the start of the point measure and the actual acquisition of the point. In this time, usually in the order of 1 or 2 seconds, the machine moves at a slow constant speed to eliminate all the dynamic effects. If this time is excessively reduced (high measuring speed or small measuring distance) the vibration of the machine are not yet damped out and two effects are possible. One is the increasing of the uncertainty value of the measured point due to the undefined dynamic forces still present and the other is the drift of the acquired point due to the oscillation of the stylus. Those effects are shown in [3.2], [3.19] and in Figure 3.10.

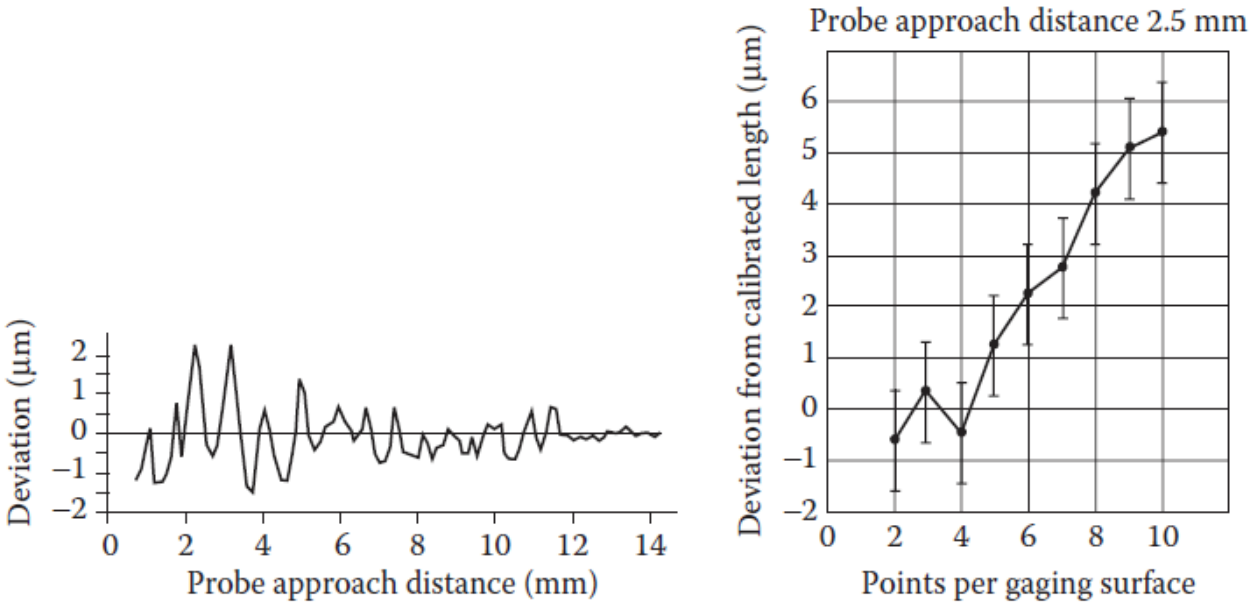

Figure 3.10 Left: increase of the deviation for shorter probe approach distances. Right: deviation from the calibrated length increasing the number of points acquired. The measurement time is shortened as more points are acquired on each surface of the gauge block [3.2].

.

To evaluate this effect, 25 points have been acquired on a calibrated sphere (25.9873 mm diameter) using a stylus with a 20 mm long stainless steel stem and a ruby sphere of 4 mm in diameter (Renishaw code A-5003-4161). The measuring speed has been kept constant at 3.00 mm/s while the measuring distance has been reduced from 4 mm (1.333 s measurement time) to 0.25 mm (0.083 s measurement time).

Due to this effect, an increase in the sphere diameter measured was expected for shorter measuring distances together with a higher variation of all the parameters (diameter, centre and form error).

The results are shown in Figure 3.11 and no effects related to the measuring time can be seen, even for extreme measuring distances (< 1 mm).

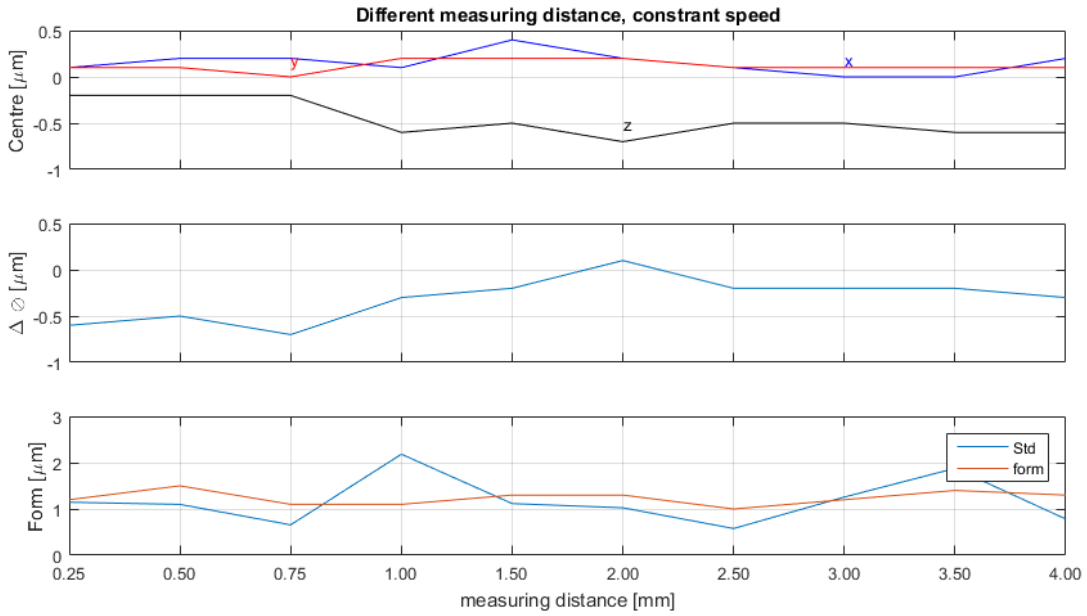

Figure 3.11 Variations in the centre, diameter, and form of a sphere acquired with a L20D4 stylus changing the measuring distance.

3.4.1.2 Measuring speed

Tests were also performed to evaluate the effect of the stylus bending with respect to the measuring speed. For higher measurement speed, the trigger is activated with higher forces leading to a deformation of the stylus stem and a diameter of the measured sphere smaller than its physical diameter. Moreover, the different stiffness of the stylus in in the axial and radial direction lead to a worst form error while acquiring a feature probing it from different directions.

This can heavily effect the performances of digital probes with kinematic trigger like the Renishaw TP20 but have a considerable effect also on the 2-stage trigger like the Renishaw TP200 under study.

The same reference sphere has been acquired with 25 points with a measuring distance equal to 2 times the measurement speed in order to avoid any measuring time effect. The test has been performed with a combination of two probe modules (Standard Force and Low force) and two styli: one is the already presented A-5003-4161 (L20D4) while the second has a 50 mm long tungsten carbide stem and a 4 mm diameter ruby sphere (Renishaw A-5003-0045, L50D4).

As can be seen in Figure 3.12, there is a variation in the diameter proportional to the speed. This variation will be compensated, anyway, during the calibration of the stylus. In some case, there is also an increase of the form error for higher measuring speed. Nevertheless, this effect can be neglected in our analysis because the measurement speed during the alignment procedure will always stay below 4 mm/s to limit the contact force.

The variation of the centre in the Z direction will be only partially compensated by the calibration of the stylus while the part related to the form error will remain.

Finally, a form error increase can be noticed with the longer stylus.

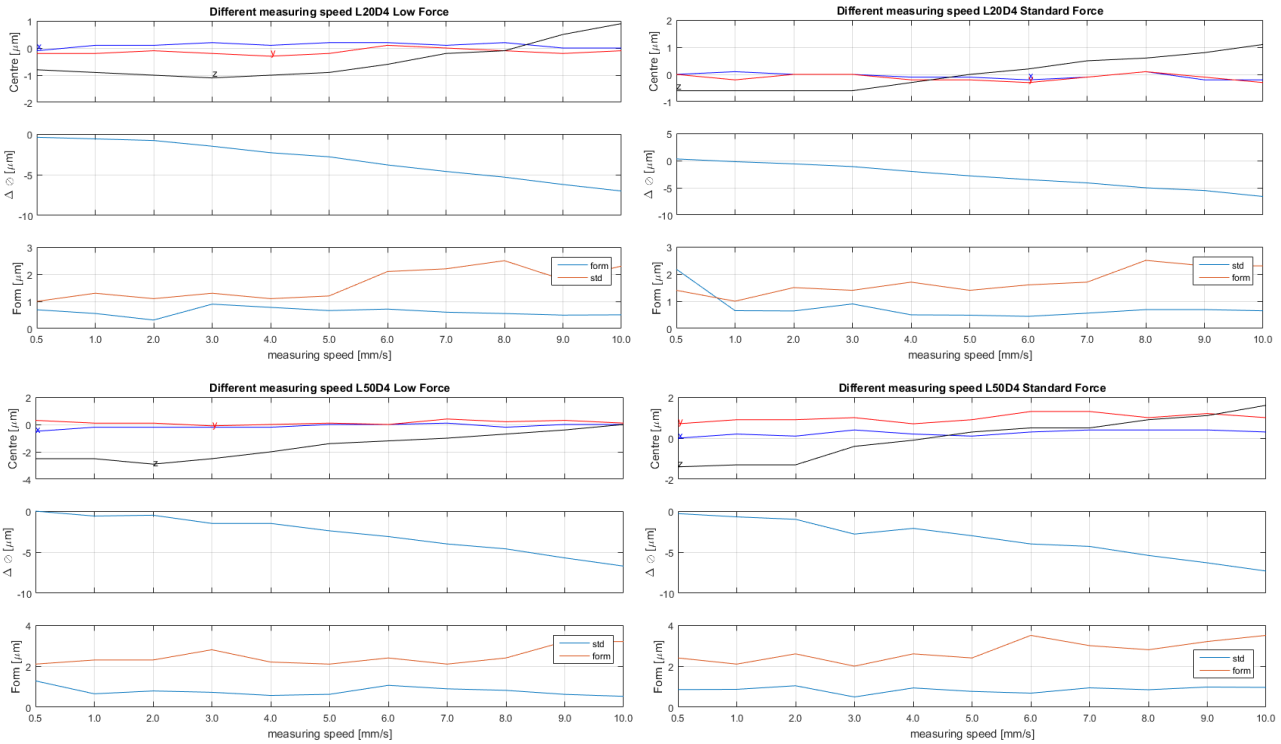

Figure 3.12 Centre, diameter and form error of a reference sphere acquired with different measuring speed with an L20D4 stylus and an L50D4 stylus mounted on a standard force and a low force probe.

3.4.1.3 Head altitude

The head altitude is usually considered a factor decreasing the quality of the measurements. In the ISO 10360-2 [3.5] 2 different test to evaluate the length measurement error are foreseen: $E_{0,MPE}$ and $E_{150,MPE}$. The $E_{150,MPE}$ evaluation is similar to the $E_{0,MPE}$ but the gauge blocks are tested with the tip offset by 150 mm (see Figure 3.13) along 2 direction instead of 7 for a total of 30 deviations measurements.

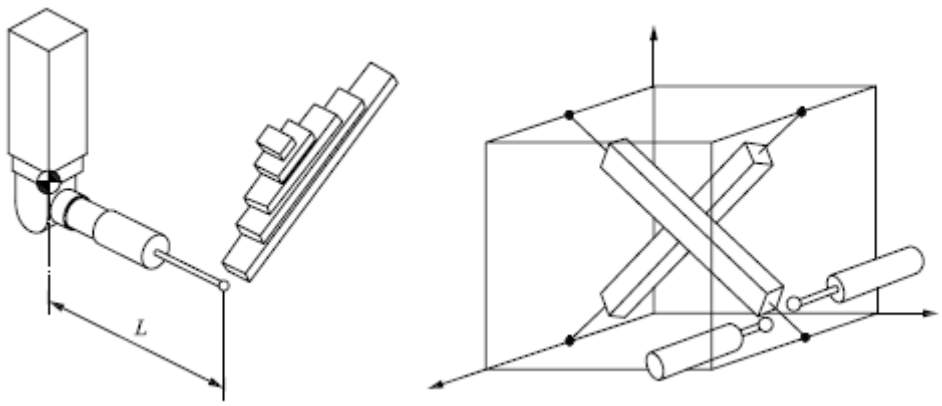

Figure 3.13 $E_{150,MPE}$ tests representation. Left: definition of the tip offset L. Right: possible positions of the calibrated lengths and possible orientations of the probe

This value is rarely provided by the CMM manufacturers. When this information is available, it is expressed in the form $E_{150,MPE} = \pm\left(a + \frac{L}{K}\right)$ with 'K' equal to the $E_{0,MPE}$ case and 'a' equal or 0.5 µm higher than in the $E_{0,MPE}$ case as a function of the angular errors of the CMM machine (see section 3.1.2).

To evaluate this effect the calibrated sphere is acquired with a measurement speed of 3 mm/s at 4 different head altitudes (0°, 30°, 60° and 90°) using three different styli. Together with the already presented A-5003-

4161 (L20D4) and A-5003-0045 (L50D4) a third stylus with a 100 mm long carbon fibre stem and a 6 mm diameter ruby sphere (Renishaw A-5003-2291, L100D6) has been used for the test.

In Table 3.4 the tip offsets evaluated are shown starting from the rotation axis of the CMM head.

Table 3.4 Tip offset calculated from the rotation axis of the CMM head.

		Tip offset [mm]			
Renishaw code	Stylus Length [mm]	0° altitude	30° altitude	60° altitude	90° altitude
A-5003-4161	20	0	65.9	114.1	131.8
A-5003-0045	50	0	90.9	140.1	161.8
A-5003-2291	100	0	105.9	183.4	211.8

The results are shown in Figure 3.14. No effect has been found due to the tip offset while the length of the stylus plays an important role on the CMM performances.

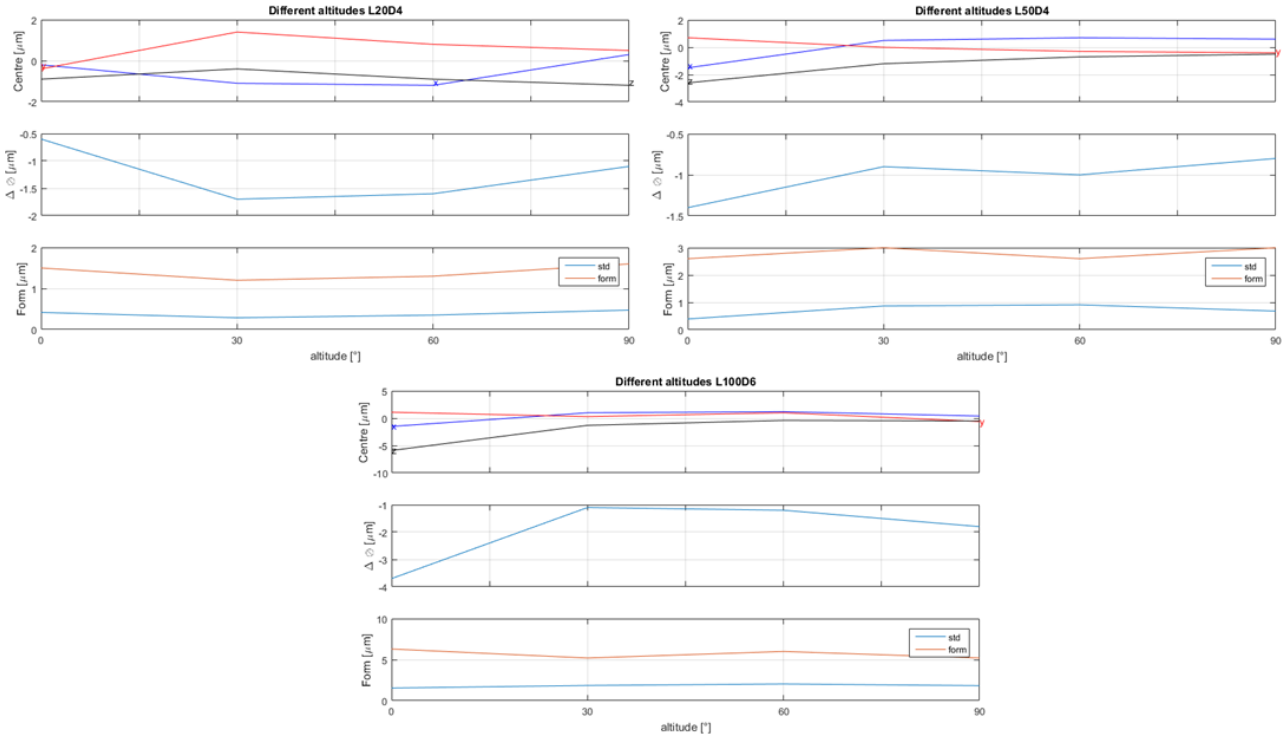

Figure 3.14 Centre, diameter variation, and form error of the calibrated sphere measured with different styli and different head altitudes.

3.4.1.4 Probe module

The last preliminary test has been performed with the usual procedure (calibrated sphere acquired with 25 points measured at 3 mm/s) changing the probe module.

The three modules tested were two Standard and one low force module for the Renishaw TP200 probe. The serial numbers used to identify them are the following:

- Standard Force module 0185L4
- Standard Force module 948J48
- Low Force module 948Q66

The test has been performed with four different styli:

- A-5000-4154, 10 mm long stem and 4 mm diameter ruby sphere (L10D4)
- A-5003-4161 (L20D4)
- A-5003-0045 (L50D4)
- A-5003-2291 (L100D6)

The results are shown in Figure 3.15 and no particular differences can be noticed between the different modules. Also in this test, the length of the stylus is by far the most important factor in the performance evaluation on small features measurement.

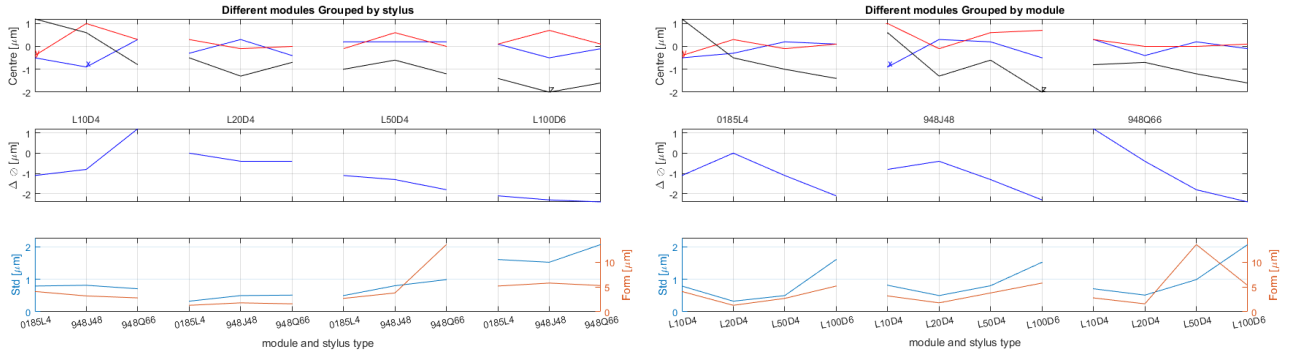

Figure 3.15 Centre, diameter variation, and form error of the calibrated sphere measured with different styli and different probe modules. Left: results grouped by styli. Right: same results grouped by module.

3.4.1.5 Styli

From the preliminary analysis presented, the choice of the stylus appears as the most relevant factor in the probe repeatability.

To evaluate this effect, the head has been placed at zero altitude and the calibrated sphere has been acquired with 490 points. To minimize the effect of the thermal drifts the measurement has been done repeating a 49 points acquisition for 10 times.

The distribution of the points along the measured hemisphere is the following: 16 points at 0°, 30° and 60° altitude and 1 point on the pole.

The obtained results are shown from Figure 3.16 to Figure 3.27 and summarized in Table 3.5. The column 'St.dev 49 pts' shows the standard deviation of the 49 points acquisition as radial deviation from the best fitted sphere while 'St.dev 490 pts' shows the standard deviation of all the 490 points. Both the values have been calculated after removing the outliers identified with a Grubb's test.

The standard deviation value in micrometres approximately follows the equation $St.dev = 0.028(|L - 20|) + 0.25D$ where D and L are the diameter of the sphere and the stem length in millimetres. All the values obtained have a maximum deviation from this regression of ±10% with the exception of L20D4OLD (-48%, probably due to an extremely low deviation from the spherical form of the ruby ball) and L40D4 (+25%, probably due to a non-perfect connection between the stem extension and the stylus).

It is worth to notice that, as shown in the 'clock [°] - position [µm]' graphs a certain anisotropy is present. One explanation to this behaviour can be the different inertia of the machine while moving in the X or Y direction. As explained before, for the sake of simplicity, this anisotropy will be considered a random error.

Table 3.5 Standard deviation of the acquired points on the reference sphere. Outliers [#] point out the number of removed point before performing the calculations.

Renishaw code	Stem (length [mm])	Sphere (diam. [mm])	Name	St.dev 49 pts [µm]	St.dev 490 pts [µm]	Outilers [#]
A-5000-4154	Stainless steel (10)	Ruby (4)	L10D4	1.30±0.13	1.32	7
A-5000-4158	Stainless steel (11)	Ruby (8)	L11D8	2.29±0.31	2.36	7
A-5000-3614	Stainless steel (0)	Ceramic (18)	L11D18	4.80±0.65	4.86	6
A-5000-3606	Stainless steel (20)	Ruby (2)	L20D2	0.56±0.05	0.57	3
A-5000-4161	Stainless steel (20)	Ruby (4)	L20D4 old	0.52±0.12	0.54	13
A-5000-4161	Stainless steel (20)	Ruby (4)	L20D4	0.88±0.17	0.92	6
A-5000-4161 M-5000-3647	Stainless steel (30)	Ruby (4)	L30D4	1.16±0.23	1.25	2
A-5000-4161 M-5000-3648	Stainless steel (40)	Ruby (4)	L40D4	1.95±0.18	1.95	2
A-5000-4161 M-5000-3647 M-5000-3648	Stainless steel (50)	Ruby (4)	L50D4	1.95±0.32	1.97	1
A-5003-0045	Tungsten carbide (50)	Ruby (4)	L50D4	1.77±0.22	1.77	3
A-5003-2287	Carbon fibre (50)	Ruby (6)	L50D6	2.32±0.28	2.32	10
A-5003-2291	Carbon fibre (100)	Ruby (6)	L100D6	3.57±0.21	3.55	0

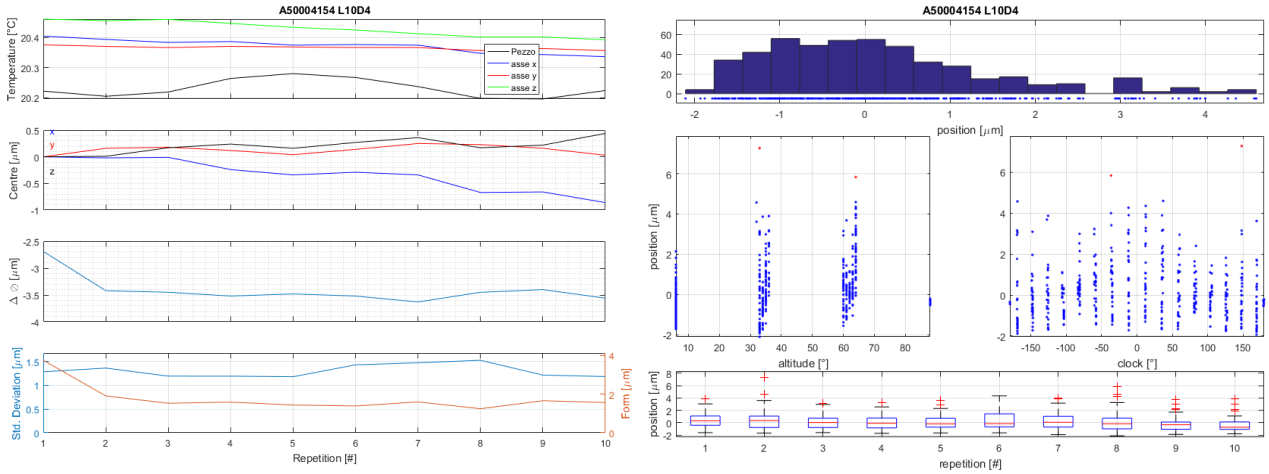

Figure 3.16 Probe repeatability test on A-5000-4154 (L10D4). Left: synthetic results from the 10 repetitions. Right: distribution of the error of all the 490 points. The red ones in the central graphs are the outliers.

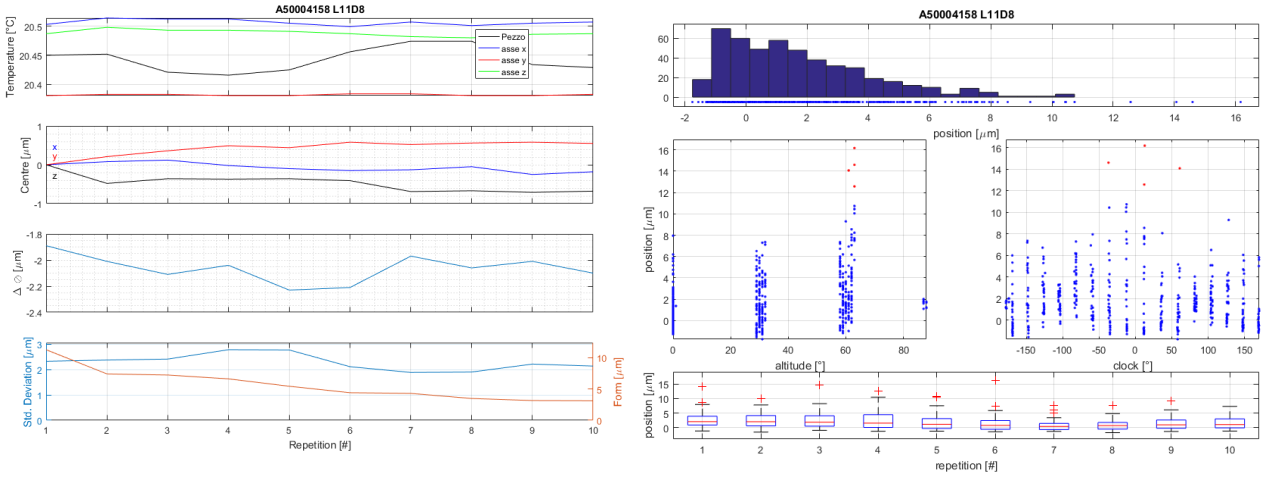

Figure 3.17 Probe repeatability test on A-5000-4158 (L11D8). Left: synthetic results from the 10 repetitions. Right: distribution of the error of all the 490 points. The red ones in the central graphs are the outliers.

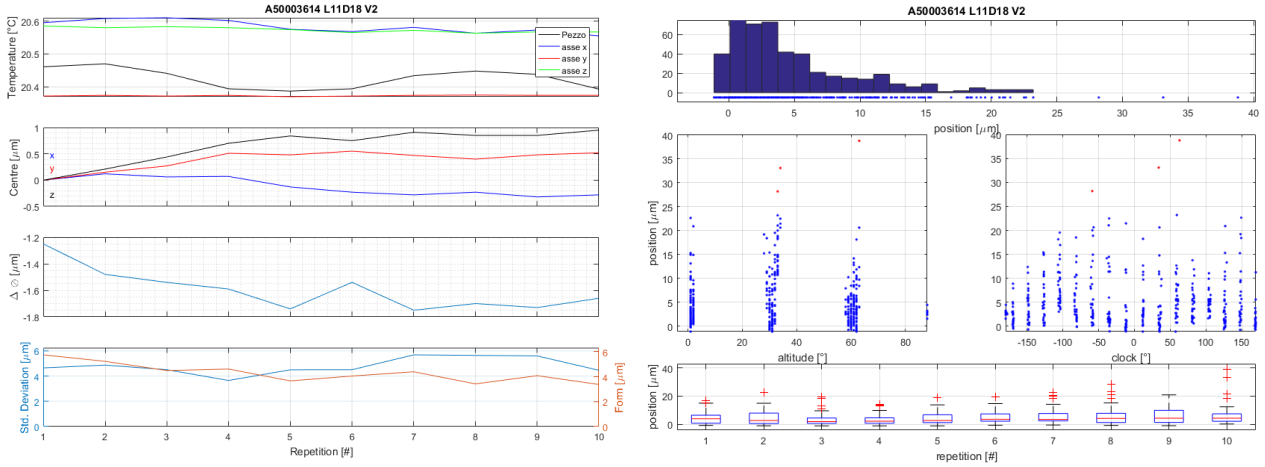

Figure 3.18 Probe repeatability test on A-5000-3614 (L11D18). Left: synthetic results from the 10 repetitions. Right: distribution of the error of all the 490 points. The red ones in the central graphs are the outliers.

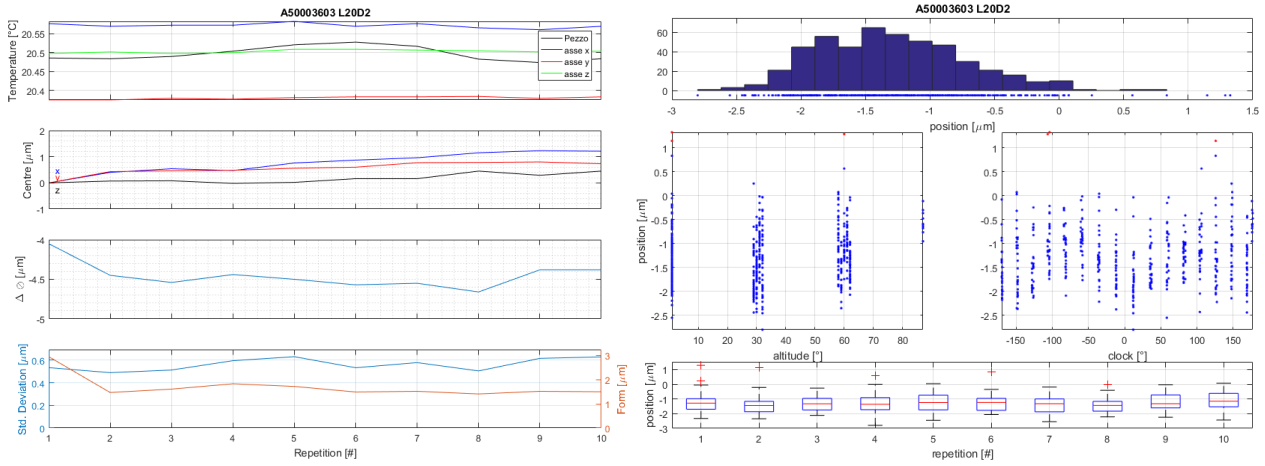

Figure 3.19 Probe repeatability test on A-5000-3603 (L20D2). Left: synthetic results from the 10 repetitions. Right: distribution of the error of all the 490 points. The red ones in the central graphs are the outliers.

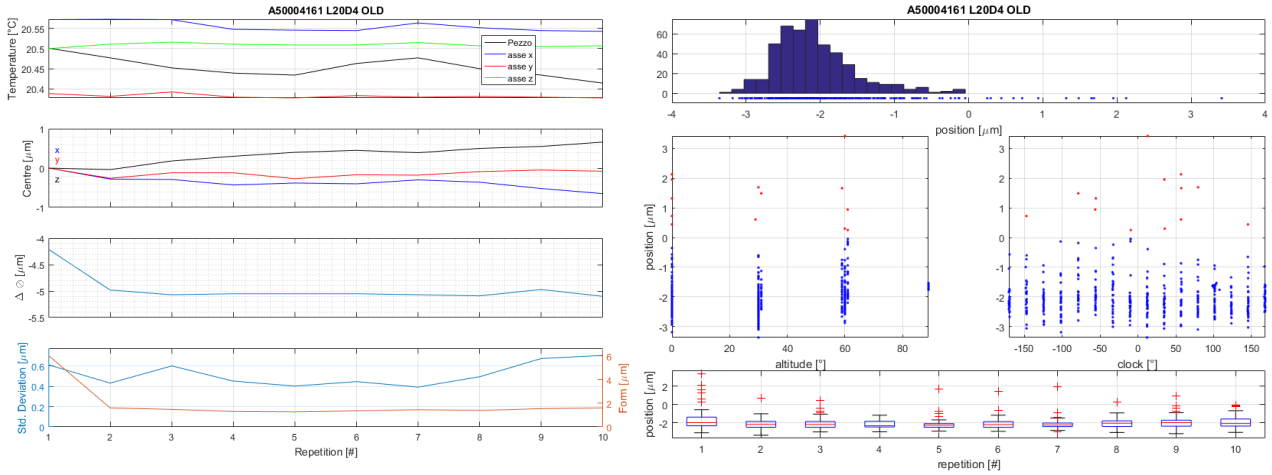

Figure 3.20 Probe repeatability test on A-5000-4161 (L20D4). Left: synthetic results from the 10 repetitions. Right: distribution of the error of all the 490 points. The red ones in the central graphs are the outliers.

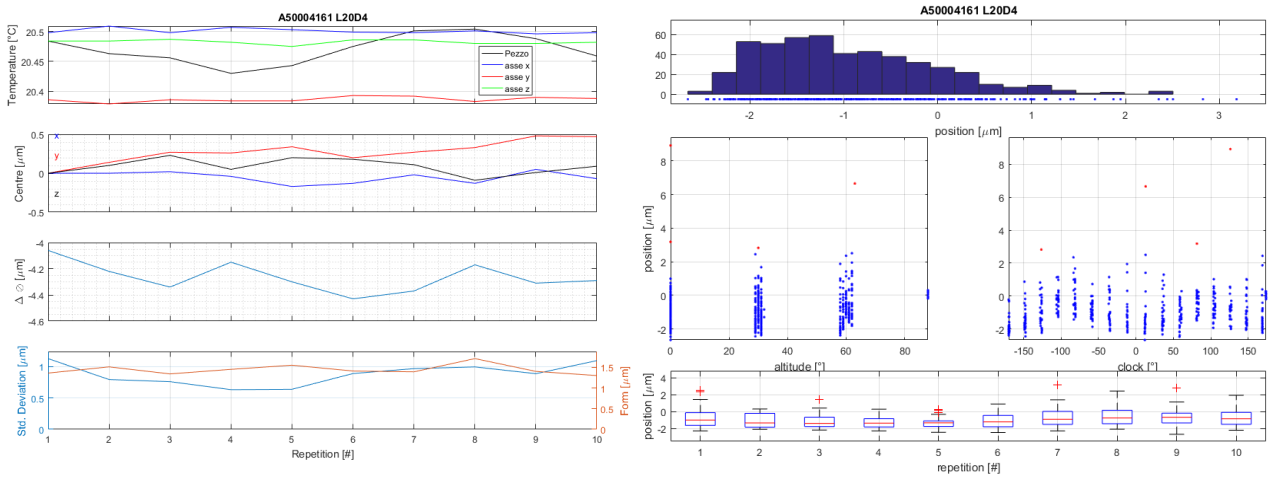

Figure 3.21 Probe repeatability test on A-5000-4161 (L20D4). Left: synthetic results from the 10 repetitions. Right: distribution of the error of all the 490 points. The red ones in the central graphs are the outliers.

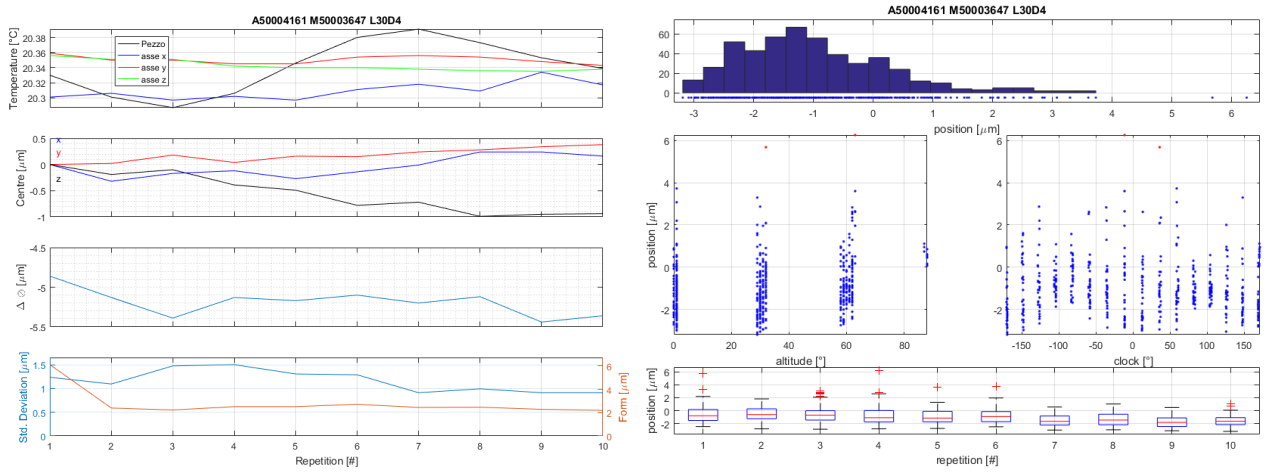

Figure 3.22 Probe repeatability test on A-5000-4161 with M-5000-3647 extension (L30D4). Left: synthetic results from the 10 repetitions. Right: distribution of the error of all the 490 points. The red ones in the central graphs are the outliers.

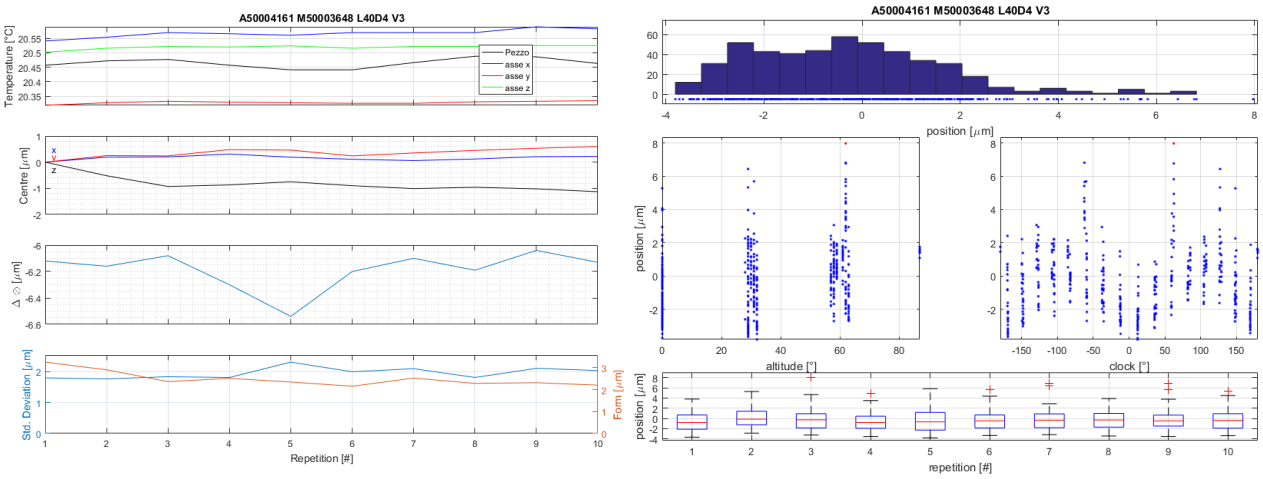

Figure 3.23 Probe repeatability test on A-5000-4161 with M-5000-3648 extension (L40D4). Left: synthetic results from the 10 repetitions. Right: distribution of the error of all the 490 points. The red ones in the central graphs are the outliers.

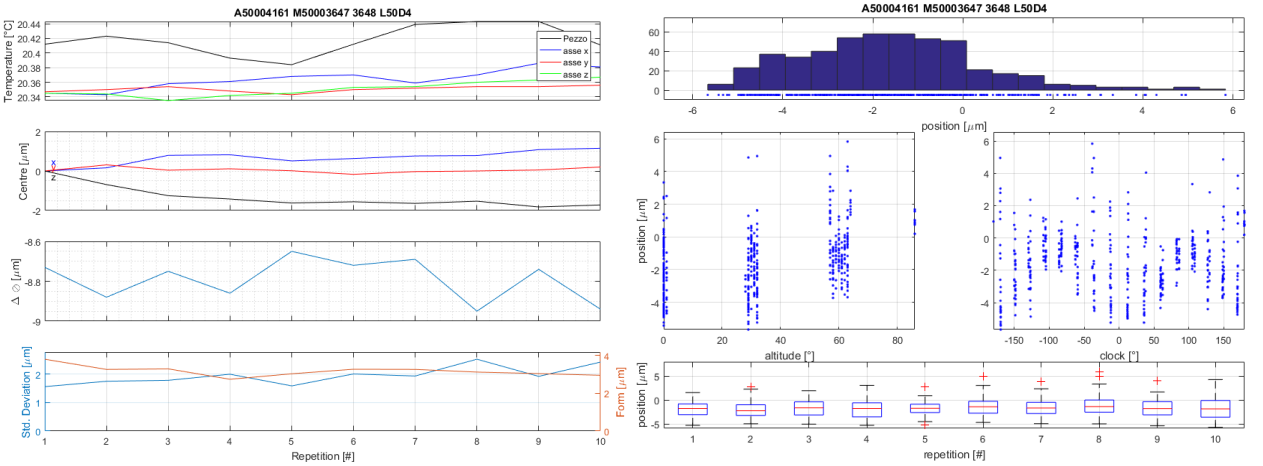

Figure 3.24 Probe repeatability test on A-5000-4161 with M-5000-3647 and M-5000-3648 extensions (L50D4). Left: synthetic results from the 10 repetitions. Right: distribution of the error of all the 490 points. The red ones in the central graphs are the outliers.

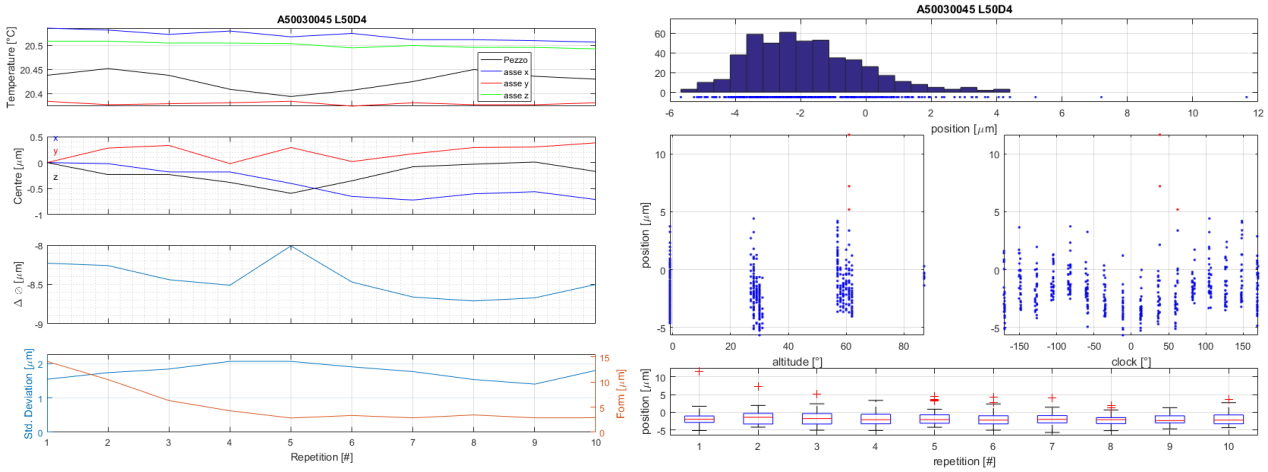

Figure 3.25 Probe repeatability test on A-5003-0045 (L50D4). Left: synthetic results from the 10 repetitions. Right: distribution of the error of all the 490 points. The red ones in the central graphs are the outliers.

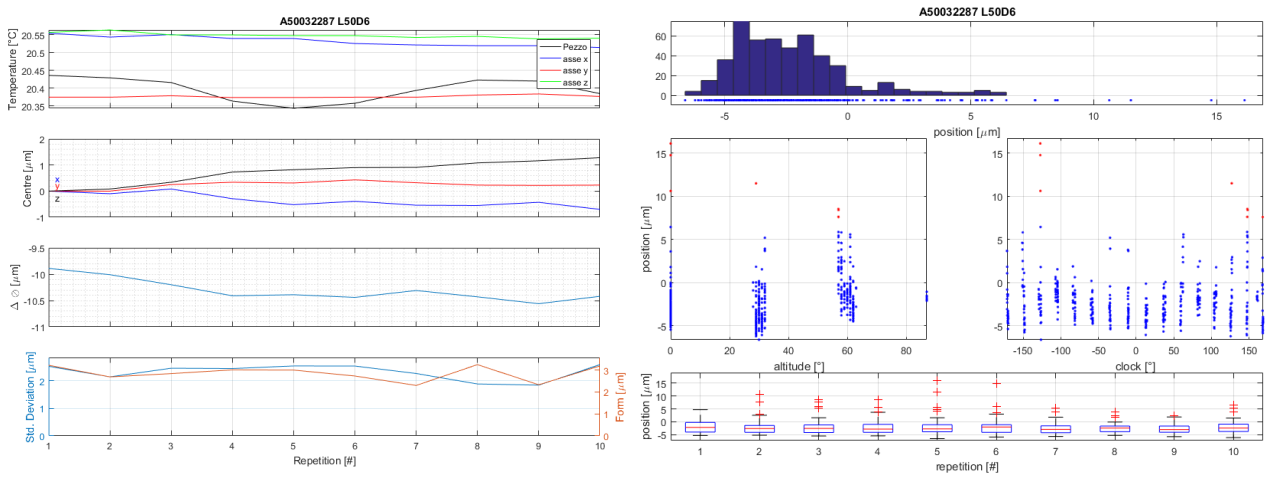

Figure 3.26 Probe repeatability test on A-5003-2287 (L50D6). Left: synthetic results from the 10 repetitions. Right: distribution of the error of all the 490 points. The red ones in the central graphs are the outliers.

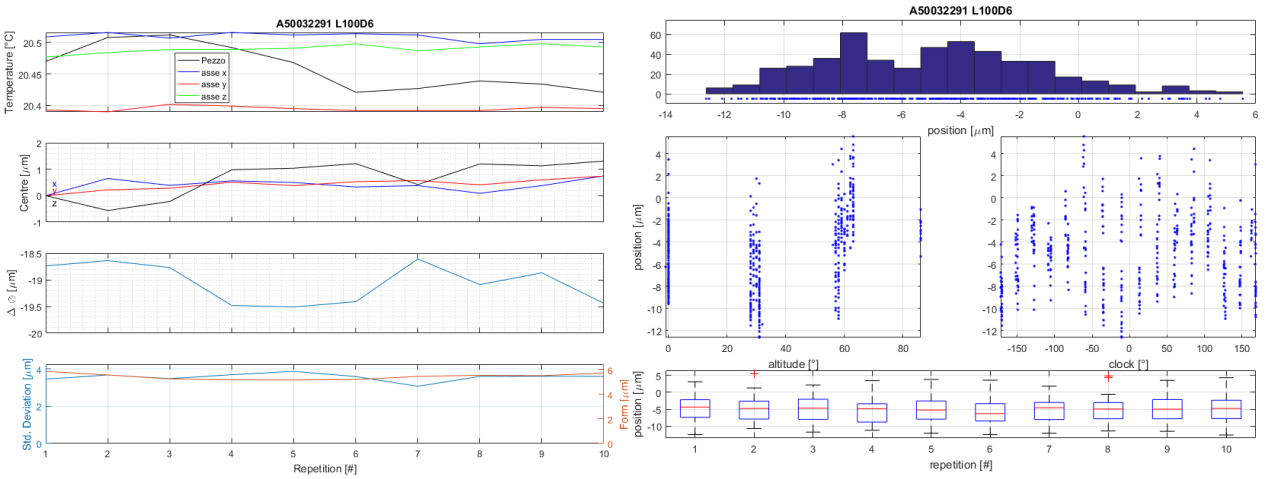

Figure 3.27 Probe repeatability test on A-5003-2291 (L100D6). Left: synthetic results from the 10 repetitions. Right: distribution of the error of all the 490 points. The red ones in the central graphs are the outliers.

3.4.2 Machine error (trueness)

The deviations related to the machine geometrical errors are one of the most challenging to evaluate. An extensive study of those errors can be performed in different ways. The most used one is performed with a laser interferometer and measures the parameters presented in equations (3.5), (3.6), and (3.7) along three perpendicular lines passing through the centre of the CMM measuring volume. This procedure is typically used during the CMM calibration and an example of the results is shown in Figure 3.9. Another method used to evaluate the overall effect of the errors inside the measuring volume is performed with a Laser Tracer and is presented in [3.17]. The main disadvantage of those methods is the high cost of the measuring systems required. Moreover, due to the environment and the wear of the machine, those parameters slowly drift and periodic reacquisition is necessary.

To have a simple estimation of the machine geometrical errors the chosen strategy consists in the repeated measurement of a gauge block to extract the deviations in terms of length deviation and tilts.

The tests have been performed with a 50mm steel gauge block (actual length 49.9999±0.00018 mm, flatness 0.15 µm) acquiring 14 points on each face as shown in Table 3.6. The reference system is shown in Figure 3.28.

The gauge block has been acquired 30 times in each point and only the average value has been used to estimate the geometrical error. This has been done in order to reduce the effect related to the repeatability of the probing system.

Table 3.6 Points distribution on each gauge block face.

Points	X=2	X=7	X=12	X=17	X=22	X=27	X=32
Z=1	•	•	•	•	•	•	•
Z=7	•	•	•	•	•	•	•

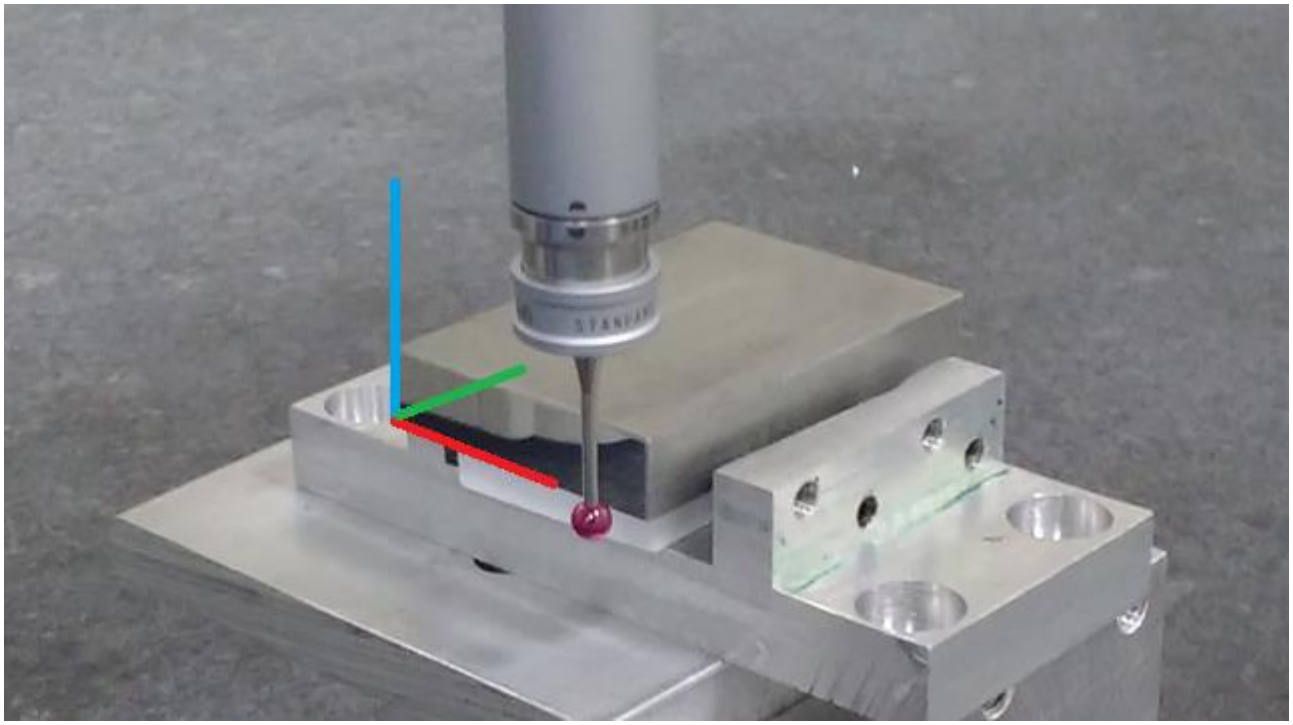

Figure 3.28 Gauge block during the test together with the reference system used.

The geometrical error values can be influenced by different factors. One is the anisotropy of the system due to its different radial stiffness in different measuring directions (see figures in 3.4.1.5). The part related to the machine measuring direction will be considered rotating the gauge block during the final tests while a series of measurements performed at different head clock will be performed to understand if part of this effect is related to the probing system. Another effect is the one typically captured by the $E_{150,MPE}$ value: the effect of some angular errors will be amplified by the horizontal distance between the ram and the measured element. To investigate this effect a test has been performed varying the altitude of the head and, therefore, progressively increasing this distance from zero to 211.8 mm.

3.4.2.1 Head clock

The effect of the head clock has been evaluated using the L100D6 stylus (Renishaw A-5003-2291) as it was the one with the highest anisotropy. The objective was to verify if this anisotropic behaviour shown in the repeatability test was related to the measuring direction or it was also due to the probing system. The two faces of the gauge block have been measured 30 times and the results in terms of tilt along the X direction of the block and length (as average value between the 30*14=420 lengths measured) have been calculated.

An example of the results obtained is shown in Figure 3.29 while the overall results in terms of deviation from the calibrated length and tilt along the two Z are summarized in Figure 3.30. The standard deviations are compatible with the ones obtained from the repeatability test in the previous chapter.

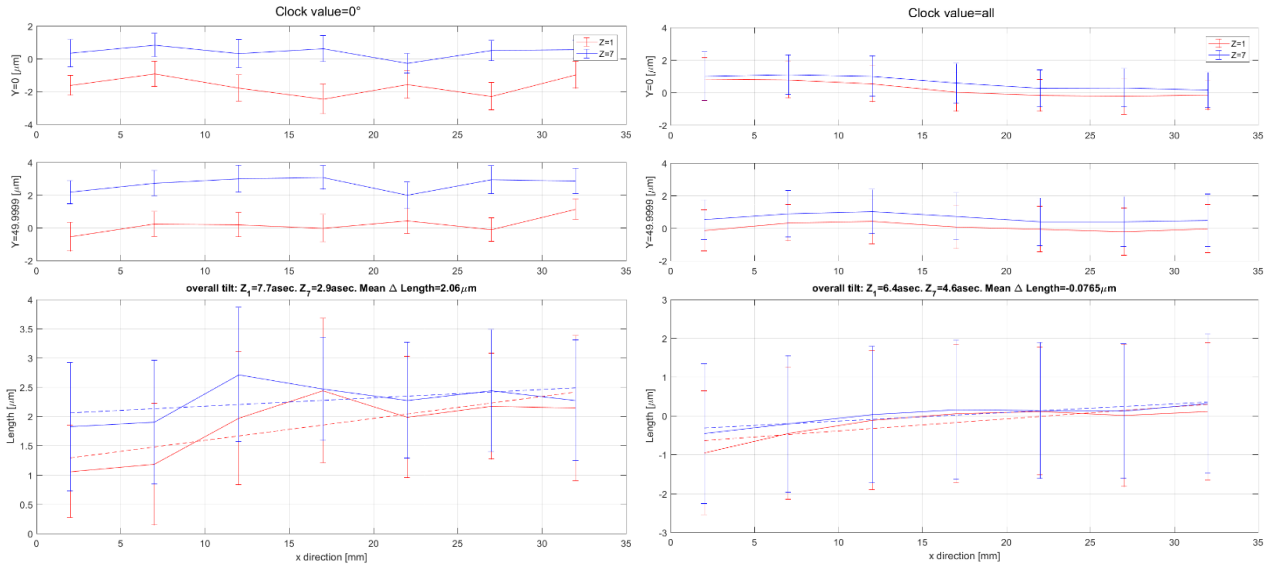

Figure 3.29 Position of the points and length distribution on the 14 points. The error bars shown the standard deviations. Left: Clock=0° case. Right: average of all the clocks.

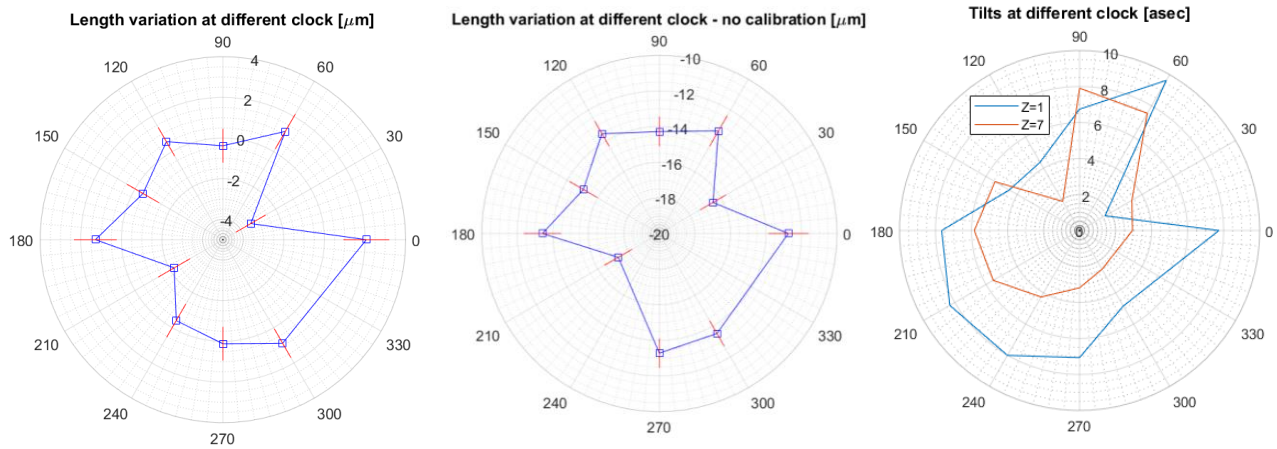

Figure 3.30 Length variation with actual (left) and nominal (centre) stylus sphere diameter at different head clocks. Right: tilts at different head clock.

A trilobe shape could be expect due to the mechanical construction of the probing system clock but no such shape can be seen in the length variation evaluation. The tilt values, even if shown in Figure 3.30 (right), are not reliable due to the low repeatability of the probing system with the L100D6 stylus.

3.4.2.2 Head altitude

To understand if important behaviour difference can be seen with increasing horizontal distance between the ram axis and the acquisition point, a series of tests have been performed increasing the altitude of the head (see Figure 3.31). The lengths have been measured along the Y-axis and the resulting offsets are shown in Table 3.7.

Table 3.7 Tip offset at different altitude angles for the Renishaw L100D6 stylus.

	Renishaw A-5003-2291 (L100D6)			
Altitude angle [°]	0	30	60	90
Height variation [mm]	0	-28.4	-105.9	-211.8
Tip offset [mm]	0	105.9	183.4	211.8

Figure 3.31 Gauge block measurement with head tilt equal to 60°.

An example of the results obtained is shown in Figure 3.32 while the overall results in terms of deviation from the calibrated length and tilt along the X-axis at the two Z are summarized in Figure 3.33 and Figure 3.34 respectively. The standard deviations are compatible with the ones obtained from the repeatability test in the previous chapter. Also in this case, the tilt values are not reliable due to the low repeatability of the probing system equipped with the L100D6 stylus.

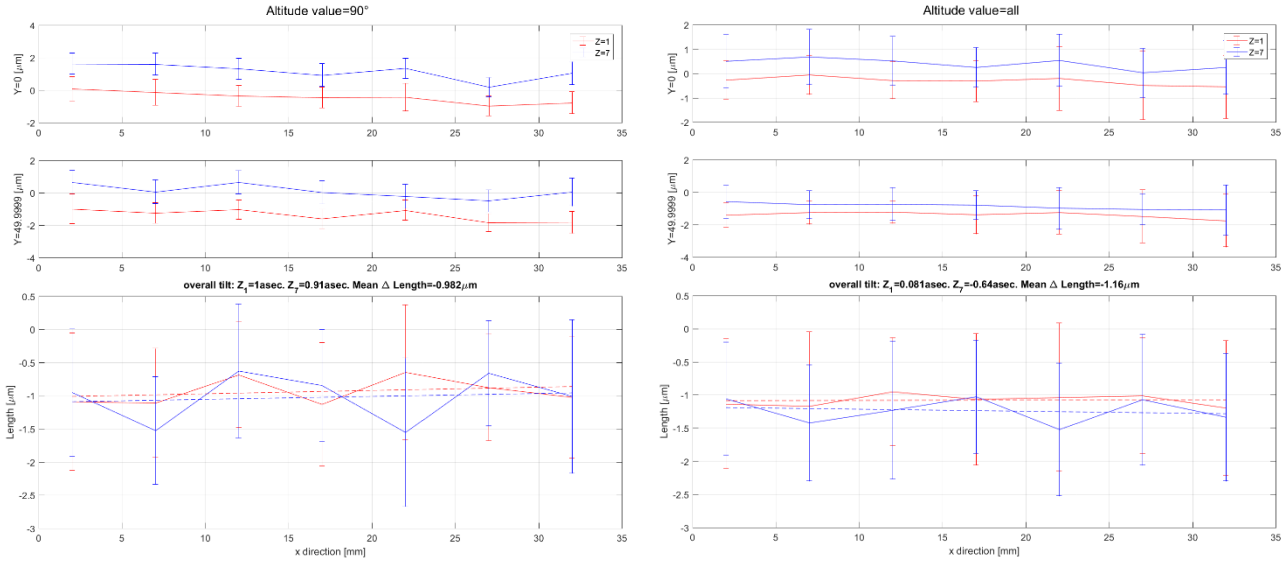

Figure 3.32 Position of the points and length distribution on the 14 points. The error bars shown the standard deviations. Left: Altitude=90° case. Right: average of all the altitudes.

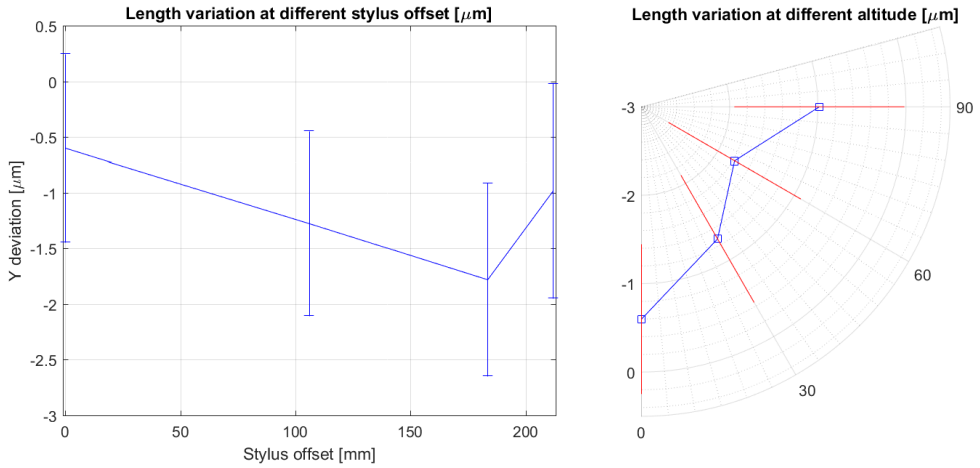

Figure 3.33 Length variation as a function of stylus offset (left) and altitude (right).

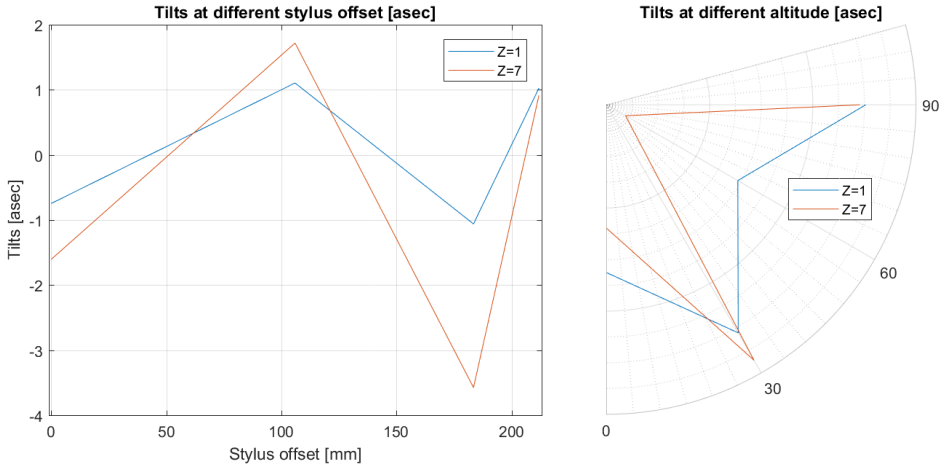

Figure 3.34 Tilts along X-axis at Z=1 mm and Z=7 mm as a function of stylus offset (left) and altitude (right).

3.4.2.3 Positions and orientations

As no particular relationship have been found related by the head clock and the stylus offset, a series of measurements has been performed with different locations and orientations of the gauge block. To minimize the effect related to the probing system repeatability, the Renishaw A-5000-4161 (L20D4) stylus has been used.

The gauge has been acquired in four different locations and two directions (X and Y) as shown in Figure 3.35. The location have been chosen to create a 600x600 mm square approximately in the centre of the measuring area at about 50 mm above the granite floor. Each of the test is performed repeating the acquisition 30 times in the 14 locations along the gauge block and 1 hour is needed for each of those tests.

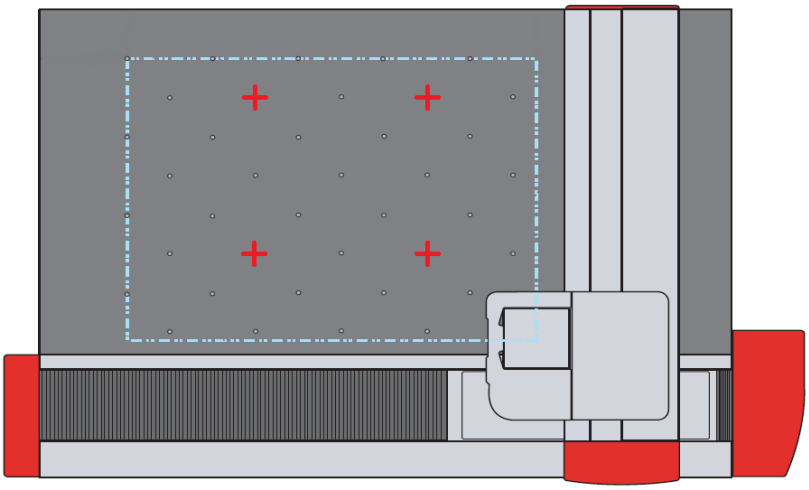

Figure 3.35 Gauge block positions and orientations for the trueness tests.

The obtained results as difference between the calibrated length and measured lengths are shown form Figure 3.36 to Figure 3.39. In addition, the standard deviations of the values, compatible with the expected standard deviations of the probing system used, and the tilts at the two level are shown.

In Table 3.8, the obtained results are summarized. The average values and their standard deviations will be used as the estimation for the geometrical effort of the machine. Those values must be considered partials as, to have a better description of the behaviour of the machine, a bigger number of tests is needed:

- Other locations inside the area of interest (e.g. 5 other locations to have a spacing of 300 mm instead of 600 mm)
- Another area about 350 mm above the granite surface
- Measurements performed also in the Z direction.

The total number of the test will be, in this case, equal to 54.

Moreover, this test is able to highlight the effect of geometrical errors with a spatial frequency of 50 mm. Performing the same test with longer gauge block (e.g. 100 and 150 mm, not available during the actual tests) could allow to capture the ones with lower spatial frequency. The results, however, will not be far from the ones obtained considering the K value in the $E_{0,MPE}$ formula, as can be noticed by the shape of the graph in Figure 3.4.

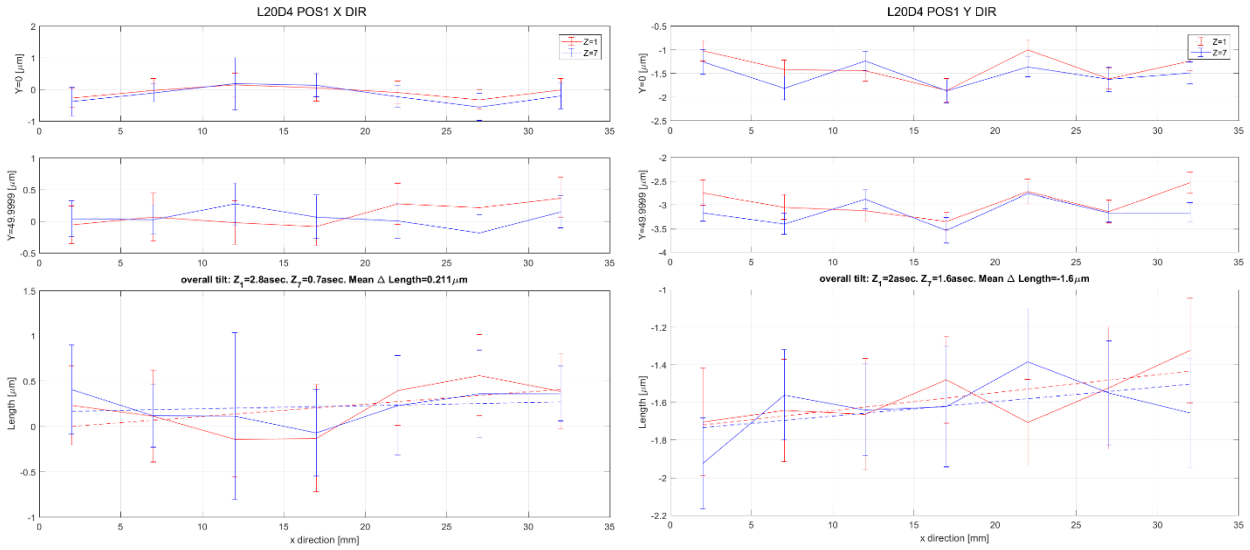

Figure 3.36 Trueness test with L20D4 in Position 1. Left: X direction. Right: Y direction.

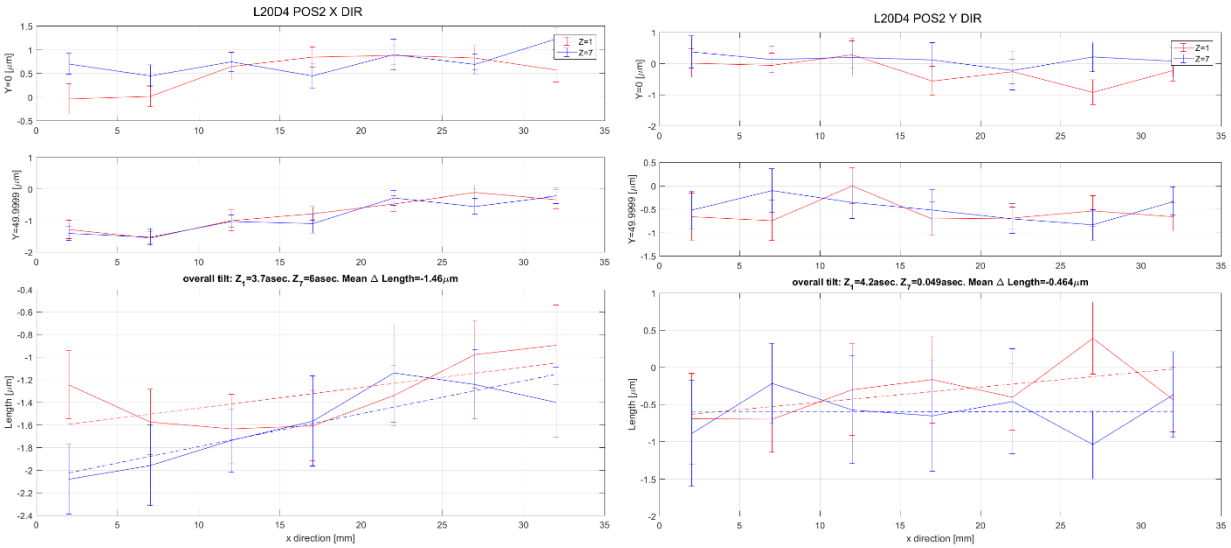

Figure 3.37 Trueness test with L20D4 in Position 2. Left: X direction. Right: Y direction.

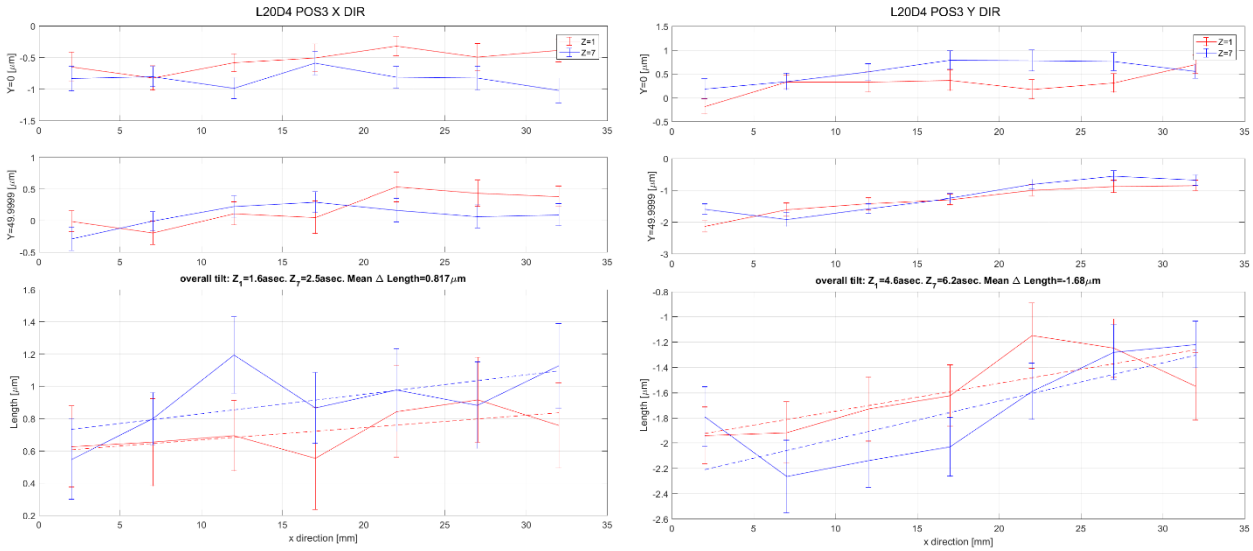

Figure 3.38 Trueness test with L20D4 in Position 3. Left: X direction. Right: Y direction.

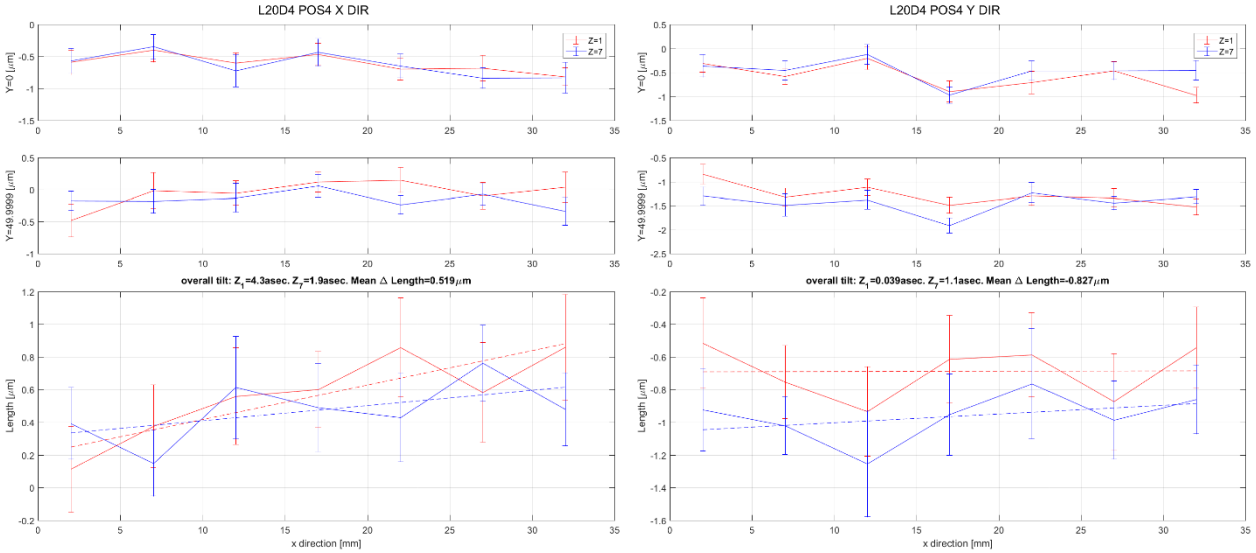

Figure 3.39 Trueness test with L20D4 in Position 4. Left: X direction. Right: Y direction.

Table 3.8 Tilt and length deviations obtained by the eight test performed. In the last two row the average and standard deviations values calculated for the length, the tilt at Z=1, the tilt at Z=7 and all the tilts together.

Position [X,Y]	Direction	Tilt Z=1 [asec]	Tilt Z=7 [asec]	Tilt Z=1,7 [asec]	Length [µm]
[0,600]	X	2.8	0.7	1.8	0.21
[0,600]	Y	2.0	1.6	1.8	-1.60
[0,0]	X	3.7	6.0	4.9	-1.46
[0,0]	Y	4.2	0.0	2.1	-0.46
[600,0]	X	1.6	2.5	2.1	0.82
[600,0]	Y	4.6	6.2	5.4	-1.68
[600,600]	X	4.3	1.9	3.1	0.52
[600,600]	Y	0.0	1.1	0.6	-0.83
Mean		**2.9**	**2.5**	**2.7**	**-0.56**
Std. dev.		1.7	2.3	1.9	0.99

3.4.3 Environmental error (drift)

The main environmental factors effecting the CMM measurements are vibration, temperature, and humidity. The vibrations decrease the CMM performances with high frequency disturbances (see Figure 3.40 for the actual CMM requirements). Considering the environment, a rigid CMM support should be enough in this particular case (see Figure 3.40 and [3.20]). Nevertheless, an active pneumatic system has been installed for the environmental vibration damping. To evaluate the effect of the vibrations, the tests shown in 3.4.1 have been repeated with different floor excitation due to a milling machine, a lathe, and human excitations on the floor and no effect has been found on the CMM performances.

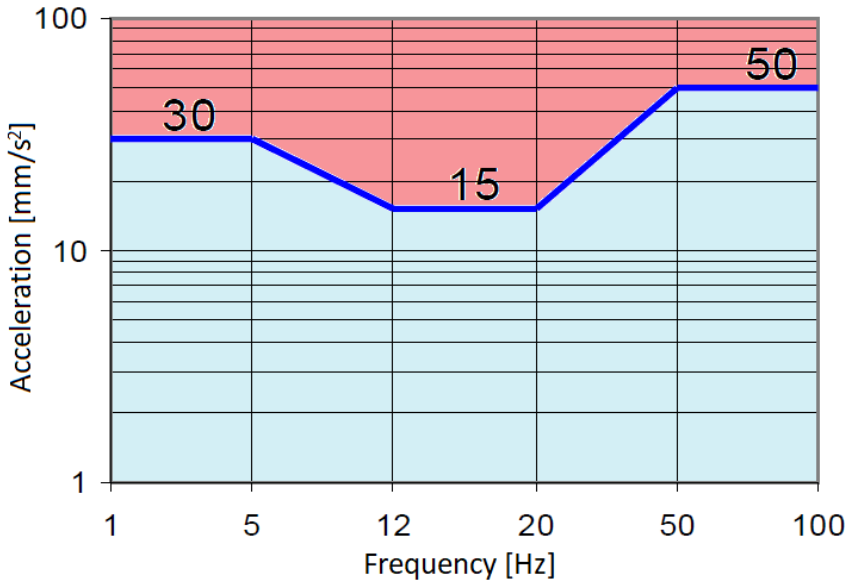

Figure 3.40 Acceptable accelerations for the Coord3 Universal CMMs. If the vibration spectrum lies in the light blue part a rigid CMM support can be used, otherwise a damping system is required.

The temperature and relative humidity (RH) variations, on the other side, act on longer time scales, deforming the CMM structure and the granite plane. The RH requirements are extremely loose (25-70%) for the clean room performances, where it always stays between 40 and 50%.

The temperature requirements are more strict (20±2°C and a maximum gradient of 0.5°C/h) and its variation a have a direct effect on the CMM performances. To quantify it a 'long' term test has been performed.

Three steel spheres (diameter 30 mm) and one Al_2O_3 ceramic calibration sphere (diameter 25 mm) have been screwed on the granite surface forming a 600 x 1200 mm rectangle at a height of about 100 mm (see Figure 3.41).

Those spheres have been acquired with 5 points every 3 minutes for about 120 hours together with the three axis and the ambient temperature (using the resistance thermometers (RTDs) integrated in the CMM).

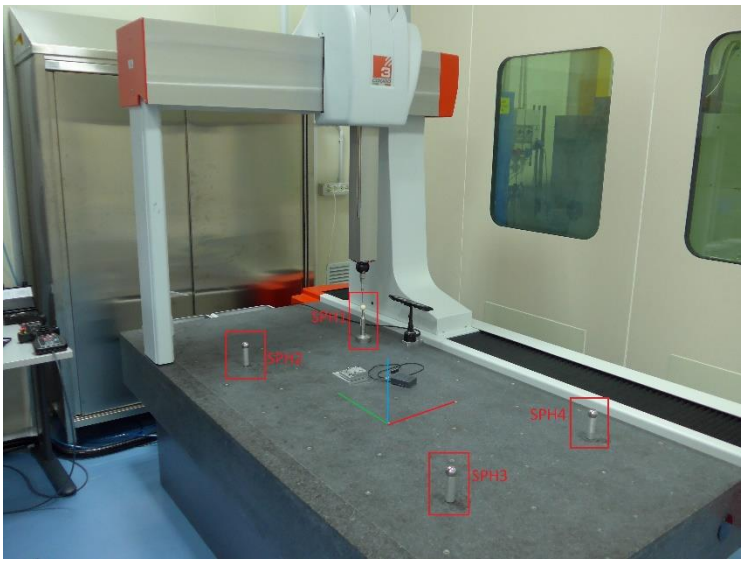

Figure 3.41 Four spheres mounted on the CMM granite plane. SPH1 is the ceramic one, while SPH2, SPH3 and SPH4 are made of steel. The reference system used is also shown.

The temperatures recorded during the test are shown in Figure 3.42. The average values are between 20.31 °C (environment) and 20.55 °C (Y-axis) while the standard deviations are between 0.040 °C (Y-axis) and 0.093 °C (environment). The main factor influencing the thermal stability is related to the day/night cycle of the heating system. The Y-axis behaviour is slightly different from the others as the sensor is located near the Wall. The difference between the four measurements is directly related to the different thermal inertia of the parts.

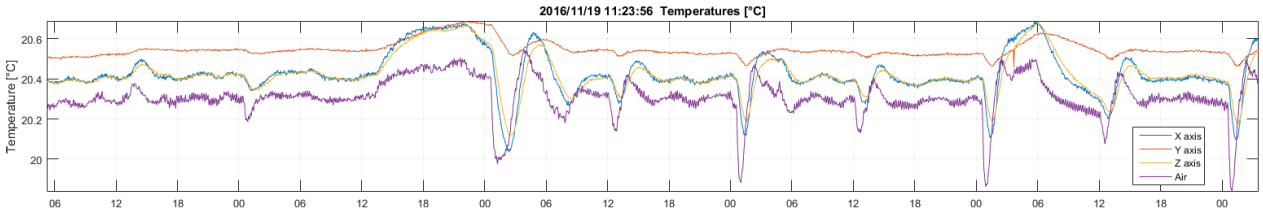

Figure 3.42 Temperatures recorded during the environment effect test.

In case no thermal compensation is foreseen on the machine, is could be useful to have a statistical estimation of the temperature stability in a certain amount of time.

The procedure used to do so is the following:

1. Each series (I=1..N) is divided in blocks of K values [I,I+K-1] with I going from 1 to N-K+1
2. The P-V difference is calculated for each block
3. The average and standard deviation of all the P-V is calculated.

This calculated is repeated for all the values of K between 2 (6 minutes blocks) and 1083 (59 hours blocks).

The average and the standard deviation of the P-V define the thermal behaviour of a certain axis or the environment. The results obtained are plotted in Figure 3.43. The average value of the measured P-V (ordinate) is plotted as a function of the observing time (or block length, abscissa).

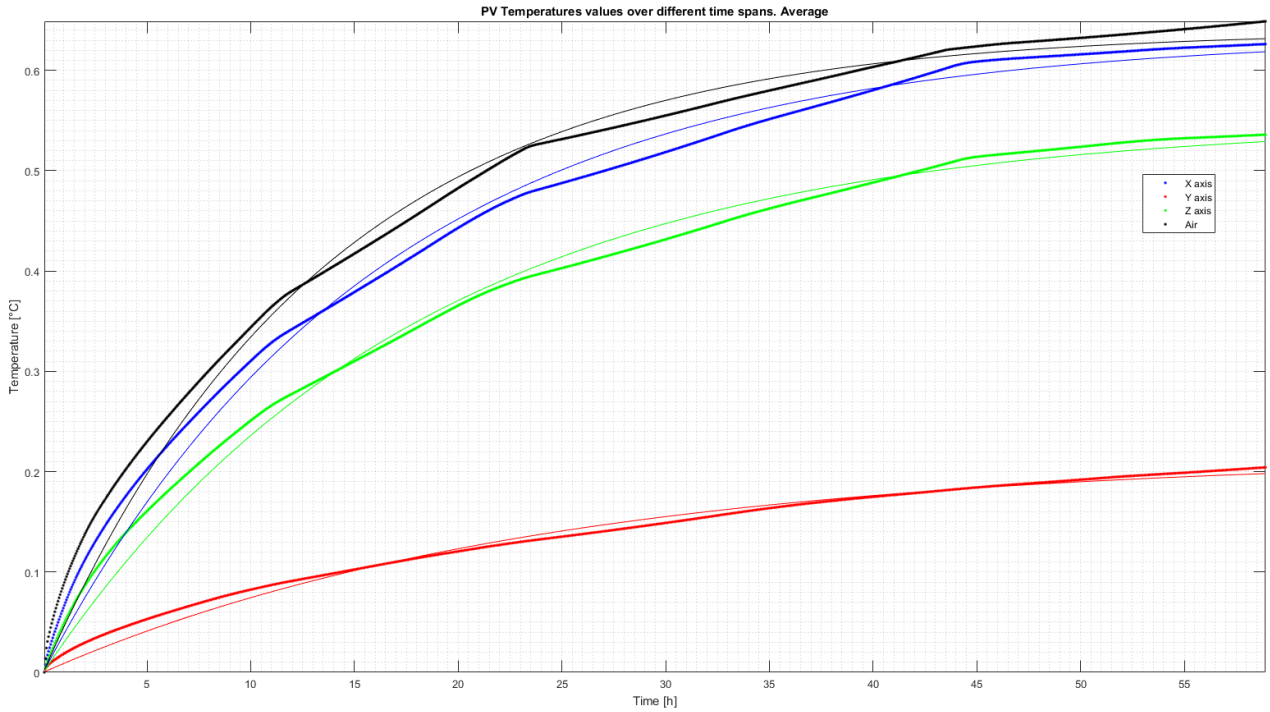

Figure 3.43 Average P-V values of the temperatures as function of the period of observation. The thick lines represent the calculated values while the fitted equations are shown using thin lines.

The fitting of those curves (thin lines in Figure 3.43) has been done using a first order system equation

$$T = K\left(1 - e^{-t/\tau}\right) \ [°C] \tag{3.8}$$

The K and τ fitting parameters obtained are shown in Table 3.9.

Table 3.9 K and τ parameters for P-V temperature estimation.

	X-axis	Y-axis	Z-axis	Air
K [°C]	0.635	0.216	0.549	0.640
τ [h]	16.07	23.70	17.80	13.53
Avg [°C]	20.42	20.55	20.42	20.31

It is possible to estimate the uncertainty due to the temperature variations with those data. This can be done using the formulae presented in 3.1.3. Calculating the values of UNE_x and $LUTM_x$, the most important factor appears to be the deviation of the temperature u_{TX1} from the calibrated value (in this case, 20 °C).

In the machine under study, as in almost all the CMMs commercially available, the temperature effect is compensated by the electronic of the machine and an indirect calculation of the geometrical deviations could be difficult if not impossible.

Thus, where the environmental conditions are quite stable during the year, a direct measurement of the geometrical deviations is a more robust solution.

The four spheres have been acquired and the position of their centres have been recorded (see Figure 3.44, Figure 3.45, and Figure 3.46)

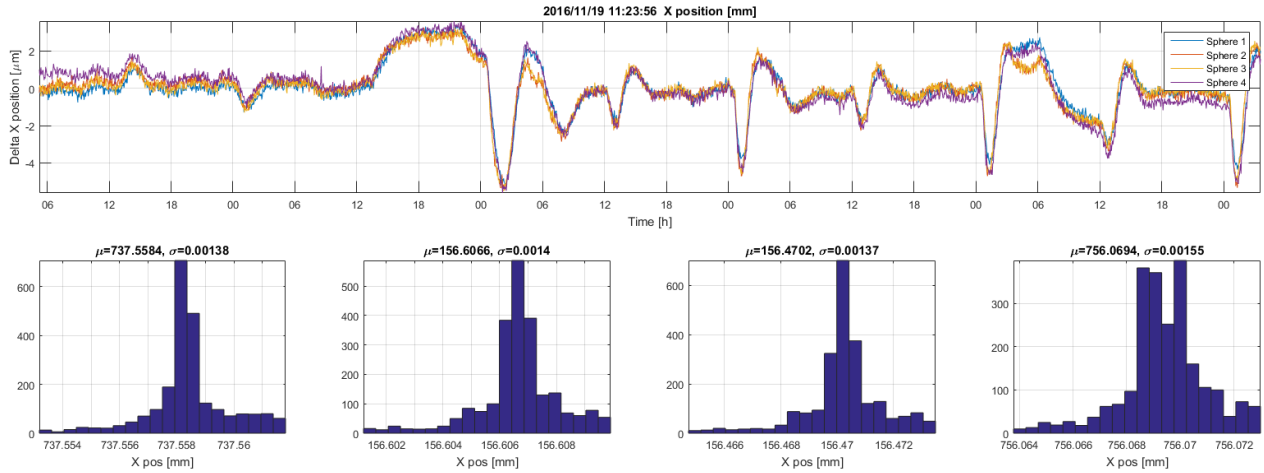

Figure 3.44 Centre position in the X direction of the four spheres during the environment effect test.

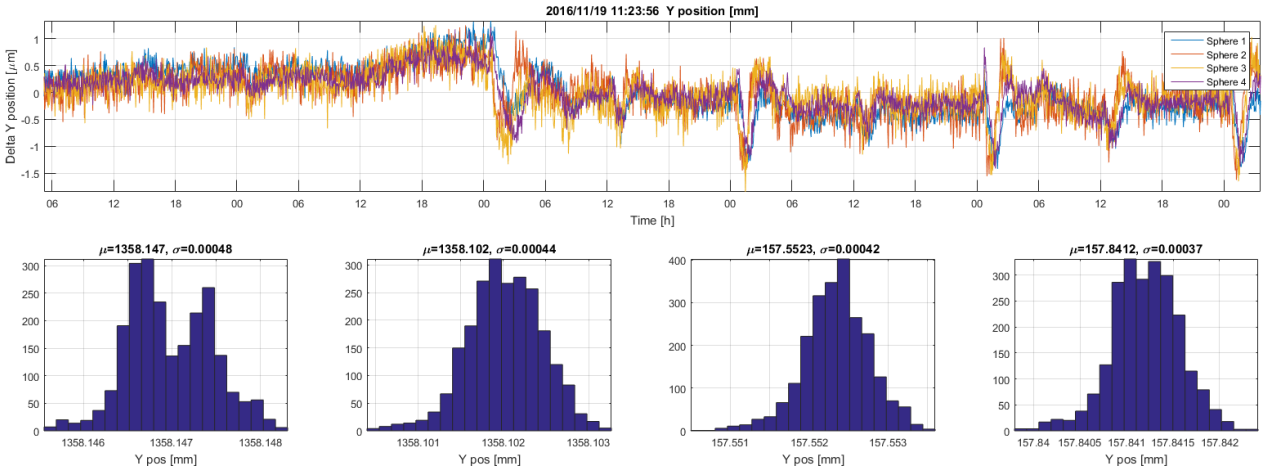

Figure 3.45 Centre position in the Y direction of the four spheres during the environment effect test.

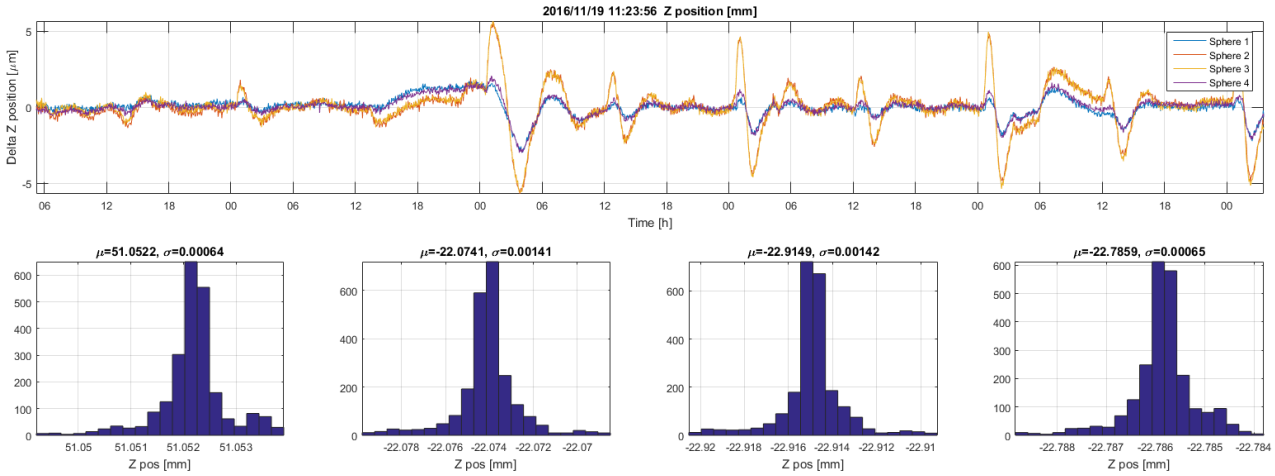

Figure 3.46 Centre position in the Z direction of the four spheres during the environment effect test.

Using the same procedure applied to the temperatures, the graphs relating the average P-V position to the length observation time have been created. The graphical results are shown in Figure 3.47, Figure 3.48, and Figure 3.49. After 24 hours, the average drift of the centre of a sphere will be between 2 and 8 microns. In the horizontal directions, the behaviour of the spheres is quite similar. In the vertical direction, otherwise, the thermal drift is higher for the spheres farther away from the main column than the other ones. This behaviour can be explained by the location of the RTD right in the middle of the main column together with the different thermal inertia of the two columns.

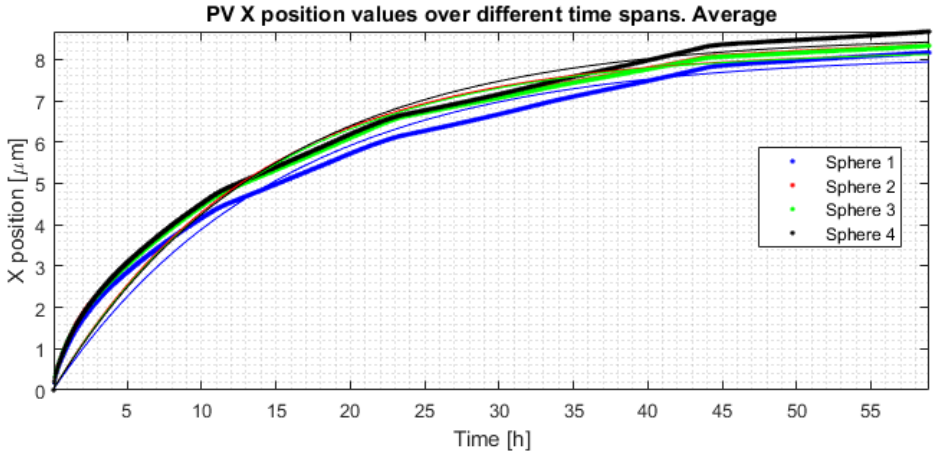

Figure 3.47 Average P-V values of the X position as function of the period of observation. The thick lines represent the calculated values while the fitted equations are shown using thin lines.

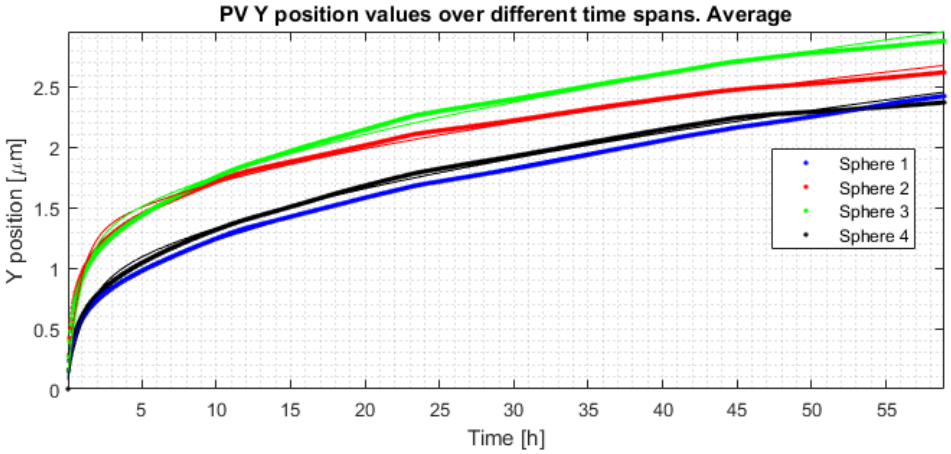

Figure 3.48 Average P-V values of the Y position as function of the period of observation. The thick lines represent the calculated values while the fitted equations are shown using thin lines.

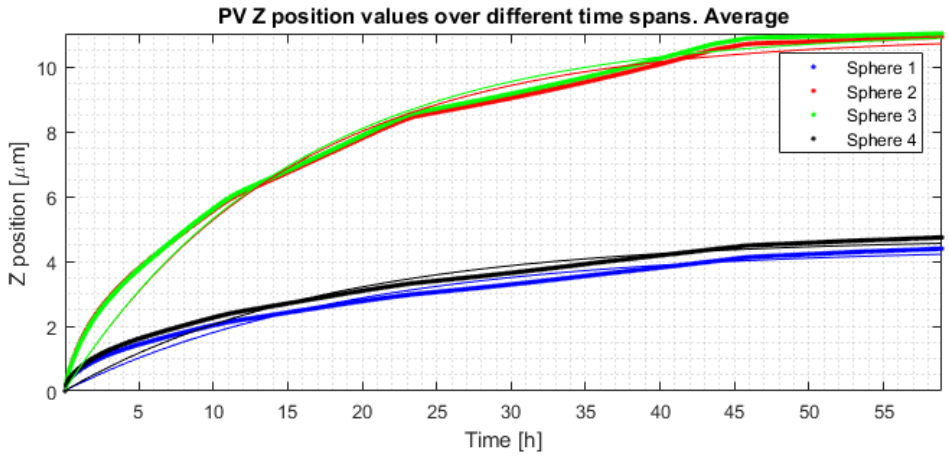

Figure 3.49 Average P-V values of the Z position as function of the period of observation. The thick lines represent the calculated values while the fitted equations are shown using thin lines.

The parameters obtained fitting with a first order system equation are shown in Table 3.10. In the Y direction, case the following modified formula has been used:

$$P = K\left(1 - e^{-t/\tau}\right) + K_2\sqrt{t}\ [\mu m] \tag{3.9}$$

This behaviour in the Y direction is due to the higher number of measurements performed for longer observing times. The effect is far less visible in the 2 other cases where the drift effect is higher.

Table 3.10 K, τ and Lin parameters for P-V spheres centre estimation.

X direction					
	SPH1	SPH2	SPH3	SPH4	**Avg**
K [µm]	8.11	8.23	8.23	8.57	**8.29**
τ [h]	15.31	13.49	13.73	13.59	**14.28**
Y direction					
	SPH1	SPH2	SPH3	SPH4	**Avg**
K [µm]	0.40	1.03	0.92	0.54	**0.72**
τ [h]	0.61	0.83	0.94	1.21	**0.90**
K_2 $[\mu m/\sqrt{h}]$	0.26	0.22	0.27	0.25	**0.25**
Z direction					
	SPH1	SPH2	SPH3	SPH4	**Avg**
K [°C]	4.42	10.95	11.14	4.72	**7.81**
τ [h]	19.07	15.16	15.39	17.54	**16.79**

Those parameters can be used to estimate the drift of an element from the actual position as a function of the elapsed time since the last reference system definition. The estimation has been done considering the maximum error in case the element is acquired every 3 minutes. With longer time spans and, even supposing one measurement every 30 minutes the results are similar (decrease of about 5%). This means that the random errors and the fast variations are negligible with respect to the long-term drifts.

Another possible effect due to the environmental variations is related to the deformations of the granite plane and the measuring error (e.g. due to the thermal differences between the CMM mechanical supports and the CMM optical scales).

The variation of the 6 lengths are shown in Figure 3.50 with both absolute (µm) and relative (part per millions) values. The red lines represent the lengths variation along X while the green lines represent the lengths variation along Y. The black/grey lines are used for the diagonal lengths.

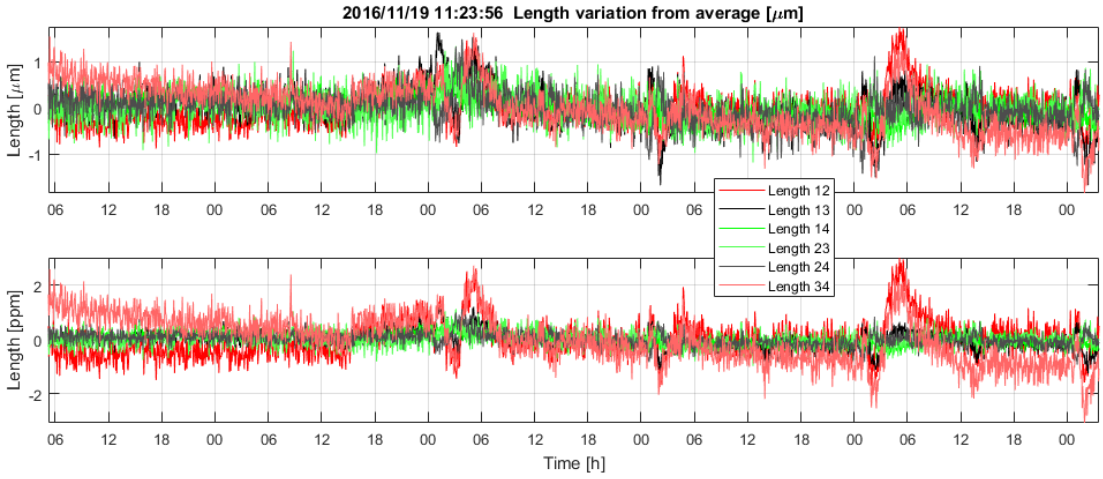

Figure 3.50 Variation of the 6 distances between the 4 spheres. Above: absolute values in µm. Below: error divided by the distance (in parts per million).

The graphs relating the average P-V lengths to the observation time have been created. The absolute values, represented in Figure 3.51, show a similar behaviour for all the lengths. The only exception is the line connecting the two spheres near the main column, which exhibits a better behaviour.

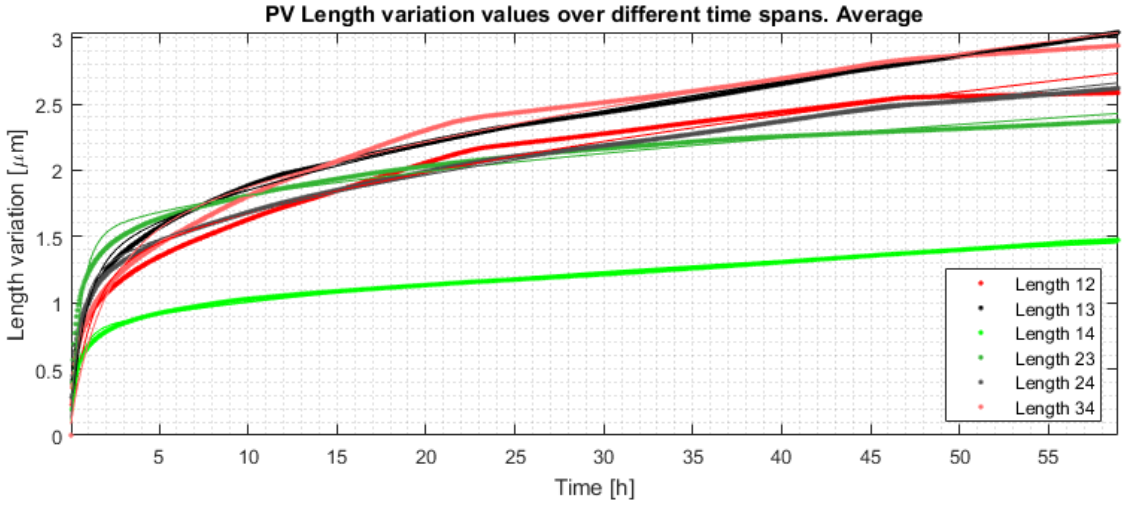

Figure 3.51 Average P-V values of the lengths variation in micrometres as function of the period of observation. The thick lines represent the calculated values while the fitted equations are shown using thin lines.

In Figure 3.52 the values are divided by the average distance between the spheres and the results are shown in parts per million. In this case all the parts have a length variation of about 1-1.5 µm/m after 24 hours with the exception of the shortest ones which have a length variation of about 3.5-4 µm/m after the same time.

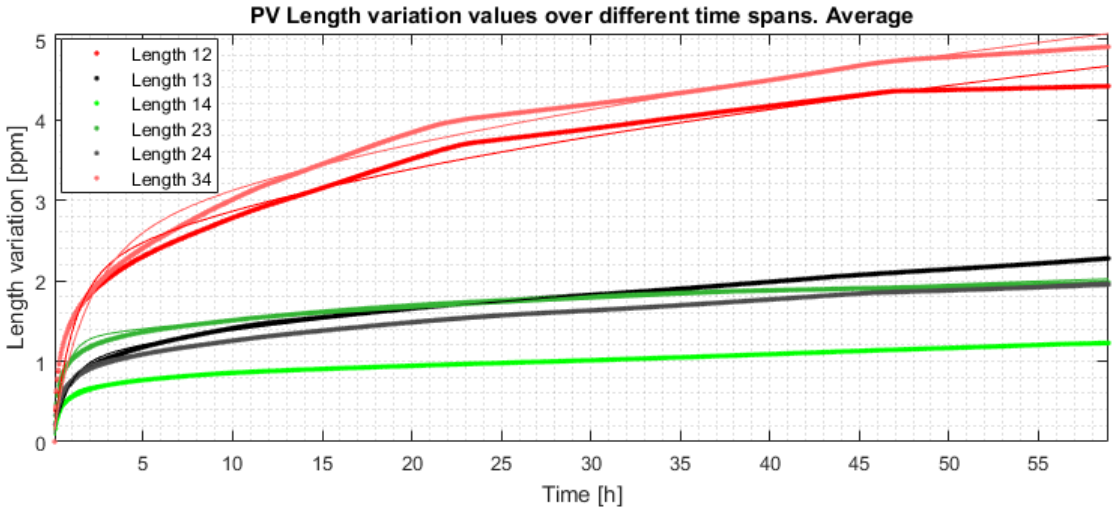

Figure 3.52 Average P-V values of the lengths variation in parts per million as function of the period of observation. The thick lines represent the calculated values while the fitted equations are shown using thin lines.

3.5 Software design

Using the obtained data, a software has been developed to predict the measurement uncertainty of an optical system composed by small optical elements. The software has been developed in Matlab® and has been kept as much modular as possible. Its general structure is shown in Figure 3.53 and it takes as input the mechanical and optical characteristics of the system and the alignment strategy (yellow background).

Those data are first processed to verify their consistency (checks) and to organize them in a structure as a preparation for the subsequent analysis. This structure is used to feed three different modules: 'machine uncertainty' where the uncertainty due to the machine is calculated, 'sampling uncertainty' where the uncertainty due to the sampling is calculated, and 'thermal uncertainty' where the uncertainty due to the environment is calculated. The sampling uncertainty module is composed by different submodules depending on the optical element to analyse (bi-spherical lens, plano-spherical lens, window, plane mirror, of spherical mirror).

The green modules are used to have an overall view of the results. The 'total mechanical uncertainty' one merge the outputs obtained from the previous parts while 'total raw optical uncertainty' use the mechanical uncertainties and the optical characteristics of the system to have a first overview of the uncertainties in terms of optical effects calculated with the paraxial equations.

The total mechanical uncertainties obtained can be also used to feed a raytracing software in order to have the real optical behaviour of the system due to the alignment uncertainties.

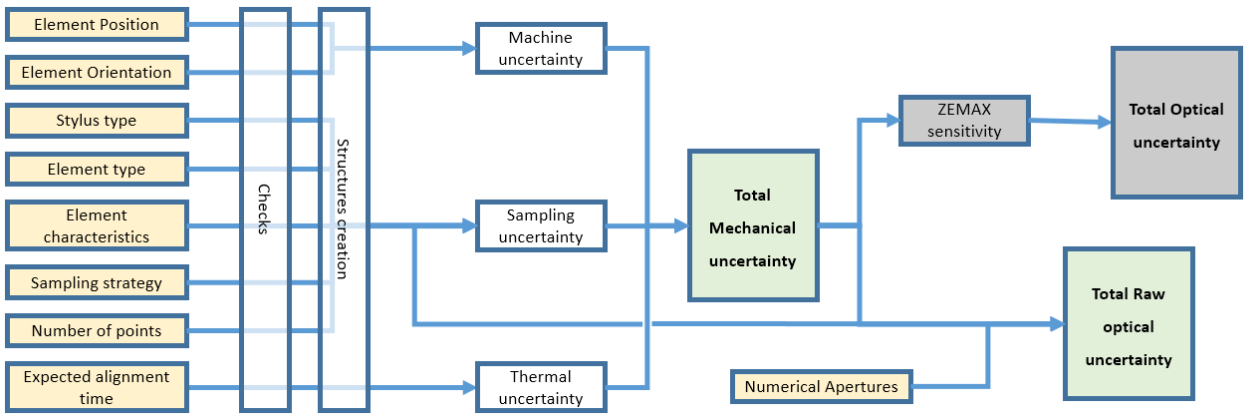

Figure 3.53 Main structure of the developed software. The required inputs and the provided output are repectively shown with a yellow and green background. The grey box shows an operation to perform with an external software.

The main modules are detailed in the next subchapers.

3.5.1 Sampling uncertainty (probe error)

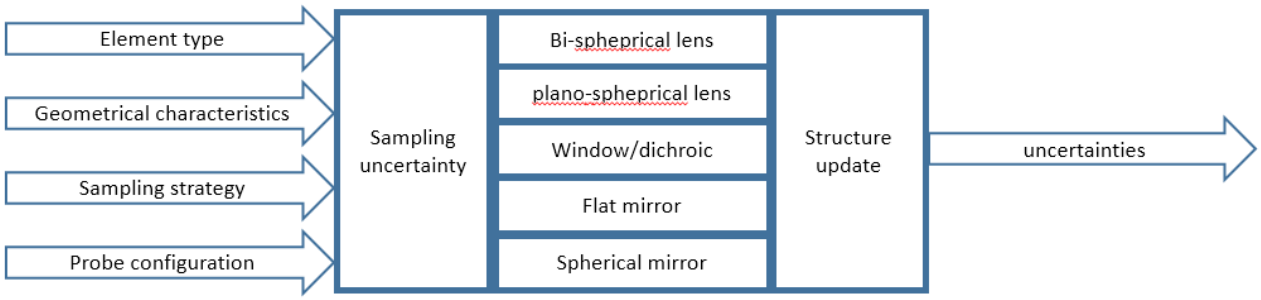

Figure 3.54 General view of the sampling uncertainty module. The 'sampling uncertainty' dispatch the inputs to the correct analysis submodule while the 'structure update' takes the results and organize them in the uncertainties structure.

Considering the small size of the optical elements (usually around 30 mm) and she short time needed to acquire them (usually below 60 seconds), the error components related to the geometrical error and the thermal drifts can be ignored.

In this case, the measurement errors will be dominated by the repeatability of the probing system. As a first approximation, this error can be considered random with a Gaussian distribution characterized by a zero average and a standard deviation function of the selected stylus (see 3.4.1).

Different functions have been developed depending on the different optical elements involved. The refractive elements actually developed are:

- bi-concave and bi-convex spherical lenses,
- plano-concave, plano-convex and meniscus spherical lenses,
- dichroics and windows.

In case of aspheric surfaces, the simulation can be performed considering an aspheric equivalent element with acceptable results.

The reflective elements actually developed are:

- spherical mirrors (concave and convex),

- flat mirrors.

Note that the spherical convex mirror is also used to define the position of the references (usually steel spheres acquired on one hemisphere).

No aspheric surface has been developed as preliminary simulations showed poor results if neither the vertex position nor the axis direction are defined with an external reference. This consideration is true for the typical aspherical surfaces used in the optical field, where the departure from the spherical surfaces is in the order of the hundredths of millimetre. For aspheric surfaces with higher departure, however, the pure mechanical measurement of a surface can still provide good results.

Every of those functions take as inputs the geometric characteristics of the element (thickness, radii of curvature (if known) and size) together with number of acquisition points and standard deviation representing the repeatability of the probing system (see Table 3.11).

The size of the element and the number of acquisition points are used to define the location of the acquired points. Different acquisition strategies are possible but the most typical for a CMM consists in an equally spaced rectangular grid. The distribution in case of rectangular aperture is trivial while for circular apertures it is possible to calculate the spacing with a relative low error solving the Gauss Circle problem (see [3.21]):

$$Spacing = \frac{Diameter}{2}\sqrt{\frac{\pi}{\#points}} \tag{3.10}$$

The generated points are perturbed, then, with the repeatability values of the probing system selected.

Table 3.11 Input provided to the substitute geometry functions.

	Surface 1	Surface 2	ROC Known?	ROC	Central thickness	Geometrical Dimension	# points	Stylus uncertainty
Lens	Spherical	Flat						
Lens	Spherical	Spherical						
Window / dichroic	Flat	Flat	-					
Mirror	Flat	-	-	-	-			
Mirror	Spherical	-		-	-			

Table 3.12 Output generated by the substitute geometry functions.

	Surface 1	Surface 2	ΔROC	Piston	Δ thickness	Centre (x, y)	Rotation (Rx, Ry)
Lens	Spherical	Flat					
Lens	Spherical	Spherical					
Window/dichroic	Flat	Flat	-			-	
Mirror	Flat	-	-		-	-	
Mirror	Spherical	-			-	-	

After the points have been fitted with a substitute geometry, the deviations from the nominal values are outputted (see Table 3.12).

In case of bi-spherical lenses, the optical axis has been calculated as the line connecting the centre of the two spheres. For plano-spherical lenses, the optical axis was defined by the line perpendicular to the planar face

and passing through the centre of the sphere. For the centre and the piston calculation, the thin lens approximations have been used.

The decentring and the rotation of a spherical mirror are equivalent, in this case it has been decided to output in terms of rotations.

3.5.1.1 Fitting algorithms

Different fitting methods can be employed for the solution of those equations. From the most general point of view, three main fitting goal can be used: the minimum-total-distance fit (L_1), the least square fit (Gaussian, L_2) or min-max fit (L_∞). All those fitting methods have different advantages and disadvantages: L_1 can be preferred if the outliers have to be removed, L_2 has the most robust algorithms, and L_∞ is the one used in the Geometrical Product Specifications standards [3.2]. Thanks to the small deviations from the substitute geometry typically seen while measuring optical elements, the difference between the 3 methods is negligible. For this reason and due to its robustness, the Gaussian one has been chosen.

For the **flat surfaces**, two Gaussian fitting methods have been tested. The first one is described in [3.22] and is based on the Single Value Decomposition (SVD) and, if x_i, y_i, z_i are the coordinates of the i-th point, the equation of the substitute plane $ax + by + d = z$ can be solved with the following equations:

$$A = [\boldsymbol{x_i} \quad \boldsymbol{y_i} \quad \boldsymbol{z_i} \quad \mathbf{1}] \tag{3.11}$$

$$[U, S, V] = svd(A) \tag{3.12}$$

$$\boldsymbol{v} = \frac{V(:,4)}{\|V(1:3,4)\|_2} \tag{3.13}$$

$$a = \frac{\boldsymbol{v}(1)}{\boldsymbol{v}(3)}; \qquad b = \frac{\boldsymbol{v}(2)}{\boldsymbol{v}(3)}; \qquad d = \frac{\boldsymbol{v}(4)}{\boldsymbol{v}(3)}; \tag{3.14}$$

The second one is described in [3.23] and the coefficients are calculated as following:

$$\bar{x}_i = \frac{1}{N}\sum_{i=1}^{N} x_i\,; \qquad \bar{y}_i = \frac{1}{N}\sum_{i=1}^{N} y_i\,; \qquad \bar{z}_i = \frac{1}{N}\sum_{i=1}^{N} z_i\,; \tag{3.15}$$

$$\begin{bmatrix} \sum_{i=1}^{N}(x_i-\bar{x}_i)^2 & \sum_{i=1}^{N}(x_i-\bar{x}_i)(y_i-\bar{y}_i) & \sum_{i=1}^{N}(x_i-\bar{x}_i) \\ \sum_{i=1}^{N}(x_i-\bar{x}_i)(y_i-\bar{y}_i) & \sum_{i=1}^{N}(y_i-\bar{y}_i)^2 & \sum_{i=1}^{N}(y_i-\bar{y}_i) \\ \sum_{i=1}^{N}(x_i-\bar{x}_i) & \sum_{i=1}^{N}(y_i-\bar{y}_i) & \sum_{i=1}^{N}1 \end{bmatrix} \boldsymbol{A} = \begin{bmatrix} \sum_{i=1}^{N}(x_i-\bar{x}_i)(z_i-\bar{z}_i) \\ \sum_{i=1}^{N}(y_i-\bar{y}_i)(z_i-\bar{z}_i) \\ \sum_{i=1}^{N}(z_i-\bar{z}_i) \end{bmatrix} \tag{3.16}$$

$$a = \boldsymbol{A}(1); \qquad b = \boldsymbol{A}(2); \qquad d = \boldsymbol{A}(3) + \bar{z}_i - a\,\bar{x}_i - b\,\bar{y}_i; \tag{3.17}$$

The second method provided better results when tested with known points cloud with high deviations from the nominal values. Moreover, its speed was about 4 times faster than the first one (3 seconds versus 13 second for a typical fitting problem repeated 10000 times). For those reasons, this method has been integrated into the software.

For the **spherical surfaces**, two different Gaussian fitting methods have been used in case the radius of curvature (ROC) of the element was known or unknown.

If the ROC is unknown, it is possible to use the equations described in [3.23]. If x_i, y_i, z_i are the coordinates of the i-th point, the 4 unknown terms of the equation of the substitute sphere $(x-x_0)^2+(y-y_0)^2+(z-z_0)^2=ROC^2$ can be calculated as following:

$$\bar{x}_i=\frac{1}{N}\sum_{i=1}^{N}x_i\,;\qquad \bar{y}_i=\frac{1}{N}\sum_{i=1}^{N}y_i\,;\qquad \bar{z}_i=\frac{1}{N}\sum_{i=1}^{N}z_i\,; \tag{3.18}$$

$$A=\begin{bmatrix}\frac{1}{N}\sum_{i=1}^{N}x_i(x_i-\bar{x}_i) & \frac{2}{N}\sum_{i=1}^{N}x_i(y_i-\bar{y}_i) & \frac{2}{N}\sum_{i=1}^{N}x_i(z_i-\bar{z}_i)\\ 0 & \frac{1}{N}\sum_{i=1}^{N}y_i(y_i-\bar{y}_i) & \frac{2}{N}\sum_{i=1}^{N}y_i(z_i-\bar{z}_i)\\ 0 & 0 & \frac{1}{N}\sum_{i=1}^{N}z_i(z_i-\bar{z}_i)\end{bmatrix} \tag{3.19}$$

$$(A+A')\begin{bmatrix}x_0\\y_0\\z_0\end{bmatrix}=\begin{bmatrix}\frac{1}{N}\sum_{i=1}^{N}(x_i^2+y_i^2+z_i^2)(x_i-\bar{x}_i)\\ \frac{1}{N}\sum_{i=1}^{N}(x_i^2+y_i^2+z_i^2)(y_i-\bar{y}_i)\\ \frac{1}{N}\sum_{i=1}^{N}(x_i^2+y_i^2+z_i^2)(x_i-\bar{x}_i)\end{bmatrix} \tag{3.20}$$

$$ROC=\sqrt{\frac{1}{N}\sum_{i=1}^{N}\sum_{j=1}^{3}([(x_i-x_0)^2\quad(y_i-y_0)^2\quad(z_i-z_0)^2])} \tag{3.21}$$

Those equations can solve the 10000 iterations of a test in about 0.8 seconds. Unfortunately, it is not possible to solve it directly in case the ROC is previously defined. If this condition applies the coefficient are estimated applying a non-linear regression fit to the equation

$$(x-x_0)^2+(y-y_0)^2+(z-z_0)^2-ROC^2=0$$

The main drawback of this solution is the computation time. The solutions of the 10000 iterations have been found in about 18.5 s, more than 23 times the time needed in the 'ROC unknown' case.

The solutions for **other** interesting **surfaces** like aspheric, cylinders and paraboloid does not exist in a closed form. The parameters of those surfaces have been found, then, using non-linear regression fits with the consequent computational time problems.

An example of a spherical mirror sampling simulation is shown in Figure 3.55 with a ρ-θ points distribution. The points are sampled on the surface and each one of them is independently perturbed considering the expected uncertainty. A ρ-θ distribution of the points has better performance in terms of ROC evaluation but behaves poorly for the definition of the sphere centre. Therefore, this distribution has been dropped in favour of a Cartesian one.

In Figure 3.56 and Figure 3.57, the output obtained while simulating a mirror and a lens are shown as an example: if the element is a spherical mirror, the uncertainty are calculated as ROC deviation, piston and tip-tilt while for a plano-spherical lens also the central thickness variation and the central point location are given as output.

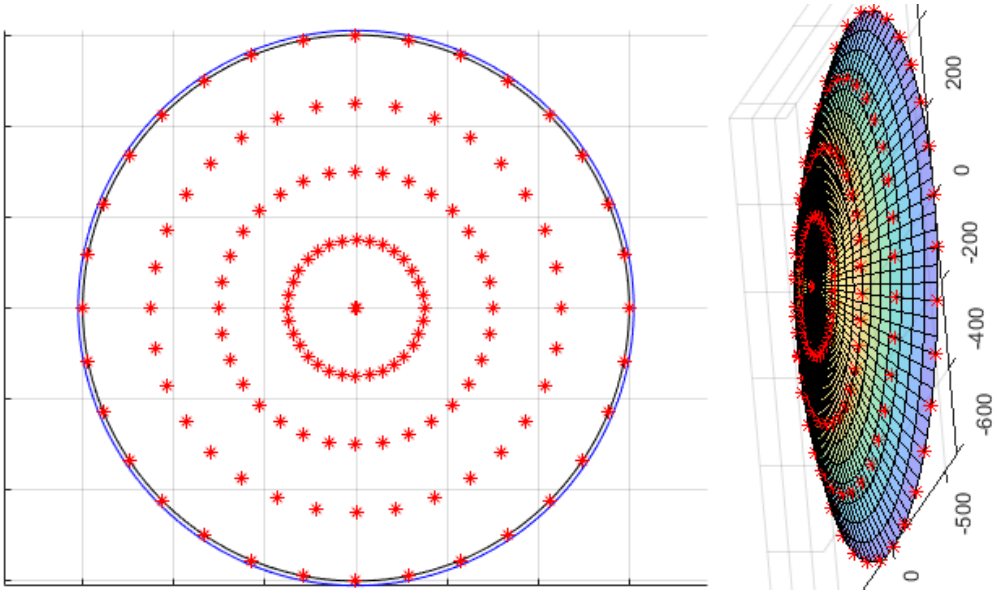

Figure 3.55 Sampling example on a spherical mirror with a ρ-ϑ sampling. Due to its performance, this sampling strategy has been dropped.

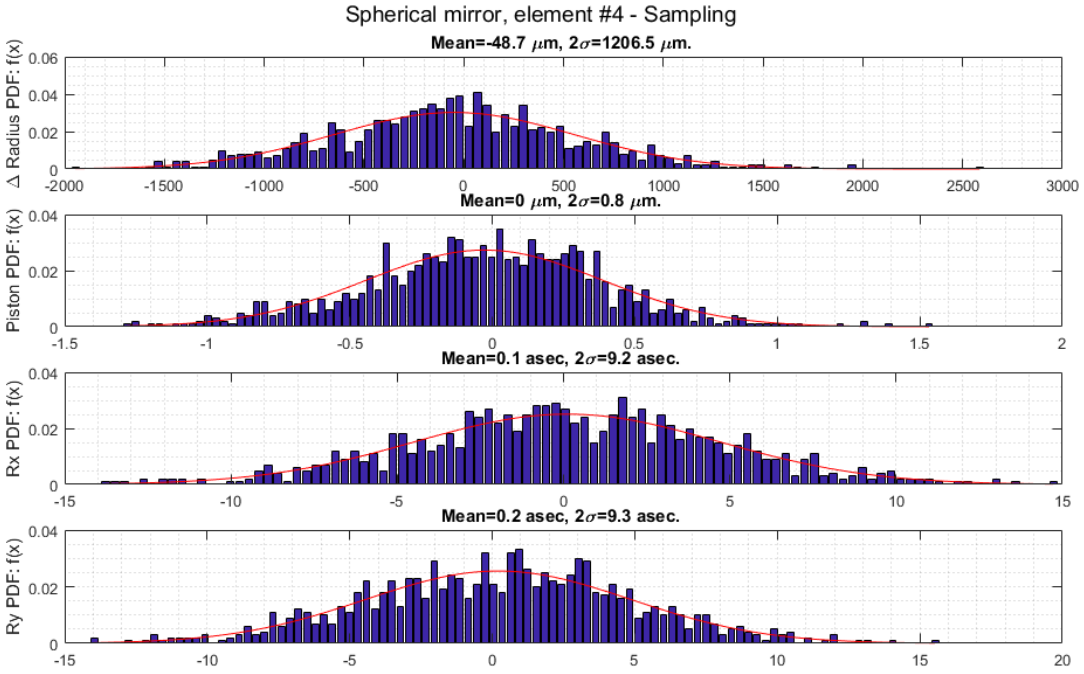

Figure 3.56 Sampling error of a spherical mirror. From top to bottom: ROC, piston, rotation around X, and rotation around Y.

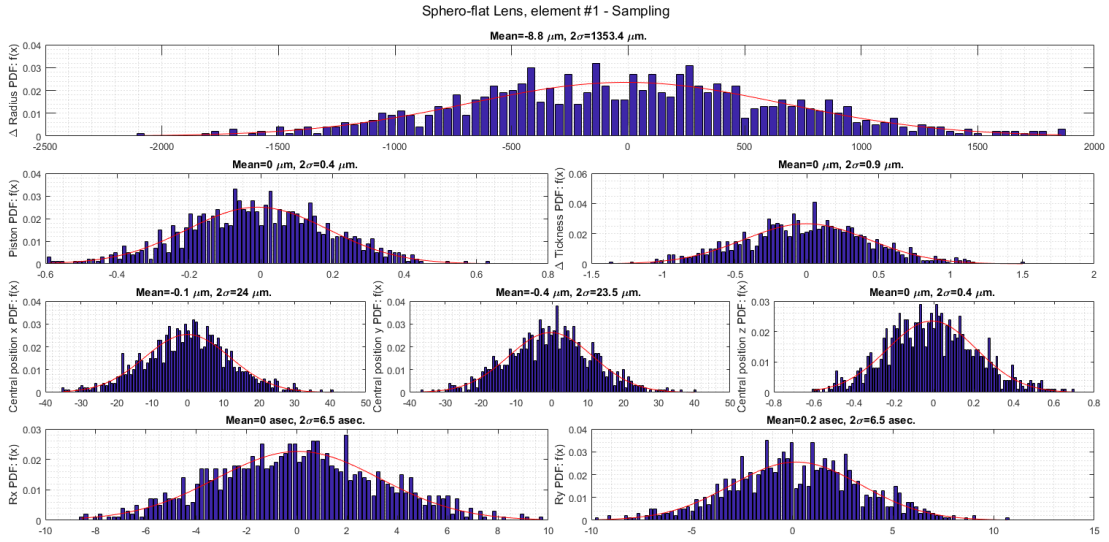

Figure 3.57 Sampling error of a planoconvex lens. From top to bottom: ROC, piston + thickness, centre position (X, Y, Z), and rotation around the X and Y axes.

3.5.2 Machine uncertainty (machine error)

Figure 3.58 General view of the machine uncertainty module. The machine uncertainty' calculates the uncertainty based on the location and the orientation of the element while the 'structure update' takes the results and organize them in the uncertainties structure.

The geometrical error of the machine is used to define the location of the sampled elements. This calculation is valid if we consider that those geometrical errors are constant along the surfaces of each element.

The available numbers are the ones obtained from the analysis in 3.4.2.3. With larger set of data, it could be possible to improve the quality of the simulation differentiating the behaviour in different directions, locations, or distances.

In this case the results have been using considering an isotropic behaviour of the machine. With this simplification, the **distance error** for lengths equal to 50 mm is -0.56±0.99 µm (one σ values) while the angular error is equal to 1.9±2.7 arcsecond (one σ values).

The distribution of the error can be extended for different lengths using the formula $\Delta L_{std} = \pm\left[\left(\sigma_{dist} - \frac{50}{333}\right) + \frac{L}{333}\right] \mu m$ with $\sigma_{dist} = 0.99\mu m$, i.e. considering the length error proportional to the distance between the elements with the same factor obtained by the $E_{0,MPE}$ evaluation.

The objective of this part of the software is to generate a certain number of parametric state of the CMM. Considering all the parametric states of the CMM, the average distance between two elements must then be equal to $\mu_{dist} = -0.56\,\mu m$ with a standard deviation of ΔL_{std}, (where L is the nominal distance). If this requirement is fulfilled, the software is correctly simulating the geometrical behaviour of the CMM. Otherwise, the simulation must be repeated.

Due to the complexity and the computational cost of a simulation including a large number of 3D Gaussian distributions, this part of the software has been developed considering a uniform distribution of the points with the limits defined as $\Delta L_{UD} = \mu_{dist} \pm \left[\left(\sigma_{dist}\sqrt{3} - \frac{50}{333}\right) + \frac{L}{333}\right] \mu m$ where L is the relative distance between each pair of elements.

The point defining the location of each element will be a point located inside an equiprobable sphere centred in its nominal centre and a radius $R = |\mu_{dist}| + \left[\left(\sigma_{dist}\sqrt{3} - \frac{50}{333}\right) + \frac{L}{333}\right] \mu m$. In this case L is defined as the distance from the origin of the reference system (0, 0, 0).

This point can be generated as

$$X_s = \frac{N_1}{\sqrt{N_1^2+N_2^2+N_3^2}} R\sqrt[3]{U}; \qquad Y_s = \frac{N_2}{\sqrt{N_1^2+N_2^2+N_3^2}} R\sqrt[3]{U}; \qquad Z_s = \frac{N_3}{\sqrt{N_1^2+N_2^2+N_3^2}} R\sqrt[3]{U}; \tag{3.22}$$

where N_1, N_2, N_3 are three independent randomly generated variables with normal distribution N(0,1) and U is a randomly generated variable with uniform distribution [0,1].

The relative distances between each pair of elements in a parametric state of the CMM are checked. If all the values are in the range $\left[L - \left(\left(\sigma_{dist}\sqrt{3} - \frac{50}{333}\right) + \frac{L}{333}\right) + |\mu_{dist}|, L + \left(\left(\sigma_{dist}\sqrt{3} - \frac{50}{333}\right) + \frac{L}{333}\right) + |\mu_{dist}|\right]$ the simulated distances are compatible with the actual CMM behaviour and the parametric state is kept. This procedure is repeated until the needed number of simulation passed this verification.

The **tip** and **tilt errors** can be considered as constant with respect to the length and can be simulated considering a normal distribution with average 1.9 arcsecond and standard deviation of 2.7 arcsecond. Those numbers come from the tests shown in 3.4.2.3 (Table 3.8).

Repeating the measurements with gauge blocks of different lengths, also those results could be improved as the values can be related to the distances and the direction of the measurements. When such an upgrade is done, a simulation by constraints similar to the one already presented must be applied.

In Figure 3.59 and Figure 3.60, the output obtained while simulating a mirror and a lens are shown as an example. The results are function of the relative distance between the elements only and are shown in the relative reference system of each element (rototranslation from the CMM reference system).

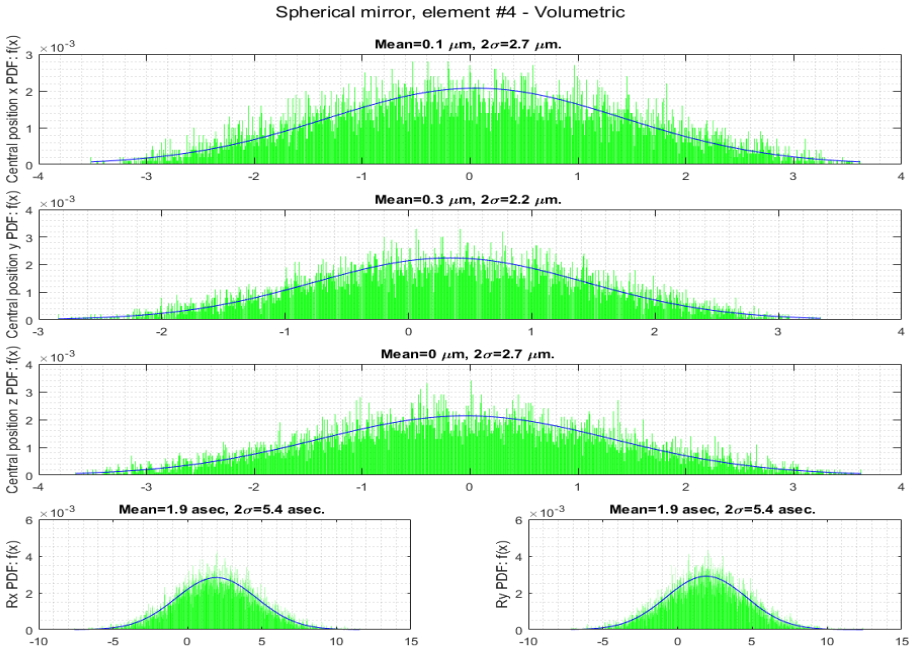

Figure 3.59 Volumetric error of an element located in (0, 0, 200) [mm]. From top to bottom: position in X, position in Y, position in Z, and rotation around X and Y.

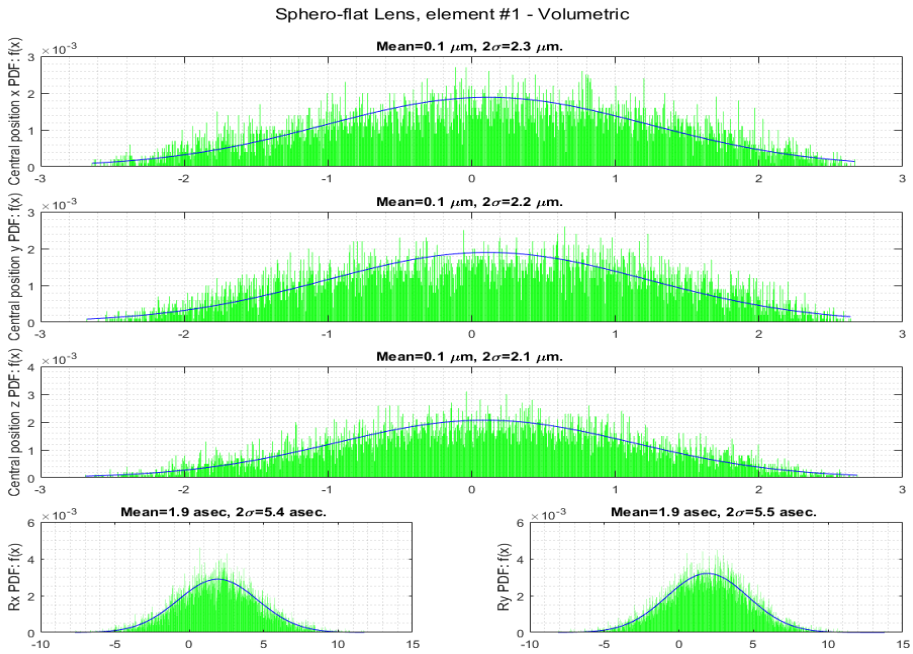

Figure 3.60 Volumetric error of an element located in (300, 200, 400) [mm]. From top to bottom: position in X, position in Y, position in Z, and rotation around X and Y.

3.5.3 Temperature uncertainty (thermal drift)

Figure 3.61 General view of the thermal uncertainty module. The machine uncertainty' calculates the uncertainty based on the orientation of the element and the expected alignment time while the 'structure update' takes the results and organize them in the uncertainties structure.

The mainly effect due to the temperature variations, as shown in 3.4.3, is a drift of the measured element as a function of the time passed since the last reference definition.

The standard deviations of this drift can be calculated using the data coming from Table 3.10 and dividing the PV value by $2\sqrt{3}$. The average values in each direction have been taken as it is supposed to have the piece under alignment in the centre of the volume.

The formulae are derived by equation (3.9) and are the following, where t is the time in hours.

$$P_x = \frac{8.2855\left(1 - e^{-t/14.2815}\right)}{2\sqrt{3}}[\mu m] \tag{3.23}$$

$$P_y = \frac{0.7219\left(1 - e^{-t/0.8967}\right) + 0.2483\sqrt{t}}{2\sqrt{3}}\ [\mu m] \tag{3.24}$$

$$P_z = \frac{7.8073\left(1 - e^{-t/16.7918}\right)}{2\sqrt{3}}[\mu m] \tag{3.25}$$

The obtained results are rototranslated from the CMM reference system to the element reference system before being outputted.

In Figure 3.62 and Figure 3.63, the output obtained simulating two elements are shown as an example. Those values are about one order of magnitude smaller than the volumetric and a sampling error, showing that a frequent realignment of the system with respect to the references could even be counter-productive.

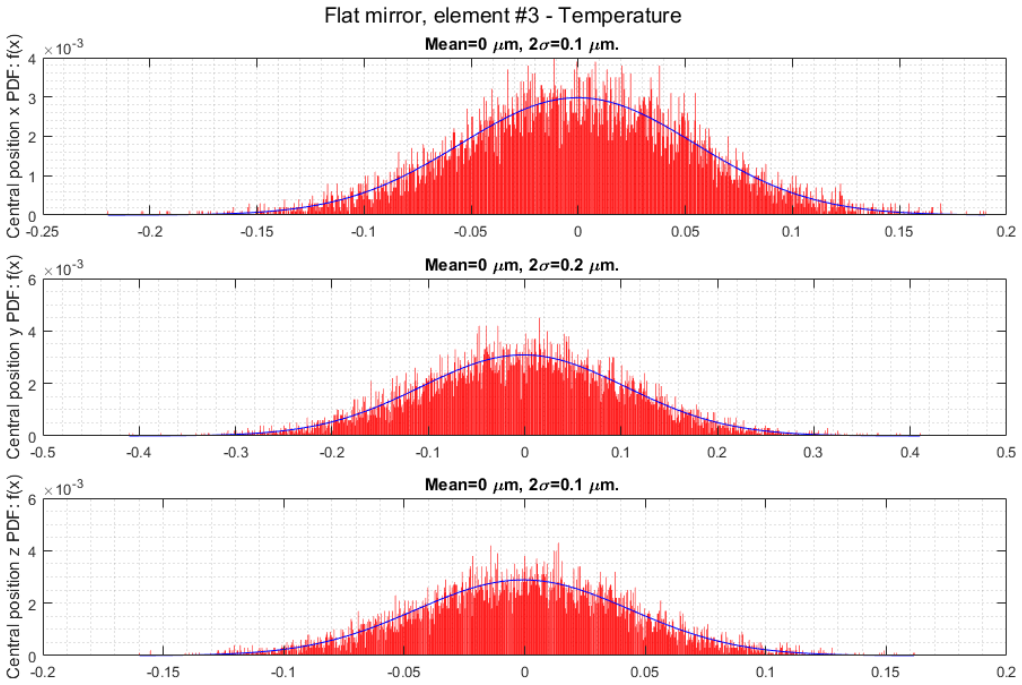

Figure 3.62 Temperature error of an element aligned in 20 minutes. From top to bottom: position in X, position in Y, and position in Z.

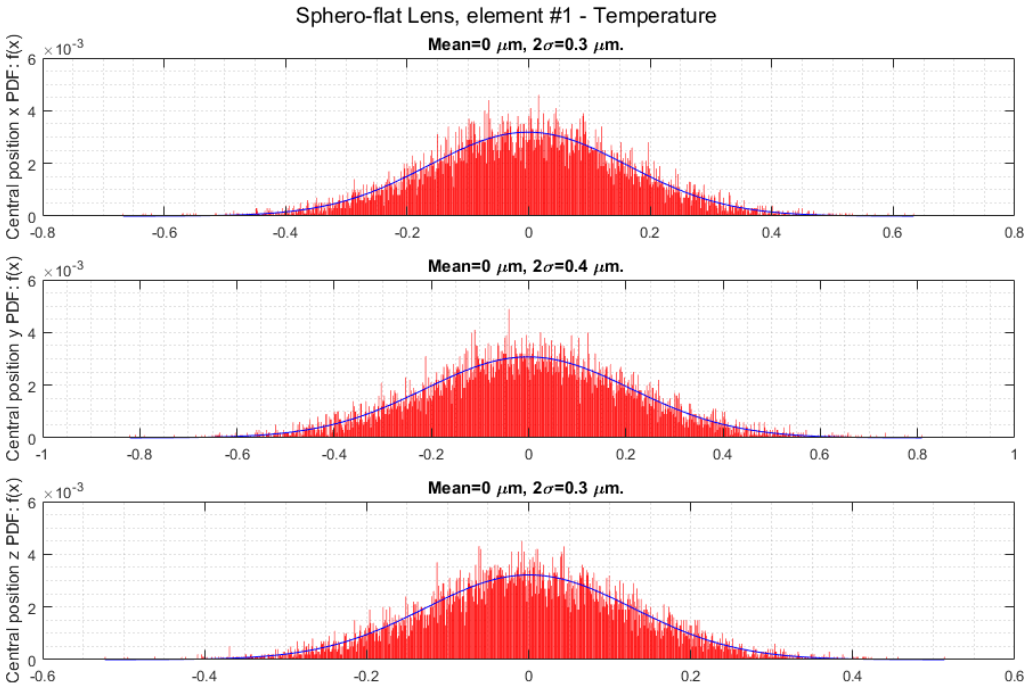

Figure 3.63 Temperature error of an element aligned in 60 minutes. From top to bottom: position in X, position in Y, and position in Z.

3.5.4 Mechanical misalignments and optical effects of mechanical misalignments

The results obtained from the previous sections have been summarized in terms of both mechanical misalignment and optical effects due to those misalignments. This operation is performed using two different software modules.

3.5.4.1 Mechanical misalignments

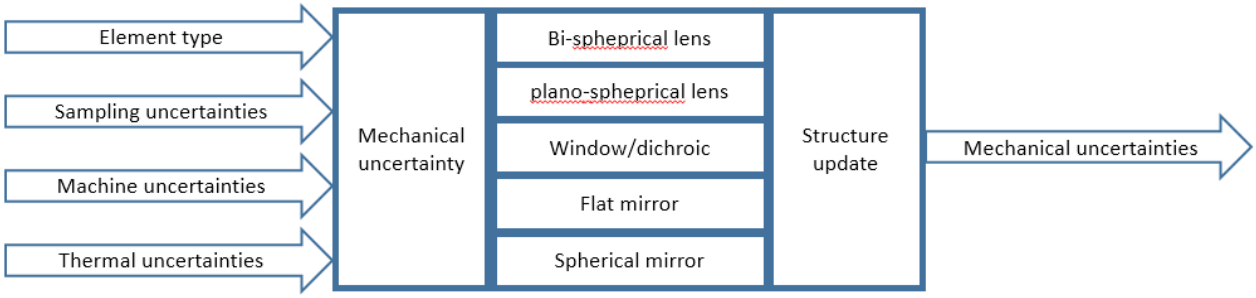

Figure 3.64 General view of the mechanical uncertainties module. The 'mechanical uncertainty' dispatch the inputs to the correct analysis submodule while the 'structure update' takes the results and organize them in the mechanical uncertainties structure and plot the results.

All the outputs of the previous modules (sampling, machine, and thermal) are used to calculate the overall mechanical misalignments and the results are plotted for each element in terms of average and standard deviations. A couple of examples of the second ones (2σ) are presented in Figure 3.65 and Figure 3.66. Those values can be used in three different ways.

During the design phase, a tolerance analysis using a raytracing software like ZEMAX can be performed with those inputs in order to quantify the performances degradation of the instrument due to the measuring accuracy of the CMM.

In the same phase, the mechanical design will be done in such a way that those values can be actually reached while mounting the elements (e.g. distances between the mounting holes and pins to have the right control on the rotations).

Moreover, during the integration, those values can be used as a lower limit to define when the alignment process can be considered complete.

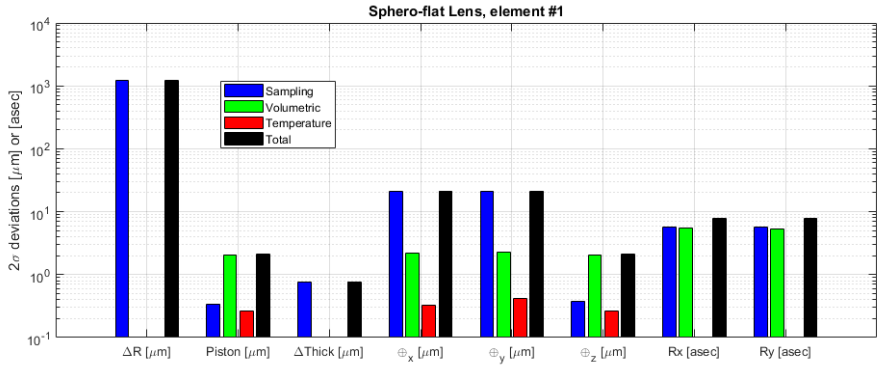

Figure 3.65 Mechanical misalignments of a plano-spherical lens. From left to right: ROC variation, piston, thickness variation, position in X, position in Y, position in Z, rotation around X, rotation around Y.

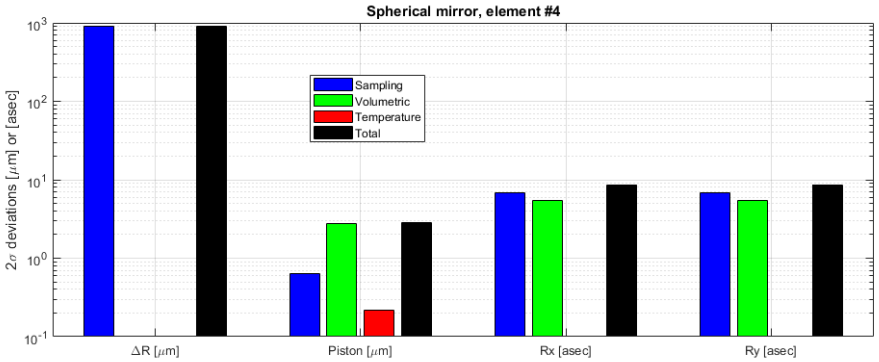

Figure 3.66 Mechanical misalignments of a spherical mirror. From left to right: ROC variation, piston, rotation around X, rotation around Y.

3.5.4.2 Raw optical effects

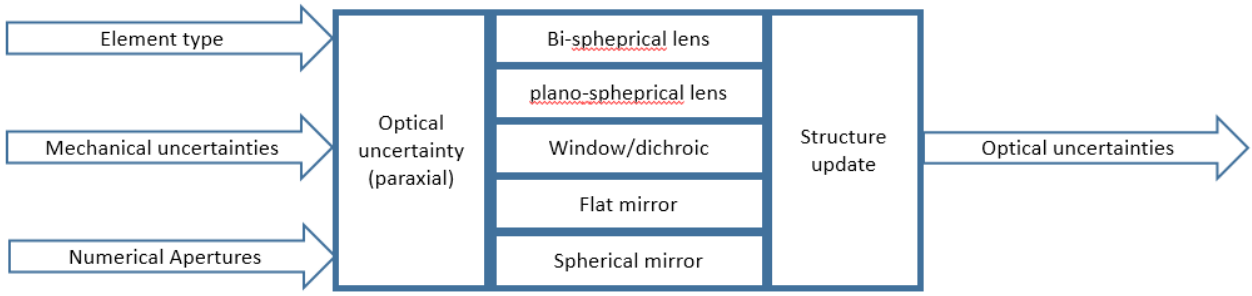

Figure 3.67 General view of the optical uncertainties module. The 'optical uncertainty' dispatch the inputs to the correct analysis submodule while the 'structure update' takes the results and organize them in the optical uncertainties structure and plot the results.

The results obtained in the previous section give a good benchmark of the expected misalignments but does not provide any information on their severity.

For example, a mirror with a small ROC will have smaller standard deviations in term of rotation, piston, and ROC itself with respect to another mirror with bigger ROC. However, those uncertainties will be more severe in terms of optical rotation and displacement of the generated image.

To identify the worst offender of an optical system it is obviously possible to perform a simulation with a dedicated raytracing software. However, a preliminary evaluation can be useful to identify the most critical elements to keep under control during the design and the alignment phases.

Those raw optical effects have been calculated using the geometrical optic formulae (see [3.24], [3.25], [3.26], [3.27]), considering each element separately, and applying the thin lens approximations.

The inputs needed are the angle of incidence of the optical beam, the Numerical Aperture (NA) of the input and output beam, and the focal length of each element.

In a **refractive element**, the defocus (related to the Z position) can be calculated ([3.24]) as

$$\Delta Z_{fp} = \Delta Z_{lens}\left(\frac{NA_{in}^2 - NA_{out}^2}{NA_{image}^2}\right)\ [\mu m] \tag{3.26}$$

or

$$\Delta W_{20fp} = \Delta Z_{lens}\left(\frac{NA_{in}^2 - NA_{out}^2}{2}\right)\ [\mu m] \tag{3.27}$$

where ΔZ_{fp} is the displacement of the focal plane, ΔW_{20fp} is the wavefront error due to the defocus , ΔZ_{lens} is the physical displacement of the refractive element and NA_{image} is the numerical aperture of the image.

The lateral displacements of the image due to the rotations of the element ([3.25]) are

$$\Delta X_{fp} = \frac{R_Y \times Th\,(n-1)}{n} \cong \frac{R_Y \times Th}{3}[\mu m]; \qquad \Delta Y_{fp} = \frac{R_X \times Th\,(n-1)}{n} \cong \frac{R_X \times Th}{3}[\mu m] \tag{3.28}$$

where R_X and R_Y are the rotations, Th is the thickness and n is the refractive index of the element. The approximation is valid for refractive index of approximately 1.5.

The tilt of the image is related to the lateral displacements of the element and can be calculated as

$$\mathrm{R_{fpx}} = \frac{\Delta Y_{lens}}{f}\ [asec]; \qquad \mathrm{R_{fpy}} = \frac{\Delta X_{lens}}{f}\ [asec] \tag{3.29}$$

where ΔX_{lens} and ΔY_{lens} are the displacements of the element and f it's his focal length. In case of a windows (f =∞) its displacements in X, Y and Z directions, clearly does not produce any effect.

For a **reflective element** the defocus can be calculated as

$$\Delta Z_{fp} = \Delta Z_{mirror} \times \cos(R)\ [\mu m] \tag{3.30}$$

in the flat mirror case where ΔZ_{fp} is the displacement of the focal plane, ΔZ_{mirror} is the physical displacement of the reflective element and R is the angle of incidence of the optical beam.

The defocus of a spherical mirror instead ([3.24]) is:

$$\Delta Z_{fp} = \Delta Z_{lens}\left(\frac{NA_{in}^2 - NA_{out}^2}{NA_{image}^2}\right)\cos(R)\,[\mu m] \tag{3.31}$$

or

$$\Delta W_{20fp} = \Delta Z_{mirror}\left(\frac{NA_{in}^2 + NA_{out}^2}{2}\right)\cos(R)\ [\mu m] \tag{3.32}$$

The displacement is related to both the piston and the rotation. The first one can be calculated as

$$\Delta X_{fp} = 2 \times \Delta Z_{mirror} \times |\sin(R_Y)|\ [\mu m]; \qquad \Delta Y_{fp} = 2 \times \Delta Z_{mirror} \times |\sin(R_X)|\ [\mu m] \tag{3.33}$$

while the second one is

$$\Delta X_{fp} = 2 \times R_Y \times \left|\frac{f}{2NA_{out}}\right|\ [\mu m]; \qquad \Delta Y_{fp} = 2 \times R_X \times \left|\frac{f}{2NA_{out}}\right|\ [\mu m] \tag{3.34}$$

The tilts of the plane can be simply calculated as

$$R_{fpx} = 2 \times R_X\ [asec]; \qquad R_{fpy} = 2 \times R_Y\ [asec] \tag{3.35}$$

Applying those formulae to the mechanical standard deviations calculated in the previous section, it is possible to obtain a representation of the expected errors as the ones in Figure 3.68, Figure 3.69 and Figure 3.70.

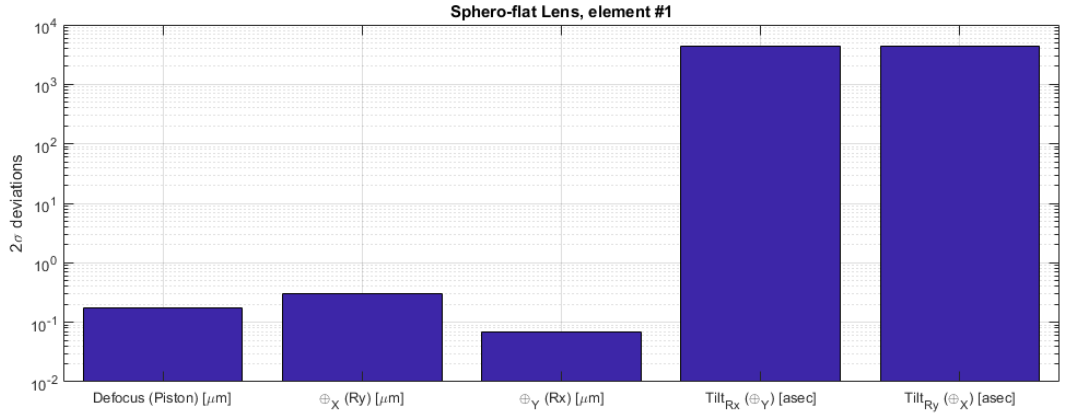

Figure 3.68 Optical effects on a plano-spherical lens (2σ values). From left to right: defocus, displacement in X direction, displacement in Y direction, tilt around the X-axis, and tilt around the Y-axis. In brackets the sources of the errors.

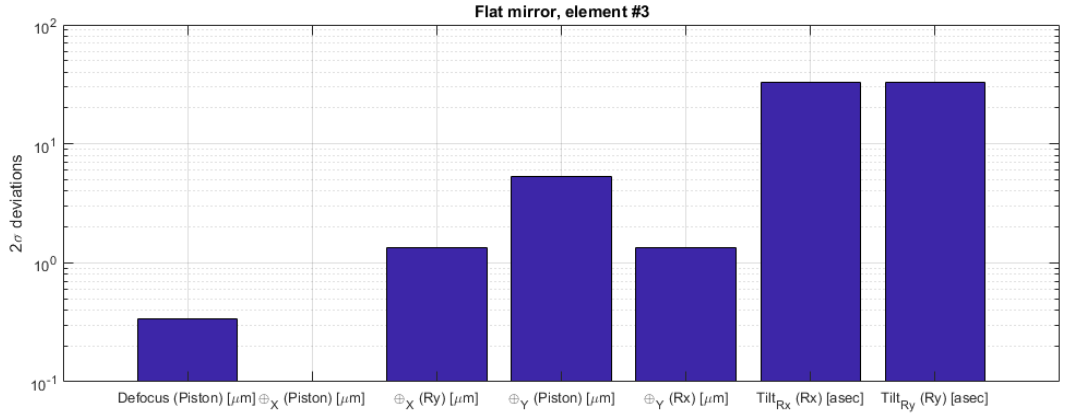

Figure 3.69 Optical effects on a flat mirror (2σ values). From left to right: defocus, displacement in X direction, displacement in Y direction, tilt around the X-axis, and tilt around the Y-axis. In brackets the sources of the errors.

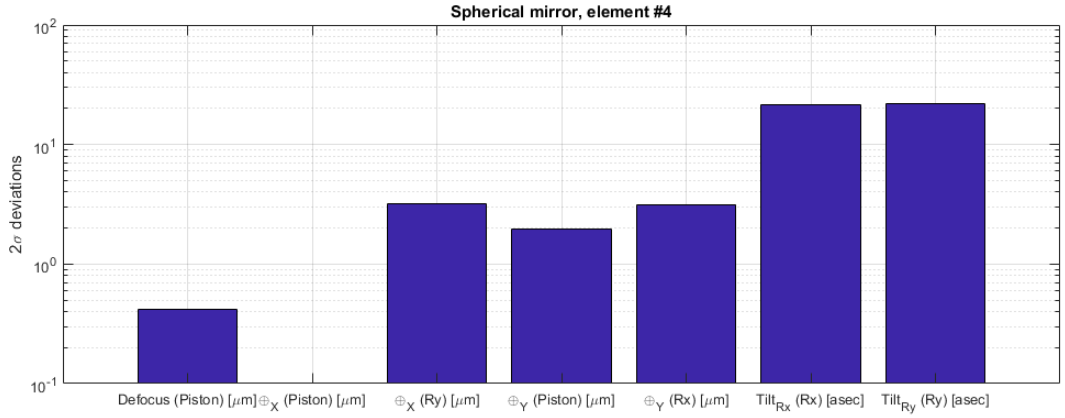

Figure 3.70 Optical effects on a spherical mirror (2σ values). From left to right: defocus, displacement in X direction, displacement in Y direction, tilt around the X-axis, and tilt around the Y-axis. In brackets the sources of the errors.

3.6 Conclusions and future improvements

An introduction on the CMMs has been done in the first part of this chapter. In particular, the techniques used to compensate the measuring errors have been described together with the methods and the standards developed to estimate the measurement uncertainty.

The second part was dedicated to the description of the uncertainty evaluation performed during the alignment of the ESPRESSO FEU done with an AACMM.

This coarse estimation highlighted the importance of a better evaluation of the uncertainty values in order to be able to predict the expected performances of the final system and to assess the applicability of a purely mechanical alignment of the optical system under investigation.

In the last three sections, the developed software has been presented considering the alignment of optical systems composed by a number of small optical elements. The three main error sources have been identified as the probing error, the machine error, and the temperature drift. The needed information have been acquired using a CMM and the software has been developed in order to provide the expected geometrical and optical errors. If the temperature and probing results can be considered complete, the results of the machine error will be improved to better define it along the whole measuring volume.

To validate the result a dummy optical system has been measured with different techniques and the results, shown in chapter 6, have been compared with the output of the simulation software.

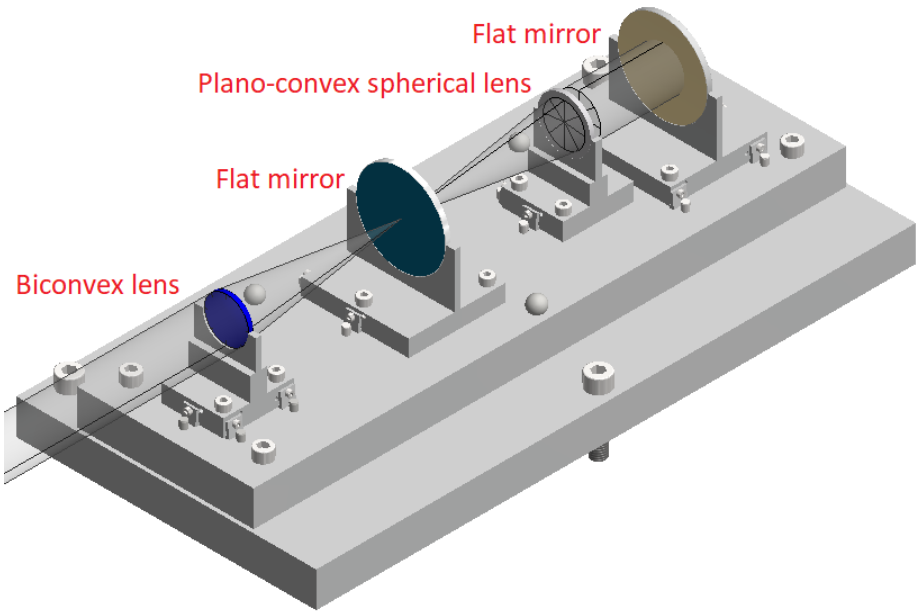

Figure 3.71 Dummy optical system used as a validation of the alignment procedure. The 2 reflective and the 2 refractive optical elements are shown together with the optical beam (in transparency).

3.7 References

[3.1] ISO 10360-1:2002. Geometrical Product Specifications (GPS) - Acceptance and reverification tests for coordinate measuring machines (CMM) - Part 1: Vocabulary

[3.2] Hocken RJ, Pereira PH, editors. Coordinate measuring machines and systems. CRC Press; 2016 Apr 19.

[3.3] Weckenmann A, Estler T, Peggs G, McMurtry D. Probing systems in dimensional metrology. CIRP Annals-Manufacturing Technology. 2004 Jan 1;53(2):657-84.

[3.4] Zhang G, Veale R, Charlton T, Borchardt B, Hocken R. Error compensation of coordinate measuring machines. CIRP Annals-Manufacturing Technology. 1985 Jan 1;34(1):445-8.

[3.5] ISO 10360-2:2009. Geometrical product specifications (GPS) - Acceptance and reverification tests for coordinate measuring machines (CMM) - Part 2: CMMs used for measuring linear dimensions

[3.6] ISO 10360-5:2010. Geometrical product specifications (GPS) - Acceptance and reverification tests for coordinate measuring machines (CMM) - Part 5: CMMs using single and multiple stylus contacting probing systems

[3.7] ISO 14253-2:2011. Geometrical product specifications (GPS) — Inspection by measurement of workpieces and measuring equipment Part 2: Guidance for the estimation of uncertainty in GPS measurement, in calibration of measuring equipment and in product verification

[3.8] ISO/TR 16015:2003. Geometrical product specifications (GPS) — Systematic errors and contributions to measurement uncertainty of length measurement due to thermal influences

[3.9] ISO/TS 15530-1:2013. Geometrical product specifications (GPS) — Coordinate measuring machines (CMM): Technique for determining the uncertainty of measurement Part 1: Overview and metrological characteristics

[3.10] ISO/DTS 15530-2:2003. Geometrical Product Specifications (GPS) - Coordinate measuring machines (CMMs): Techniques for evaluation of the uncertainty of measurement - Part 2: Use of multiple measurement strategies

[3.11] ISO/TS 15530-3:2011. Geometrical product specifications (GPS) — Coordinate measuring machines (CMM): Technique for determining the uncertainty of measurement Part 3: Use of calibrated workpieces or measurement standards

[3.12] ISO 15530-4:2008. Geometrical Product Specifications (GPS) — Coordinate measuring machines (CMM): Technique for determining the uncertainty of measurement Part 4: Evaluating task-specific measurement uncertainty using simulation

[3.13] ASME B89.4.22. Methods for Performance Evaluation of Articulated Arm Coordinate Measuring Machines (CMM)

[3.14] Wilhelm RG, Hocken R, Schwenke H. Task specific uncertainty in coordinate measurement. CIRP Annals-Manufacturing Technology. 2001 Dec 31;50(2):553-63.

[3.15] Phillips SD, Borchardt BR, Sawyer DS, Estler WT, Ward DE, Eberhardt K, Levenson M, McClain MA, Melvin B, Hopp T, Shen Y. The calculation of CMM measurement uncertainty via the method of simulation by constraints. In American Society for Precision Engineering 1997.

[3.16] Phillips SD, Borchardt B, Estler WT, Buttress J. The estimation of measurement uncertainty of small circular features measured by coordinate measuring machines. Precision Engineering. 1998 Apr 30;22(2):87-97.

[3.17] Sładek J, Gąska A. Evaluation of coordinate measurement uncertainty with use of virtual machine model based on Monte Carlo method. Measurement. 2012 Jul 31;45(6):1564-75.

[3.18] Baldwin JM, Summerhays KD, Campbell DA, Henke RP. Application of simulation software to coordinate measurement uncertainty evaluations. NCSLI Measure. 2007 Dec 1;2(4):40-52.

[3.19] Phillips SD, Borchardt B, Caskey G. Measurement uncertainty considerations for coordinate measuring machines. NASA STI/Recon Technical Report N. 1993 Apr;93.
[3.20] Bachmann H, Ammann W. Vibrations in structures: induced by man and machines. Iabse; 1987.
[3.21] Hardy GH. On the expression of a number as the sum of two squares. 1915.
[3.22] Arun KS, Huang TS, Blostein SD. Least-squares fitting of two 3-D point sets. IEEE Transactions on pattern analysis and machine intelligence. 1987 Sep(5):698-700.
[3.23] Schneider P, Eberly DH. Geometric tools for computer graphics. Morgan Kaufmann; 2002 Oct 10.
[3.24] Schwertz K, Burge JH. Relating axial motion of optical elements to focal shift. InProc. of SPIE Vol 2010 Aug 19 (Vol. 7793, pp. 779306-1).
[3.25] Burge JH. An easy way to relate optical element motion to system pointing stability. InProc. SPIE 2006 Aug 31 (Vol. 6288, p. 62880I).
[3.26] Greivenkamp JE. Field guide to geometrical optics. Bellingham, WA: SPIE Press; 2004 Jan 20.
[3.27] Wyant JC, Creath K. Basic wavefront aberration theory for optical metrology. Applied optics and optical engineering. 1992 Jan 1;11(part 2):28-39.

4 Overtravel forces estimation while measuring with CMMs

4.1 Introduction

In order to predict the effect of the contact between the CMM probe and an optical element, different variables including the contact force, the presence of a thin coating and its characteristics, the materials properties, and the shape of the surfaces in contact must be considered (detailed in chapter 5). The contact force and the size of the sphere of the stylus are the two parameter that can be changed to decrease the induced damage. Depending on the technology of the probing system, the contact force could be directly controlled, measured or could be unknown.

The most typical probing systems in commercial CMMs are the measuring probes and the digital probes [4.1]. The first ones measure the stylus deflection and are mainly used to scanning mode, while the second ones use a switch to detect the contact and, therefore, can only do discrete point probing.

In passive measuring systems (see Figure 4.1, left), the force is proportional to the deflection of the system and can widely vary during the measurement. The active measuring sensors (Figure 4.1, second from the left), instead, are able to modulate the contact force during the scanning thanks to the actuators. The large number of points acquired and the more direct control over the applied force are counterbalanced by higher costs and grater encumbrance of those systems. Those factors make them unpractical for the optical systems measurements, also considering that the 'scanning mode' cannot be applied on optical surfaces.

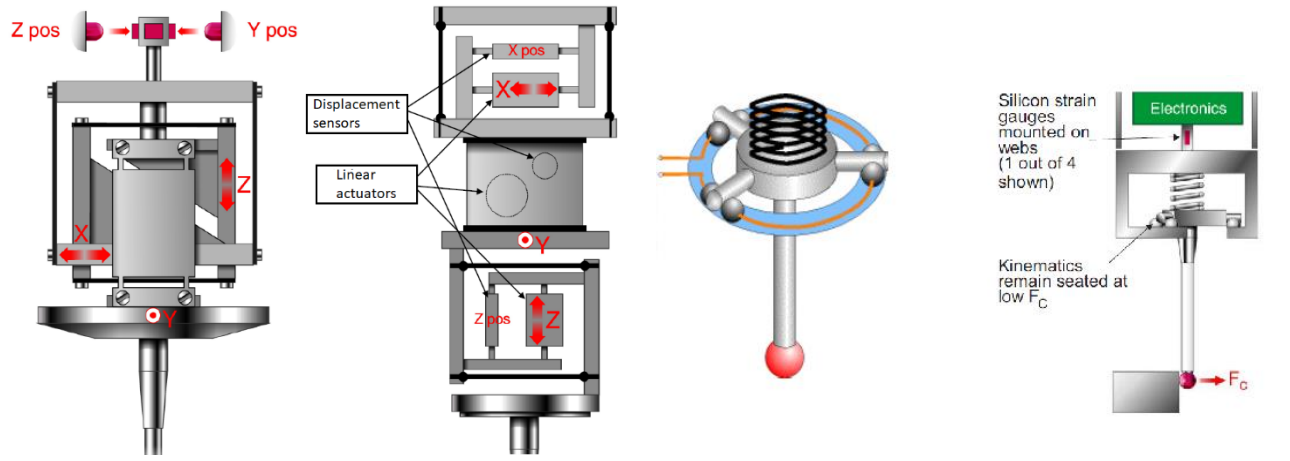

Figure 4.1. Typical CMM probing systems. From left to right: measuring passive, measuring active, digital electro-mechanic and digital strain-gauge system. Images adapted from Renishaw website.

The analysis of the forces, therefore, focused on the digital systems. Those systems are typically characterized by a pretravel force and an overtravel force. The pretravel force is the one used by the probe to define the contact with the workpiece and can be triggered in different ways: the most common are the mechanical aperture of a circuit mounted on a kinematic system (Figure 4.1, third from the left) or an electrical signal measured by strain gauge (Figure 4.1, right) or piezoelectric devices.

The pretravel force has been widely studied with different approaches (see [4.2], [4.3], [4.4], [4.5]) as its anisotropy affects the accuracy of the measurement both directly (deflection of the stylus and deformation of the workpiece) and indirectly (geometrical displacement of the kinematic system).

The overtravel force can be defined as the maximum force applied during the measurement. The study of this value did not generate the same interest as the pretravel force, as the only requirement is to keep it below the values that can generate a significant damage on the workpiece surface.

This requirement can become critical for micro-CMM where the microprobes have a stylus with a radius well below the millimetre. Unfortunately, the geometrical design of those systems is completely different from the conventional CMMs (see [4.3]) as the factors influencing the contact forces ([4.6], as an example, considers hydrostatic, electrostatic, and Van der Waals forces).

An indirect evaluation of the measuring force on conventional CMMs has been performed measuring the damage on a known sample (e.g. steel or aluminium) and deriving it with theoretical considerations (see [4.7], [4.8]). The main drawbacks of this method are the long measurement process and the lowest accuracy as the mechanical properties of the materials must be well known.

Another indirect method, again shown in [4.7] and [4.8], uses the Newton's second law and the Hertzian theory to estimate the force under the hypothesis that the system can be represented as a sphere with a certain inertia and speed impacting on the surface. Its drawback is related to the extreme simplification that ignores the mechanical characteristic of the probing system.

Other authors studied the pretravel forces to estimate the spatial hysteresis of the probe (and, therefore, its measurement error) considering the mechanical design of different digital probes (see [4.3] and [4.4] for the theoretical analysis and [4.5] for the experimental verifications). The obtained formulae can be, however, adapted to the overtravel forces of a probe like the Renishaw TP200.

This probe is composed by a strain gauge trigger system and a kinematic mount. The CMM will stop after a certain number of milliseconds after the trigger has been activated. Therefore, the overtravel force will be defined by the strain gauge or by the kinematic mount as a function of different parameters like measuring direction, stylus used and measuring speed.

This analysis, even if focused on the Renishaw TP200 can be adapted to different digital probes (e.g. the whole Renishaw TP series, Zeiss ST3, Renishaw HP series…).

4.2 Theoretical model proposed

The theoretical model proposed is a static one has been derived by the study proposed in [4.4]. The author calculated the pretravel forces for a system with an electro-mechanical trigger and the results obtained have been used to evaluate the TP200 overtravel forces in case the kinematic system is involved. In certain conditions (typically at low measurement speed), the strain gauge system is the one defining the overtravel force and another theoretical model must be used.

Even if the analysis will focus on the probe-related forces, is must be noted that a secondary role is also played by the CMM axes and therefore the location of the workpiece in the volume and the axes involved in the movement will influence the overtravel force. Those effects have been taken into account considering different correction factors in the models.

4.2.1 Kinematic system case

The scheme of the kinematic system is shown in Figure 4.2. In the drawing F_S is the sum of spring and gravity force, F_T is the triggering force (in our case, the overtravel force). Its direction is defined by β and γ: the first

is the angle between the Y axis and the F_T projection on the XY plane, while γ is the angle between that projection and F_T.

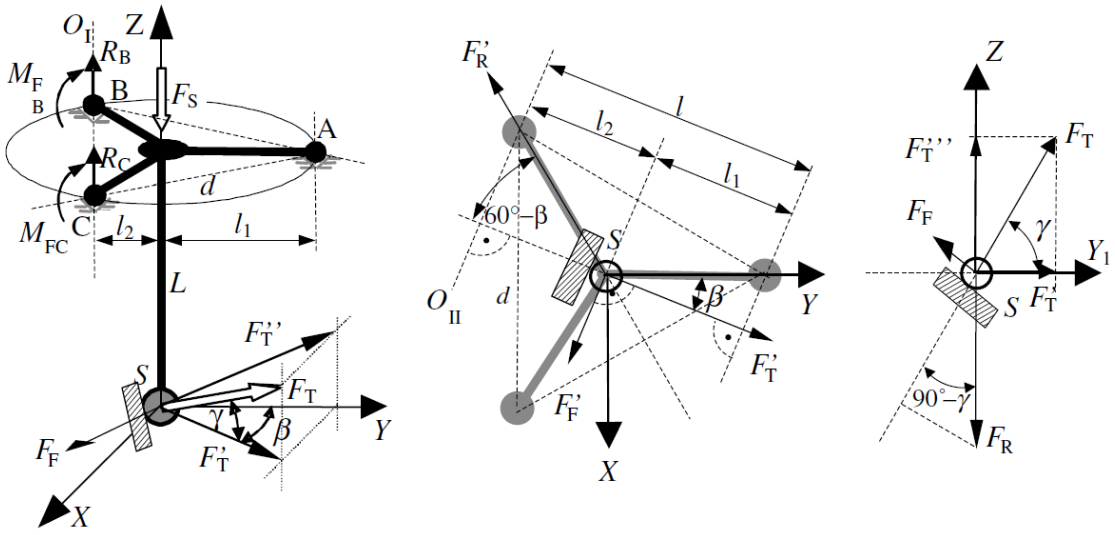

Figure 4.2. Forces distribution in an electromechanical probe. From left to right: isometric view, top view (XY plane), and lateral view (YZ plane). Figure from [4.4].

In this model, two critical angles can be found:

$\beta_g = 60° - \tan^{-1}(\mu)$. If β is above it, there is no sliding between the stylus ball and the workpiece and, therefore, the system rotates around O_{II}.

$\gamma_g = 90° - \tan^{-1}(\mu)$. If γ is below it, the stylus ball slides on the workpiece and, therefore, the system rotates around the O_I or O_{II} axes. If γ is greater than γ_g, the transducer will move along Z.

Those critical angles divide the problem in 3 different cases.

1. If $\beta < \beta_g$ and $\gamma < \gamma_g$ the rotation is around one of the axes connecting pair of nests (e.g. O_I). The force will be equal to

$$F_{T_{caseI}} = \frac{l_2 F_s + M_F}{((L+\mu l_2)\cos\gamma + (l_2 - \mu L)\sin\gamma)\sqrt{1 - \sin^2\beta\cos^2\gamma}}\ [N] \tag{4.1}$$

   where l_2 is calculated as

$$l_2 = \frac{d\ \tan(30°)}{2} = \frac{d}{2\sqrt{3}}\ [mm] \tag{4.2}$$

   with d equal to the distance between two nests.

2. The second case is applied when $\beta \geq \beta_g$ and $\gamma < \gamma_g$ and the stylus rotates around an axis perpendicular to the force (e.g. O_{II}). The value of l_2 will vary with β and will be equal to

$$l_2 = \frac{d\ \cos(60° - \beta)}{2\cos(30°)} = \frac{d\cos(60° - \beta)}{\sqrt{3}}\ [mm] \tag{4.3}$$

   and the force will be calculated as

$$F_{T_{caseII}} = \frac{l_2 F_s + M_F}{\left((L + \mu d \cos(60° - \beta)/\sqrt{3} \cos\gamma + \left((d \cos(60° - \beta)/\sqrt{3} - \mu L\right) \sin\gamma\right) \sqrt{1 - \sin^2\beta \cos^2\gamma}} \; [N] \quad (4.4)$$

3. If $\gamma \geq \gamma_g$, the prove moves along Z and the force is equal to

$$F_{T_{caseIII}} = \frac{F_s}{\sin\gamma + \mu \cos\gamma} \quad (4.5)$$

An example of the results obtained is shown in Figure 4.3.

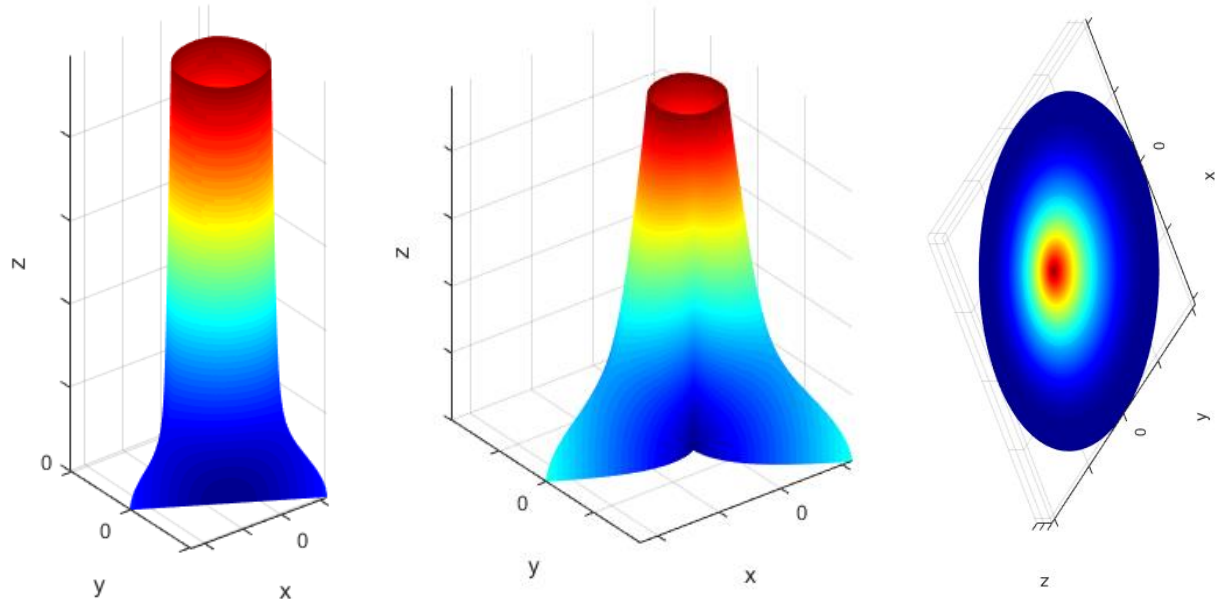

Figure 4.3. Example of forces at different β (0 to 360°) and γ. The force is equal to the distance from the origin (0,0,0). From left to Right: case I (0< γ <γ_g), case II (0< γ <γ_g) and case III (γ_g < γ <90°).

Considering the three cases together, the force plot appears as in Figure 4.4, left. The third case is applied only when the contact is quasi perpendicular to the stylus axis while the two other cases strongly depend on the coefficient of friction (see also Figure 4.5 and Figure 4.6).

In Figure 4.4 on the right, it is also shown the expected experimental plot considering that the head moves with steps of 7.5° in both altitude and azimuth direction.

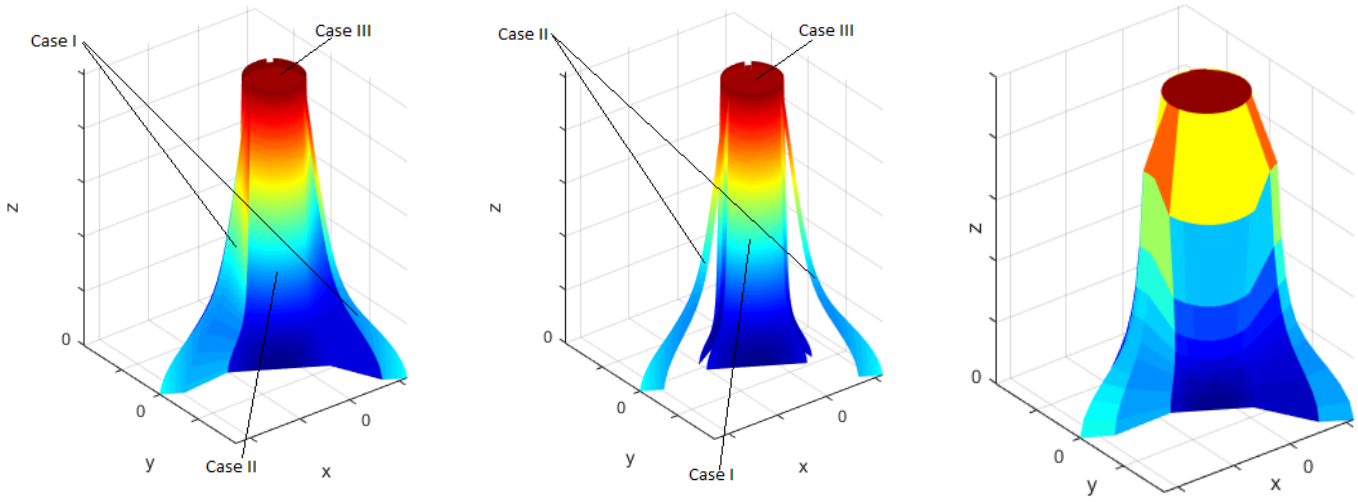

Figure 4.4. Forces considering the three cases together with low coefficient of friction. In the centre, the same plot with the discontinuity between Case I and Case II highlighted. Right: expected experimental results consider the head increment resolution (friction coefficient changed from 0.1 to 0.2 for clarity).

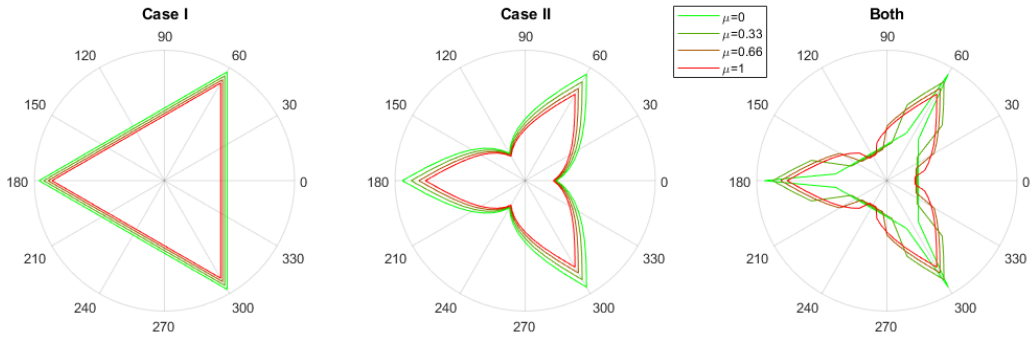

Figure 4.5. Forces at γ=0° for different coefficient of frictions.

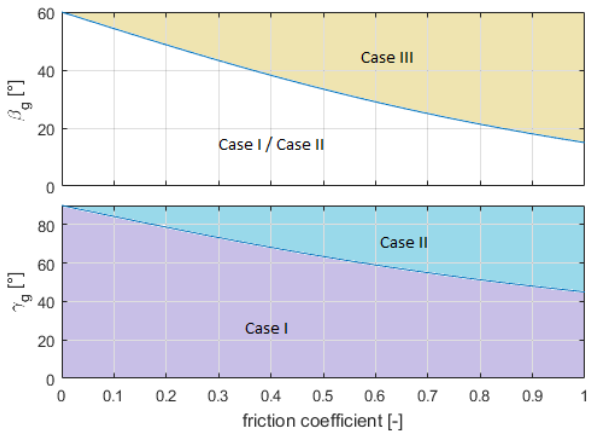

Figure 4.6. Critical angles for different coefficient of friction.

The experimental analysis presented in the next sections, never shown a shape similar to the 'Case II' one. Therefore, in order to fit the experiments with the theoretical model, only Case I and Case III have been

considered. Consequently, the parameters F_{kins} M_f and l_2 have to be considered as parameters and not as the physical quantities of the probing system.

$$F_{T_{case}I} = \frac{l_2 F_{kins} + M_F + mg(s\cos(TP_{clock} - \beta)\sin\phi + l_2\cos\phi)}{((L+\mu l_2)\cos\gamma + (l_2 - \mu L)\sin\gamma)\sqrt{1 - \sin^2\beta\cos^2\gamma}} \quad (4.6)$$

$$F_{T_{case}III} = \frac{F_{kins} + mg\cos\phi}{\sin\gamma + \mu\cos\gamma} \quad (4.7)$$

Where ϕ is the angle between the stem of the stylus and the gravity vector and TP_{clock} is the head axis clock defined by the probe (line perpendicular to O_I and passing through A in Figure 4.2) with respect to the β angle.

An example of the results obtained with a radial contact (γ=0°) is shown in Figure 4.7. The maximum force increase if the workpiece surface is pointing upward while decrease down to zero for a measurement in the opposite direction. In the extreme case where this force goes below zero, the measurement is not possible as the probe will be triggered by the weight of the stylus alone.

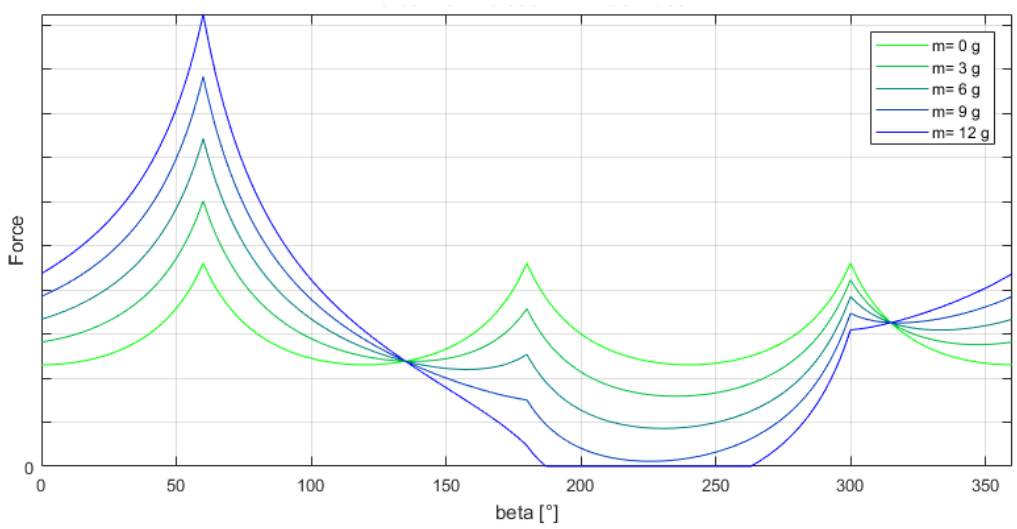

Figure 4.7. Overtravel force with γ=0°, TP_{clock}=-45° and increasing stylus mass.

4.2.2 Strain gauge system case

If the measuring speed is slow enough for the mounted stylus, the kinematic system will rest and the overtravel force will be defined by the resistance offered by the strain gauge trigger.

In this case, the geometrical and electrical characteristic of the electro-mechanical system are unknown. Therefore, the preliminary assumption done is that the overtravel force is derived by a certain normal force F_{ssL} or a certain lateral force F_c generated by the strain gauge system.

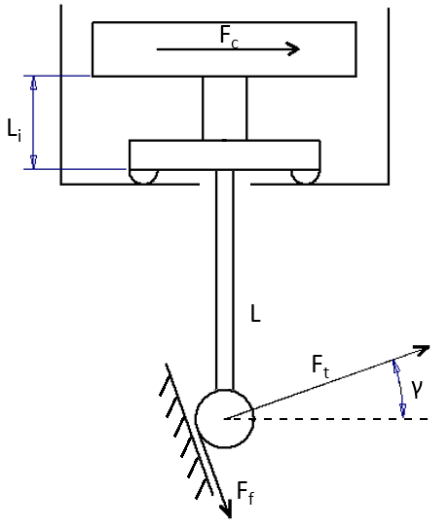

Figure 4.8. Forces distribution for a strain gauge trigger in case of lateral forces.

With simple geometrical considerations (see Figure 4.8), it is possible to calculate the overtravel force due to the lateral forces as

$$F_{TsgL}=\frac{F_{sgL}}{\left(\frac{L}{L_i}+\frac{\mu d_{sph}}{2\,L_i}+1\right)\cos\gamma+\mu\,\left(\frac{L}{L_i}+1\right)\sin\gamma}\,v\;[N] \tag{4.8}$$

Where d_{sph} is the diameter of the sphere and v is the measurement speed.

F_{sgL}, expressed in N*s/mm, takes into account the effect of the measuring speed. After the trigger has been activated, the CMM will slow down and the contact force will increase in an almost linear fashion until the axes stop. Therefore, the overtravel forces will be linearly proportional with respect to measuring speed.

L_i, expressed in mm, is a parameter that considers both the relative weight between the lateral force and the momentum applied to the strain gauge.

The overtravel force due to the force F_{sgN}, directed as the stem of the stylus, can be calculated as

$$F_{TsgN}=\frac{F_{sgN}}{\mu\cos\gamma+\sin\gamma}\,v\;[N] \tag{4.9}$$

The expected shape is shown in Figure 4.9 and is composed by two cones with different apertures. In this case, the behaviour is constant for all the cases as no trilobe effect is present.

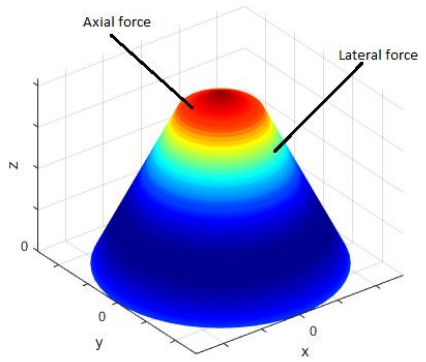

Figure 4.9. Example of overtravel forces at different β and γ due to the strain gauge system.

4.3 Measurement setup and methodology

To measure the forces in some particular case, derive the parameters of the theoretical model, and validate it, two force transducers have been prepared.

Those transducers, shown in Figure 4.10, are made of aluminium and measure the shear stress via a strain gauge system in full bridge configuration. The four elements, therefore, are all glued on one side of the transducer near the flexures. Two different versions are needed as for low forces the 'high load' transducer (HLT) has a low signal to noise ratio while at high forces the 'low load' transducer (LLT) is heavily deformed. By FEM analysis, this deformation is equal to 0.15 mm for a load of 4 N (see Figure 4.11) and, being the contact force function of the distance travelled by the probe after the triggering, the LLT tends to underestimate this force for high loads.

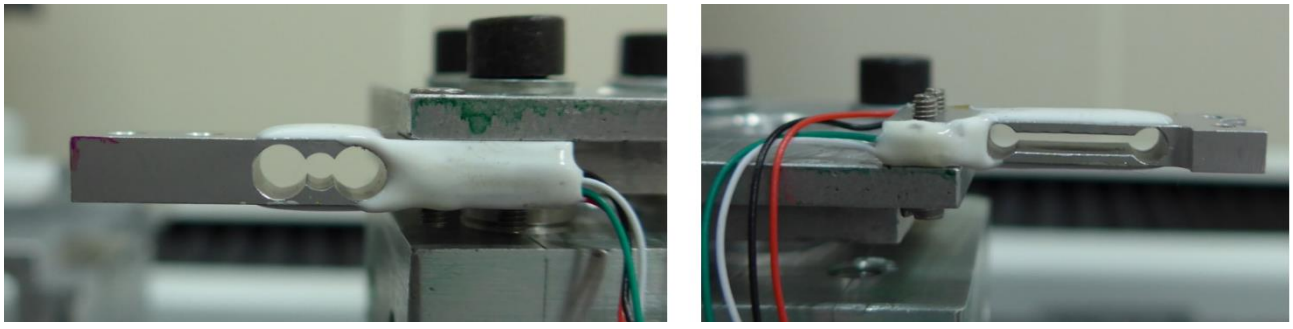

Figure 4.10. Transducers used for the forces measurements. Left: high load one. Right: low load one.

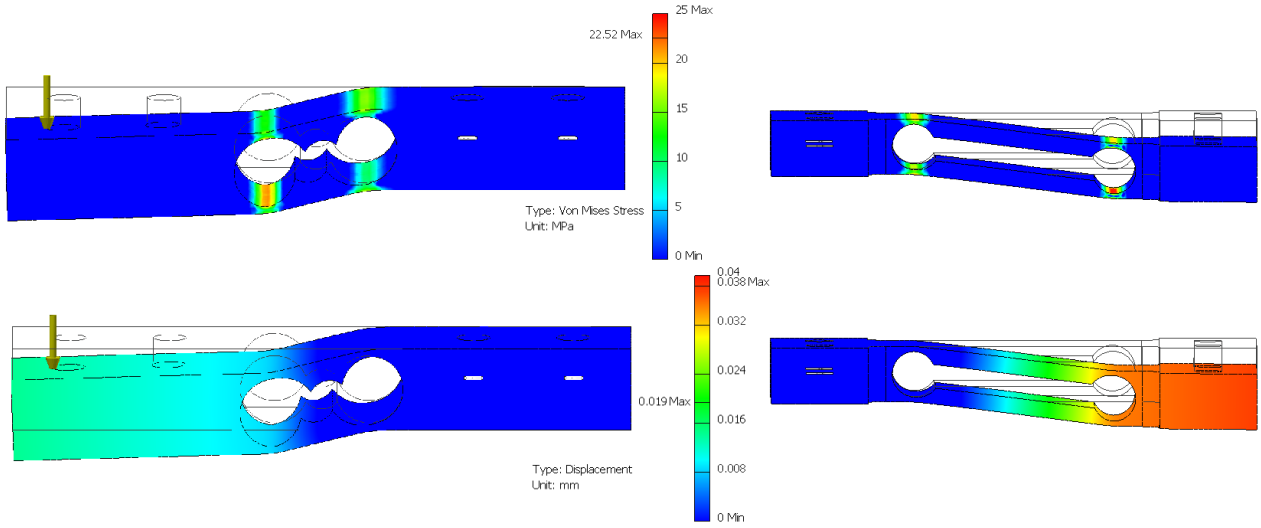

Figure 4.11. Von Mises stress (top) and maximum displacement (bottom) of the two transducers. Left: HLT under a 4 N load. Right: LLT under a 1 N load.

The calibration of the transducers has been performed with applying different masses known with a 2σ accuracy of ±0.0002 g. The behaviour of the systems is linear and the equations describing it are

$$Force\ [N] = 1833.196 * Tension[V] - 0.087 \tag{4.10}$$

$$Force\ [N] = 9330.047 * Tension[V] + 0.749 \tag{4.11}$$

for the LLT and the HLT respectively.

The coefficient of determination R2 is equal to 1.000 in both cases while the 2σ uncertainty is 0.57 mN for the HLT and 0.88 mN for the LLT.

Due to thermal variations, however, variations of the intercept up to 3.04 mN for the HLT and 11.2 mN for the LLT have been found. To remove those errors and to account for the self-weight of the transducer in different orientations, the system is automatically zeroed before each measurement.

The dynamic behaviour of the transducers has been evaluated applying an impulse and extracting their dynamic properties. The bode diagram obtained by them is shown in Figure 4.12. The amplification stays in a band of ±5% for frequencies below 145 Hz and 319 Hz for The LLT and the HLT respectively.

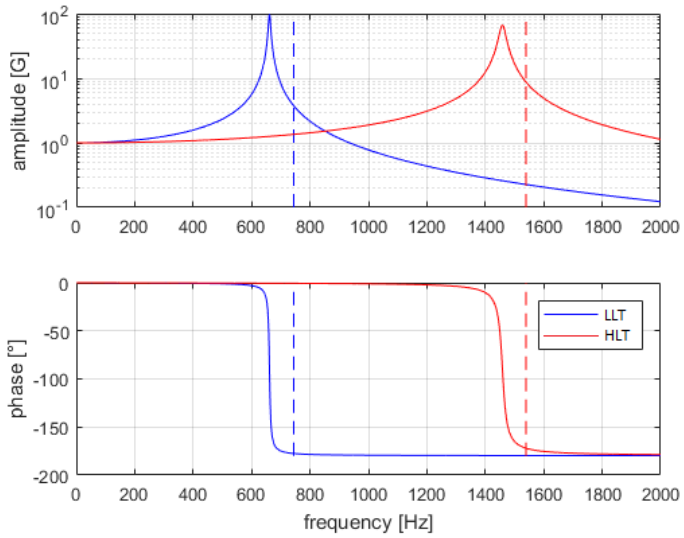

Figure 4.12. Frequency response of the two transducers. The solid lines represent the experimental values while the dashed lines show the values obtained by the FEM analysis.

4.4 Obtained results

To obtain the parameters describing the behaviour of the probe different force measurements have been acquired using different probes, stylus and measurement directions.

The measurements have been divided in three parts: axial, radial and intermediate.

The axial forces have been performed with the force acting in the direction of the stylus in order to evaluate the parameters of the $F_{TcaseIII}$ (kinematic system) and F_{CsgL} (strain gauge system). In the radial forces case the forces are directed perpendicular to the axis of the stylus and will be used to obtain the remaining parameters in F_{TcaseI} and all the parameters in F_{TsgN}.

The intermediate cases will be performed in order to evaluate the shape of the forces for all the γ values.

4.4.1 Axial forces

The forces have been first acquired at 1000 Hz with the HLT and mounting different modules in the Z direction: two standard force modules (SFM) and one low force module (LFM).

A second test has been performed measuring in the X, Y, and Z direction of the CMM to evaluate the effect of the different axes involved.

In Figure 4.13 an example for the acquisition in axial direction is shown.

Figure 4.13. Example of force acquisition in axial direction. In this particular case the probe is composed by an L20D4 stylus (Renishaw code A5000-3603) and a Standard Force module and the acquisition is performed in the Y direction. In the background the Nationa Instrument 9237 module used for the signal conditioning.

The forces have been acquired ten times using the probes listed in Table 4.1 and the results are shown in Figure 4.14. All the three probes tested have similar shapes. In the low speed region, approximately below 2.5 mm/s for the SFMs and 0.9 mm/s for the LFM, there are three damped oscillations with the peak linearly increasing with the measurement speed. The maximum value is always reached 0.01 s after the initial contact between workpiece and stylus ball. This area is the one where the kinematic system is not involved and there is a deformation of the strain gauge system alone.

The second range can be located in between 2.5 mm/s or 0.9 mm/s (SFM and LFM respectively) and 6 mm/s. In this part, the kinematic system defines the maximum force and the value is constant and independent from the measurement speed.

Above this measurement speed other effects increase the maximum force but, as there is no reason to use such high speed, especially in the measurement of delicate parts, the fitting with a theoretical model will not be performed in this area.

In the bottom left of Figure 4.14, also the forces obtained while using a different stylus are presented. The stylus is a ceramic one with an 18 mm diameter hemisphere (Renishaw code A5000-3614) and it has been chosen as it is one of the heaviest stylus that this probe can carry. In particular, it has a mass of 3.18 g while the L20D4 weight 0.41 g. No effect is expected in the 'strain gauge area' as the trigger value is calculated as a difference from the resting condition.

In the 'kinematic area' the weight difference could produce a variation with respect to the L20D4 case of 27 mN that is less than 0.8% for a SFM force and about 2.2% for a SFM. As a result, no difference in terms of shape and values can be seen using different stylus.

The behaviour is similar for the three probes in the strain gauge part. In the kinematic part, instead, the SFMs apply a force of about 3700 mN while the LFM limits the force to 1200 mN.

Table 4.1. Probes tested in Z direction. In grey, the different measurement speeds applied.

Probe	Stylus	Measurement speed [mm/s]																
		0.2	0.3	0.4	0.5	0.6	0.8	1	1.5	2	2.5	3	3.5	4	5	6	8	10
948J48 SFM	L20D4																	
948J48 SFM	L0D18																	
0185L4 SFM	L20D4																	
948Q66 LFM	L20D4																	

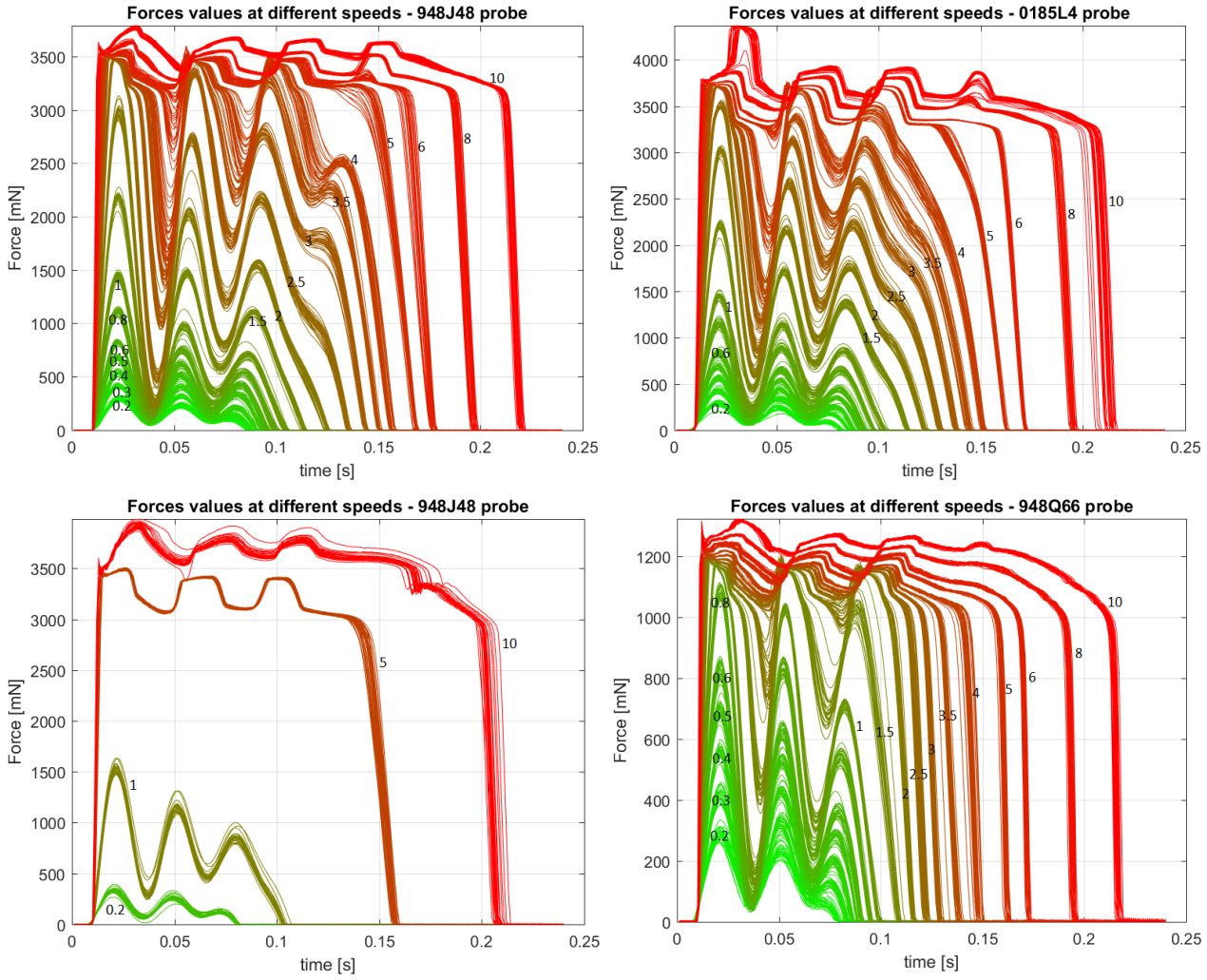

Figure 4.14. Forces at different speed. Top: SFMs with L20D4 stylus. Bottom left: SFM with L0D18 stylus. Bottom right: LFM with L20D4 stylus. Some of the measurement speeds are shown in the graphs in mm/s.

The curves have been fitted with two lines. The first one can be modelled with a linear equation passing through zero and describes the strain gauge part. Its slope is equal to the F_{sgN} value in Equation (3.9). The second one has been fitted with a constant value that can be used, then, to obtain F_{kins} in Equation (3.7).

The obtained results are shown in Figure 4.15 while the residuals of the two fittings are plotted in Figure 4.16. The regression model could be improved allowing for an intercept different from zero in the strain gauge part and using a linear equation for the kinematic part. However, as the residual remains at an acceptable level, the fitting equation has been kept as simple as possible.

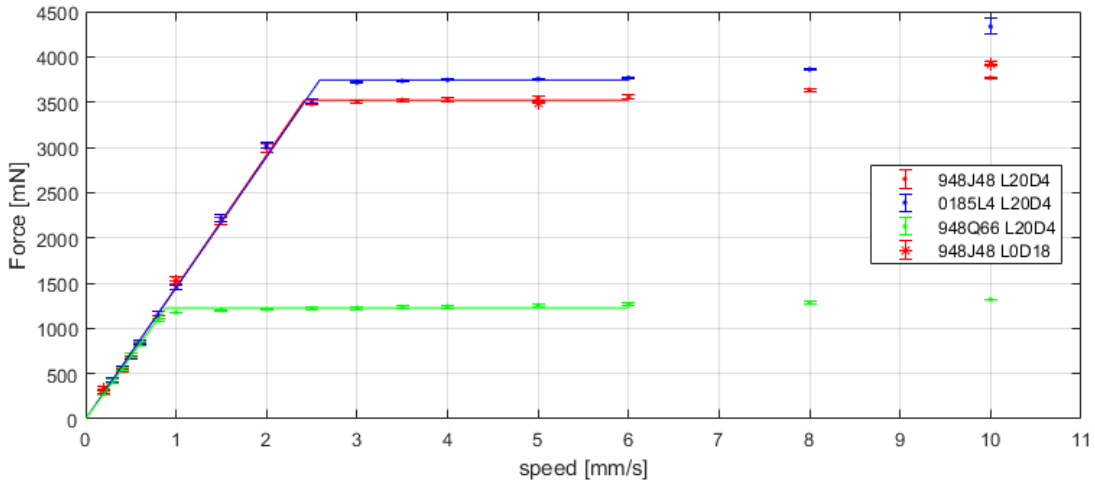

Figure 4.15. Forces in Z direction for different probes and stylus. The small horizontal lines represent the standard deviation of the 10 repetitions. The behaviour of each probe is modelled with two lines: one tilted for low measurement speeds and one horizontal for higher measurement speeds.

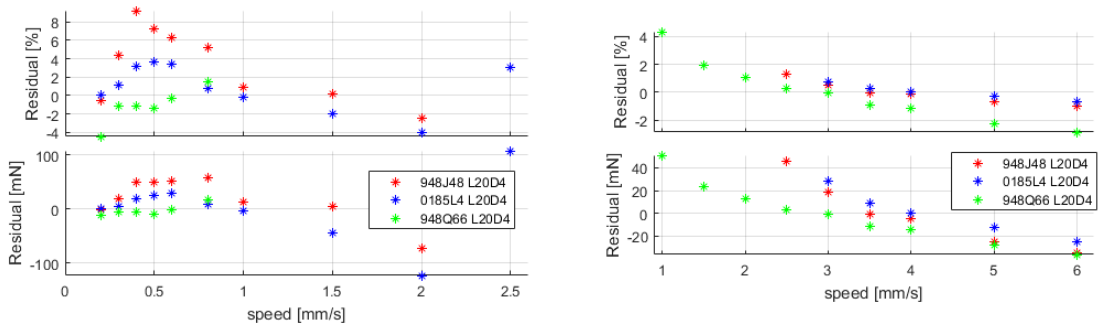

Figure 4.16. Fitting residuals on the tests with different probe. Left: strain gauge part with linear fitting. Right: kinematic part with constant fitting.

The same test has been performed changing the measurement direction. Moving in different directions involve different parts of the CMM with different inertia and different motors. The already presented test in the Z direction involves the movement of the ram only. The measurements in X directions have been performed moving the CMM carriage and the remaining measurement in Y direction have been performed moving the whole bridge.

The measurement speeds tested are shown in Table 4.2. The 0.1 mm/s case failed in two of the three campaign probably due to the slow increase of the contact force that led to frequent false triggering. The results are shown in Figure 4.17 (X and Y direction) and Figure 4.14 (top right for the Z direction).

The shapes in the high-speed region are quite similar and also the maximum values have comparable values. This means that, in this part, the maximum force is solely defined by the kinematic system.

In the low speed region, comprised between 0 and 2.5-3 mm/s, the shape of the contact force varies with the direction of the contact together with the maximum values (that is, again, reached after approximately 0.01 s from the initial contact).

As the relationship between force and speed remain linear it is possible to exclude, at least in a first approximation, the effect of inertia and CMM axes deformation as they should have a quadratic effect due

to the acceleration. Another factor playing against those affect is the measurement in X direction should have been the highest while the measurement in Z direction should have been the lowest.

This variation of the slope can be explained, then, with different behaviour of the motors and the control system used to decelerate the CMM axis after the trigger is activated. For this reason, it is possible to expect small differences in terms of forces while measuring in different locations of the CMM volume.

Table 4.2. Directions tested with the 948J48 SFM and L20D4 stylus. In grey, the different measurement speeds applied.

Direction	Measurement speed [mm/s]																	
	0.1	0.2	0.3	0.4	0.5	0.6	0.8	1	1.5	2	2.5	3	3.5	4	5	6	8	10
X																		
Y																		
Z																		

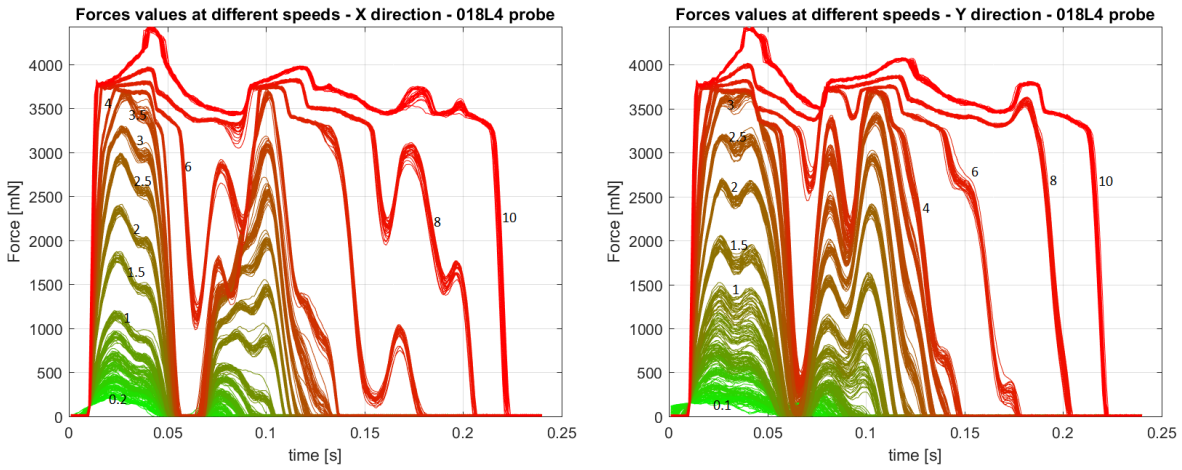

Figure 4.17. Forces with different measuring direction obtained with a SFM and a L20D4 stylus. Left: X direction (carriage moved). Right: Y direction (bridge moved). Some of the measurement speeds are shown in the graphs in mm/s.

As in the previous case, the curves have been fitted with two lines. The results are shown in Figure 4.18 and the fitting residuals are highlighted in Figure 4.19.

The value at 0.1 mm/s is higher than expected (213 mN instead of the 130 mN predicted by the linear model) as a minimum contact force should be reached to trigger the probe.

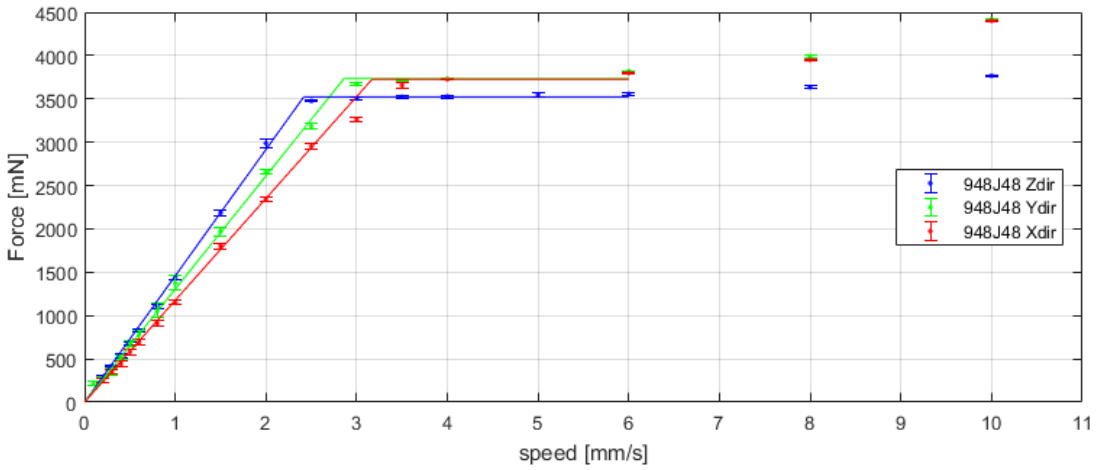

Figure 4.18. Forces with a SFM for different measurement directions. The small horizontal lines represent the standard deviation of the 10 repetitions. The behaviour of each axis is modelled with two lines: one tilted for low measurement speeds and one horizontal for higher measurement speeds.

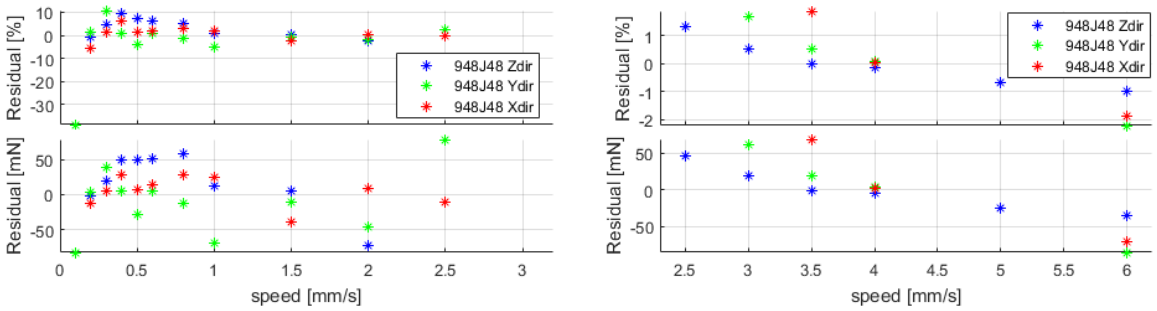

Figure 4.19. Fitting residuals on the tests with different measurement directions. Left: strain gauge part with linear fitting. Right: kinematic part with constant fitting.

The results are summarized in Table 4.3 and in Figure 4.20 (SFMs) and Figure 4.21 (LFM). For the extrapolation of the missing slopes (strain gauge case) the same percentage change seen in the 948J48 SFM has been applied has been applied.

The same procedure has been applied for the 0185L4 SFM average value in the kinematic case while for the LFM both a percentage change and a value change has been applied. The actual forces of the LFM in this range will be probably included in between those values.

The average and the slope values will be used as F_{kins} and F_{sgN} in the formulae (3.7) and (3.9) respectively.

Table 4.3. Fitting parameters obtained by the axial tests. The Deltas represent the difference with respect to the 'standard' case (948J48 in Z direction). The rows with a grey background are the extrapolated values.

		Low measurement speed Strain gauge system			High measurement speed Kinematic system	
Probe	Dir.	Slope [mN/mm*s^{-1}]	Δ 948J48 Zdir [%]	Threshold [mm/s]	Average [mN]	Δ 948J48 Zdir [%]
948J48 SFM	X	1176	- 19%	3.17	3727	+ 6%
	Y	1305	- 10%	2.86	3734	+ 6%
	Z	1458	-	2.42	3523	-
0185L4 SFM	X	~1180	- 19%	3.36	~3970	+ 13%
	Y	~1310	- 10%	3.03	~3970	+ 13%
	Z	1447	- 1%	2.59	3743	+ 6%
948Q66 LFM	X	~1120	- 23%	1.16/1.28	~1300/1430	- 63% / - 59%
	Y	~1240	- 15%	1.05/1.16	~1300/1440	- 63% / - 59%
	Z	1379	- 5%	0.89	1226	- 65%

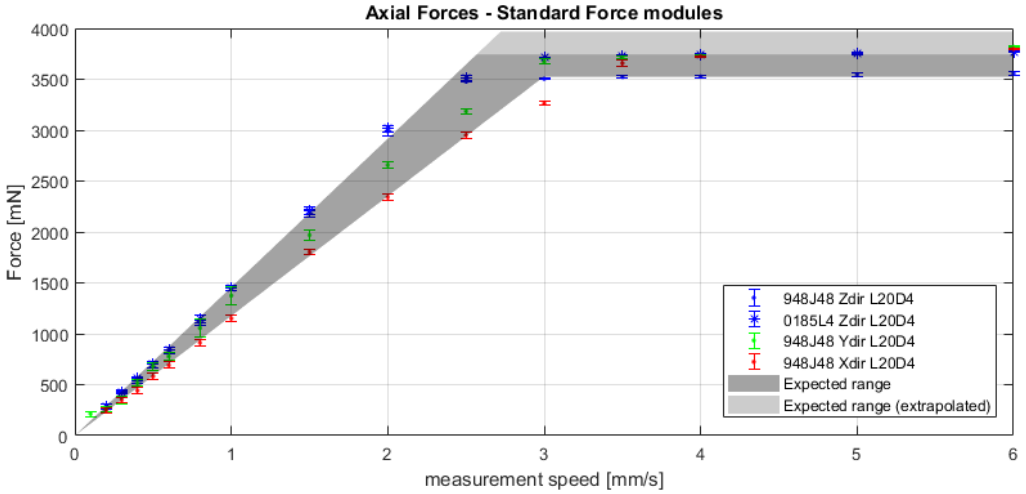

Figure 4.20. Axial forces with different directions and different SFMs. In dark grey the area included in the maximum and minimum fitting lines. In light grey the area including the expected values of 0185L4 measured in X and Y direction.

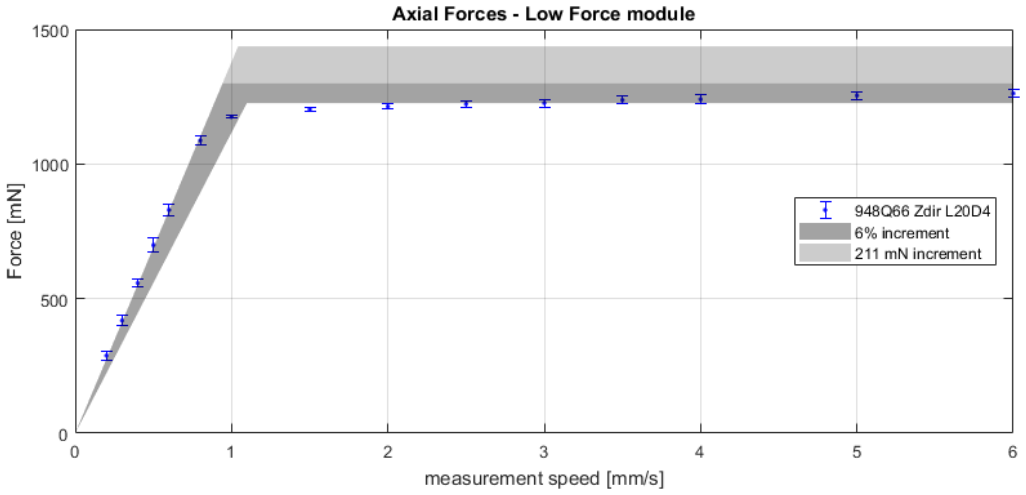

Figure 4.21. Axial forces for the LFM. In grey the area including the expected values if measured in X and Y direction assuming a 6% increment (dark) or a 211 mN increment (light) in the kinematic zone.

4.4.2 Radial forces

For the radial tests, the forces have been acquired varying different parameters like stylus length, head altitude, head clock, measuring direction, and measuring speed. Due to the large number of parameters, the inhomogeneous behaviour of the system, and the complexity in acquiring certain combination of parameters, only some of the combinations have been studied. The study focused on a single probe (0185L4 SFM) but a few measurements have also been performed with the other modules.

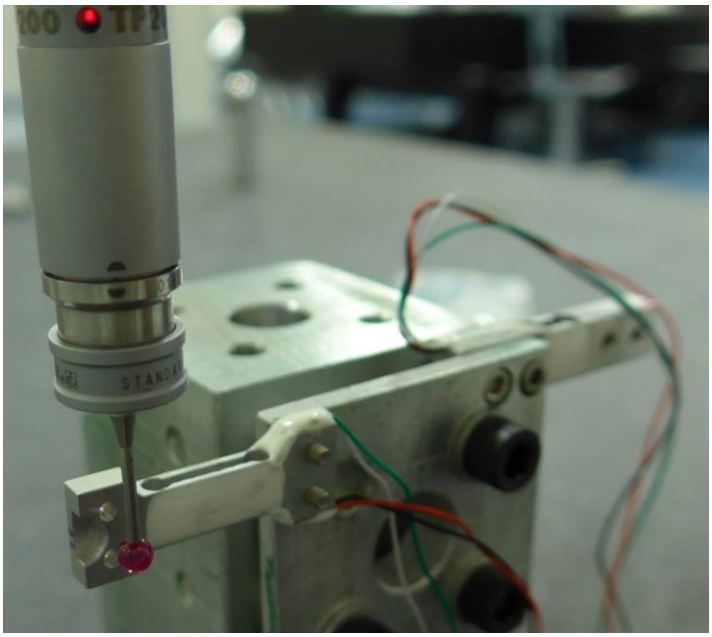

Figure 4.22. Example of force acquisition in radial direction. In this particular case the probe is composed by an L20D4 stylus (Renishaw code A5000-3603) and a Standard Force module and the acquisition is performed in the Y direction with both the altitude and clock axes set to 0.

The first series of tests have been performed with the altitude axis at 0 (see Figure 4.22) and measuring in the X direction of the CMM. In addition to the ones already presented in the previous sections, also the L50D4 (Renishaw code A-5003-0045) and the L100D6 (Renishaw code A-5003-2291) styli have been tested.

To keep the testing time under control, each measurement has been repeated 5 times only.

Table 4.4. Probes and stylus used for the radial forces tests made at zero altitude. In grey, the different measurement speeds applied.

Probe	Stylus	Measurement speed [mm/s]													
		0.3	0.5	0.6	1.0	1.5	2	2.5	3	3.5	4	4.5	5	5.5	6
948J48 SFM	L20D4		■		■	■	■	■	■	■	■	■			
948Q66 LFM	L20D4	■		■											
948J48 SFM	L0D18		■		■	■	■	■	■	■	■				
948J48 SFM	L50D4		■		■	■	■	■	■	■	■	■	■		
948J48 SFM	L100D6		■		■	■	■	■	■	■	■	■	■	■	■

An example of the results is shown in Figure 4.23. On the left the kinematic system is activated for lower forces (β=0° in Figure 4.2) and limits the maximum contact force at high measurement speed. On the right

the contact force, even at high measurement speed, is not enough to activate the kinematic system and the forces are still defined by the strain gauge system. For this reason the forces $F_{TcaseII}$, calculated as in equation (3.4), have never been encountered even for higher measuring speed. As in the axial case, also here the maximum force in the strain gauge area is reached after a fixed amount of time (about 0.02 s).

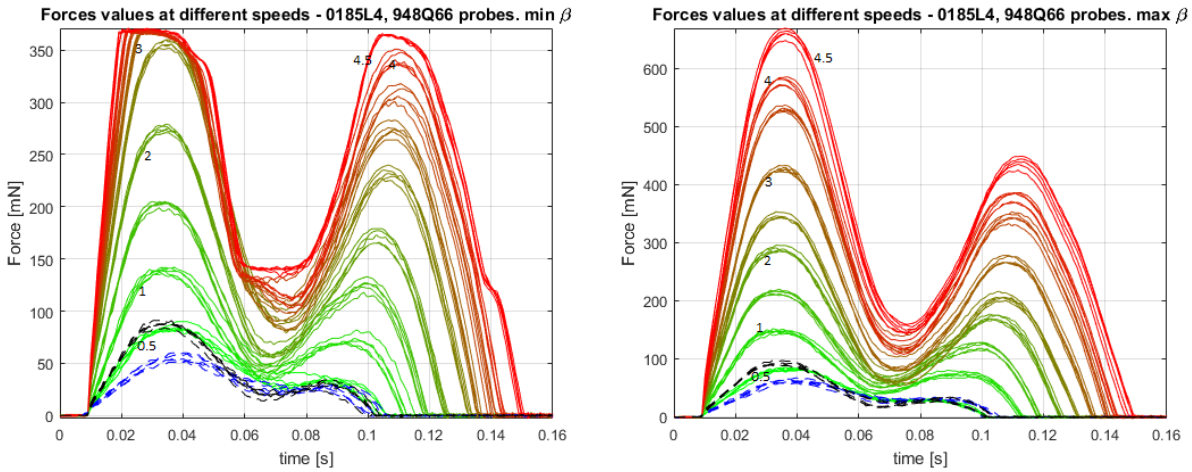

Figure 4.23. Forces with different measuring direction obtained with a SFM (continuous line) and a LFM (dashed line) and a L20D4 stylus. Left: β value with the minimum forces ('min' in Figure 4.24, top right). Right: β value with the maximum forces ('max' in Figure 4.24, top right). Some of the measurement speeds are shown in the graphs in mm/s.

This behaviour can be also seen in Figure 4.24. The most important consideration is that the kinematic system is rarely involved while measuring in radial direction with the SFM. Moreover, a strong anisotropy can be noticed in the trilobe shape while the strain gauge system has an isotropic behaviour with different β values.

The maximum forces described by the strain gauge system are shown in Figure 4.25. The averages and standard deviations have been calculated using the data acquired at all the clock positions. As already noticed in the axial case, at low speed the contact forces foreseen by the regression model underestimate the actual ones. This effect is clearer as the forces involved are smaller and can be seen for measurement speeds of about 0.5 mm/s and below.

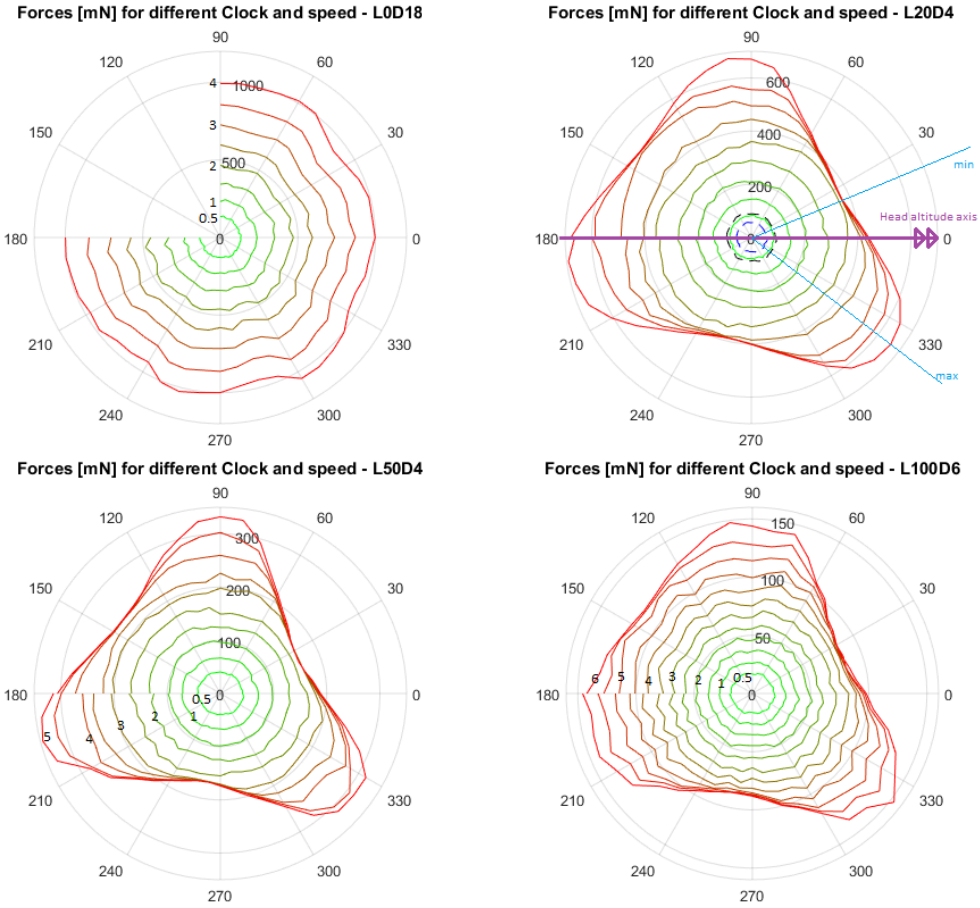

Figure 4.24. Forces for different stylus as presented in Table 4.4. The forces are in mN and the angles in degrees. Some of the measurement speeds are shown near the lines. The purple line indicates the altitude rotation axis of the head.

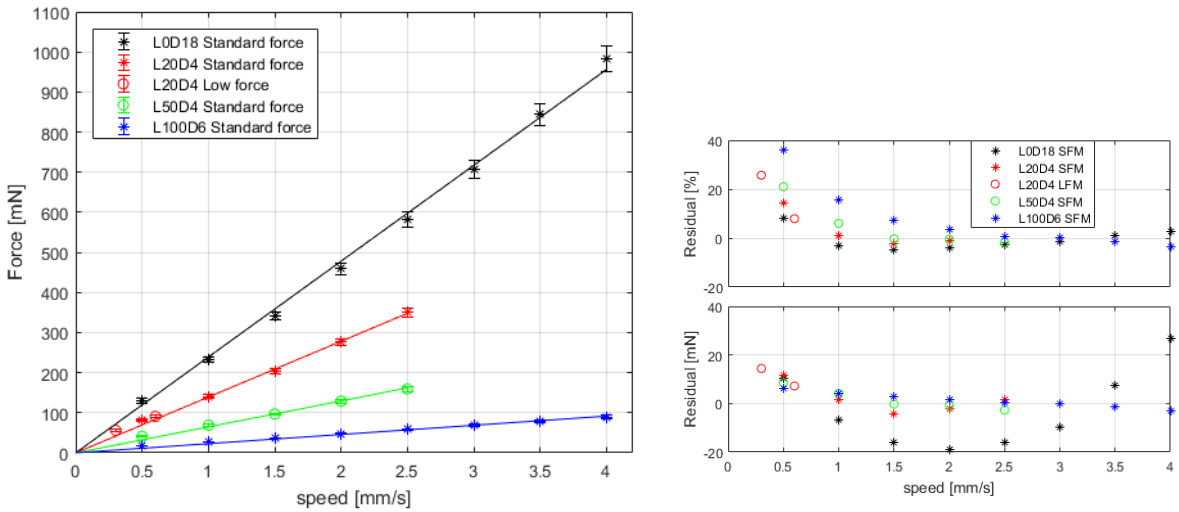

Figure 4.25. Maximum radial forces with the head at zero altitude. Left average and standard deviation of the points acquired at all the clock with a fitting line. Right: Fitting residuals.

A second series of test has been performed with the altitude axis at 90° and moving the ram axis (see Figure 4.25). The Z+ indication means that the axis is moving against the gravity while Z- indicates a movement towards the granite base.

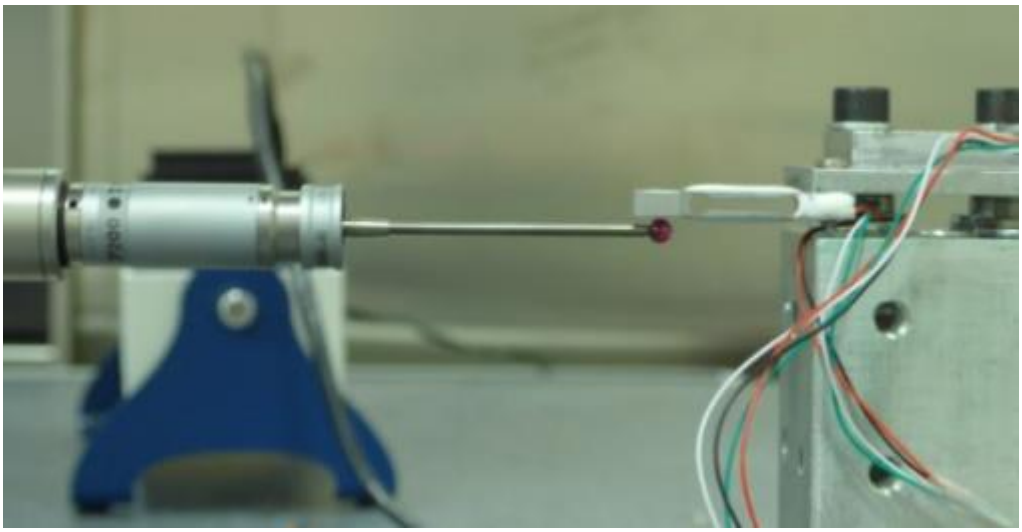

Figure 4.26. Example of force acquisition in radial direction. In this case the probe is composed by an L50D4 stylus (Renishaw code A-5003-0045) and a Standard Force module and both the altitude and clock axis at 90°. The acquisition is performed in the +Z direction meaning that the ram is moving against the gravity.

The test has been performed with three stylus 20, 50 and 100 mm long with a measurement speed ranging between 0.5 and 6 mm/s with 0.5 mm/s steps. Due to the mechanical construction of the system, it was only possible to perform the measurements with a fixed value of β, 90° for Z+ and 270° for Z-. The results are shown in Figure 4.27 for the first two. In Figure 4.28 the test performed with the L100D6 stylus is shown. Only with this stylus a noticeable vibration of the stylus itself at 530 Hz appeared. During this analysis the results have been removed but it is important to notice that this vibration can sensibly increase the maximum force when working at low speeds (e.g. +20% at 1 mm/s). Due to the vibrations of the stylus, the transducer is also excited, this is the reason for the small negative forces plotted on the left in Figure 4.28.

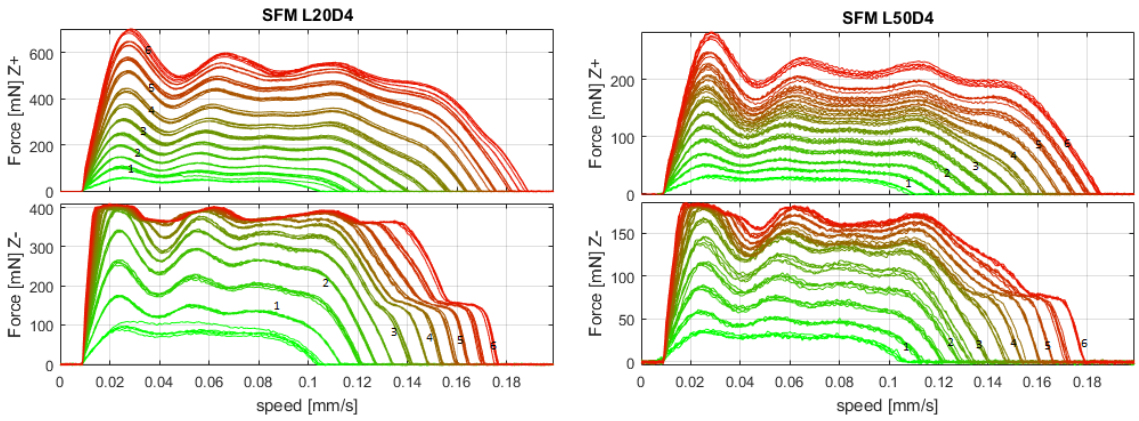

Figure 4.27. Forces with different measuring speed obtained with a SFM probing in Z+ and Z- direction. Left: L20D4 stylus. Right: L50D4 stylus.

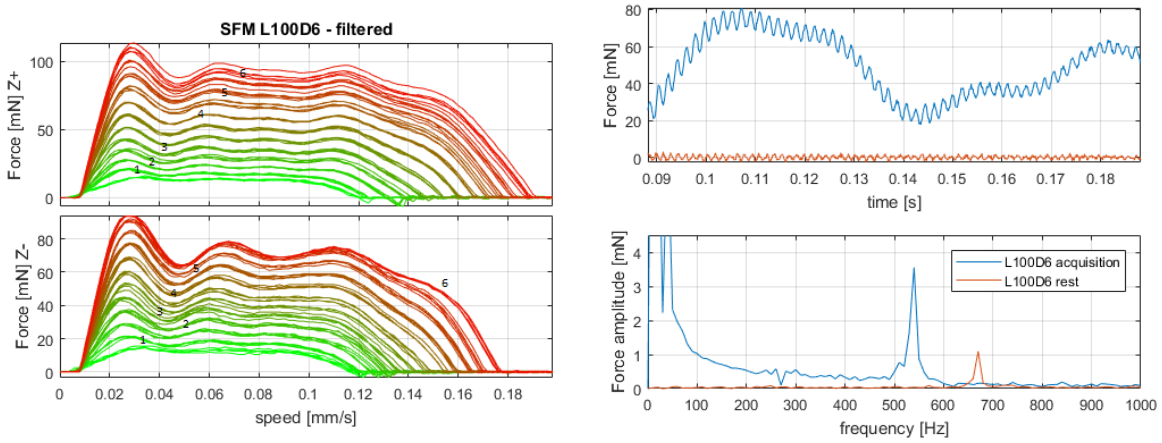

Figure 4.28. Forces with different measuring speed obtained with a SFM and a L100D6 stylus probing in Z+ and Z- direction. Left: filtered results. Right: detail of the unfiltered results and FFT analysis of the signal.

The maximum values in the strain gauge range have been plotted in Figure 4.29. In this case the averages and standard deviations have been calculated using the five repetitions. Also here, at low speed the contact forces foreseen by the regression model underestimate the actual ones.

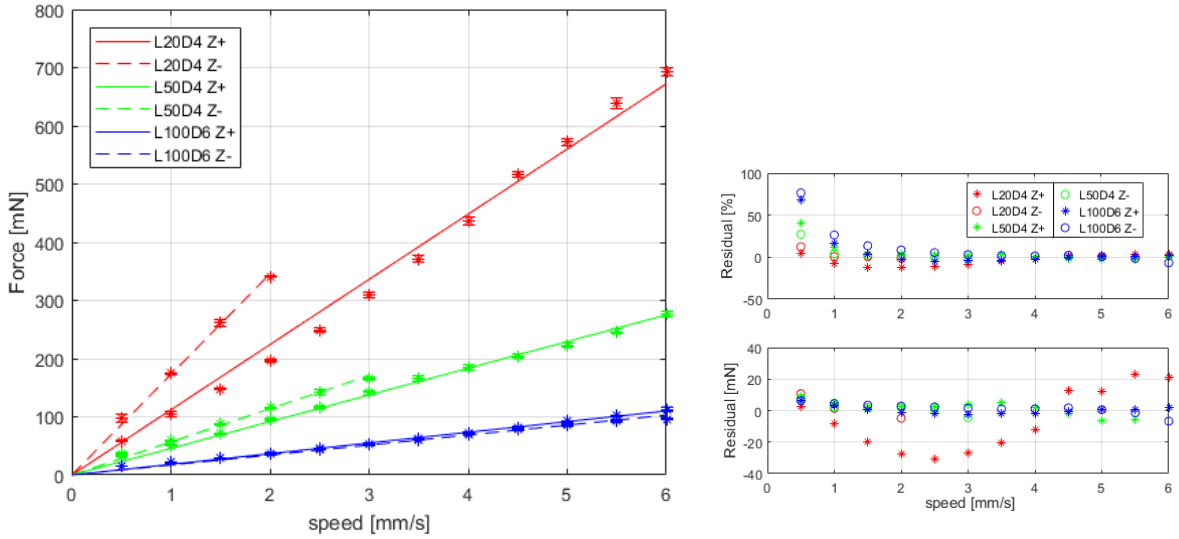

Figure 4.29. Maximum radial forces with the head at 90° altitude. Left average and standard deviation of the points acquired in Z+ and Z- measuring direction with a fitting line. Right: Fitting residuals.

All the slopes obtained by the linear regression analysis are indicated in Table 4.5. The parameters have been calculated using the formula (3.8) modifying the constant value from +1 to -1 like in (3.12). This means that the lateral force acts against the moment generated by the contact force.

$$F_{sgL}=\left(\frac{(L+L_p)}{L_i}+\frac{\mu d_{sph}}{2\,L_i}-1\right)\frac{F_{TsgL}}{v}\ [N] \tag{4.12}$$

The best results have been obtained considering the parameter L_i equal to 12 mm. The coefficient μ has been considered equal to zero due to the quasi-perpendicular contact direction. The length of the stylus has been also corrected adding L_p=2.92 mm in order to include the length internal to the probe (this parameter has been retrieved from the following part).

The value of F_{TsgL}, however, ranges between values of 102 and 221 mN/mm*s^{-1} without any apparent rule. Even if the main factor influencing the contact forces is the length of the stylus, a complete and correct evaluation cannot dismiss the effects due to the CMM motors (variability between vertical and horizontal axes) and, most of all, the electronic system (non-linearity with different stylus lengths).

Some test, not shown in the previous graphs, has also been performed in the Y direction using both the SFM available. Comparing the results obtained, no significant role is played by the probe chosen or by the measurement direction while limited to the horizontal plane.

Despite the low predictability of the value and the consequent need to test every combination of stylus lengths and measuring directions, it is clear that even with short stylus the contact forces can be limited to values below 200 mN in the typical measuring condition. In case the contact force must be limited even accounting for some decrease in the measuring performances it is possible to use the L100D6 stylus who has a maximum overtravel force of 14.9-17.9 mN at a reasonable measuring speed of 0.5 mm/s.

Table 4.5. Fitting parameters obtained by the radial tests in the strain gauge zone. The elements in grey have been obtained by a series of measurements on a single speed.

Module	Stylus	Direction	Slope [mN/mm*s^{-1}]	Slope range [mN/mm*s^{-1} ± %]	F_{TsgL} [mN/mm*s^{-1}]
0185L4 SFM	L0D18	X	239.0		181
0185L4 SFM 948Q66 LFM	L20D4	X	139.2	142.5±21%	127
0185L4 SFM 948J48 SFM		Y	143-145		130-131
0185L4 SFM		Z+	112.1		102
		Z-	172.8		157
0185L4 SFM	L50D4	X	64.8	55.3±17%	221
		Z+	45.9		157
		Z-	56.9		194
0185L4 SFM	L100D6	X	22.9	19.8±15%	173
		Y	21.6		164
		Z+	17.9		137
		Z-	16.8		127

The forces generated by the kinematic system in all the possible configurations are more difficult to evaluate without a complex experimental setup. For this reason, the study has been performed only with the stylus vertically oriented. A check has been done, then, with the results obtained with the head at 90° altitude for the only 2 available points: β=90°, corresponding to the contact obtained in the +Z movement, and β=270°, corresponding to the contact obtained in the –Z movement).

The results for the vertically oriented stylus cases have been obtained from the tests already shown in Figure 4.24 and are detailed in Figure 4.30. The maximum forces at the points of minimum (β equal to 22.5°, 142.5°, and 262.5°) are shown together with the values oriented with β equal to 90° and 270°.

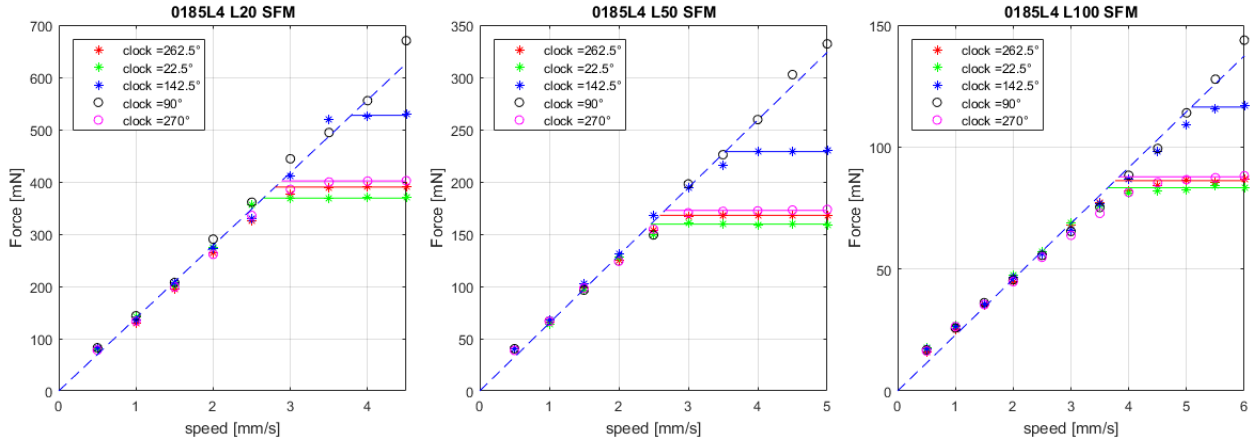

Figure 4.30. Maximum radial forces with the head at 90° altitude for the three styli. The circles are the values obtained with θ of 90° and 270°.

The maximum force as a function of the measuring speed, as in the axial case, reaches a plateau at a certain speed depending on the stylus length and on which of the three kinematic seating have been activated.

With the data obtained, it is possible to estimate the parameters of the equation (3.2) simplified for this particular case:

$$F_{T_{case}I} = \frac{F_s + mg}{(L + L_p)} \frac{d}{2\sqrt{3}} \tag{4.13}$$

where L_p is the length of the stylus included in the probe. The parameter M_f has been also found to be approximately equal to zero and, therefore, has been removed.

The obtained results are summarized in Table 4.6. Some of the values have been calculated starting from the measurement obtained by a single measuring speed (3.5 mm/s) and a similar angle (respectively 30°, 150°, and 255° instead of 22.5°, 142.5°, and 262.5°).

The best results have been obtained considering μ equal to zero (quasi-perpendicular contact) and L_p=2.92 mm. The three distances between the kinematic seats have been calculated for the three probes and the theoretical model shows similar values for different stylus length and measuring directions.

Table 4.6. Fitting parameters obtained by the radial tests in the kinematic zone. The elements in grey have been obtained by a series of measurements on a single speed and a similar clock with Y as measuring direction.

Clock [°]	Probe	Direction	Stylus	F_{Tcasel} [mN]	m*g [mN]	d [mm]
262.5	0185L4 SFM	X	L20D4	390.1	5.7	7.79
	0185L4 SFM	Y		390.2		7.79
	948J48 SFM	Y		369.0		7.83
	948Q66 LFM	Y		134.2		7.72
	0185L4 SFM	X	L50D4	167.9	24.0	7.71
	0185L4 SFM	X	L100D6	86.2	17.6	7.71
22.5	0185L4 SFM	X	L20D4	368.9	5.7	7.37
	948J48 SFM	Y		417.0		8.85
	948Q66 LFM	Y		120.7		6.94
	0185L4 SFM	X	L50D4	159.5	24.0	7.32
	0185L4 SFM	X	L100D6	83.3	17.6	7.45
142.5	0185L4 SFM	X	L20D4	527.4	5.7	10.53
	948J48 SFM	Y		427.1		9.07
	948Q66 LFM	Y		151.6		8.72
	0185L4 SFM	X	L50D4	229.0	24.0	10.51
	0185L4 SFM	X	L100D6	116.4	17.6	10.41

The results obtained while measuring radially with β=270° have been plotted in Figure 4.31. As expected, the maximum forces in the high-speed zone increased, as the kinematic system must counteract also the moment generated by the stylus itself.

The increase of the force is equal to 1.4%, 6.4%, and 9.5% for the stylus L20D4, L50D4 and L100D6 respectively. Considering a constant value of F_{kin} and calculating the parameter 's' considering the equivalent load of the stylus (concentrated ruby mass + uniformly distributed mass of the stem) the expected increase are 0.6%, 7.1% and 13%. The main difference between the percentages in the D100D6 case can be explained by the fact that most of the stem's weight in concentrated near the probe.

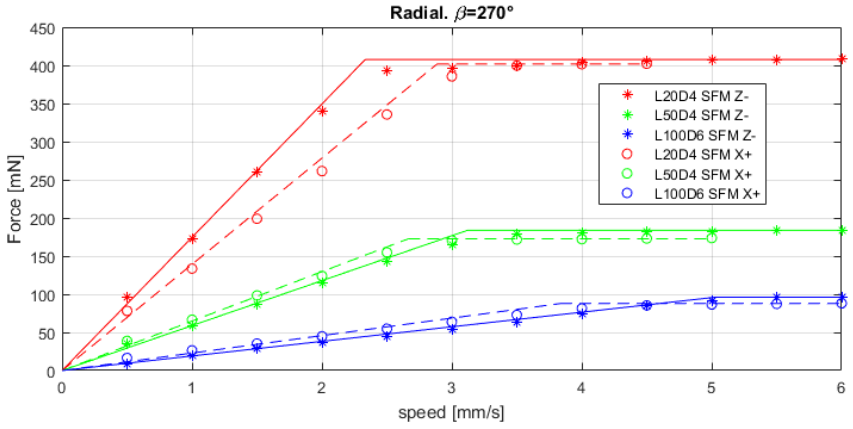

Figure 4.31. Maximum radial forces for the three styli with β=270°. The circles (dashed lines) are the values obtained with head in vertical direction and moving the CMM carriage while the asterisks represent the ones obtained with the head in horizontal direction and moving the CMM Z direction (ram moved).

4.4.3 Intermediate cases and comparison with the theoretical model

As all the parameter needed for the theoretical models have been found in the previous sections (see Table 4.3, Table 4.5, and Table 4.6), a series of tests varying the altitude angle of the head have been performed.

The measurements have been done moving in Z- direction at different speed with altitude angles between 0° (axial contact) and 97.5° (radial contact) with step of 7.5°. The contact happened at a β value of 270° according to Figure 4.24 and the test has been repeated for the stylus L20D4, L50D4 and L100D6.

All the results are shown in Figure 4.32 and Figure 4.33. In all the cases it is possible to notice 3 main zones:

- a low force corner for quasi radial contacts and low speed
- a plateau for quasi radial contact and high speed
- a high force line for axial contact.

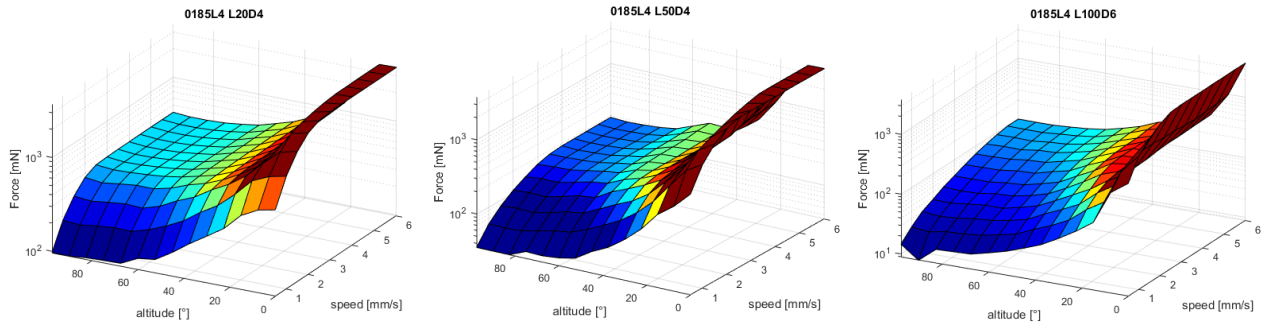

Figure 4.32. 3D view of the forces at different head altitudes and measuring speeds. From left to right: L20D4, L50D4 and L100D6 stylus.

The axial contact zone interests only a small fraction of the measuring directions while for most of the altitudes the contact remains in the radial zone. This effect is more pronounced for longer styli. In the L100D6 case, moreover, the maximum force is almost always defined by the kinematic model.

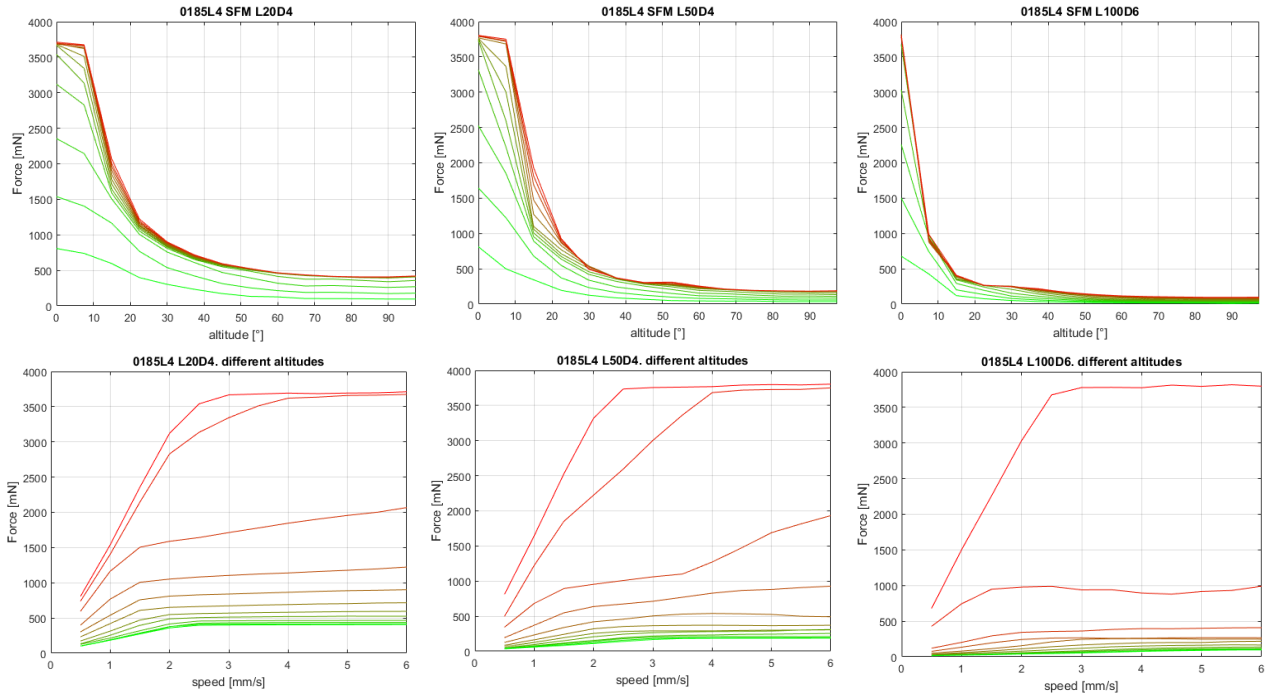

Figure 4.33. Forces at different head altitudes and measuring speeds. Top: colours representing the measuring speed (green is 0.5 mm/s and red is 6 mm/s). Bottom: colours represent different altitudes (green is radial contact, red is axial contact).

The comparison with the theoretical model is shown in Figure 4.34. In the first two plots, the L20D4 stylus is analysed. The theoretical kinematic model has a μ value of 0.16 while for the strain gauge model the value has been kept equal to zero. A good fit of the kinematic model with the experimental values has been found in the whole range even if the μ value has been chose arbitrarily. Also the strain gauge model shows a good match with the experimental values but only in the range 0-7.5° (axial contact) and 52.5-90° (radial contact). In between those two areas the model underestimates the experimental values with a predicted force 40% lower than the actual one in the worst case (altitude 15-22.5°). This error decreases for higher altitudes and is reduced to 22% at 45°.

A similar behaviour can be also found with the L50D4 stylus with higher errors at an altitude of 7.5° where the 'flat' part is smaller than the predicted one. In this case also the kinematic model underestimates the maximum forces at 15° and 22.5°.

With longer styli the underestimation of the theoretical model in the range 7.5°-45° is even stronger while the kinematic model overestimates the size of the flat part. In this case a model considering a μ of 0.08 better fit the obtained results.

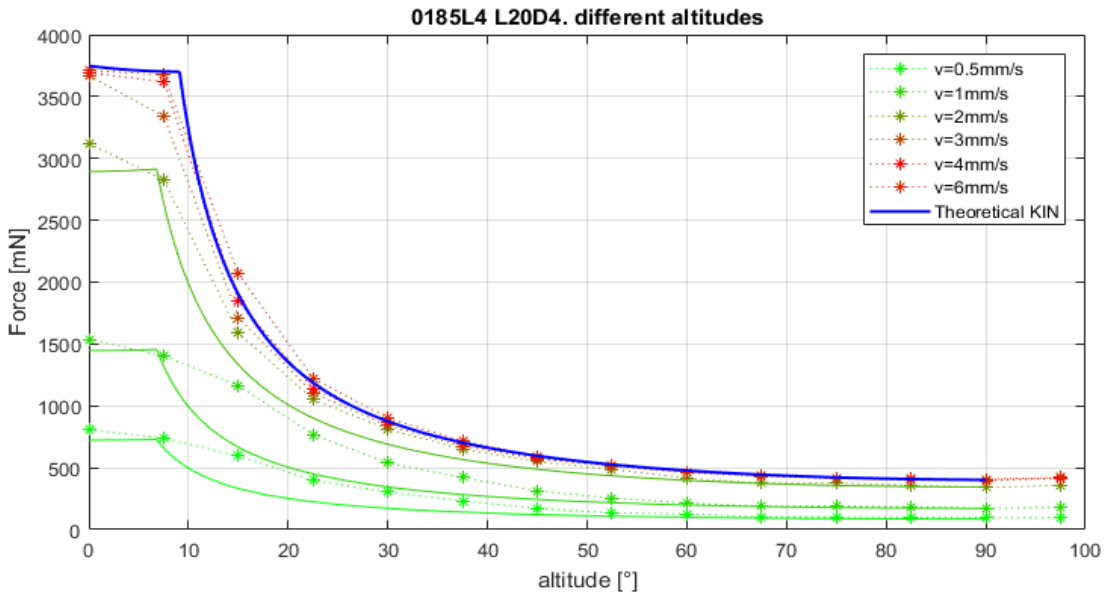
0185L4 L20D4. different altitudes
Force [mN]
altitude [°]
v=0.5mm/s
v=1mm/s
v=2mm/s
v=3mm/s
v=4mm/s
v=6mm/s
Theoretical KIN

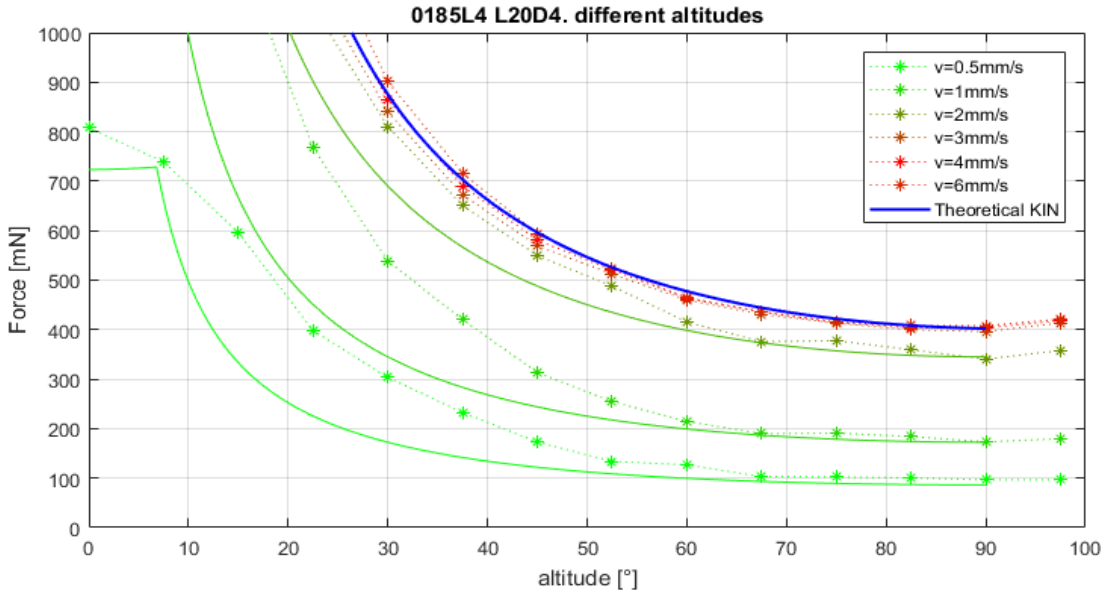
0185L4 L20D4. different altitudes
Force [mN]
altitude [°]
v=0.5mm/s
v=1mm/s
v=2mm/s
v=3mm/s
v=4mm/s
v=6mm/s
Theoretical KIN

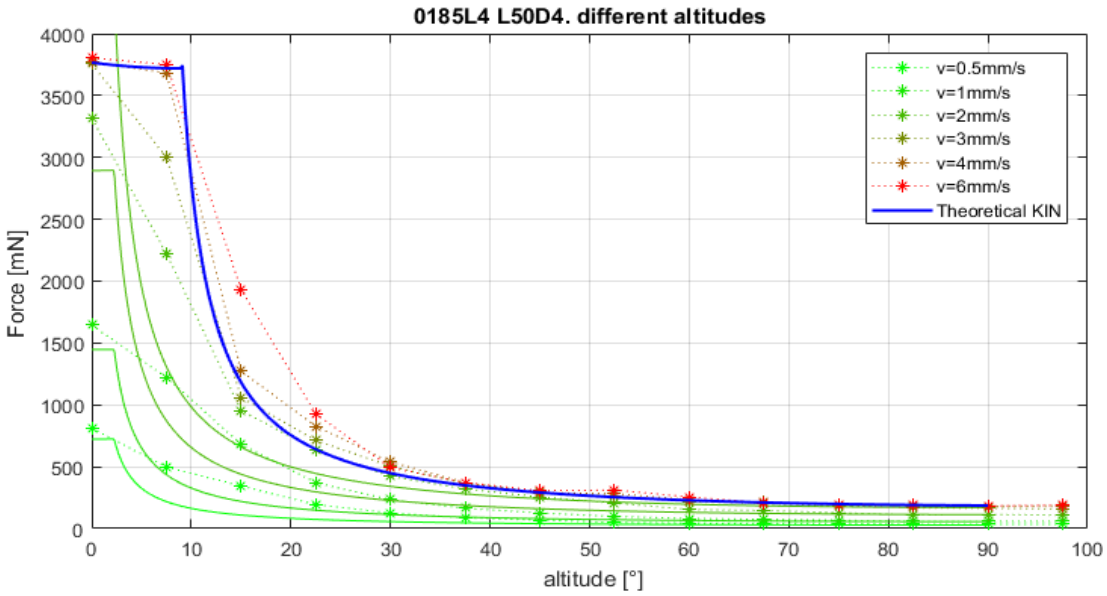
0185L4 L50D4. different altitudes
Force [mN]
altitude [°]
v=0.5mm/s
v=1mm/s
v=2mm/s
v=3mm/s
v=4mm/s
v=6mm/s
Theoretical KIN

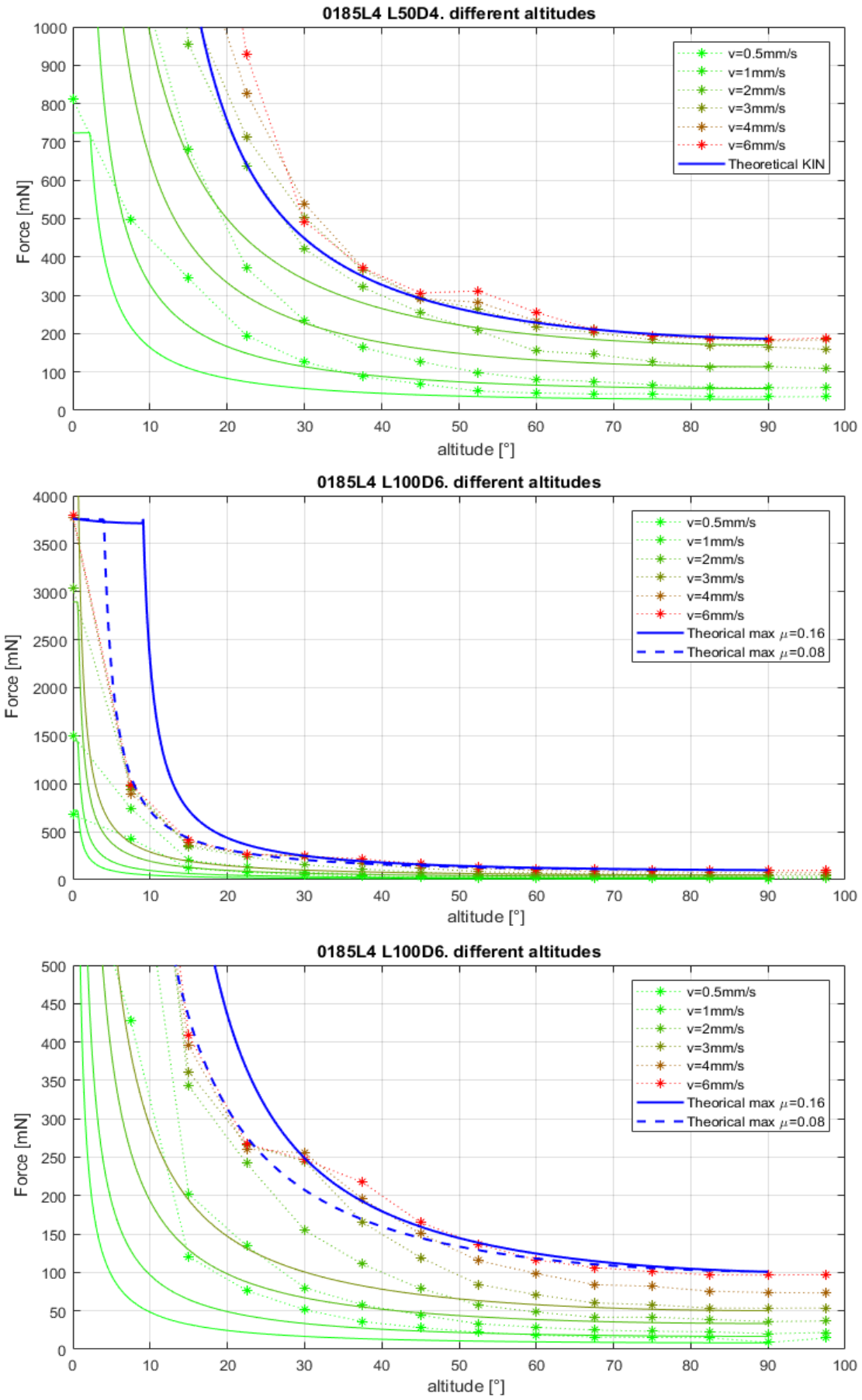

Figure 4.34. Some of the measured speeds (dotted lines) compared to the theoretical model.

4.5 Theoretical model proposed

The strain gauge part proved to be the most difficult one to predict. The parameters used to describe it heavily depend on the moving axis and on the chosen stylus. The equations describing this part are

$$F_{TsgL} = \frac{F_{sgL}}{\left(\frac{(L + L_p)}{L_i} - 1\right)} v\ [N] \tag{4.14}$$

$$F_{TsgN} = \frac{F_{sgN}}{\sin\gamma} v\ [N] \tag{4.15}$$

for the lateral and the axial forces respectively. The maximum value in a certain condition will be defined by the smaller of the two. In Figure 4.35 the forces are shown for different β (0-180°) and γ (0-90°) values. The force (in mN) and the colours are proportional to the distance between each point and the origin. The only the lower part and the top follows the theoretical model. However, those are the most used directions used in a typical measurement. Moreover, due to the independence of the actual values to the gravity and β, if a more accurate force definition is required in the intermediate case, it is straightforward to measure them for a certain altitude, stylus, and measurement direction.

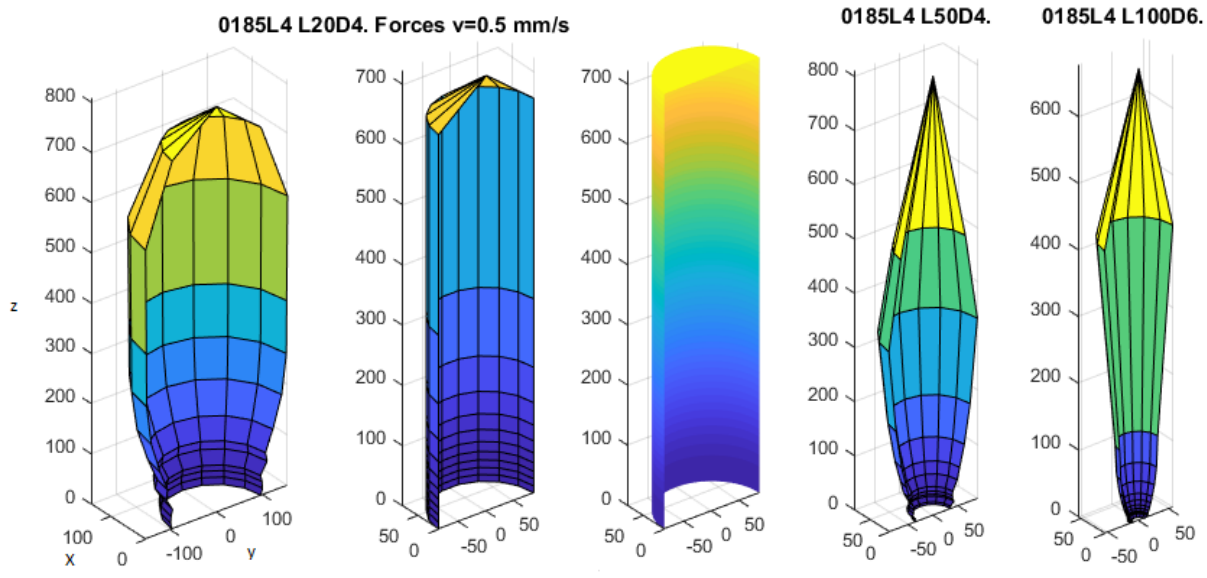

Figure 4.35. 3D plot of the forces in the theoretical and the measured cases (strain gauge system). The rotation around the z-axis represents β while the rotation around a perpendicular axis represents γ. From left to right: experimental L20D4, theoretical model for L20D4 with 7.5° steps, theoretical model for L20D4 with smaller steps, experimental L50D4, experimental L100D6.

The kinematic system is usually involved with the LFM in the radial direction or with the SFM moving at high speed and the equations describing it are

$$F_{TkinL} = \frac{l_2 F_{kins} + mg(s\cos(TP_{clock} - \beta)\sin\phi + l_2\cos\phi)}{\left((L + L_p + \mu l_2)\cos\gamma + (l_2 - \mu(L + L_p))\sin\gamma\right)\sqrt{1 - \sin^2\beta\cos^2\gamma}} \quad (4.16)$$

$$F_{TkinN} = \frac{F_{kins} + mg\cos\phi}{\sin\gamma + \mu\cos\gamma} \quad (4.17)$$

In Figure 4.36 the forces in mN are shown for different value of β and γ. The factor μ has almost no effect for altitude value near 0° and 90° while it plays a fundamental role in the intermediate cases. The combination of materials involved during the analysis (ruby and aluminium) has a coefficient of static friction that can be expected to be in between 0.6 and 0.8 ([4.9], [4.10], [4.11]). This is the maximum value that the factor μ can reach; however, the actual relationship between forces normal and tangential to the contact is depending by a number of factors. The main two can be the angle between the surface and the measurement speed vector and the sliding of the stylus ball to the surface due to the geometrical design of the module.

During the analysis, a value between 0.08 (L100D6) and 0.16 (L20D4 and L50D4) proved to give good results and, as the measurements have always been performed with a perfectly normal direction, it can be thought as an intrinsic characteristic of those modules.

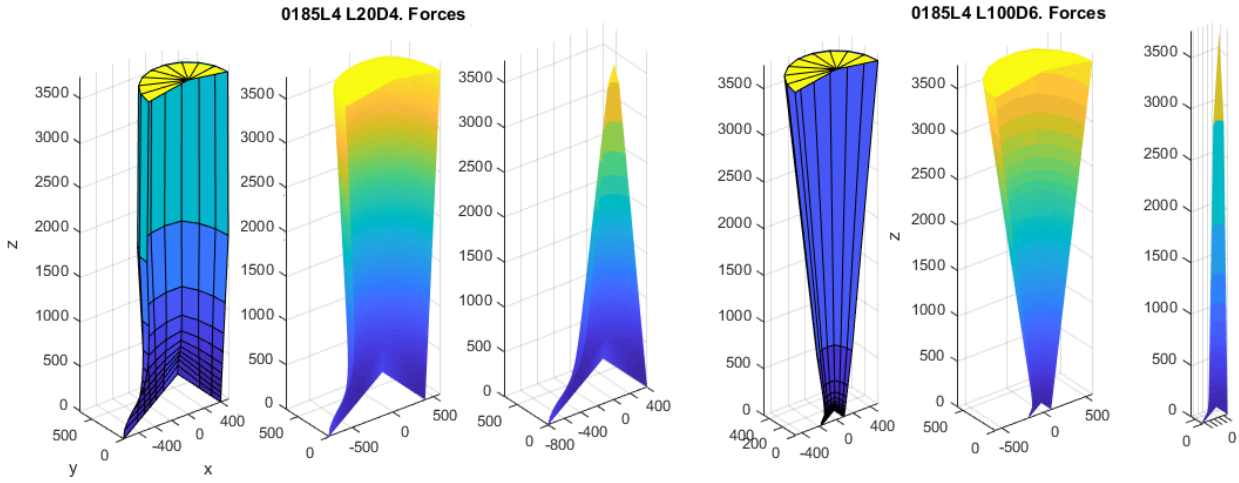

Figure 4.36. 3D plot of the forces in the theoretical cases (kinematic system). The rotation around the z-axis represents β while the rotation around a perpendicular axis represents γ. Left: L20D4 stylus and SFM with 7.5° steps and μ=0.16, smaller steps and μ=0.16, smaller steps and μ=0. Right: same for L100D6.

While measuring a component, it is possible to estimate an effect of the non-perpendicularity between the measurement direction and the surface. In particular, for each degree it can be expected a variation of the factor μ of ±0.087 depending on the direction of the angle itself.

Another interesting result is the effect due to the gravity (Figure 4.37). The gravity vector is applied at β=352.5° as found by the analysis and the expected forces considering the vertical (ϕ=0°) and the horizontal (ϕ=90°) orientation of the probe are considered.

The gravity plays a small effect for a SFM while it is important in case a LFM is used. As a matter of fact, stylus with a stem of 100 mm as the one shown or stylus with a stem of 50 mm with a stem not made of carbon fibre, can only be used in the vertical direction.

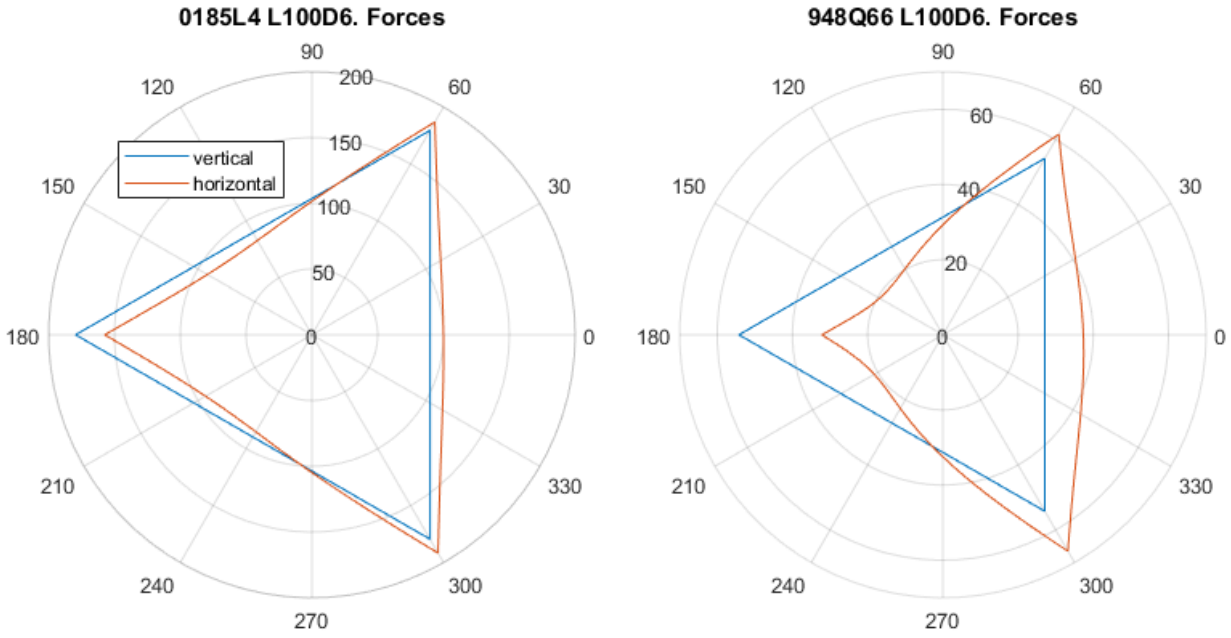

Figure 4.37. Gravity effect on a L100D6 stylus. Left: SFM. Right:LFM.

The actual force diagrams can be obtained considering both the kinematic and the strain gauge systems together. Two examples of the results are shown in Figure 4.38 and Figure 4.39. As expected the forces for a LFM are mainly defined by the kinematic system while for a SFM the involvement of the two systems widely vary with the measurement speed and the approach direction. On the other hand, a similar graph with a longer stylus will show the radial forces as only defined by the strain gauge system.

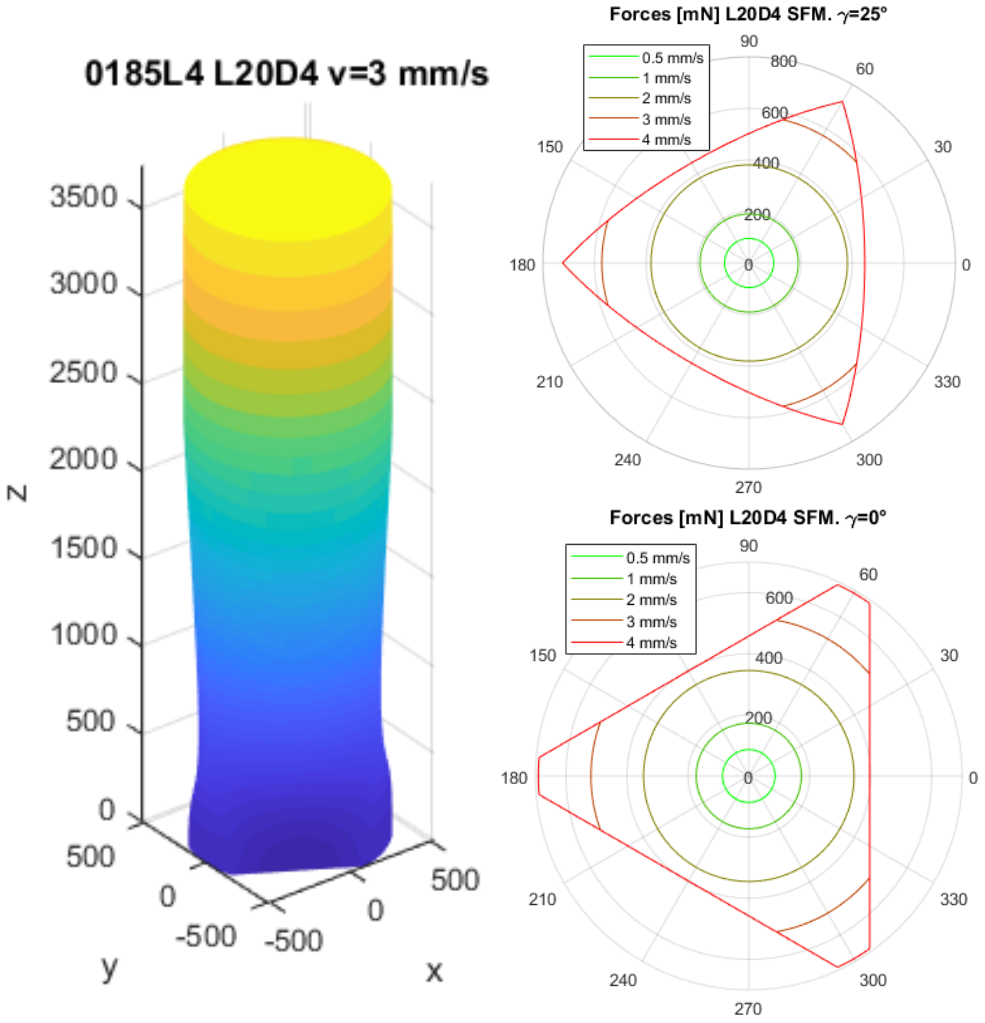

Figure 4.38. Simulated behaviour of a SFM with an L20D4 stylus. Left: the 3D graph of the forces at 3 mm/s. Right: forces at γ=25° and γ=0° for different speeds.

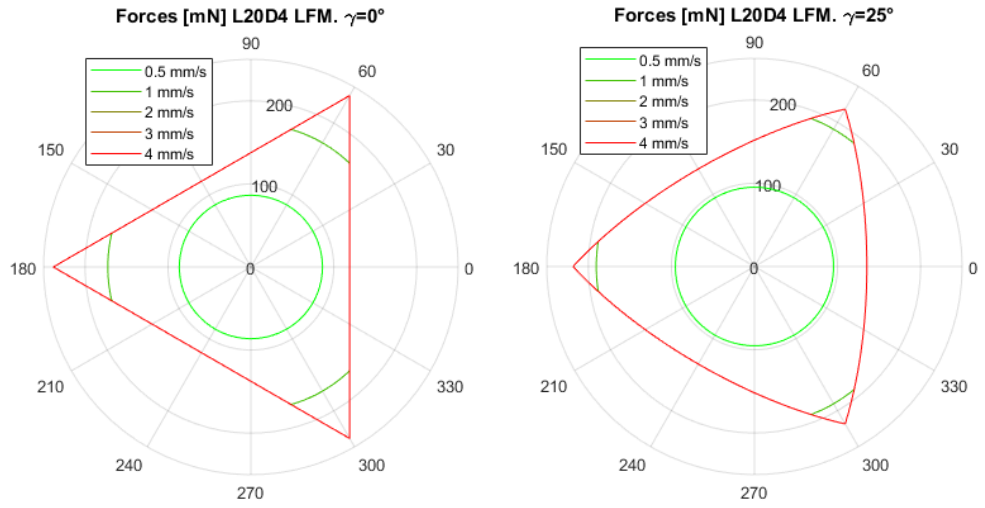

Figure 4.39. Simulated behaviour of a LFM with an L20D4 stylus. Left: forces at γ=0°. Right: forces at γ=0° for different speeds.

4.6 AACMM and Laser Tracker results

Manually operating measuring machines are not usually used to acquire points on optical surfaces. However, in some particular cases, this operation could be unavoidable. For this reason, the forces obtained measuring with an AACMM and a Laser Tracker has been evaluated.

The AACMM used is a Faro Arm edge with a 2 mm or 6 mm diameter ceramic probe (see Figure 4.40). This instrument, due to its portability, can be useful for on field operations on measuring small volumes or for fast measurements.

The Laser tracker Vantage, instead, uses Spherical Mirror Retroreflectors (SMRs) made of a steel sphere of 0.5 inch or 1.5 inch diameter (see Figure 4.40). Its main advantage is the capability to measure elements on large distances. This is due to the capability to measure elements located up to 60 m from where it is located.

Figure 4.40. Manually operated measuring machines. Left: AACMM and a detail of the probe. Right: Laser tracker vantage and an SMR.

The forces have been acquired with the same measuring setup as the CMM ones. Due to the electrical noise (50Hz disturbance), the maximum values obtained in the initial peak (impact) have an uncertainty of ±50mN (noise amplitude). This disturbance cannot be removed after the acquisition without distorting the impact signal while for the evaluation of the maximum forces a simple moving average of 500 points (final frequency 20 Hz) can remove this disturbance.

Due to the nature of the measuring operation, the results are strongly dependent on the manual skills of the operator, the position of the workpiece with respect to the instrument, the operator and the gravity and, most of all, the tiredness of the operator. For the last reason a limited number of points, between 25 and 55, have been acquired.

The AACMM acquisition has been performed with both the 2 mm and the 6 mm probe. As expected, no differences between the two have been found.

In Figure 4.41, four examples of acquisitions are shown. In the first two, the AACMM head was held with two hands while in the third an external support was used to unload the weight of the AACMM head. The last one has been performed dragging the AACMM head on the surface for a continuous acquisition.

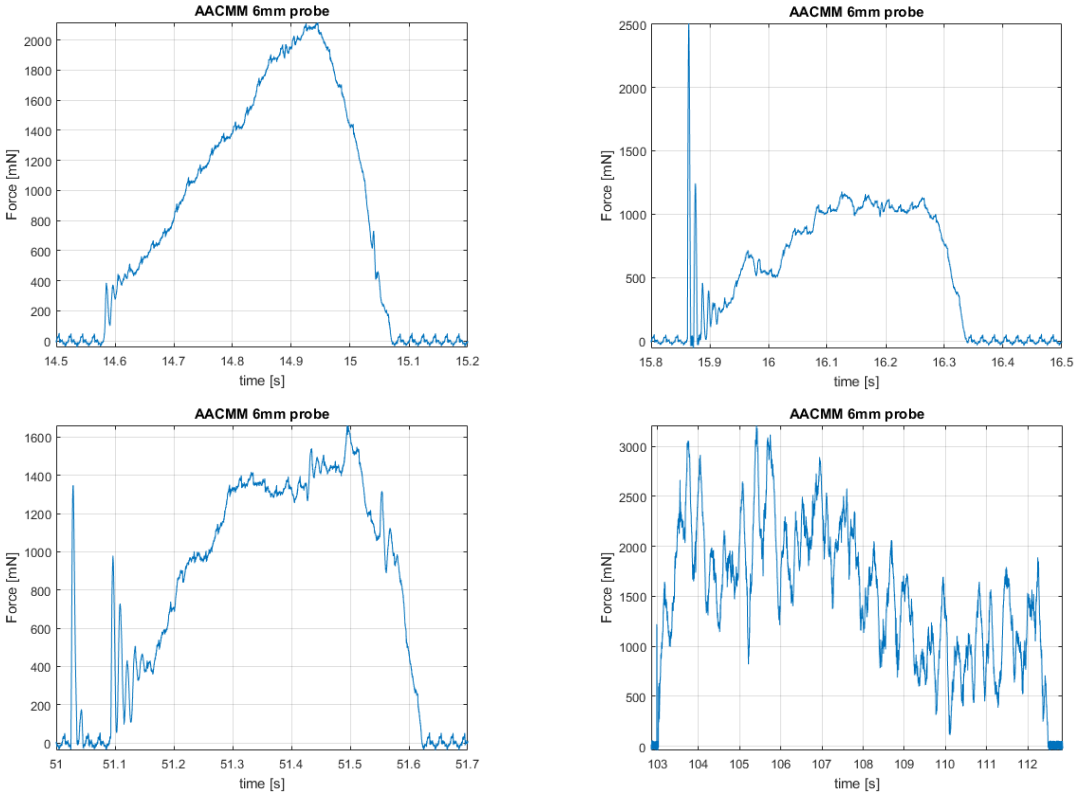

Figure 4.41. Four examples of acquisition with AACMM. Top: single points acquisitions without external support (acquisition time 0.7 s). Bottom left: single point acquisition with external support (acquisition time 0.7 s). Bottom right: continuous acquisition (acquisition time 10 s).

The contact forces of the Laser Tracker have been acquired using both the available SMRs. In Figure 4.42, some typical force profile is shown. With the small SMR, no impact force has been noticed and the signal shown is the filtered one.

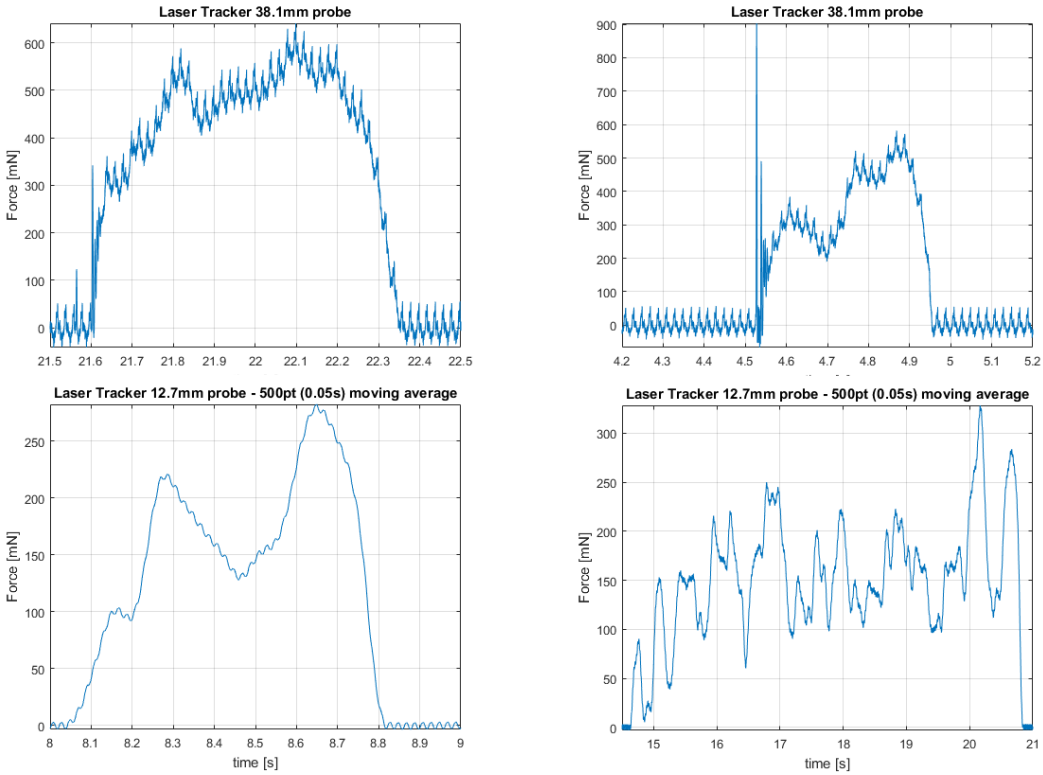

Figure 4.42 Four examples of acquisition with Laser Tracker. Top: single points acquisitions with 1.5" SMR (acquisition time 1 s). Bottom left: single point acquisition 0.5" SMR (acquisition time 1 s). Bottom right: continuous acquisition with 0.5" SMR (acquisition time 6.5 s).

In Figure 4.43, all the obtained results have been summarized. The 'impact' bars show the maximum force when approaching the element while the 'measurement' bars show the force value once the contact between probe and specimen is established. 'Maximum' considers the bigger of the two values for each measurement.

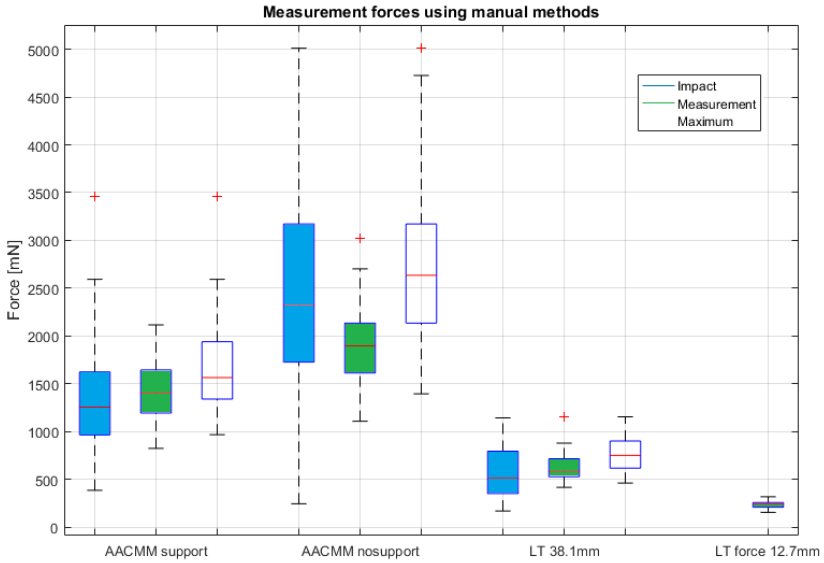

Figure 4.43. Boxplot summarizing the results f the AACMM and Laser tracker acquisitions.

The AACMM forces when measuring using an external support to unload the weight of the AACMM head. In this case, the maximum forces values are around 1 and 2.5N. If no support is foreseen, the maximum forces are more scattered and range between 1.5 and 4.5N.

Due to the smaller mass of the SMR and its simple manoeuvrability, the laser tracker values, instead, have maximum forces values around 0.5-1.2N for the 1.5" one and 0.15-0.35N for the 0.5".

Even if in some case the maximum values can be lower than the ones obtained with an automatic CMM, it must be remembered that such measurements are more prone to errors. Moreover, because of the vibration of the operator's arm, the damage due to the sliding of the probe is higher and extended to a larger area.

4.7 Conclusion and future improvements

Two theoretical models for the estimation of the normal force generated by the contact have been proposed. Direct measurements of the contact forces, then, have been evaluated for the most interesting cases. Those values have been used both to improve the knowledge of the system and to evaluate the parameters of the theoretical models.

The first of the two models deals with the forces generated by the strain gauge system. This condition usually applies to SFMs when the measurement speeds are limited or for longer styli when the force is applied perpendicularly to the stylus direction. Due to the limited knowledge of the mechanical construction of the probing system and of the electronic and control system of the stage, no general rule for different parameters (e.g. stylus length) has been found. Moreover, the model gives a sufficiently good estimation of the forces only for axial contact and for quasi-radial contact (usually in the range between 55° and 97.5°, where 90° is a radial contact).

The results in the most interesting cases, however, have been investigated and, due to the good linearity of the system, it has been proven sufficient the acquisition of two measurements at low speed (one radial and one axial) to extrapolate its behaviour in a certain condition (stylus and measurement direction) in the most interesting cases of contact direction.

An improvement of the prediction of the strain gauge system's behaviour could consist in the development of a model not related to the physical construction of the system itself.

The second model has been derived by literature and improved. This model well describes the behaviour of SFMs at high speed and LFMs in all the measurement conditions.

As in the previous case, also the parameters of this model can be derived by two measurements or, considering the mechanical construction of the probe approximately constant, even by a single measurement in axial direction. All the remaining parameters like TP_{clock} and the stylus properties can be measured or derived by the datasheet values.

The results of the model proposed, however, are extremely dependent on the value of the coefficient μ. A reasonable number well describing the obtained results has been found. In order to evaluate the correctness of the assumptions done on this coefficient, a number of tests done with a zero and a controlled value of the coefficient of friction could be done.

Also the effect on the μ value of the non-perpendicular direction between workpiece surface and the measurement direction could be interest to evaluate. Finally, the repetition of the measurements using a multi axial force transducer will surely increase the level of understanding of the system.

During the tests, it has been observed a variation of more than two order of magnitude of the forces as a function of different parameters. Those parameters can be used to reduce the contact forces on the most critical optical elements. However, it must be considered that the lowest values can be obtained only with longer styli, making the measurements less accurate as shown in chapter 3. Therefore, a trade-off between accuracy and force could be required.

As a last test, the forces applied while using alternative measuring systems like an AACMM and a Laser Tracker have been acquired. The knowledge of those values can be useful in the specific cases when the acquisitions of the optical surfaces with those systems are needed.

4.8 References

[4.1] Weckenmann A, Estler T, Peggs G, McMurtry D. Probing systems in dimensional metrology. CIRP Annals-Manufacturing Technology. 2004 Jan 1;53(2):657-84.

[4.2] Cauchick-Miguel PA, King TG. Factors which influence CMM touch trigger probe performance. International Journal of Machine Tools and Manufacture. 1998 Mar 1;38(4):363-74.

[4.3] Estler WT, Phillips SD, Borchardt B, Hopp T, Witzgall C, Levenson M, Eberhardt K, McClain M, Shen Y, Zhang X. Error compensation for CMM touch trigger probes. Precision Engineering. 1996 Oct 1;19(2-3):85-97.

[4.4] Woźniak A, Dobosz M. Metrological feasibilities of CMM touch trigger probes. Part I: 3D theoretical model of probe pretravel. Measurement. 2003 Dec 1;34(4):273-86.

[4.5] Dobosz M, Woźniak A. Metrological feasibilities of CMM touch trigger probes: Part II: Experimental verification of the 3D theoretical model of probe pretravel. Measurement. 2003 Dec 1;34(4):287-99.

[4.6] Bos EJ. Aspects of tactile probing on the micro scale. Precision engineering. 2011 Apr 1;35(2):228-40.

[4.7] Van Vliet WP, Schellekens PH. Accuracy limitations of fast mechanical probing. CIRP annals. 1996 Jan 1;45(1):483-7.

[4.8] Meli F, Küng A. AFM investigation on surface damage caused by mechanical probing with small ruby spheres. Measurement Science and Technology. 2007 Jan 12;18(2):496.

[4.9] Buckley DH. Friction characteristics of single-crystal and polycrystalline aluminum oxide in contact with various metals in vacuum.

[4.10] Sliney HE, DellaCorte C. The friction and wear of ceramic/ceramic and ceramic/metal combinations in sliding contact.

[4.11] Davis JR. Concise metals engineering data book. ASM international; 1997.

5 Contact damage on optical elements due to CMMs stylus contact

5.1 Introduction

As soon as the load applied by the CMM probing system to the optical surface is known, it is possible to evaluate the possible induced damage on the optical surface and keep it under an acceptable level adapting the measurement strategy.

The first important step consists in having a clear understanding on how a surface damage can affect the optical quality of an element. This is also useful to have a criterion for comparison of the measured damages.

Different possible theoretical models used to generalize as much as possible the obtained results will be also presented. Unfortunately, due to different factors, the most complex and complete models could not be applied. For this reason, the tests have been performed on the main families of optical materials and some general rules have been derived.

5.2 Surface damage effects on optical elements

The most straightforward way to classify surfaces damage is using the **scratch and dig specifications** and was introduced in 1945 [5.1]. According to this first proposal, the digs included all the round appearing defects (including bubbles) while scratches included all the elongated defects.

Their evaluations were simply performed comparing the surface under study with a calibrated master and, due to its simplicity became the MIL-O-13830 standard [5.2] in 1954 (revised in 1963 as MIL-O13830A and in 1997 as MIL-PRF-13830B). Several misconceptions arose in the definition of scratch and dig as this was intended as a purely cosmetic standard and little correlation was found between the damage appearance and their size [5.3], even by their original authors. Another military specification, the MIL-C-48497, was created to specify the scratch specifications as physical width for quantitative measurements. Unfortunately, this specification only increased the confusion around this matter.

This ‘loose attitude’ on the problem was justified not only by the lack of scratch/dig measuring systems but also by the fact that little defects on the surfaces often does not usually impact on the performance of a system.

Two exceptions are high-power systems and lenses placed near image planes. In the first ones a small imperfection can increase the energy absorption and damage the element while in the seconds, cosmetic imperfections can be reimaged on a sensor placed on the focal plane. In all the other cases, those defects simply translate in a reduction of the throughput and an increase of the scattered light.

Nowadays the old MIL specifications, even if still in common use, have been replaced by two valid alternatives: the ANSI/OEOSC OP1.002-2017 [5.4] and the ISO 10110-7:2017 [5.5]. Both of them include an evaluation based on the measurement of the damage size and a qualitative visibility specification.

During this analysis, as the CMM is always used in single point mode due to its digital trigger, only the dig definition is of interest.

According to ANSI/OEOSC OP1.002-2017, the dig specifications are defined as in MIL-PRF-13830B for the cosmetic evaluation and as in MIL-C-48497A for the dimensional evaluation. In this second case, a letter is used to specify the maximum size of the dig.

The maximum number of maximum size digs is

$$N = \frac{\emptyset\ [mm]}{20} \tag{5.1}$$

(rounded up) on every surface where Ø is the diameter of the optical element. In addition, the sum of the digs of every dimension must not exceed the value defined by the equation

$$\sum d \leq 2 \times N \times D\ [mm] \tag{5.2}$$

where D is the maximum dig size allowed. The digs with a diameter smaller than a variable value between 0.16 D and 0.29 D, depending on the grade, must not be taken into account into this calculation.

In MIL-PRF-13830B a minimum separation of 1 mm is also required for maximum dig diameters specifications equal or better than 100 µm while the digs to be ignored are the ones with a diameter smaller than 2.5 µm.

According to ISO 10110-7:2017 the maximum permissible surface imperfections must be accounted as 'general imperfections'. For single optical surfaces (5/ symbol), the required indication is

$$5/N_g \times A_g \tag{5.3}$$

where N_g is the maximum number of allowed imperfections and A_g is the square root of the area expressed in millimetres.

To account surfaces imperfections with a smaller grade, the sum of their areas must not exceed

$$\sum \left(\frac{d}{2}\right)^2 \pi \leq N_g \times A_g^2 \tag{5.4}$$

Some interesting properties related to the ISO choice of using only values in the Renard series R5 (a geometric sequence composed by the base 1.00, 1.60 2.50, 4.00, 6.30 repeated after every 10-fold change) are shown in [5.6] together with the inspections methods foreseen.

All the imperfections with a grade number of $0.16A_g$ and below must not be considered. This value is approximately equal to 14% of the maximum acceptable dig diameter.

A comparison between the different standards is presented in Table 5.1. The values in the last column are rounded to the Renard R5 series. The reason is that those numbers are the ones allowed by ISO 10110-7:2017. The column of 'quality' and 'relative cost [%]' are rough indications obtained by an optical manufacturer table.

Table 5.1 Maximum dimension of the dig according to MIL, ANSI, and ISO standards.

Quality	Relative cost [%]	Max dig diameter [μm]	13830B	OP1.002	ISO 10110-7	ISO 10110-7 (Renard R5 series)
		n	n/10	An	$\frac{n}{2}\sqrt{\pi}$	-
Very high	375%	50	5	A	$5/N_g \times 0.044$	$5/N_g \times 0.063$
High	200%	100	10	B	$5/N_g \times 0.089$	$5/N_g \times 0.1$
Moderate	125%	200	20	C	$5/N_g \times 0.18$	$5/N_g \times 0.25$
Low	110%	300	30	D	$5/N_g \times 0.27$	$5/N_g \times 0.4$
		400	40	E	$5/N_g \times 0.35$	$5/N_g \times 0.4$
Very low	100%	500	50	F	$5/N_g \times 0.44$	$5/N_g \times 0.63$
		700	70	G	$5/N_g \times 0.62$	$5/N_g \times 0.63$
		1000	100	H	$5/N_g \times 0.89$	$5/N_g \times 1.0$

A conservative approach to account for the digs created while measuring the surface with the CMM consists in considering the ruined part as completely obscured. With this assumption, the effect will be a reduction in the overall throughput of the system.

An example of this calculation is shown in Table 5.2. Note that the percentage is calculated considering scratches and digs in the worst condition for the specified quality.

Table 5.2 Percent obscured area with different surface diameters according to OP1.002. Scratches and digs values taken by [5.6], digs only values calculated by the author.

	Obscured area [%] - Scratches and digs					**Obscured area [%] - Digs only**				
Diam [mm]	**10**	**20**	**30**	**40**	**50**	**10**	**20**	**30**	**40**	**50**
A-A	0.132	0.033	0.022	0.017	0.013	0.0025	0.00063	0.00056	0.00031	0.00030
B-B	0.275	0.069	0.047	0.034	0.028	0.010	0.003	0.0022	0.0013	0.0012
C-C	0.589	0.147	0.103	0.074	0.061	0.040	0.010	0.0089	0.0050	0.0048
D-D	1.199	0.300	0.210	0.150	0.123	0.090	0.023	0.020	0.011	0.011
E-E	1.848	0.462	0.326	0.231	0.191	0.160	0.040	0.036	0.020	0.019
F-F	2.537	0.634	0.451	0.317	0.264	0.250	0.063	0.056	0.031	0.030
G-G	4.036	1.009	0.727	0.504	0.423	0.490	0.123	0.109	0.061	0.059
H-H						1.000	0.250	0.222	0.125	0.120

Another possible approach to the problem is to consider the **scattering** of the light related to the non-perfect shape of the surface. This phenomenon can be separated in three different regions:

- If the size of the particles is one tenth and below the wavelength of the incident light, the problem can be resolved with the Rayleigh equation.
- If the size is comparable to the wavelength different solutions are possible. In case, the scattering is generated by a homogeneous sphere, a closed for solution is possible with the Mie solution.
- If the particle is at least 10 times than the wavelength, like in this case, the solution can be modelled using the geometric optics laws.

Measuring the scatter of a surface, however, does not distinguish between them and the results will be a superposition of different sources like periodic cusps, one dimensional roughness, isotropic roughness, grain boundaries, scratches, and digs [5.8].

A correlation between the scattering values and the scratch and digs has been tested by [5.9]. In particular, the increase of the Bidirectional Transmittance Distribution Function (BTDF) at 0.57°, called $0.05B_0$, has been calculated while illuminating different portion of two scratch/dig standards from Beale Optical.

In order to have a sufficient variation the measurement has been acquired with a 1 mm diameter beam and the obtained values have been corrected for area or edge scattering and extended over a 20 mm diameter specimen. The first correction considers the BTDF value as related to the dig area and the average illumination over it while the second done relates the scattering to the illumination density at the dig diameter. The results are shown in Figure 5.1 and, as the 'corrected area' values are not constant and the 'corrected edge' values are not inversely proportional to the BTDF, the size of a dig cannot be uniquely compared to the scattering value.

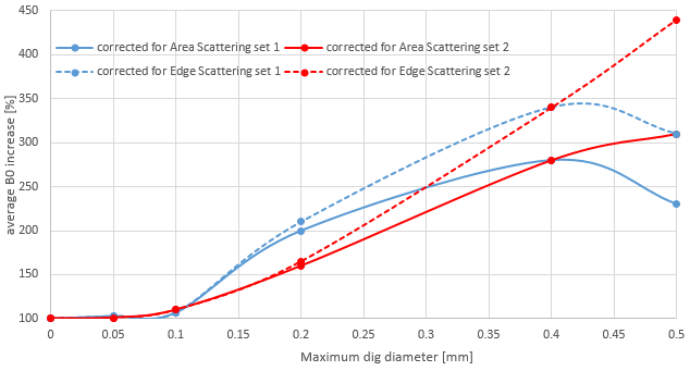

Figure 5.1 BTDF increment in case a dig of a certain diameter is present. Data elaborated from [5.9].

The direct measurement of the scattering for the damage evaluation requires a calibration of the specimen and a good alignment of the scatterometer to the dig created by the CMM. As the damages created could be easily by orders of magnitude smaller than the dig specifications, this approach was not feasible both due to the practical difficulties of the procedure and to the low signal to noise ratio of the expected results.

A simplified approach considers the measurement of the surface and the subsequent calculation of its maximum slope. For small angles it can be calculated as

$$\theta = \frac{4h}{d}\ [rad] \tag{5.5}$$

where h is the depth and d is the diameter of the indentation.

This value can be used, then, to calculate directly the geometrical scattering in reflective elements as

$$\theta_{optR} = 2\frac{4h}{d}\ [rad] \tag{5.6}$$

and, using the Snell's law, in refractive elements as

$$\theta_{optT} = \left(\frac{n-1}{n}\right)\frac{4h}{d}\ [rad] \tag{5.7}$$

where n is the refractive index of the glass.

For an element working in transmission and considering n=1.5 the deviation of the beam will be one sixth than the same element reflecting the light.

In this case, the final result will depend on the characteristics of the rest of the optical elements. As an example, in case the optical element is a window the displacement of the beam will be equal to

$$S_{opt2T} = \left(\frac{n-1}{n}\right) t \frac{4h}{d} \; [mm] \tag{5.8}$$

where t is the window thickness. The angular deviation can be calculated, then, as

$$\theta_{opt2T} = (n-1) \frac{4h}{d} \; [rad] \tag{5.9}$$

In a more general case of a lens, however, a geometrical calculation must be performed case by case considering thickness, RoCs, refractive index, and location of the dig.

This approach has been applied when the damage observed on the specimen had a hemispherical shape. As most of the tests have been performed in materials used for mirrors, the value of θ_{optR} as calculated in (5.6) has been shown. For homogeneity reasons, the same value have been also shown in the materials typically used in transmission only, but its subsequent translation to θ_{optT} is straightforward.

5.3 Damage evaluation in literature and theoretical prediction

5.3.1 Uncoated materials

Using the damage done on a known sample made of aluminium or steel has been used by different authors as an indirect measurement of the applied force (see [5.10] and [5.11]). This operation can be effective for micro-CMM, where the forces are extremely low, and the probing spheres small.

This calculation can be performed considering the Hertzian theory. According to it, the diameter (d_{el}) and the depth (h_{el}) of the indentation between a flat and a spherical surface can be calculated ([5.12]) as

$$\frac{1}{E^*} = \frac{1-\nu_1^2}{E_1} + \frac{1-\nu_2^2}{E_2} \left[\frac{1}{MPa}\right] \tag{5.10}$$

$$d_{el} = \sqrt[3]{\frac{6F \times R_p}{E^*}} [mm] \tag{5.11}$$

$$h_{el} = \frac{d_{el}^2}{4\,R_p} [mm] \tag{5.12}$$

where F is the total load, R_p is the probe radius, and E* is the equivalent Young modulus (calculated from the Young modulus and the Poisson ratio of the two materials involved).

The contact pressure along the radial direction can be calculated as

$$p = \frac{6F}{\pi d^2} \sqrt{1 - \frac{4r^2}{d_{el}^2}} \; [MPa] \tag{5.13}$$

where r is the distance from the rotation axis of the problem.

With this formula, it is possible to estimate the pressure distribution between an elastic sphere and an elastic plane.

According to the Tresca's maximum shear criterion ($max\{|\sigma_I - \sigma_{II}|, |\sigma_{II} - \sigma_{III}|, |\sigma_I - \sigma_{III}|\} = \sigma_{Yield}$) and considering a Poisson coefficient of ν=0.3, the onset of plastic yield occurs when the maximum contact pressure p_0 is above 1.6 times the yield stress of the material (see [5.12]).

Using the presented formulae and given the material probed, the stylus diameter, and the probing force, it is possible to predict if the specimen will withstand a damage. As an example, the ruby-aluminium contact case is shown in Figure 5.2.

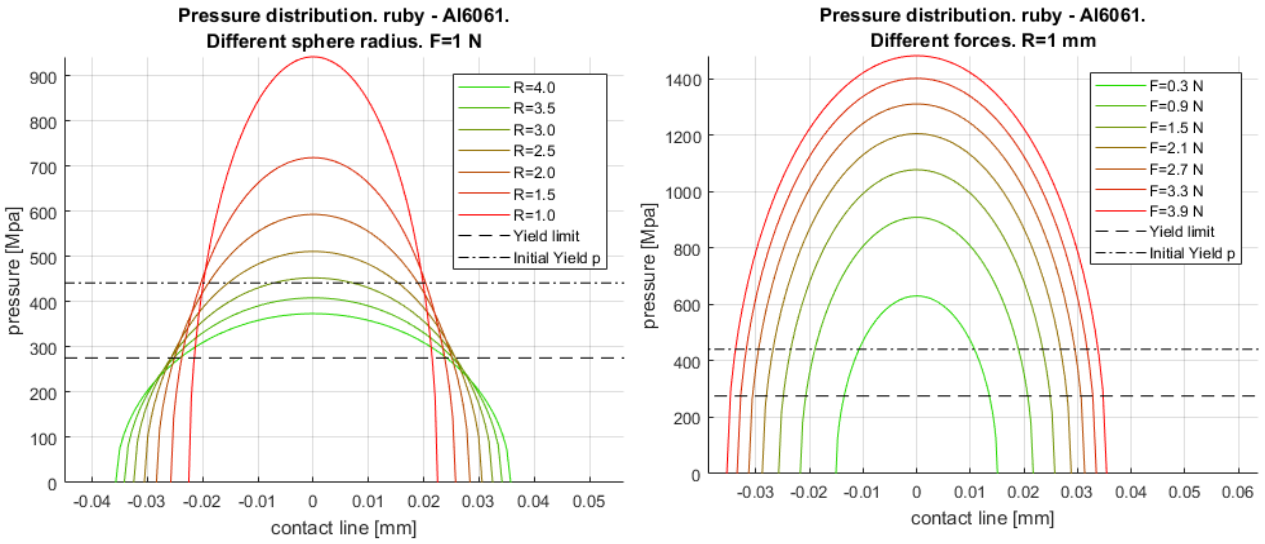

Figure 5.2 Pressure distribution when a specimen made of Aluminium 6061-T6 is probed with a ruby stylus sphere with different forces and diameters. The dash-dot line is 1.6 times the yield stress.

One important parameter while evaluating the damage is the size of the circular dig left after the load has been removed. To have a preliminary understanding of the behaviour, the field distribution of the stress below the surface must be analysed.

Considering a cylindrical reference system z (depth), θ (tangential), and r (radial) and reducing the coordinates as R=2*r/d and Z=2*Z/d, the stress components can be calculated as shown in [5.13].

$$\sigma_r = p_0\left\{-\frac{L^3R^2Z}{(L^4+Z^2)(1+L^2)^2} - (1-2\nu)\left[\frac{Z}{L(1+L^2)} - \frac{1}{3R^2}\left(1-\frac{Z^3}{L^3}\right)\right] + \right.$$
$$\left. + \frac{Z}{L}\left[L(1+\nu)\tan^{-1}\left(\frac{1}{L}\right) - (1-\nu)\frac{L^2}{1+L^2} - 2\nu\right]\right\} \tag{5.14}$$

$$\sigma_\theta = p_0\left\{-\frac{(1-2\nu)}{3R^2}\left[1-\left(\frac{Z^3}{L^3}\right)\right] + \frac{Z}{L}\left[L(1+\nu)\tan^{-1}\left(\frac{1}{L}\right) - (1-\nu)\frac{L^2}{1+L^2} - 2\nu\right]\right\} \tag{5.15}$$

$$\sigma_z = -\frac{Z^3 p_0}{L(L^4+Z^2)} \tag{5.16}$$

$$\tau_{zr} = -\frac{LRZ^2 p_0}{(L^4+Z^2)(1+L^2)} \tag{5.17}$$

$$\tau_{r\theta} = 0 \tag{5.18}$$

$$\tau_{z\theta} = 0 \tag{5.19}$$

where L is a positive value calculated as

$$L = \sqrt{0.5\left[R^2 + Z^2 - 1 + \sqrt{(R^2 + Z^2 - 1)^2 + 4Z^2}\right]} \tag{5.20}$$

The principal normal stresses can be computed, then, as

$$\sigma_I = 0.5(\sigma_r + \sigma_z) + \sqrt{0.25(\sigma_r - \sigma_z)^2 + \tau_{zr}^2} \tag{5.21}$$

$$\sigma_{II} = \sigma_\theta \tag{5.22}$$

$$\sigma_{III} = 0.5(\sigma_r + \sigma_z) - \sqrt{0.25(\sigma_r - \sigma_z)^2 + \tau_{zr}^2} \tag{5.23}$$

and are shown in Figure 5.3 considering an average pressure of 1 MPa.

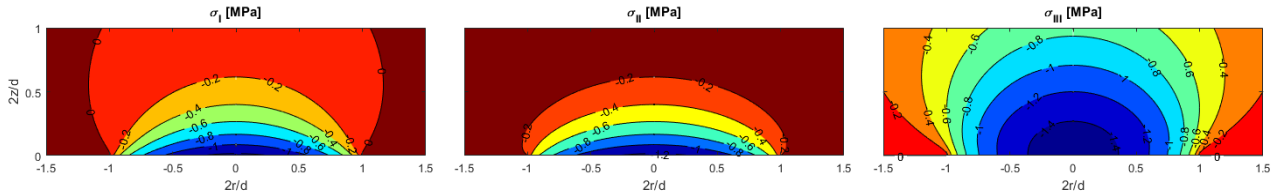

Figure 5.3 Principal stresses below the surface of an aluminium 6061-T6 specimens probed with a ruby sphere.

Using the Tresca's criterion the yield is related to the maximum shear stress, calculated as

$$\tau_{I-III} = 0.5(\sigma_I - \sigma_{III}) \tag{5.24}$$

Its distribution is shown as percentage of the maximum value in Figure 5.4. As can be seen the diameter of the pit can be smaller or larger than the actual contact diameter depending on the ration between the contact pressure and the yield strength of the material. The graph in the bottom part of Figure 5.4 can be useful to have a first estimate of the dig dimension, keeping in mind that it is a purely elastic model and, therefore, does not account for the modifications related to the plasticization of the material.

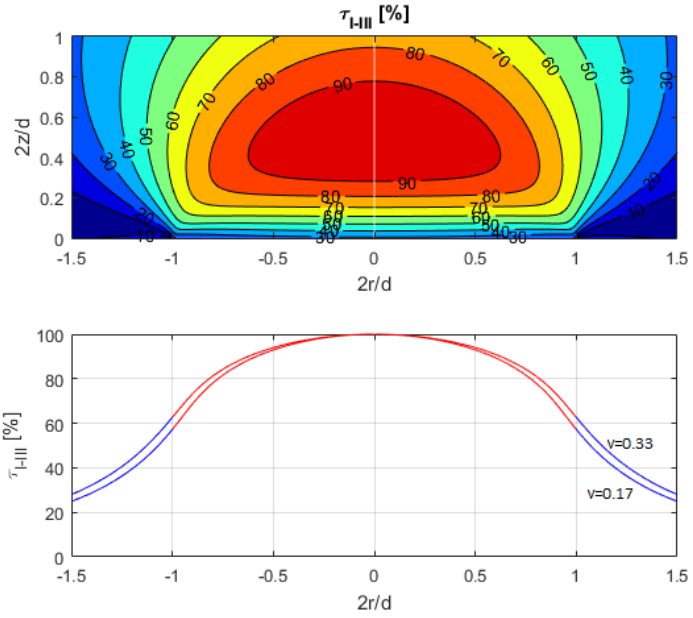

Figure 5.4 $\tau_{I\text{-}III}$ distribution below the surface, normalized over the maximum stress value. Top: 2D distribution with ν=0.33. Bottom: maximum value along the radial direction with ν=0.17 and ν=0.33.

The depth of the indentation and, therefore, the scattering of the light can be calculated using the equation (5.12). Again, the values obtained are related to the indentation depth in the maximum load condition and can be extremely conservative.

When the plasticized material is contained below the surface, as it happens in most of the conditions under test, due to the complex stress field present, no theoretical closed form solution exists.

However, a lower boundary can be calculated considering the material in a fully plastic state during the load (i.e. the plasticized material is not anymore contained below the surface and a plastic flow occurs) and a perfectly elastic unload. As the fully plastic state is reached when the average contact pressure is about 3 times the yield stress (Y), the residual depth of the indentation can be calculated as [5.12]:

$$h_{resEP} = \sqrt[3]{\frac{9F^2}{16\,R_p\,E^{*2}}} - \sqrt{\frac{27\,\pi\,F\,Y}{16\,E^{*2}}}\,[mm] \tag{5.25}$$

As the full plasticity is reached for a load about 40 times the load at first yield, it will be never reached during the test.

In order to have a complete understanding of the behaviour in the elastoplastic condition, the best solution is to perform a FEM analysis. An example of this simulation is shown in Figure 5.5 and Figure 5.6. The axisymmetric model has been developed simulating a ruby tip with a diameter of 2 mm and considering the strain hardening of the aluminium 6061-T6 and a coefficient of friction of 0.8.

In Figure 5.5 the stress field and the displacements with due to a 1 N load are shown while Figure 5.6 displays the residuals after the force has been removed. The diameter of the plastically deformed part is comparable to the maximum diameter of the indentation while the indentation depth is two orders of magnitude smaller than the elastic value.

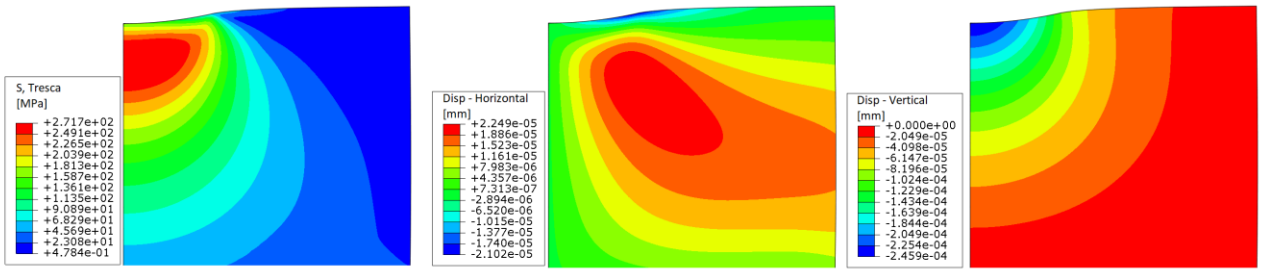

Figure 5.5 Indentation of a ruby sphere (2 mm diameter) on aluminium Al6061-T6 with a force of 1 N. Left: Stress values (Tresca). Centre: displacement in the radial direction. Right: displacement in the probing direction.

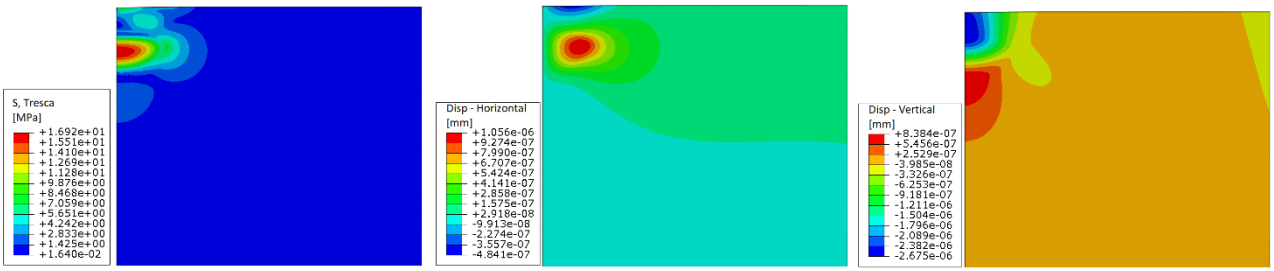

Figure 5.6 Indentation of a ruby sphere (2 mm diameter) on aluminium Al6061-T6 after the removal of the 1 N force. Left: Stress values (Tresca). Centre: displacement in the radial direction. Right: displacement in the probing direction.

5.3.1.1 Brittle materials

Glasses are well known for having an extremely better behaviour in compression than in traction. This is related to the presence of small defects where a strong stress concentration, not compensated by the plasticization of the material, lead to a crack growth and, finally, to the failure of the piece.

An evaluation of the stress components on the surface is possible using, again, the Hertzian theory. Considering a cylindrical reference system z/θ/r, their values are equal to [5.12]:

$$\sigma_{ri} = p_0 \left\{ \frac{1-2\nu}{3} \frac{a^2}{r^2} \left[1 - \left(1 - \frac{r^2}{a^2} \right)^{1.5} \right] - \left(1 - \frac{r^2}{a^2} \right)^{0.5} \right\} [MPa] \tag{5.26}$$

$$\sigma_{\theta i} = -p_0 \left\{ \frac{1-2\nu}{3} \frac{a^2}{r^2} \left[1 - \left(1 - \frac{r^2}{a^2} \right)^{1.5} \right] - 2\nu \left(1 - \frac{r^2}{a^2} \right)^{0.5} \right\} [MPa] \tag{5.27}$$

$$\sigma_{zi} = -p_0 \left(1 - \frac{r^2}{a^2} \right)^{0.5} [MPa] \tag{5.28}$$

$$\sigma_{re} = p_0 \frac{(1-2\nu)a^2}{3r^2} [MPa] \tag{5.29}$$

$$\sigma_{\theta e} = -p_0 \frac{(1-2\nu)a^2}{3r^2} [MPa] \tag{5.30}$$

where a is equal to d/2 and the subscripts ‘i’ and ‘e’ designate the values internal or external to the loaded circle. All those values are compressive with the exception of σ_r as can be seen in Figure 5.7.

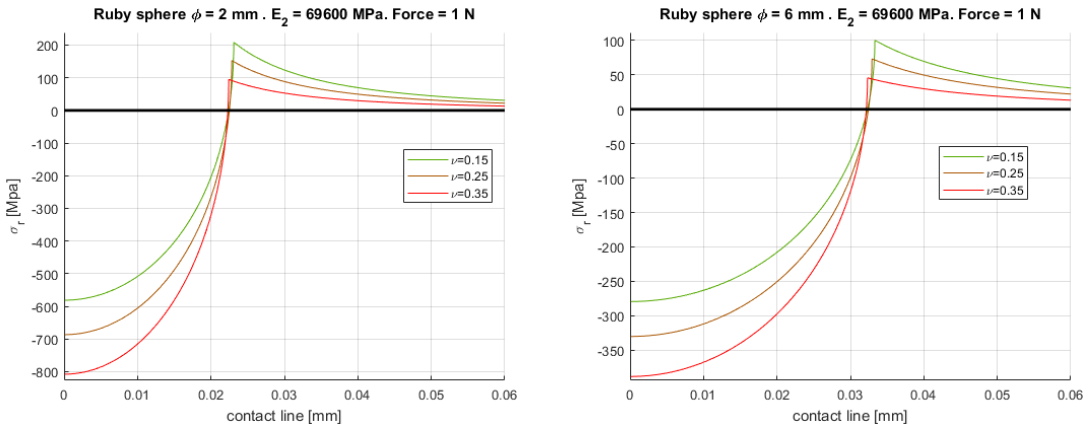

Figure 5.7 Radial stress on the surface varying the specimen's Poisson coefficient and considering a Ruby ball and an Aluminium 6061-T6 specimen. Left: sphere diameter 2 mm. Right: sphere diameter 6 mm.

This tensile radial stress reaches a maximum value of

$$\sigma_r = \frac{(1-2\nu)p_0}{3}\ [MPa] \tag{5.31}$$

which, as can be seen in Figure 5.7, can be in the order of hundreds of megapascals for small ruby spheres and glasses with low Poisson coefficient.

Such tensile stresses can open the existing cracks creating a ring outside the indented part. The full process is shown in Figure 5.8: Hertzian cone cracks and plastic deformation are discussed here, while median (step 3), radial (step 5), and lateral (step 6) cracks are not discussed, as they appear with forces several order of magnitude higher than the ones involved in the measuring process.

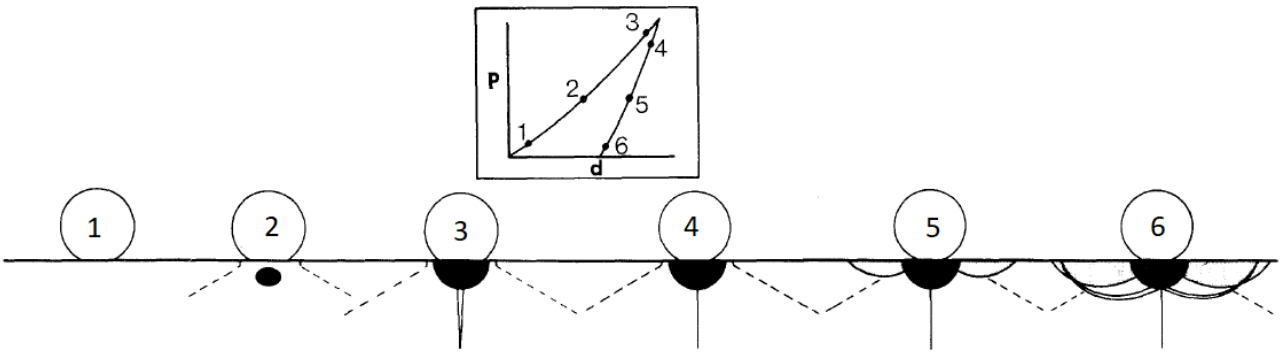

Figure 5.8 Cracking in quasi-static indentation. Top: load-displacement graph. Bottom: evolution of the cracks during the loading and unloading phases. The black area is the plastic deformation while the dashed line represents the Hertzian cone cracks. The median, radial and lateral cracks are also shown. Adapted from [5.14].

An example of the ring creation in a soda-lime glass is also shown in Figure 5.9. Once the crack starts from a pre-existent defect, it quickly grows all around the indentation perimeter.

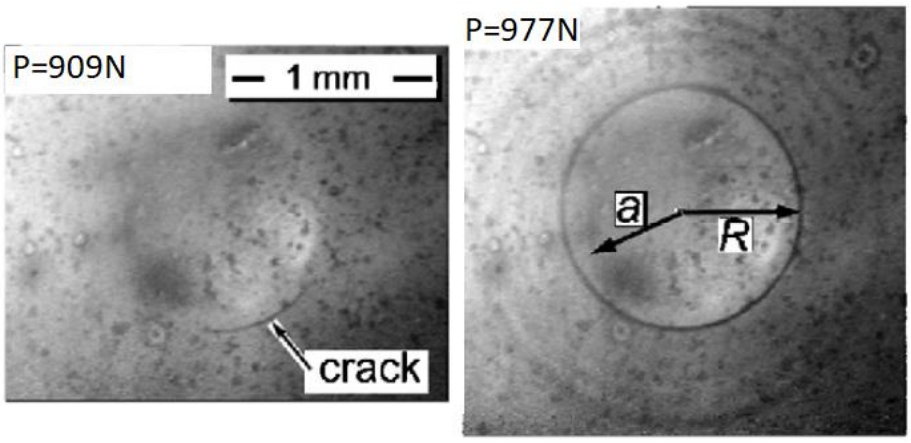

Figure 5.9 Ring cracks development using a Tungsten Carbide spherical indenter (25.4 mm diameter). Adapted from [5.15].

A ring crack, however, occurs only if an existing crack with a minimum size is present in the tractive stress zone. This condition is well explained by the Griffith's law

$$\sigma_c = \frac{K_{IC}}{f\sqrt{\pi a_c}}[MPa] \tag{5.32}$$

where K_{IC} is a characteristic of the material expressed in $MPa\sqrt{m}$ and represent the critical stress intensity factor in the opening mode of the crack. The parameter f depends on the shape and location of the crack and, in this case, is equal to 1.12 while a_c is the depth of the crack [5.16].

In most of the glasses, the K_{IC} value ranges between 0.6 and 1.1 $MPa\sqrt{m}$ [5.17]. In Figure 5.10 (left) an example with the N-BK7 glass ($K_{IC} = 1.08\ MPa\sqrt{m}$) critical stress for different crack dimension is shown. The horizontal lines represent the minimum strength obtained by breakage tests performed with the double ring method (EN 1288-5 standard, [5.18]) and different surface conditions: D64 means a ground with bonded diamond grains (diameter 58-63 µm) while SiC 600 is a lapping with Silicon carbide (diameter 9-19 µm).

In Figure 5.10 (right), the distribution of the crack sizes during different grinding process is shown as a metric.

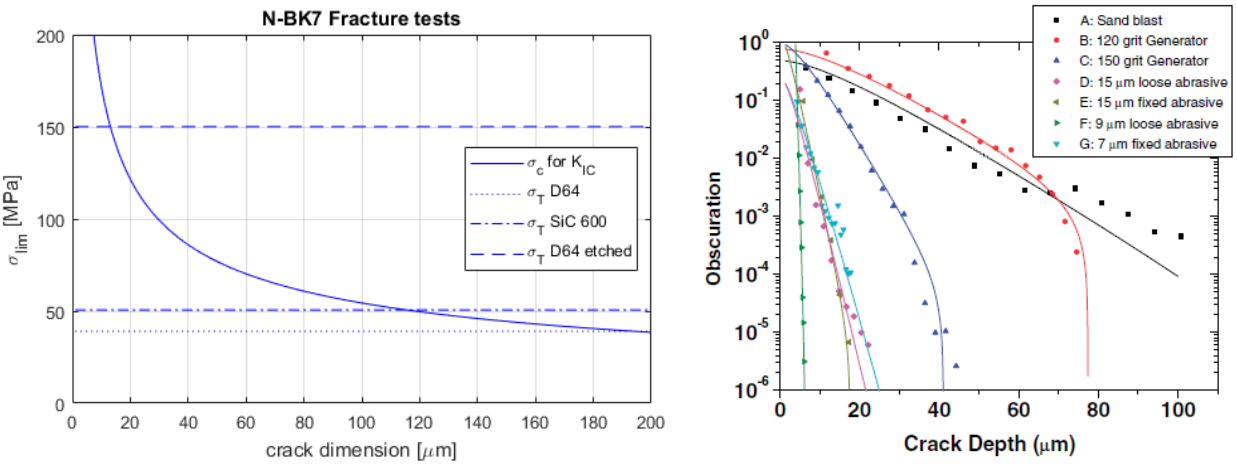

Figure 5.10 Left: Griffith law applied to N-BK7 borosilicate glass. Data from [5.17] Right: distribution of the crack depths in grinded fused silica specimens. Image from [5.19].

Considering that the fine polishing of the optical surface should remove all the scratches created by the grinding operations well below the micrometre level, the ring crack is an event that should not occur.

Moreover, those potential scratches should be located in a rather small area: in the most severe case (see Figure 5.7), the tensile stress will be above 50 MPa in less than 0.01 mm^2 for each acquired point.

Nevertheless, as some scratch can remain after the final polishing or appear due to the handling of the optic, keeping the maximum tensile stress below the 7 MPa dictated by the historical rule of thumb is still a good practice.

5.3.2 Coated materials

All the analysis performed so far are not fully exhaustive when dealing with coated optical elements. By Hertzian calculations, the maximum stress zone lays 0.94*d below the surface of the material analysed which translate to values between 0 and 50 µm depending on the material involved, the force applied, and the diameter of the spherical indenter. On the other side typical multilayer coatings have an overall thickness below the micrometre for anti-reflection (AR) ones and a few microns for high-reflection (HR) elements.

A mathematical approach has been developed in the past years to solve the Hertzian problem in a coated half space [5.20]. It has been originally studied to derive the mechanical properties of the substrate and coating performing measurements with a spherical indenter but could also be used conversely.

A comparison between the coated and uncoated case is shown in Figure 5.11. As can be seen a steep variation in the radial stress appears at the interface between the coating and the substrate. Tangential and axial stresses are not shown, as the difference between the two cases is much smaller.

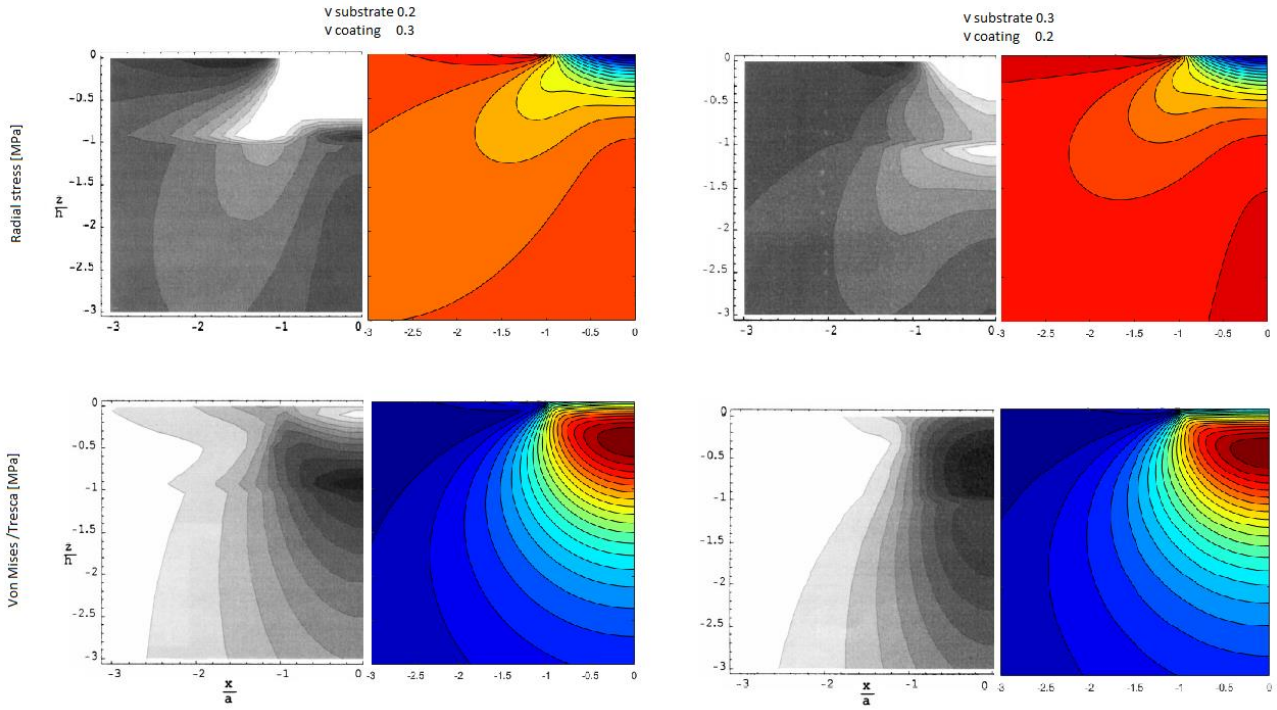

Figure 5.11 Comparison between Hertzian stress with coated (black and white images, from [5.20]) and uncoated substrate (coloured images, analytical Hertzian stress distribution). In the coated case, the diameter of the indentation is 4 times the thickness of the coating.

Another possible solution consists in the use of FEM simulations as per Van der Zwaag [5.21]. The analyses were performed considering single and bilayer thin hard coatings on soda lime glass. The overall thickness of the coating was kept at 1.5% than the diameter of the indentation and a reduction of the radial stress on the substrate was observed, with a stronger effect for thicker and stiffer coating. This effect was compensated by an increase of the coating stress.

Within the framework of this thesis, the same FEM analysis done for the uncoated elements has been performed considering the most typical cases in terms of substrate and coating materials. Two examples are shown in Figure 5.12 and Figure 5.13 and the parameters of the materials are listed in Table 5.3. The analysis has considered a perfect bonding between coating and substrate, a frictionless contact with the 2 mm diameter ruby sphere, and a contact force of 1 N.

The unprotected gold coating is a material used for metallic HR elements while an MgF2 layer 150 nm thick is the simplest AR coating for lenses working in the visible range (maximum transmission at 600 nm).

Table 5.3 Materials properties used for the FEM analysis on N-BK7 glass.

	Young's Modulus [MPa]	Poisson's ratio [-]	Coating thickness [nm]
Ruby (sphere)	370000	0.220	-
N-BK7 (substrate)	82000	0.206	-
MgF2	138500	0.276	150
Gold	79000	0.420	500

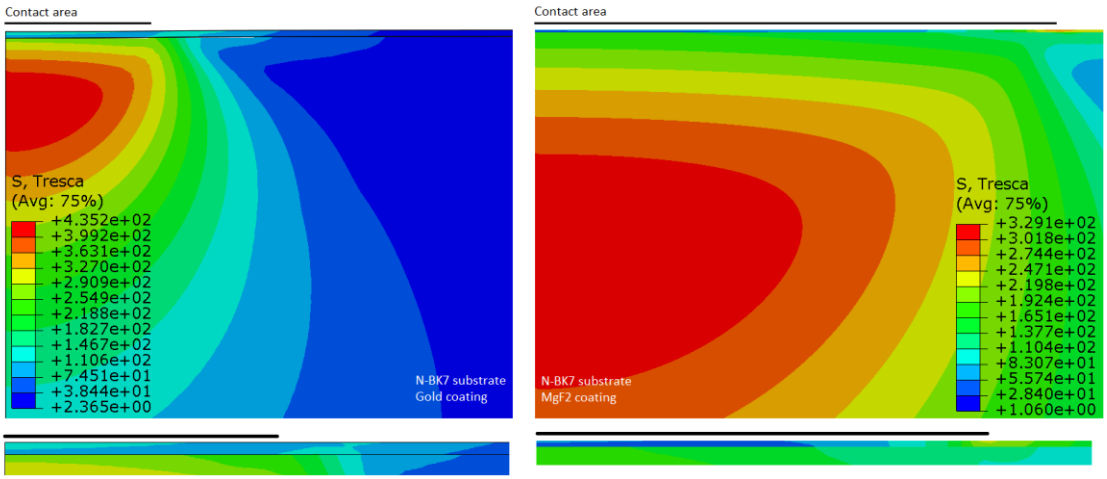

Figure 5.12 FEM analysis of an N-BK7 substrate with gold (left) and MgF2 (right) coating with a detailed view on the bottom. Tresca's equivalent stress values [MPa]. In the uncoated case the maximum stress is equal to 3.308e+02 MPa. Note that the two images have been plotted with different scales.

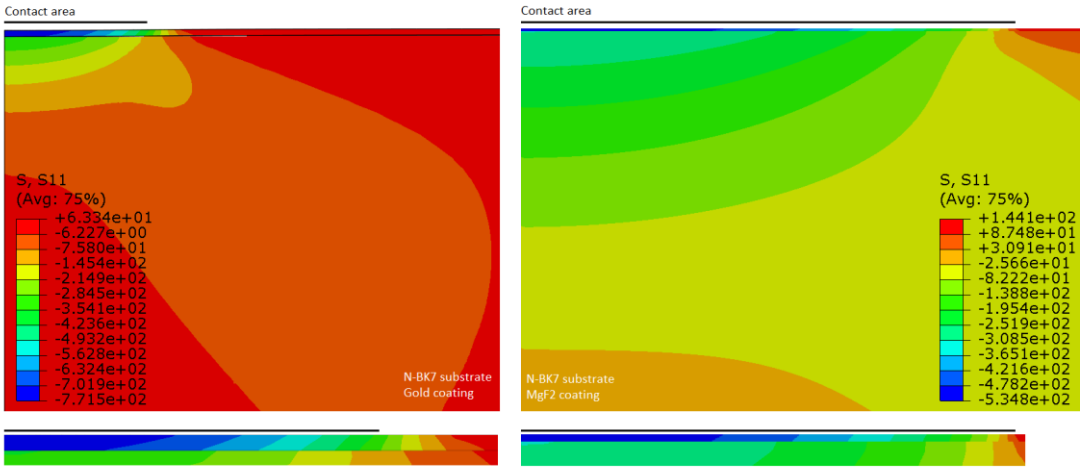

Figure 5.13 FEM analysis of an N-BK7 substrate with gold (left) and MgF2 (right) coating with a detailed view on the bottom. Radial stress values [MPa]. In the uncoated case the maximum tensile and compressive stresses are equal to 7.88e+01 MPa and -3.864e+0.2 MPa. Note that the two images have been plotted with different scales.

The obtained results confirmed the ones found in the literature even if an increase in the stress has been found when coatings with high Poisson coefficient are involved.

Even is this method can be extremely powerful it has different drawbacks:

1. a perfect adhesion between the layers is considered (same limitation in the theoretical model in [5.20]),
2. the friction coefficient between ruby and the last coating surface is usually unknown. Nevertheless, it's influence in the Tresca's stress is small and a frictionless contact is a conservative assumption regarding the radial stresses,
3. the parameters of the materials most of the time are the ones find in literature for bulk materials,
4. the materials and thicknesses must be known.

Typical methods for coating depositions are evaporation (reactive, non-reactive, ion plating, and plasma-ion assisted deposition to name a few) and sputtering (direct current diode sputtering, triode sputtering, magnetron sputtering, and ion-beam sputtering) and the process can be tuned using different parameters in each method [5.22].

All those methods create thin films with nanocrystalline structures that exhibit anisotropy in the thickness plane and are characterized by higher hardness [5.23] and strength due to grain structure, dislocation density, and vacancy concentration differences [5.24]. This behaviour can be found in both ceramic and metallic materials. As an example, copper films have a hardness about 5 times higher than the bulk equivalent and a similar trend has been observed in gold [5.25].

Due to those reasons, tests specific for the mechanical characterization of film coatings have been developed in the past years [5.24]. An example of the results obtained on optical coatings with different production methods can be seen in [5.26] and have been summarized in Figure 5.14. The technologies used were ion-beam-assisted deposition (IBAD), magnetron sputtering (MS), dual ion-beam sputtering (DIBS), plasma-enhanced chemical-vapour deposition (PECVD), and filtered cathodic arc deposition (FCAD).

The compressive stress ranged between -150 and -450 MPa on SiO_2, between -100 and -150 MPa on Ta_2O_5, and between -1000 (compressive) and +100 MPa (tensile) on TiO_2. This parameter is important as, if the material is characterized by a large stiffness to yield stress ratio and once the stress is released with external stimulations, it could generate a pile-up or a sink-in of the coating depending on the compressive or tensile stress status.

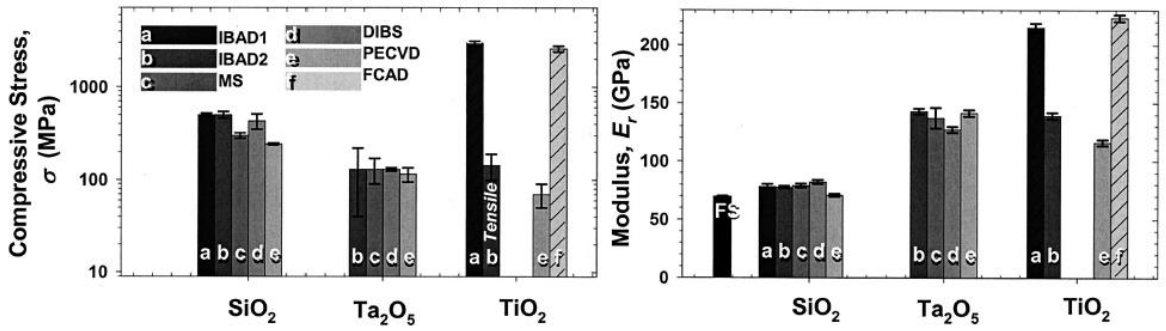

Figure 5.14 Mechanical properties of thin optical coatings created with different processes. Courtesy of [5.26].

Even if those parameters are less influenced by the process, variations in hardness and reduced Young modulus can also be observed. Other authors pointed out that even changing the parameters used for the deposition have an important influence on their mechanical characteristics. An example [5.27] is shown in Figure 5.15, where coatings are generated with DIBS varying voltage and current. Again, large variations in the internal stress can be found together with minor variations (up to 15-20%) in the Young's modulus.

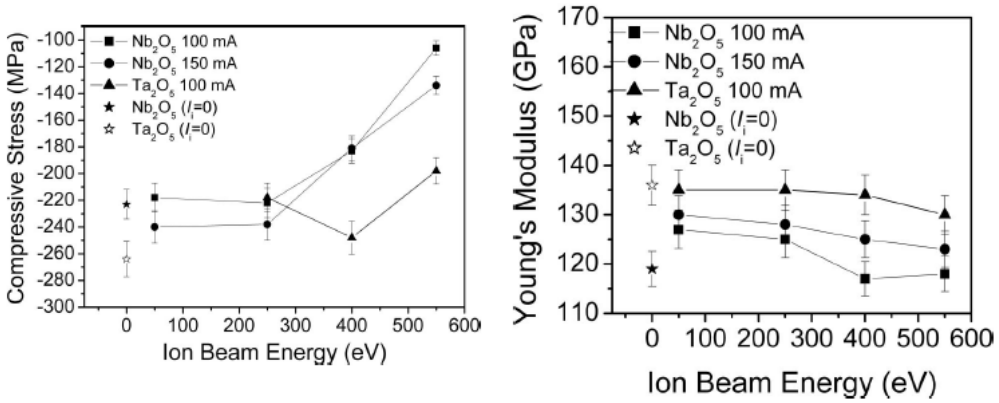

Figure 5.15 Mechanical properties of thin optical films created using DIBS and changing the deposition parameters. Courtesy of [5.27].

As is has been shown in a previous examples, knowing the production process and parameters is a fundamental step to search for the coating's mechanical properties in literature. Unfortunately, those informations are usually kept as a secret by the coating manufacturer and, unless a specific 'recipe' for the coating is required, neither materials nor thicknesses are shared with the customer.

For all those reasons, the only valid method to evaluate damages on the optical coating consists in a direct measurement on the coating involved (e.g. requiring a small sample for the test). In order to have some guideline, different common substrates and coatings have been tested and the results are presented and discussed in the next sections.

5.4 Measurement setup and methodology

Two possible options have been investigated for the damage evaluation: the Atomic Force Microscope (AFM) and the MicroFinish Topographer (MFT).

The first one is a typical solution for surface evaluation in non-coated materials: a small tip is kept at a few nanometres from the surface thanks to the Van der Waals forces and a small surface is measured in raster mode. This instrument has been used in the past to evaluate the effect of spherical indenters on metals but has a few disadvantages:

- the damage location must be quite well known,
- for small indentations the line density must be strongly increased with a direct effect on the measuring time,
- no damage can be detected if it remains below the surface.

To overcome those limitations a MFT has been used for the measurements. This instrument shown in Figure 5.16, is a Point Source Microscope (PSM) with a Kohler illumination system (full field source in the figure) working at 632.8 nm equipped with a Mirau interferometer in the objective and a CCD camera looking at the interference fringes (field 0.953 mm x 0.714 mm, pixel scale 0.931 µm/pixel). To align the PSM with respect to the sample, 3 screws-type piezo motors are used.

Tests showed a repeatability better than 0.06 nm rms without vibration insulation. Averaging a certain number of measurements acquired consecutively can improve this value and reduce the high-frequency noise. In all the tests performed, the images have been acquired 50 to 100 times depending on the reflectivity of the surface.

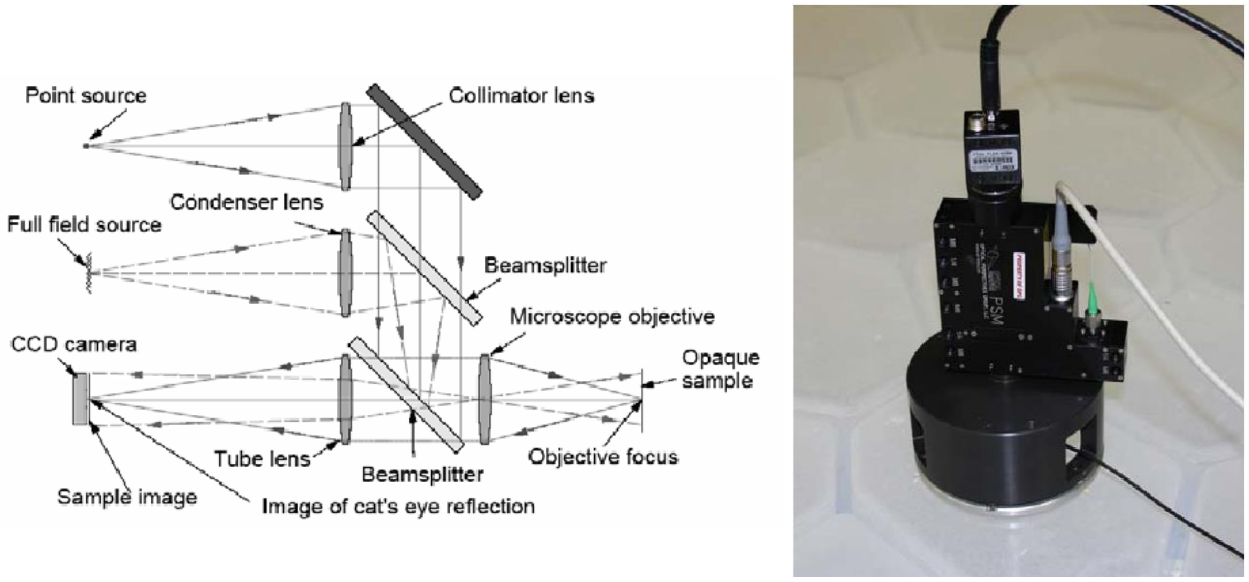

Figure 5.16 Left: optical scheme of the PSM. Image from [5.28] Right: MFT measuring the primary mirror of the Giant Magellan Telescope. Image from [5.29]

With the MFT is possible to find damages on the element with a size down to a few micrometres and a sub-nanometre depth quickly. Another important advantage is that, as it works with a 632.8 nm light, it can detect

variations in the reflected light related to modification below the surface. In this case, the measurement obtained will not be the effective shape of the surface but, instead, the deviation of the optical beam due to the indentation that is, after all, the objective of the research.

All the elements have been impinged with the CMM equipped with a SFM and an L20D2 stylus. The forces applied ranged between 0.15 N and 3.5 N and at least 5 repetitions were performed for each force. As measuring the samples at 3 mm/s and 4 mm/s produces the same maximum force (3.5 N), for clarity the latter value are shown in the graph with a fake force value of 4 N. Anyway, this can account for the more sever force profile at higher measuring speed.

When the dig was circular, the size of each dig has been obtained directly measuring the diameter of the disturbed surface. If the pit had a more complex shape due to material anisotropy, damage rings, or pitting, the equivalent diameter was derived by the disturbed area. The depth has been always calculated removing the scratches and roughness of the original surface.

When meaningful, in addition to the mechanical shapes also the obscuration and maximum deviation values will be shown. The first are calculated supposing that the deformed part is not anymore able to transmit or reflect the light and the values are calculated supposing that a 25 mm diameter optical element is impinged 50 times. The maximum deviations are calculated geometrically considering the depth and the diameter of the impinged hemisphere.

In order to evaluate possible 'fatigue' effects, the same test have been repeated impinging the same point on the element for 100 times (N=100 tests) instead of just one (N=1). Due to the relatively low stiffness of the CMM, the 100 points were scattered in circle of about 10 µm radius.

5.5 Tests and results

In order to derive some general rule, different materials have been tested. The theoretical parameters used both for the simulations shown in the previous part and to draw the theoretical lines are shown in Table 5.4 while the list of tested elements is in Table 5.5. The choice has been done to cover the main families of optical elements with different metallic and glass elements, 'hard' glass substrates with metallic and dielectric coatings and one 'soft' glass substrate (CaF_2) with and without a dielectric coating.

Table 5.4 Material properties of the substrate tested. The asterisk indicates the materials where multiple sources have been used for the Yield stress values.

	Young modulus [MPa]	Poisson [-]	Yield Stress [MPa]	Knopp Hardness HK	Source
Substrates					
Ruby	380000	0.29			[5.30]
Aluminium 6061-T6	69600	0.33	235-276	120	[5.31]*
X33CrS16	212000	0.29	750-950	340	[5.31]*
Copper	117000	0.31	63.5	48	[5.31]
Borosilicate	65000	0.20		480	[5.32]
CaF2	75800	0.26		158	[5.32]
Fused silica	73100	0.30		500	[5.32]
N-BK7	82000	0.21		610	[5.32]

Table 5.5 Tested optical elements with materials (if known), transmittive (T) or reflective (R) performances and commercial names.

Substrate	Coating		Type	Model
Aluminium 6061-T6	Uncoated		Reflective	In-house polishing
Steel X33CrS16	Uncoated			In-house polishing
Copper (annealed)	Uncoated			II-VI custom mirror
	Dielectric	HR R>99.5% @ 10600 nm		II-VI custom mirror
Borosilicate	Dielectric	HR R>99% @350 – 1100 nm		Semrock MI1050-SBB
	Aluminium + SiO_2	Metallic – Protected		Thorlabs ME05S-G01
	Silver + SiO_2	Metallic – Protected		Thorlabs ME05S-P01
	Gold + SiO_2	Metallic – Protected		Thorlabs ME05S-M01
Fused Silica	Gold	Metallic – Unprotected		Thorlabs PFSQ05-03-M03
Borosilicate	Metallic	T=10±1% @350-800 nm	Neutral Density Filter	CVI-ND-100-0.50
	Metallic	T=1±0.1% @350-800 nm		CVI-ND-200-0.50
	Metallic	T=0.1±0.01% @350-800 nm		CVI-ND-300-0.50
	Metallic	T=0.01±0.001% @350-800 nm		CVI-ND-400-0.50
Fused Silica	Uncoated		Transmissive	Thorlabs WG41050
	Dielectric	AR R<0.75% @350-700 nm		Thorlabs WG41050-A
	Dielectric	AR R<0.75% @1050-1700 nm		Thorlabs WG41050-C
Calcium Fluoride	Uncoated			Thorlabs WG50530
	Dielectric	AR R<1.5% @1650-3000 nm		Thorlabs WG50530-D

5.5.1 Metallic mirrors

The metallic mirrors tested were made of aluminium, high strength steel and copper.

The **aluminium 6061-T6** sample was impinged with speeds ranging between 0.5 and 4 mm/s with a single measure and at 0.5 and 1 mm/s with 100 measures. In Figure 5.17 (right) an example of the indentation is shown, and it exhibits a purely Hertzian shape.

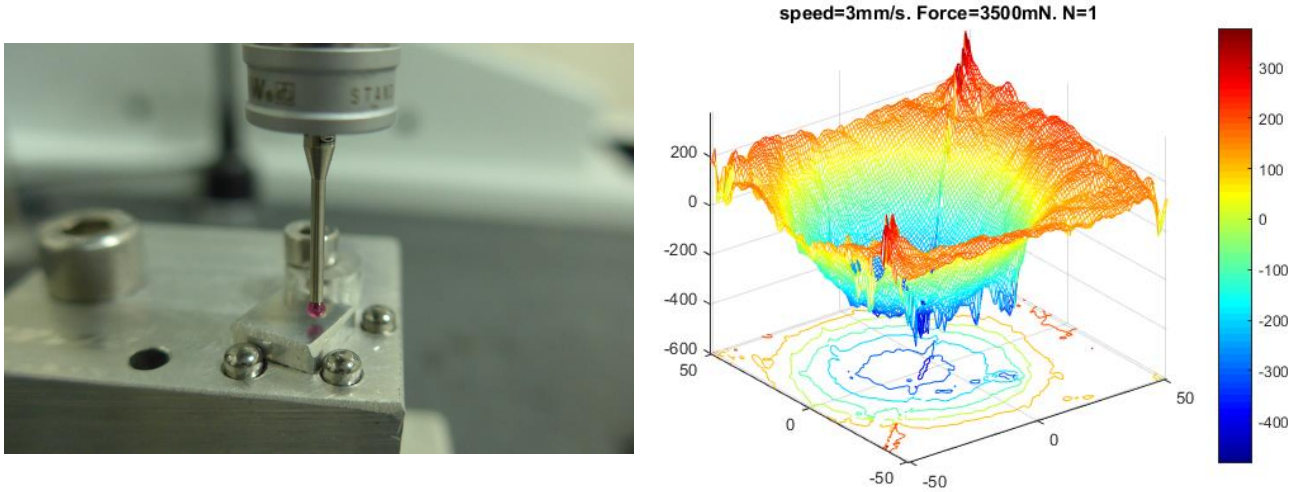

Figure 5.17 Aluminium indentation test. Left: picture of the sample under test. Right: example of indentation measured with the MFT.

All the results are summarized in Figure 5.18. The diameter of the indentation and, therefore, the obscuration, is well predicted by the elastic Hertzian model that, instead, overestimates the depth of the indentation. Little differences can be seen in the size of the indentation when the same spot is impinged 100 times. This can be both related to a less severe stress due to the modified shape in contact and the work hardening of the material.

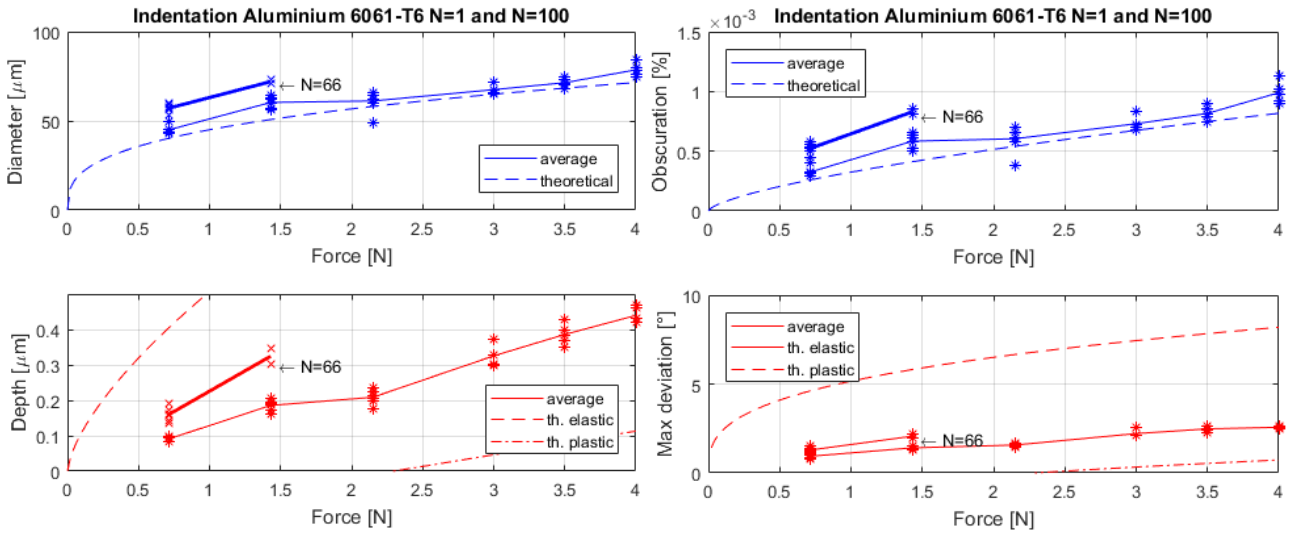

Figure 5.18 Aluminium indentation test. Left: Diameter and depth of the indentations. Right: Obscuration and maximum deviation of the rays. The continuous line represent the average value (thick for N=100). One test, marked with '66', failed due to a software problem before reaching the 100 contacts expected.

Due to the low Yield strength of the **annealed copper** the results on this material are, by far, the worst ones encountered during the campaign. The shape follows quite well the values predicted by the elastic Hertzian even if some pile-up of material appears around the hole (see Figure 5.19, right).

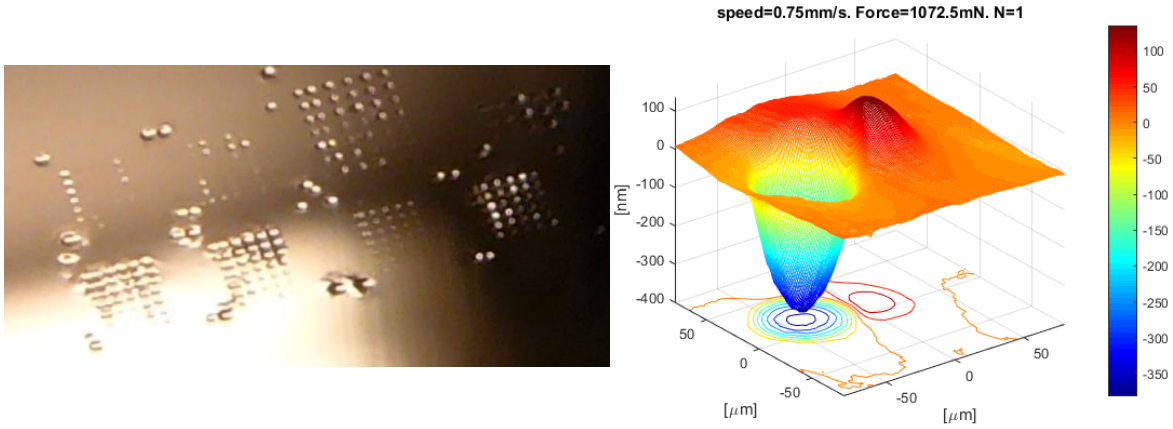

Figure 5.19 Copper indentation test. Left: picture of the sample after the test. Each matrix is about 1 mm x 1 mm. Right: example of indentation measured with the MFT.

Due to the strong plasticization of the material, at higher forces the diameter of the perturbed circle exceed the diameter of the elastic indentation (see Figure 5.20) and the depth is better explained by the elastoplastic model (equation (5.25)). To study the effect at lower forces, the tests have been repeated with maximum contact forces down to about 150 mN and the results are shown in Figure 5.21.

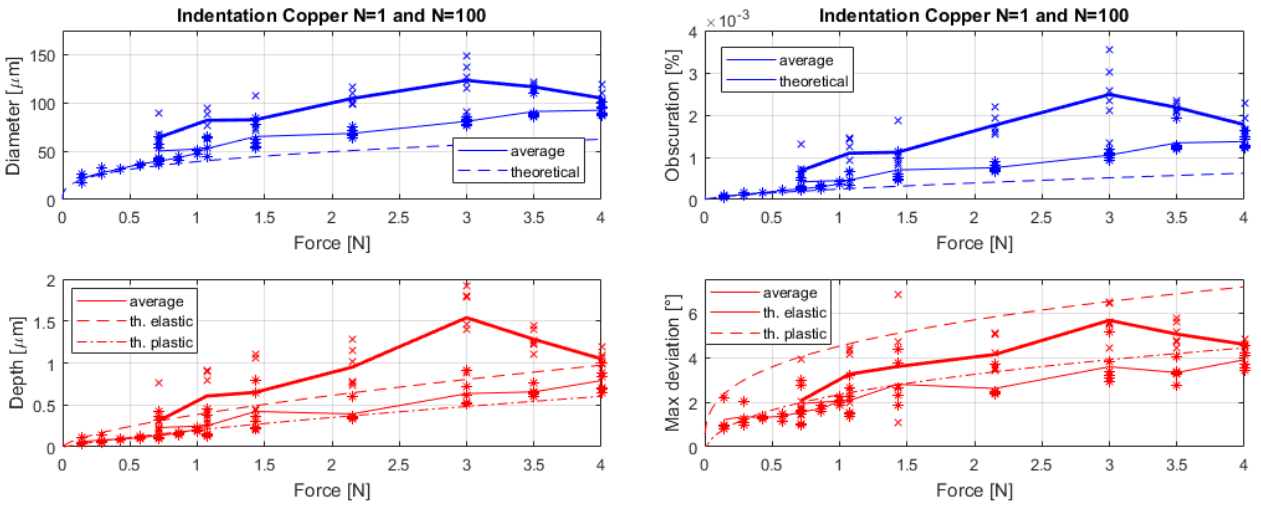

Figure 5.20 Copper indentation test. Left: Diameter and depth of the indentations. Right: Obscuration and maximum deviation of the rays. The continuous line represent the average value (thick for N=100).

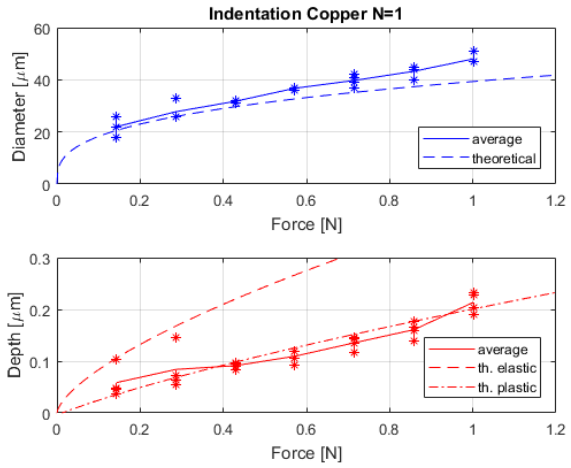

Figure 5.21 Copper indentation test. Detail of the results between 0.15 and 1 N.

Repeating the test on a **high strength steel (X33CrS16)**, the typical Hertzian deformation has been found (Figure 5.22, right). The diameter is similar to the one theoretically expected while the indentation depth was heavily lower, meaning that the contact is almost purely elastic. For this reason and, as the plasticized shape is quasi-flat, the depth keeps increasing with the number of repeated contacts.

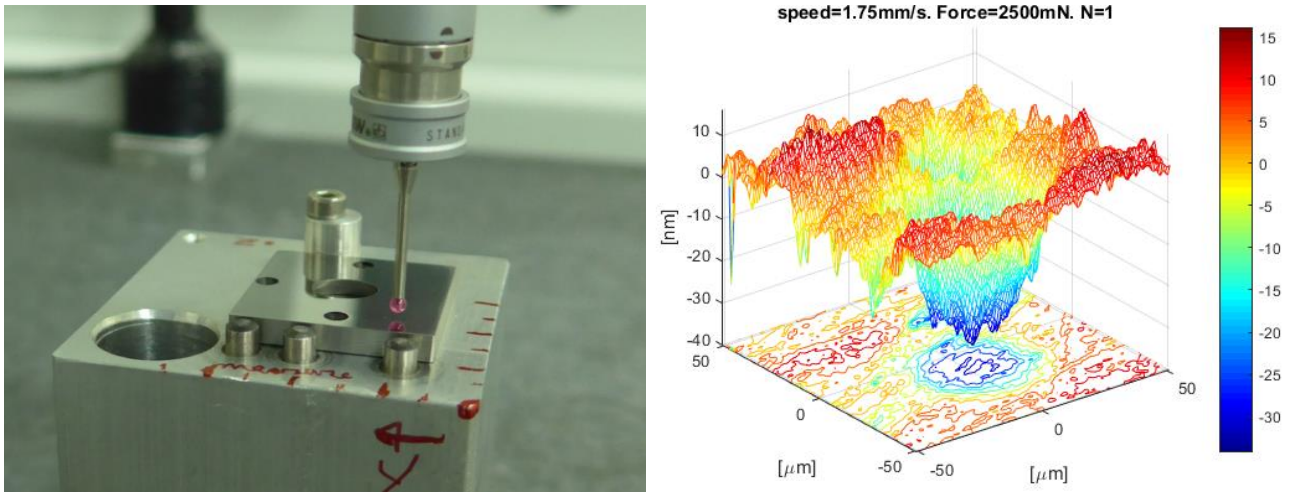

Figure 5.22 Steel indentation test. Left: picture of the sample during the test. Right: example of indentation measured with the MFT.

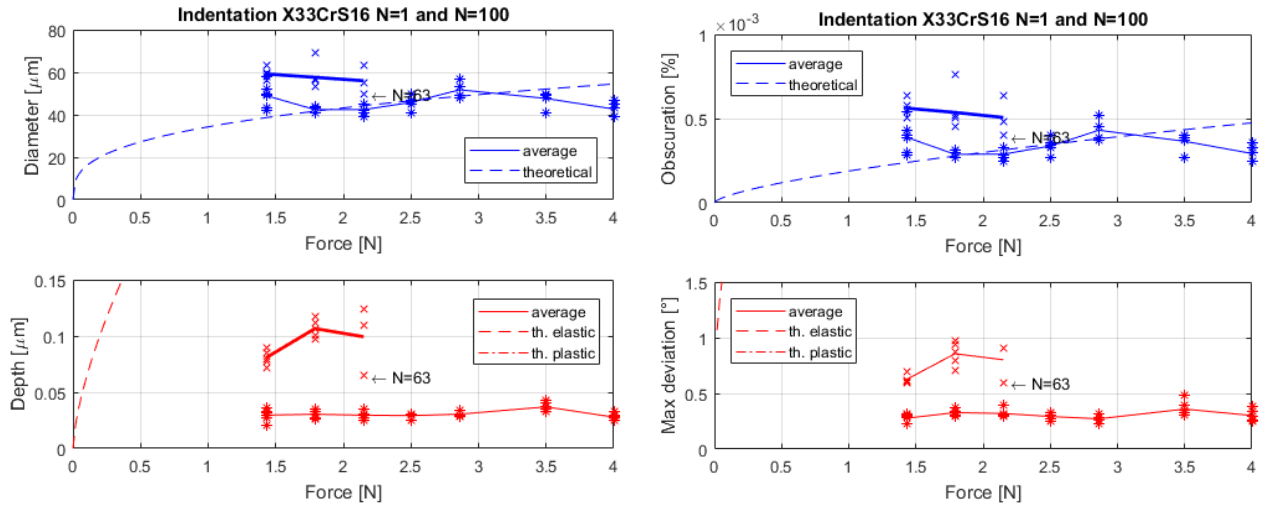

Figure 5.23 Steel indentation test. Left: Diameter and depth of the indentations. Right: Obscuration and maximum deviation of the rays. The continuous line represent the average value (thick for N=100). One test, marked with '63', failed due to a software problem before reaching the 100 contacts expected.

5.5.2 Dielectric coatings on metallic substrates

The same copper substrate has also been tested with an HR coating with a peak reflection at 10.8 µm (CO_2 laser). Even if no specific information is available for this coating, it is probably made of zinc selenide (ZnSe), gallium arsenide (GaAs), Germanium, and Molybdenum. Given the optical performances declared it is possible to suppose a $[H\text{-}L]^N$ coating with a configuration $[Ge\text{-}ZnSe]^6$ having a total thickness of about 29 µm (see [5.33]).

A can be seen in Figure 5.24, the digs are clearly visible at naked eye. The results obtained are almost equal to the ones of the uncoated copper, meaning that the soft substrate drives the deformation of the coating.

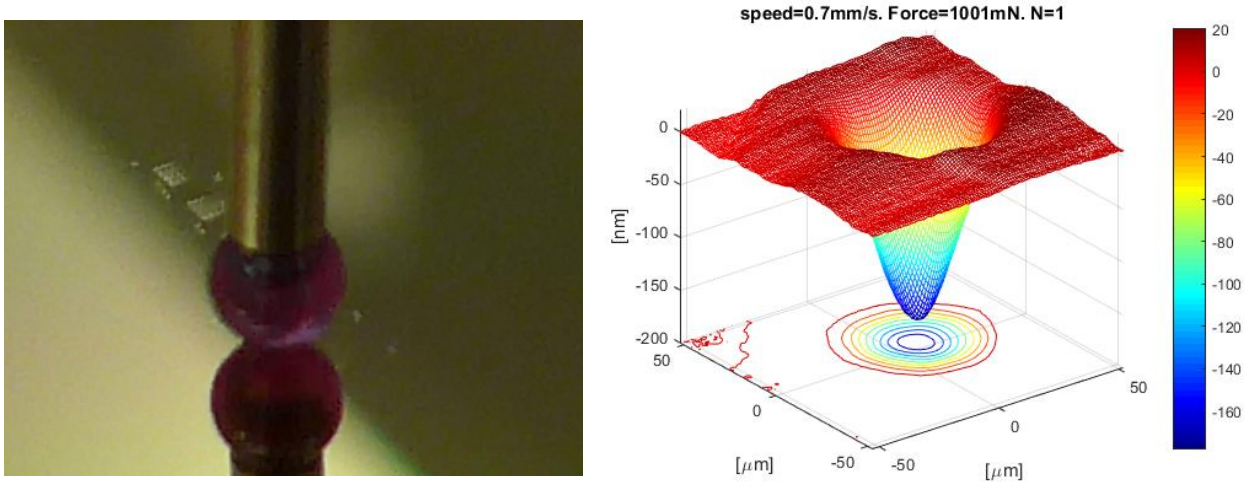

Figure 5.24 Indentation test of a HR coating on copper substrate. Left: picture of the sample during the test. Each matrix is about 1 mm x 1 mm. Right: example of indentation.

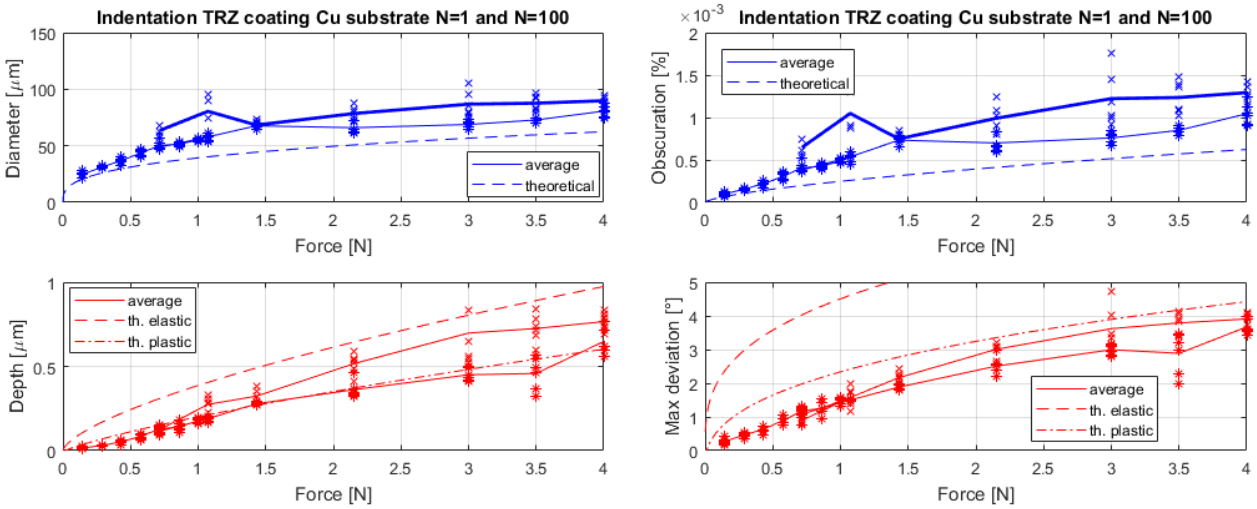

Figure 5.25 HR coating on copper indentation test. Left: Diameter and depth of the indentations. Right: Obscuration and maximum deviation of the rays. The continuous line represent the average value (thick for N=100).

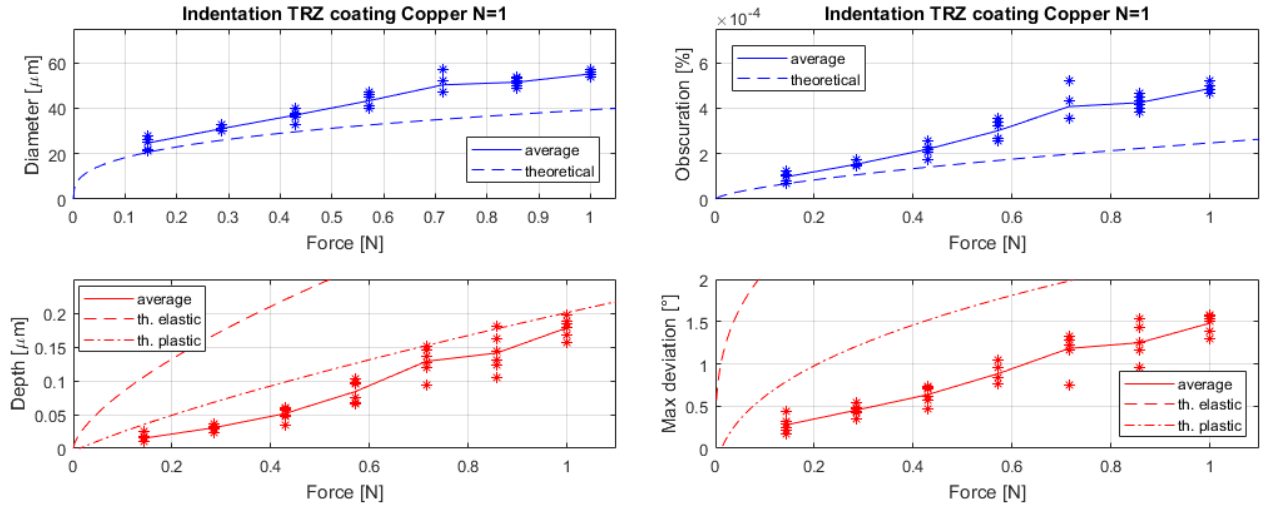

Figure 5.26 HR coating on copper indentation test. Details of the results between 0.15 and 1 N.

5.5.3 Metallic coatings on glass substrates

The metallic coating on glass substrate tested were of two different types. The first were made of aluminium, silver or gold on Borosilicate. They had a thickness of a few hundred nanometres with a protective SiO_2 overcoat on top to improve the resistance to oxidation and mechanical stresses (Figure 5.27, left). The second one had a gold coating on fused silica substrate with no protection (Figure 5.27, right).

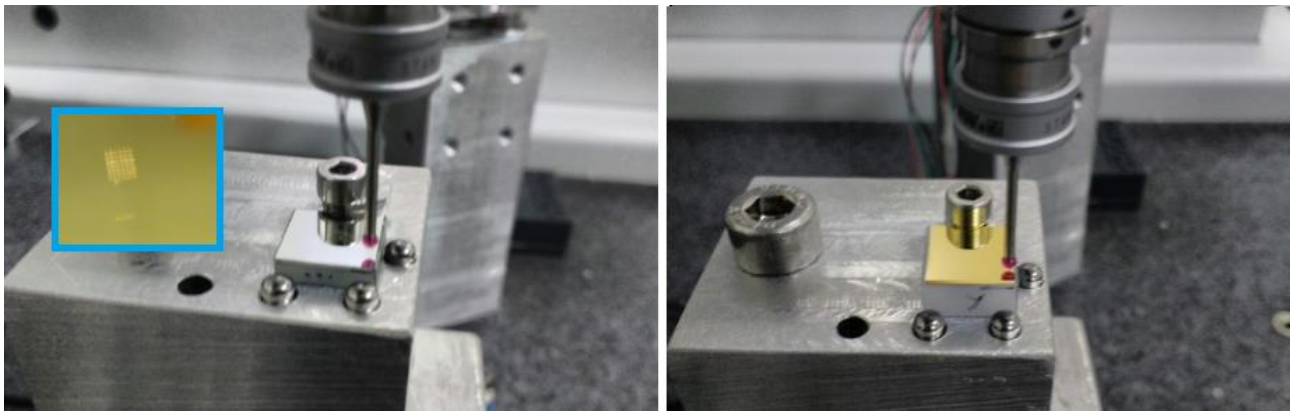

Figure 5.27 Left: protected metallic coating on Borosilicate with a detail of the damage in the blue box (rectangle size about 1 mm x 1 mm). Right: unprotected gold on fused silica.

None of the three specimen tested showed any damage when the contact was performed only once. The same result was obtained impinging the surface of silver and aluminium for 100 times while the protected gold exhibited the damage shown in Figure 5.27 (left) and Figure 5.28.

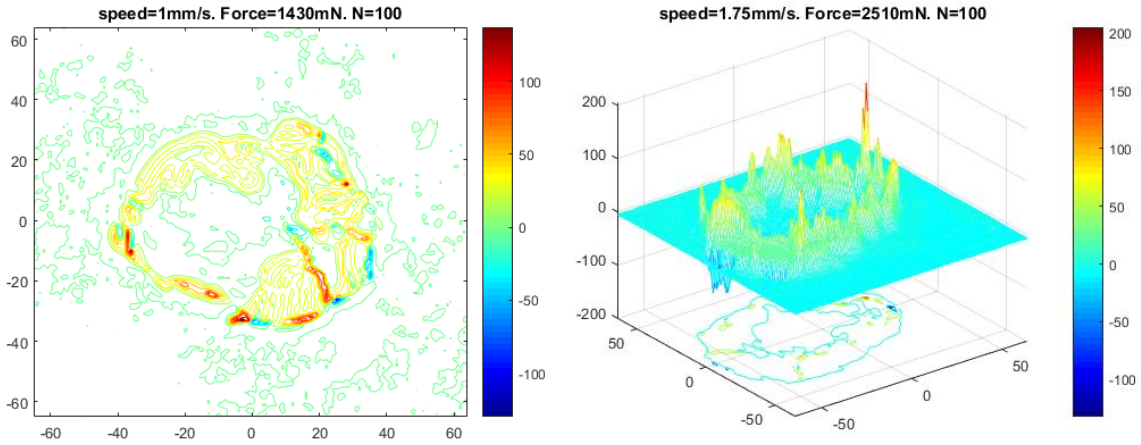

Figure 5.28 Protected gold over Borosilicate. Damage after 100 contacts. Left: 2D view. Right: 3D view.

In this case, no central dig has been found and this damage is clearly caused by the radial surface stress and has not been found while testing the unprotected gold. For this reason, it is possible to relate this damage to the low thickness of the SiO_2 and the strong difference in Poisson coefficient between it (0.15-0.19) and the gold (0.42). A similar coefficient can be found in silver (0.36-0.40) but it was not possible to replicate the same results, probably due to its higher Yield strength and different internal residual stress.

In order to quantify the damage an application has been developed to recognize the damaged feature (Figure 5.29, left). After defining a proper threshold depending on the surface quality of the original specimen (in this case ±8 nm as shown in Figure 5.29, centre) it calculates the area of the enveloped surface (Figure 5.29, right).

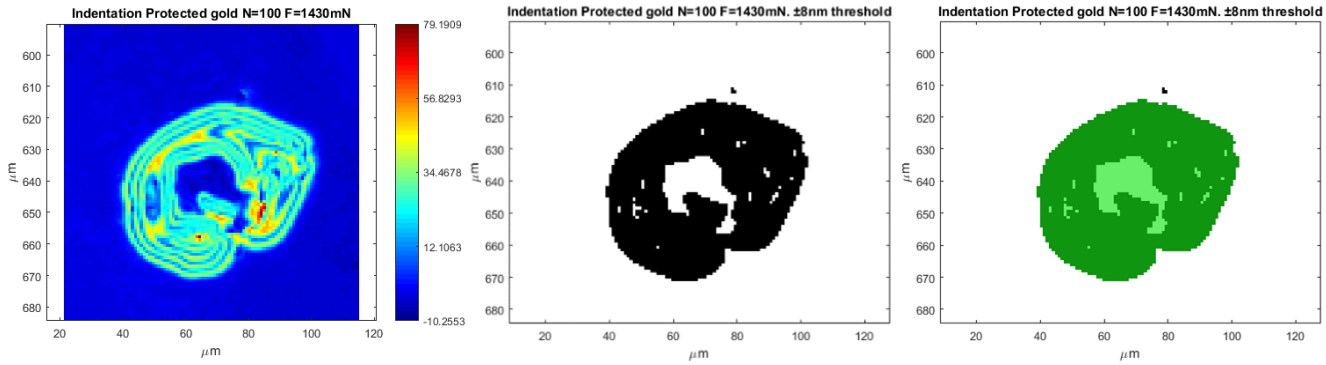

Figure 5.29 Damage evaluation on protected gold. Left: original shape of the damaged surface. Centre: portion of the surface out of the ±8 nm limit. Right: part considered as damaged (both light and dark green).

The results are summarized in Figure 5.30 and the most important consideration is that, differently from the previous cases, the damage disappears when the applied force is equal or less than 0.7 N. The diameter is the equivalent one calculated as $d = 2\sqrt{A/\pi}$.

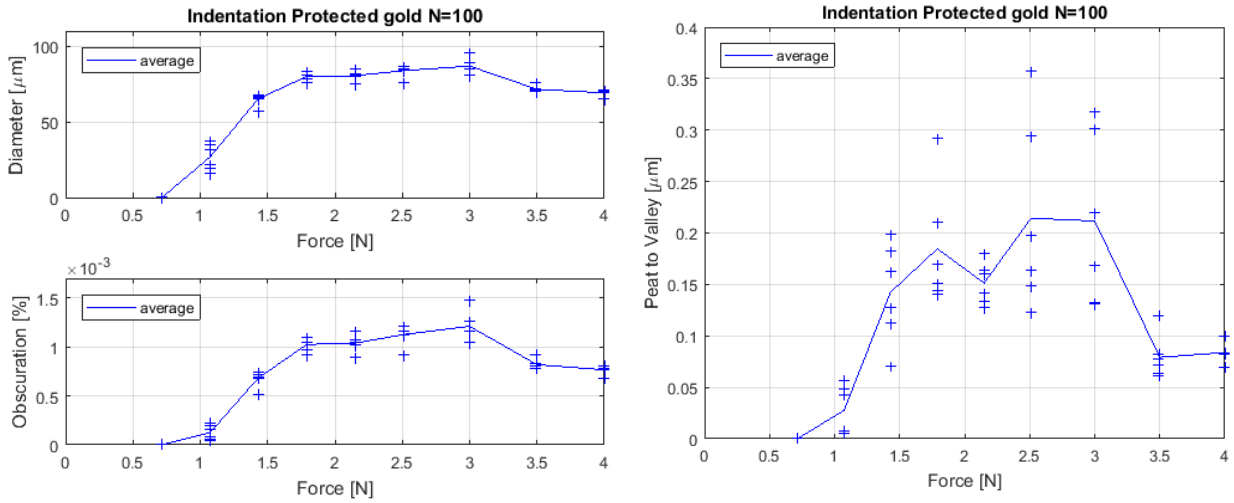

Figure 5.30 Protected gold on Borosilicate indentation test. Left: equivalent diameter of the damaged surface and corresponding obscuration. Right: peak to valley values.

Performing the same test on unprotected gold leaded to the behaviour shown in Figure 5.31. The damage is mostly concentrated near the ring of maximum radial stress but, instead of having an overall pile-up of the material, it appears like a series of chips with a few microns of diameter are involved. In this case, the damaged portion was indistinguishable by the rest of the specimen with naked eyes.

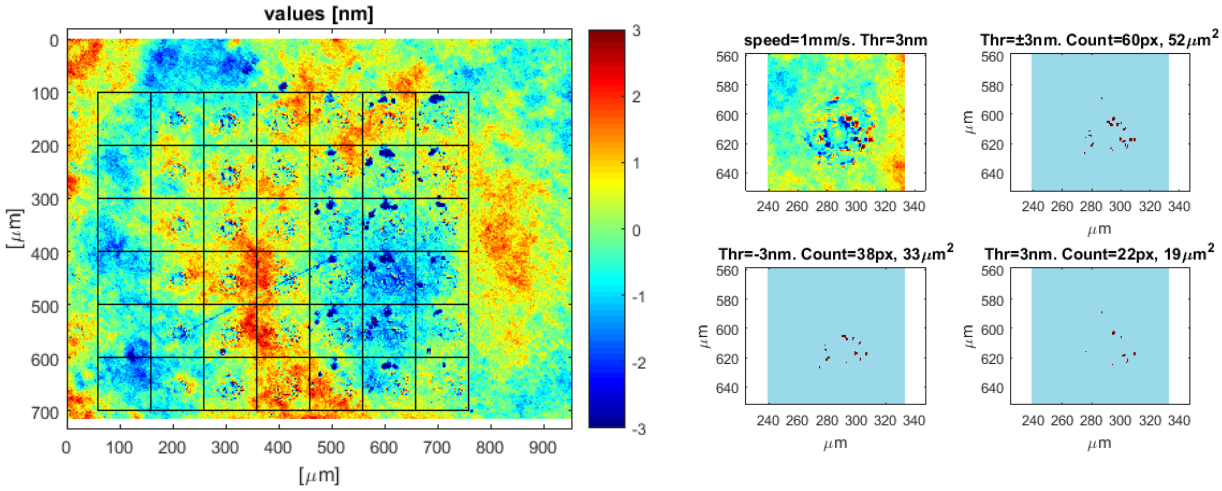

Figure 5.31 Unprotected gold on fused silica. Left: overall view of the performed tests. Right: Portion of the surface above and below the ±3 nm threshold.

The results are summarized in Figure 5.32 and three different situations can be observed. Below a certain force (about 1 N) no damage can be found, between 1 N and 2.5 N the damage appears as a displacement of material, while above this value it appears that the material is completely removed by some portion of the coating (see Figure 5.31, left and Figure 5.32).

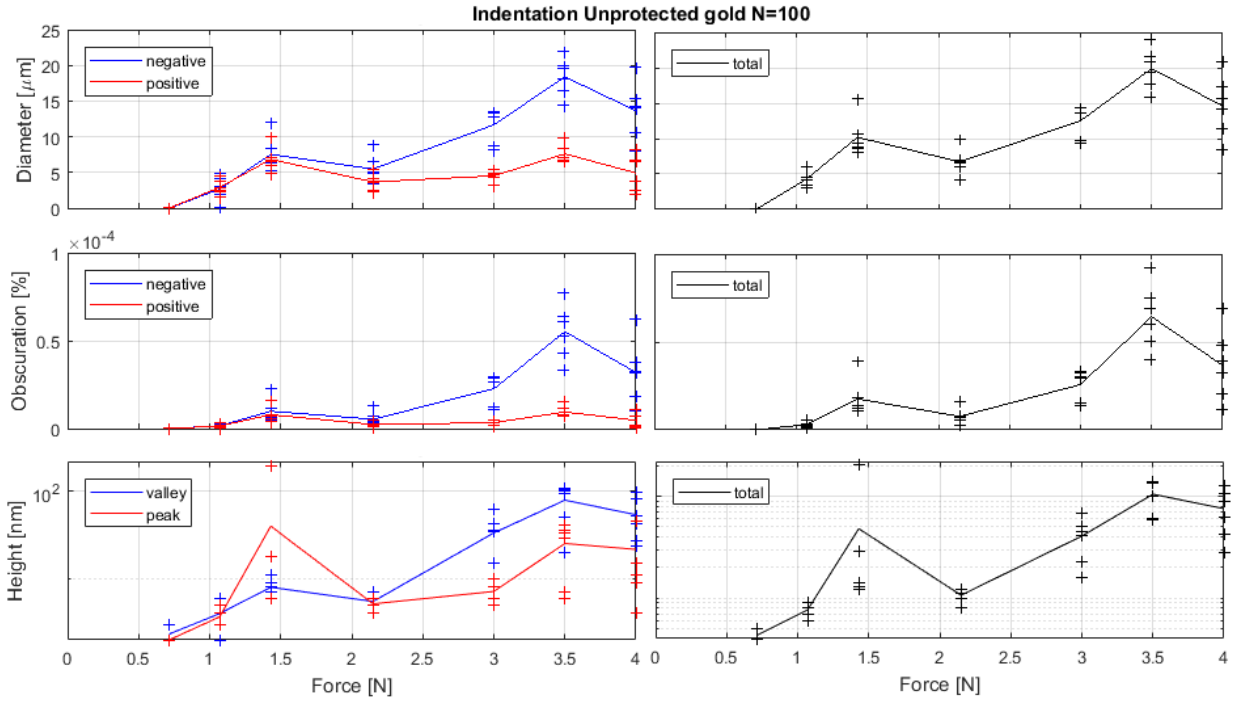

Figure 5.32 Unprotected gold on fused silica. From top to bottom equivalent diameter, corresponding obscuration and maximum height/depth. Left: positive and negative values. Right: sum of the two.

5.5.4 Dielectric coatings on glass substrates (reflective elements)

The HR mirror tested was made by a dielectric multilayer coating mounted on a borosilicate substrate. In this case, no information was available on the coating materials but a thickness of a few micrometres can be expected. The surface was damaged by both the single and the multiple contact tests.

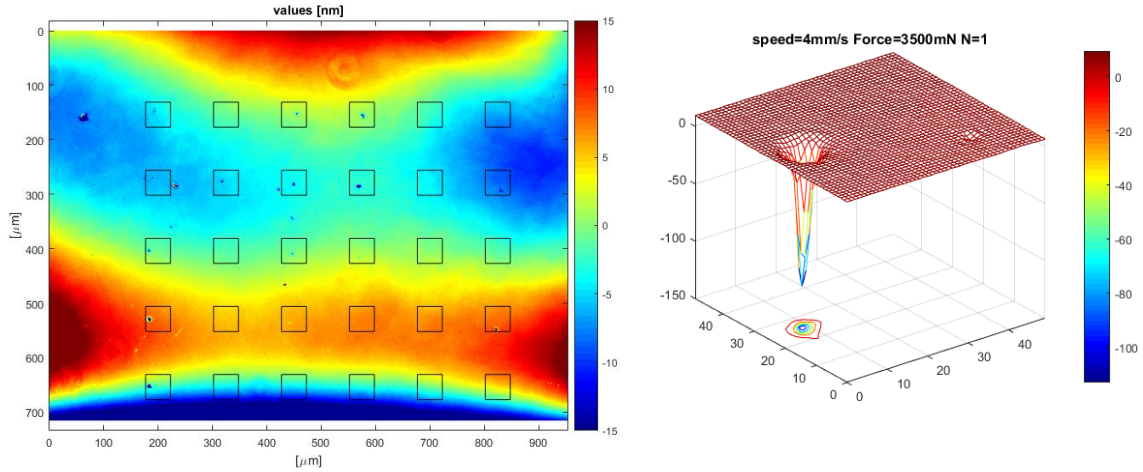

Figure 5.33 Multilayer HR coating on borosilicate substrate. Left: MFT view of the damaged surface for N=1. Right: example of damage.

The single contact case is shown in Figure 5.33 and the results are detailed in Figure 5.34. The contact generates a single pit with a small diameter for forces of 1.75 N and above while for smaller ones no damage was found.

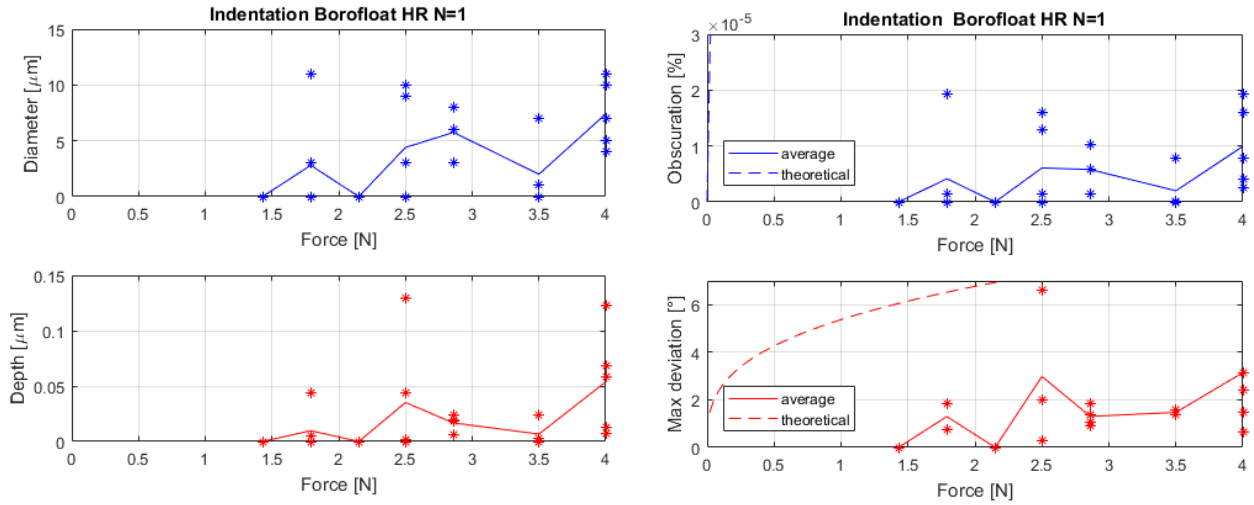

Figure 5.34 Multilayer HR coating on borosilicate substrate for N=1. The dashed lines show the theoretical results of the borosilicate glass. Left: Diameter and depth of the indentations. Right: Obscuration and maximum deviation of the rays.

The same test has been performed with multiple contacts (100) and an example of the results is shown in Figure 5.35. The damage appears as a mix between a plastic deformation (central pit) and a superficial displacement of material similar to the 'unprotected gold' case. The damage quantification has been done calculating the damaged area as shown in Figure 5.35.

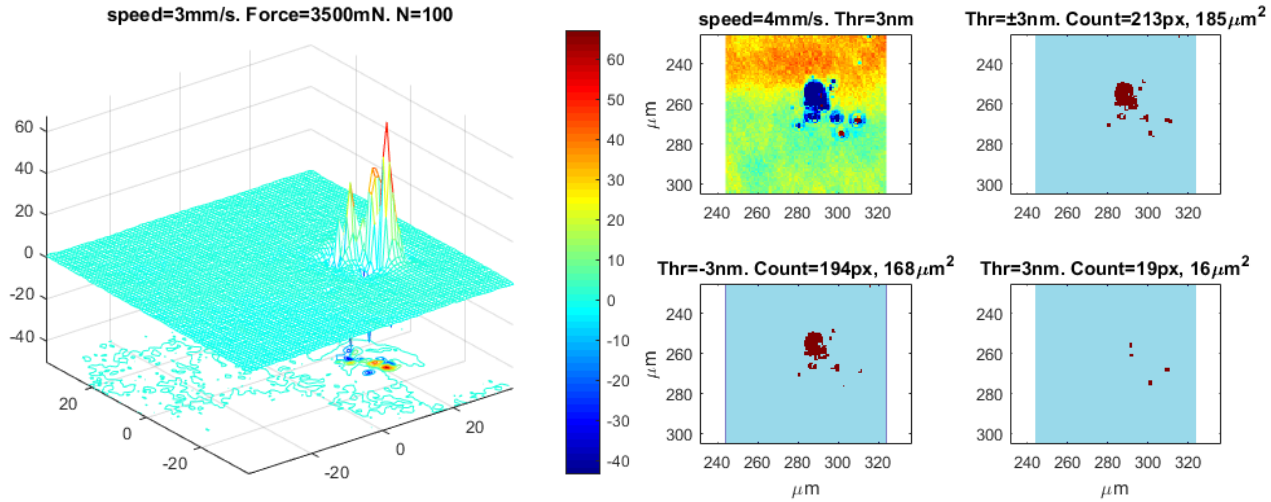

Figure 5.35 Multilayer HR coating on borosilicate substrate. Left: example of damage for N=1. Right: portion of the surface above and below the ±3 nm threshold.

Surprisingly, no damage were found at forces were a single contact appeared to be critical (see Figure 5.36 compared to Figure 5.34). The only possible explanation is that the strength of the coating was decreased in the N=1 case due to the proximity to the lens edge.

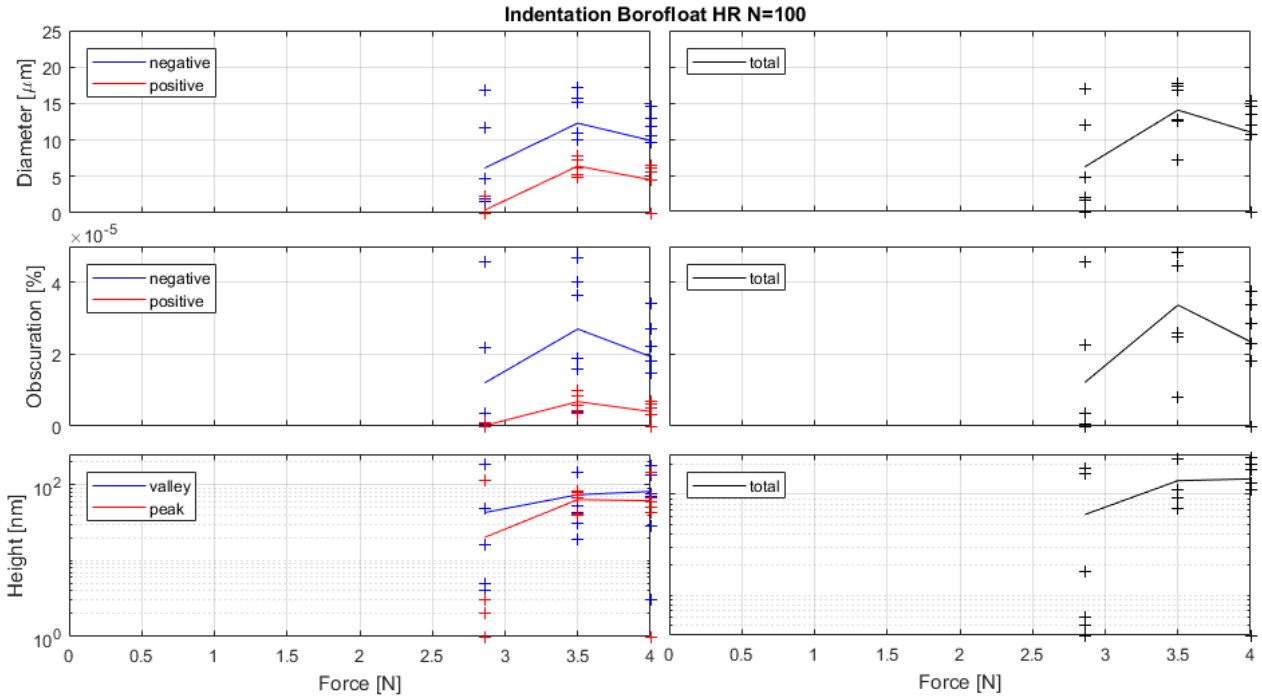

Figure 5.36 Multilayer HR coating on borosilicate substrate for N=100. From top to bottom equivalent diameter, corresponding obscuration and maximum height/depth. Left: positive and negative values. Right: sum of the two.

5.5.5 Reflective Filter on glass substrates

Four different neutral density (ND) filters with different optical densities (OD) were tested. All of them are made of a borosilicate substrate and a thin coating reflecting part of the light. The thickness of the coating, typically metallic, defines the portion of light transmitted by the surface and different materials lead to different spectra of the exiting beam.

To have ND filter one possible solution is to use Inconel. Varying the Inconel thickness between 10 and 100 nm changes the transmittance of the element by different orders of magnitude [5.34], as shown in Table 5.6. Using different metallic materials for the coating (e.g. Silver, Aluminium, Gold, or Chromium) the thicknesses remains similar.

Table 5.6 Main characteristics of the ND filters tested damage mechanisms encountered.

	OD	Transmittance [%]	Thickness [nm]	Damage		
				N=1	N=10	N=100
ND100	1	10	15-25	None	None	None
ND200	2	1	40-55	None	Dig	Dig
ND300	3	0.1	70-90	None	Dig	Dig + light ring
ND400	4	0.01	100-125	None	Dig	Dig + ring

In Table 5.6, also the results obtained with the four specimen are shown. When the element is impinged just once, no damage has been found. Increasing the number of measurements on the same point up to 10 and excluding the filter with the thinner coating, small digs appears (Figure 5.37, left). When the contact is performed for 100 times, those digs remain approximately of the same size but a ring appears in the zone of maximum radial stress (Figure 5.37, left). As can be seen in the scale the indentations depths are of the same order of magnitude of the surface roughness and, therefore, the extracted results are prone to errors due to pre-existing local surface deviations.

A general consideration looking at Table 5.6 is that smaller thicknesses of coating are less damaged than bigger ones. This can be easily explained by the lower number of atoms and imperfections in the depth direction and, therefore, the higher force needed to move them.

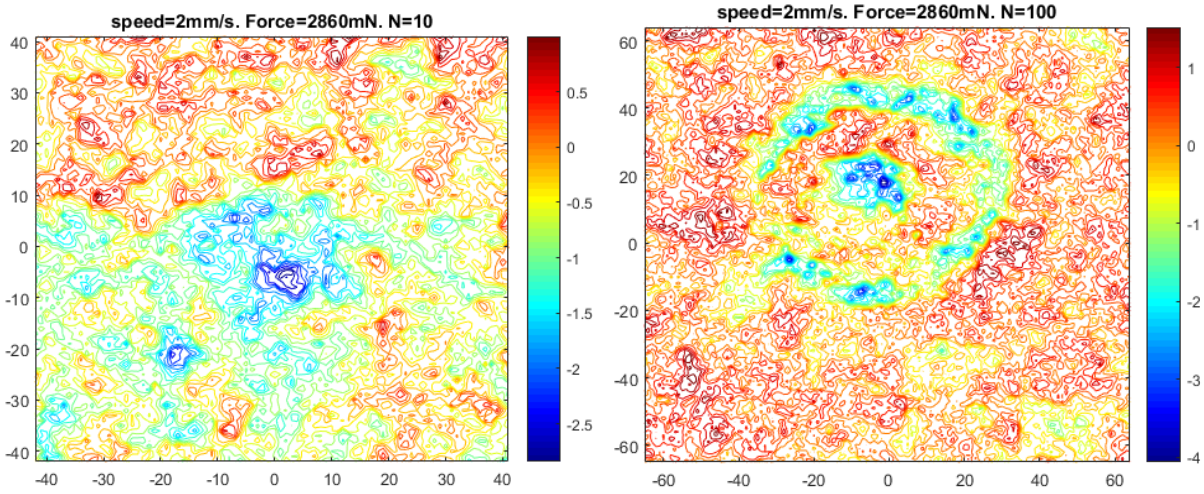

Figure 5.37 Neutral Density filter with OD=4. Left: example of damage for N=10. Right: example of damage for N=100.

An example of the results at N=10 is shown in Figure 5.38. The indentation depths reveal a quasi-elastic deformation of the specimen and increases marginally for higher coating thicknesses (about 0.004 µm for ND400). The average diameter also increases from about 20 µm (ND200) to about 25 µm (ND400).

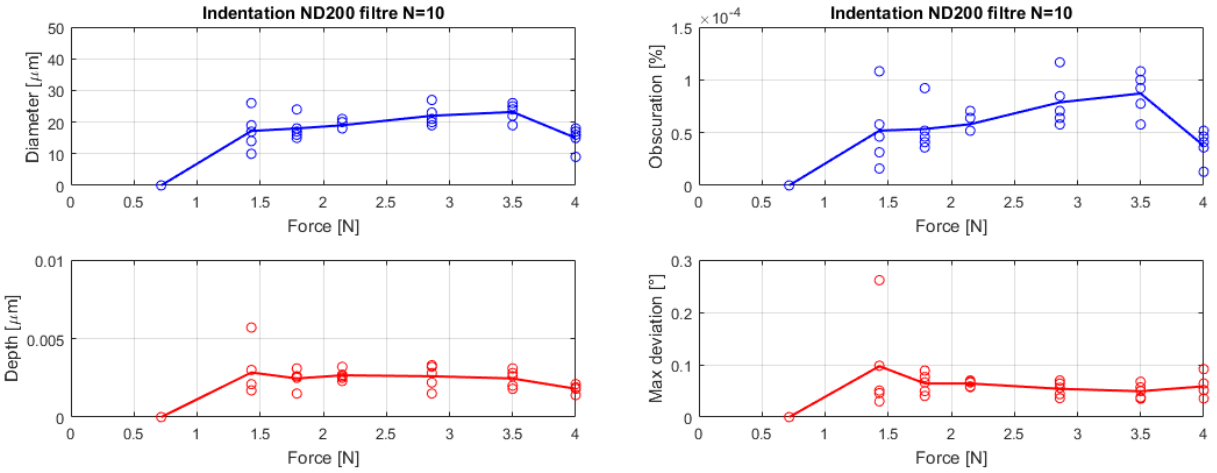

Figure 5.38 Neutral Density filter with OD=2 with contact repeated 10 times. Left: Diameter and depth of the indentations. Right: Obscuration and maximum deviation of the rays.

When the impingement is repeated 100 times (Figure 5.39 and Figure 5.40) the diameter of the central dig increases by a few micrometres, probably due to small variations in the contact location during the test. In all the tests, forces of 1 N and below didn't generate any damage.

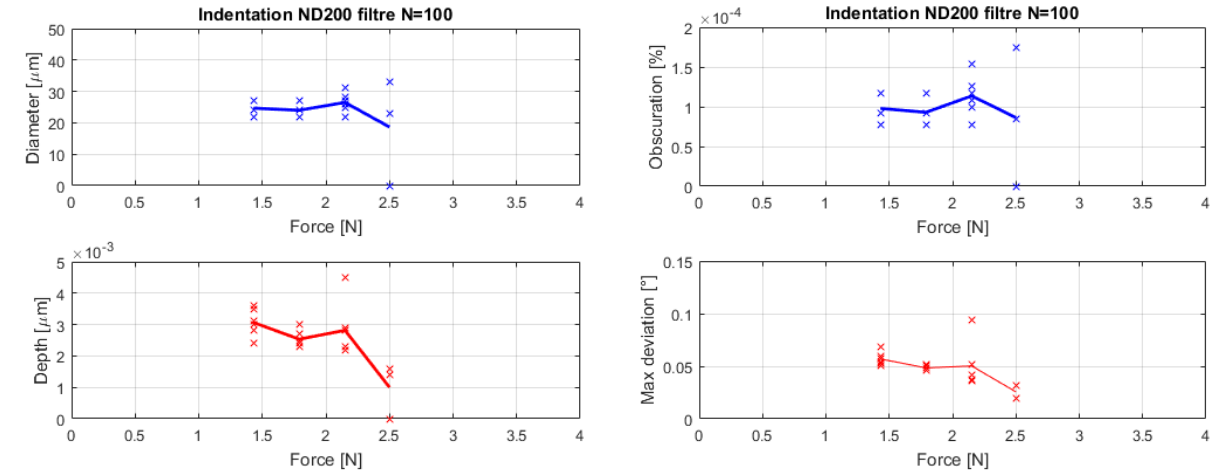

Figure 5.39 Neutral Density filter with OD=2 with contact repeated 100 times. Left: Diameter and depth of the indentations. Right: Obscuration and maximum deviation of the rays.

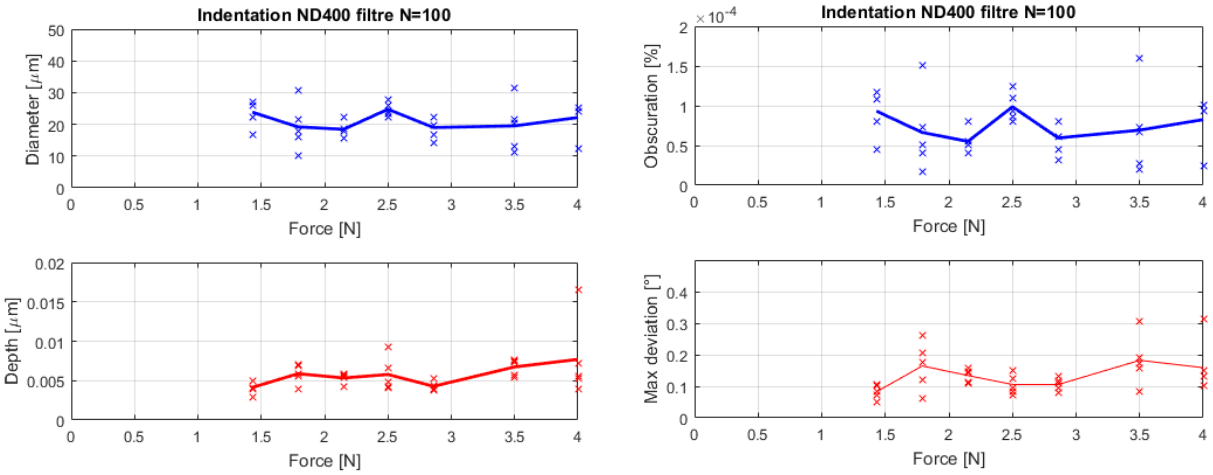

Figure 5.40 Neutral Density filter with OD=4 with contact repeated 100 times (central dig size). Left: Diameter and depth of the indentations. Right: Obscuration and maximum deviation of the rays.

In the ND300 and ND400 a ring was also generated by the N=100 test. The external diameter of the ring is comparable in both the specimens and is shown in Figure 5.41 for the ND400 one.

The depth of the ring was always smaller than the dig depth and decreased for lower contact forces and lower coating thicknesses. Related to this, in the ND300 specimen the ring was never complete but, instead, was composed by a series of short arcs.

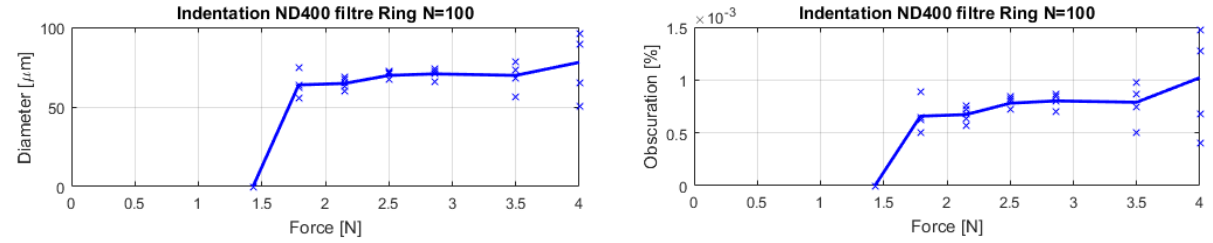

Figure 5.41 Neutral Density filter with OD=4 with contact repeated 100 times (ring size). Left: Diameter of the indentations. Right: Obscuration of the rays.

5.5.6 Dielectric coatings on soft glass substrates (refractive elements)

This test has been performed using CaF2 windows, one uncoated and another one with an IR broadband coating. As can be seen in Figure 5.42 and Figure 5.43, a central dig is created but, unlike the other cases, the material is characterized by a strong anisotropy. In the uncoated material (Figure 5.42), the central hole is elongated and the pile-up of the material is concentrated in three 90° spaced locations. The coated material showed a single preferential direction for the pile-up (Figure 5.43).

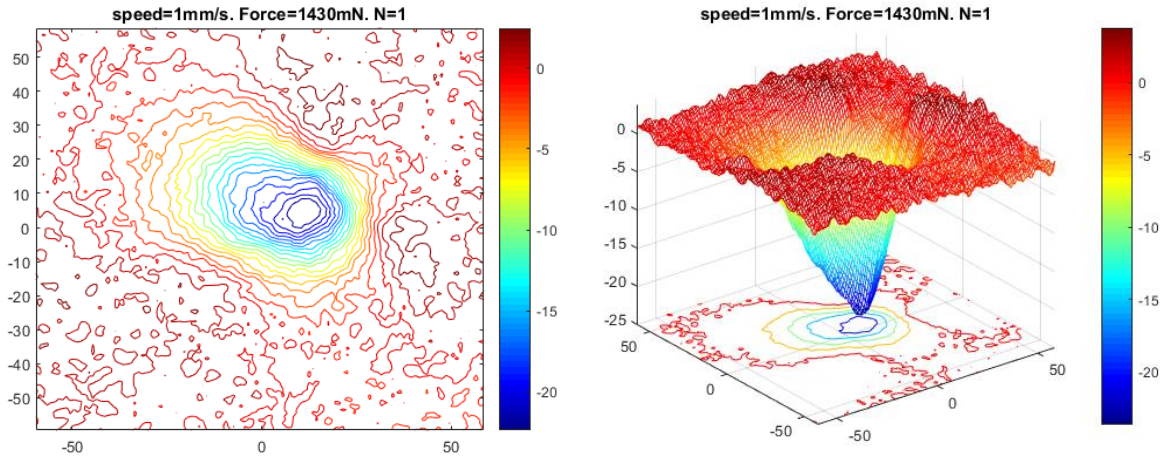

Figure 5.42 Example of damage on uncoated CaF_2 glass. Left: 2D view. Right: 3D view.

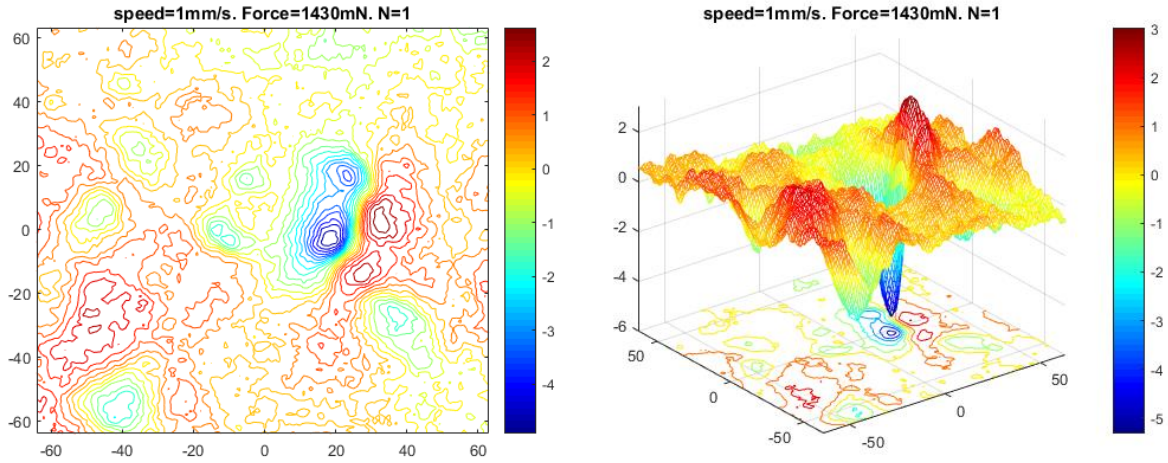

Figure 5.43 Example of damage on IR broadband coated CaF_2 glass. Left: 2D view. Right: 3D view.

The CaF_2 results are shown in Figure 5.44 and the diameters of the indentation well follow the theoretical values. The difference between N=1 and N=100 cases appears to be just related to the variation of the impinging location.

The same material with the IR coating appeared to have an increased resistance as shown in Figure 5.45 and for lower forces appears to work in a purely elastic regime. The damages for N=100 between the uncoated and IR coated cases showed little to no differences.

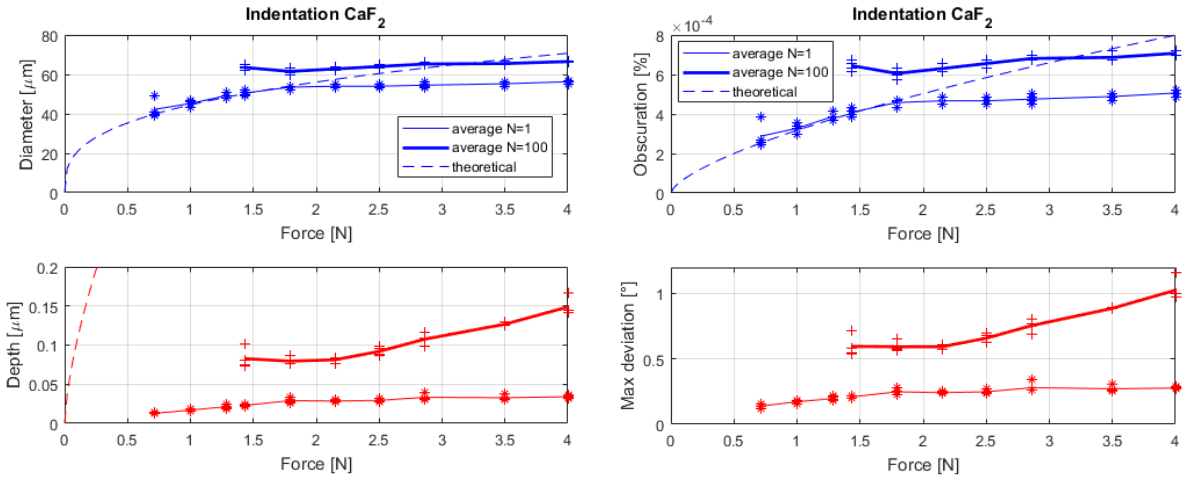

Figure 5.44 Uncoated CaF_2 glass with contact repeated 1 and 100 times. Left: Diameter and depth of the indentations. Right: Obscuration and maximum deviation of the rays.

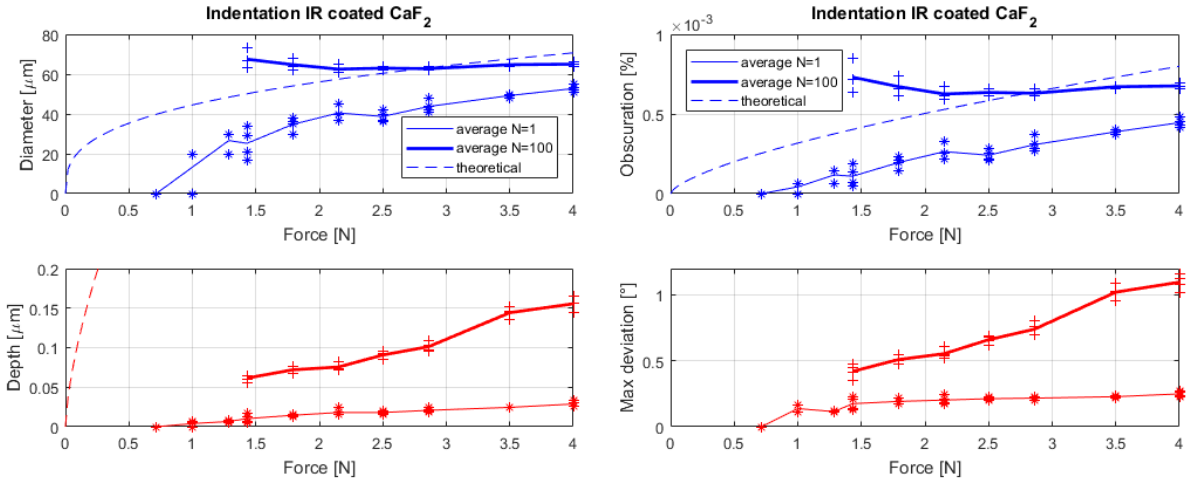

Figure 5.45 IR coated CaF_2 glass with contact repeated 1 and 100 times. Left: Diameter and depth of the indentations. Right: Obscuration and maximum deviation of the rays. Theoretical results refereed to the uncoated material.

5.5.7 Dielectric coatings on hard glass substrates (refractive elements)

A fused silica substrate has been tested as a reference to analyse the effect of the two different broadband coatings: one for the visible range (350-700 nm) and one for the near infrared (1050-1700 nm). This material has been chosen as it has a lower Poisson coefficient with respect to most of the glasses and higher stress can be expected at the interface with the coating.

As usual, the 3 specimen shown in Figure 5.46 (left) have been tested impinging them 1 or 100 times with different forces. In none of the cases, some damage has been recorded. The only exception is the uncoated case impinged 100 times where 2 and 1 extremely small pits appeared at 1.5 mm/s and 2 mm/s of measurement speed respectively. The three digs were located one near the other indicating a zone of the glass with slightly poorer mechanical properties.

The presence of the coating was probably sufficient to decrease the stresses in the substrate material enough to have a purely elastic indentation.

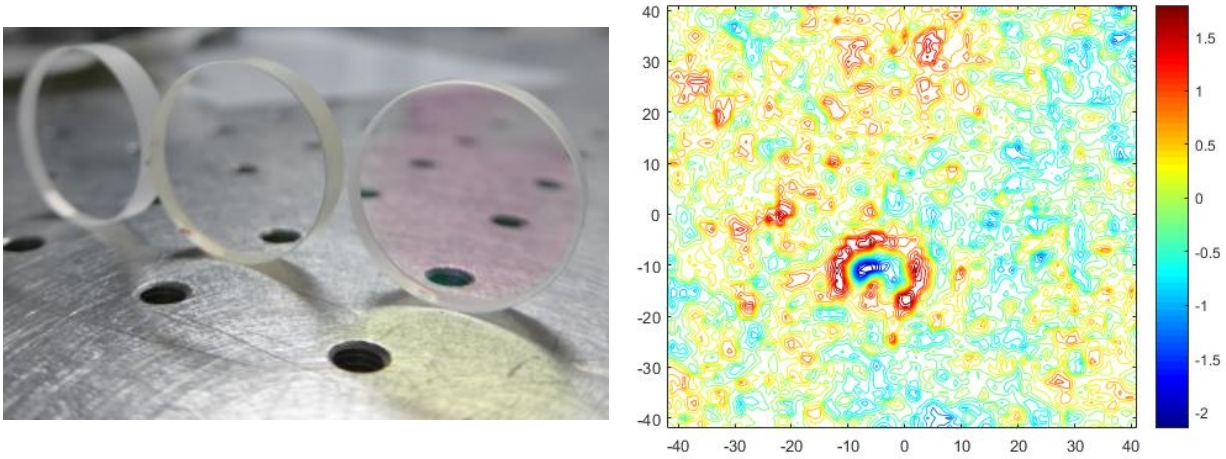

Figure 5.46 Left: fused silica glasses tested. From left to right: uncoated, VIS coating, and NIR coating. Right: uncoated fused silica. Example of one of the 3 pits found.

5.6 Conclusion and future improvements

The main effects due to damages on the surfaces of optical elements can be a loss of throughput and a scattering of the light. To predict those values and define a measuring strategy and, therefore, an alignment procedure a theoretical and an experimental approach is possible.

The theoretical approach using the Hertzian theory proved to be an effective method for uncoated materials. Unfortunately, those materials are quite uncommon in high performance optical systems. A theoretical approach of coated materials is more complicated due to the lack of information about the production process and the materials involved in the coatings.

As a general rule, when using soft substrates (e.g. aluminium, copper, CaF_2, ZnSe) the optical element behaviour is similar for the uncoated and coated case and thinner coatings on hard substrates exhibit higher resistance but in most of the cases the outcome of the test were difficult to quantify.

For this reason, an experimental approach is always preferable and a campaign to perform with different CMM measurement speeds has been defined and completed. This campaign has been performed with a SFM and a L20D2 stylus working in axial direction to simulate the most stressful condition for the material. An increasing number of impingement has been performed on the same location to highlight micro-damages impossible to detect with the MFT and to verify the effect of the fatigue on the specimen.

The results confirmed the expected theoretical prediction: for soft materials, the damage appears as a central dig and the presence of coating increase the specimen resistance. For hard glasses, the damage appears as a central dig eventually with an annular pile-up of material and is usually more severe when the overall thickness of the coatings is higher.

Similar tests must be performed for every material to measure during the optical system alignment and the outcome must be used to choose the most appropriate measurement strategy (number of points, measurement direction, measurement speed, stylus, and CMM module).

For our applications, a standard procedure has been defined. It includes the repetition of the tests presented here to simulate the most stressful conditions for the material, the comparison of the obtained value with

the requirements, and the replication of the same tests with stylus, module, and parameters similar to the ones defined by the updated alignment strategy.

The choice of some of the parameters like measurement direction and CMM module are limited by the mechanical design of the instrument while number of points, measurement speed, and stylus are in contrast with the accuracy of the measurement. The choice of those parameters will be chosen in order to satisfy both the accuracy and the damage requirements and, considering that the maximum stresses analysed in this chapter can be easily reduced by 2 or more orders of magnitude without affecting the accuracy, it is reasonable to expect a satisfactory combination of those parameters.

5.7 References

[5.1] McLeod JH, Sherwood WT. A proposed method of specifying appearance defects of optical parts. JOSA. 1945 Feb 1;35(2):136-8.

[5.2] MIL-O-13830. Optical components for fire control instruments; general specification governing the manufacture, assembly, and inspection of. 1954

[5.3] Young M. The scratch standard is only a cosmetic standard. In Surface Characterization and Testing II 1989 Dec 20 (Vol. 1164, pp. 185-191). International Society for Optics and Photonics.

[5.4] ANSI/OEOSC OP1.002-2017: Optics and Electro-Optical Instruments – Optical Elements and Assemblies – Surface Imperfections.

[5.5] ISO 10110-7:2017. Optics and photonics — Preparation of drawings for optical elements and systems — Part 7: Surface imperfections

[5.6] ISO 14997:2017. Optics and photonics — Test methods for surface imperfections of optical elements

[5.7] Aikens DM. Meaningful surface roughness and quality tolerances. In International Optical Design Conference 2010 Jun 13 (p. ITuD3). Optical Society of America.

[5.8] Stover JC. Optical scattering: measurement and analysis. Bellingham: SPIE optical engineering press; 2012.

[5.9] Lewis IT, Ledebuhr AG, Bernt ML. Stray-light implications of scratch/dig specifications. In Optical Scatter: Applications, Measurement, and Theory 1991 Dec 1 (Vol. 1530, pp. 22-35). International Society for Optics and Photonics.

[5.10] Van Vliet WP, Schellekens PH. Accuracy limitations of fast mechanical probing. CIRP annals. 1996 Jan 1;45(1):483-7.

[5.11] Meli F, Küng A. AFM investigation on surface damage caused by mechanical probing with small ruby spheres. Measurement Science and Technology. 2007 Jan 12;18(2):496.

[5.12] Johnson KL, Johnson KL. Contact mechanics. Cambridge university press; 1987 Aug 28.

[5.13] Louapre D, Breder K. Hertzian Indentation Stress Field Equations. International Journal of Applied Ceramic Technology. 2015 Sep 1;12(5):1071-9.

[5.14] Knight CG, Swain MV, Chaudhri MM. Impact of small steel spheres on glass surfaces. Journal of Materials Science. 1977 Aug 1;12(8):1573-86.

[5.15] Chai H. Crack propagation in glass coatings under expanding spherical contact. Journal of the Mechanics and Physics of Solids. 2006 Mar 1;54(3):447-66.

[5.16] Pepi JW. Strength Properties of Glass and Ceramics. Spie Press; 2014 May 30.

[5.17] www.schott.com. Bending strength of optical glass and ZERODUR®. 2015

[5.18] EN 1288-5:2000. Glass in building - Determination of the bending strength of glass - Part 5: Coaxial double ring test on flat specimens with small test surface areas.

[5.19] Suratwala T, Wong L, Miller P, Feit MD, Menapace J, Steele R, Davis P, Walmer D. Sub-surface mechanical damage distributions during grinding of fused silica. Journal of non-crystalline solids. 2006 Dec 15;352(52-54):5601-17.

[5.20] Schwarzer N, Richter F, Hecht G. The elastic field in a coated half-space under Hertzian pressure distribution. Surface and Coatings Technology. 1999 May 12;114(2-3):292-303.

[5.21] Van der Zwaag S, Field JE. The effect of thin hard coatings on the Hertzian stress field. Philosophical magazine A. 1982 Jul 1;46(1):133-50.

[5.22] Frey H. Handbook of thin film technology. Khan HR, editor. Berlin, Heidelberg: Springer; 2015 May 6.

[5.23] Chudoba T, Schwarzer N, Richter F. Determination of elastic properties of thin films by indentation measurements with a spherical indenter. Surface and Coatings Technology. 2000 May 1;127(1):9-17.

[5.24] Vinci RP, Vlassak JJ. Mechanical behavior of thin films. Annual Review of Materials Science. 1996 Aug;26(1):431-62.

[5.25] Cortie MB. The weird world of nanoscale gold. Gold Bulletin. 2004 Mar 1;37(1-2):12-9.

[5.26] Klemberg-Sapieha JE, Oberste-Berghaus J, Martinu L, Blacker R, Stevenson I, Sadkhin G, Morton D, McEldowney S, Klinger R, Martin PJ, Dligatch S. Mechanical characteristics of optical coatings prepared by various techniques: a comparative study. Applied optics. 2004 May 1;43(13):2670-9.

[5.27] Çetinörgü E, Baloukas B, Zabeida O, Klemberg-Sapieha JE, Martinu L. Mechanical and thermoelastic characteristics of optical thin films deposited by dual ion beam sputtering. Applied optics. 2009 Aug 10;48(23):4536-44.

[5.28] Parks RE, Kuhn WP. Optical alignment using the point source microscope. InOptomechanics 2005 2005 Sep 9 (Vol. 5877, p. 58770B). International Society for Optics and Photonics.

[5.29] Parks RE. MicroFinish Topographer: surface finish metrology for large and small optics. InOptical Manufacturing and Testing IX 2011 Sep 27 (Vol. 8126, p. 81260D). International Society for Optics and Photonics.

[5.30] http://www.renishaw.com

[5.31] http://www.matweb.com

[5.32] www.crystran.co.uk

[5.33] Bass M, DeCusatis C, Enoch J, Lakshminarayanan V, Li G, MacDonald C, Mahajan V, Van Stryland E. Handbook of Optics, Volume IV: Optical Properties of Materials. Nonlinear Optics, Quantum Optics. 2009 Oct;4.

[5.34] Balasubramanian K, Wilson DW, Muller RE, Kern BD, Sidick E. Thickness-dependent optical properties of metals and alloys applicable to TPF coronagraph image masks. InTechniques and Instrumentation for Detection of Exoplanets III 2007 Sep 19 (Vol. 6693, p. 66930Z). International Society for Optics and Photonics.

6 Alignment accuracy validation via a dummy optical system

6.1 Introduction

In order to validate the whole procedure an optical system has been aligned and tested. The alignment has been performed following the recommendations from chapter 2 with the goal of a maximum error equal to 10 µm on the shims or limited by the expected accuracy of the CMM. Those accuracy limits in each degrees of freedom have been calculated both theoretically, with the software presented in chapter 3, and experimentally, using the results obtained by multiple measurements of the system.

The two methods have also been compared to understand if the software is able to predict the CMM precision for each optical element.

A final comparison between the expected misalignments of the system and the images obtained with an interferometer has been done to appreciate the CMM values trueness and to have an independent verification.

6.2 Optical and mechanical design of the system

The optical design has been developed in order to have a system were as many degrees of freedom as possible could be verified in an optical way. One of the main problem while using an interferometer is related to the double path of the optical beam needed to generate the interferometric fringes.

This, in addition to the compensation of tilt and coma aberrations when both a tilt and decentre of the optical element are present ([6.6]), can complicate the identification of the different misalignments.

Following those considerations and trying to keep the number of optical elements low, the optical system sketched in Figure 6.1 has been developed.

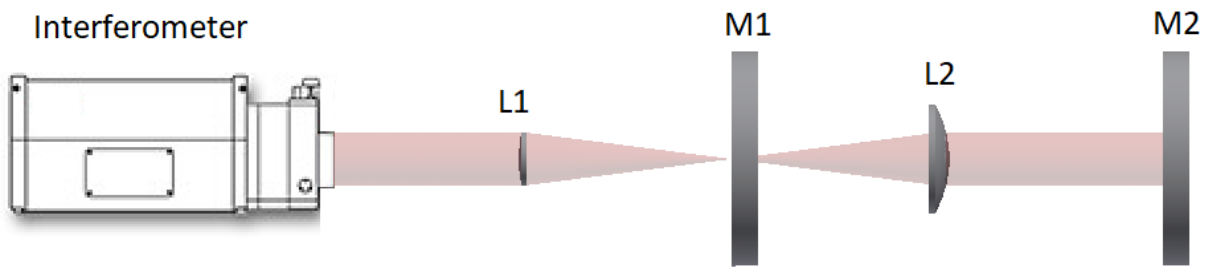

Figure 6.1. Representation of the dummy optical system while measured with the interferometer.

The system is composed by two reflective and two refractive optical elements and is thought to be verified with the interferometer having a transmission flat reference surface. The main mechanical dimensions and

optical properties of the elements are summarized in Table 6.1. Both the lenses have a focal length calculated at 587.6 nm. As the interferometric test will be performed at 632.8 nm, the focal length at this wavelength has been derived using Sellmeier and Lens-maker's equations.

Table 6.1. Main characteristics of the optical elements used.

	L1 lens	**M1 mirror**	**L2 lens**	**M2 mirror**
Type	Biconvex spherical	Flat	Plano-convex spherical	Flat
Thorlabs Model	LBF254-100	ME2-P01	LA1031	ME2-G01
Material	N-BK7	Float glass	N-BK7	Float glass
Coating	Uncoated	Silver+SiO_2	Uncoated	Aluminium+SiO_2
Diameter [mm]	25.35±0.05	50.7±0.1	29.95±0.05	50.7±0.1
Focal length [mm]	100.0±1.0 @587.6 nm	-	100.0±1.0 @587.6 nm	-
	100.3±1.0 @632.8 nm	-	100.3±1.0 @632.8 nm	-
RoC 1 [mm]	60.02	∞	∞	∞
RoC 2 [mm]	-353.30	-	-51.5	-
Central thickness [mm]	4.0±0.1	3.1±0.1	4.7±0.1	3.1±0.1
Surface power	3λ/2 (spherical)	5λ (flatness)	λ/2 (flatness) 3λ/2 (spherical)	5λ (flatness)
Surf. irregularity	λ/4	-	λ/4 PV	-

The first configuration foresees the presence of L1 and M1. The mirror will be used to align the optical beam to the interferometer and the L1 tilt and defocus will be seen by the returning beam. After the M1 mirror removal, the external parts of the beam will be reflected by M2 and the flat surface of L2, allowing for the evaluation of their tilts. The beam passing through L1 and L2 will be reflected by M2 and it will highlight the relative decentring and defocus between L1 and L2.

The mechanical design of the system is shown in Figure 6.2. The four elements have been glued to the optomechanical support with cyanoacrylate. Those elements are connected to the optical bench via three M4 screws and are fixed laterally and in the focus direction with three pins.

The supports will be aligned placing holed shims below the M4 screws and fixing rectangular shims between the mount and the L-shaped elements. In order to keep the shims in position each L element is fixed to the optomechanical support using an M2 screw. The rotation of those pieces around their screw axis during the installation is eliminated thanks to a small cylindrical pin.

The bench is used as a reference as it accommodates the steel sphere that will be periodically used to realign the system. A larger plate is finally used to mount the bench and will be connected to the CMM granite plate. Both the connections are done using 3 screw and 6 spherical washers in order to minimize the bending of the system while fixing it.

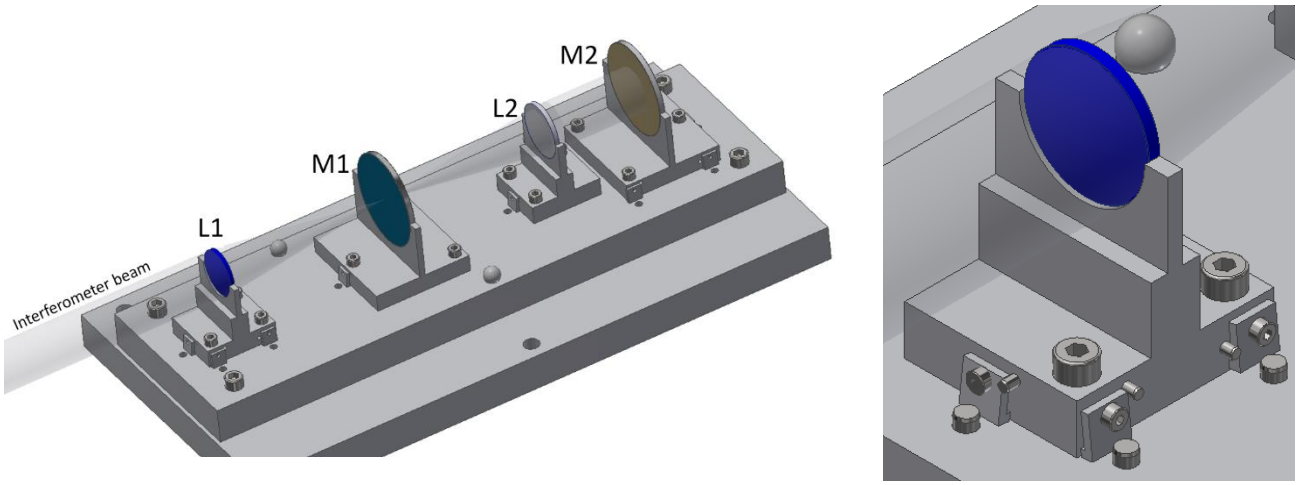

Figure 6.2. Mechanical design of the dummy system. Left: overall view with optical beam (semi-transparent). Right: detailed view of a single mount.

6.3 Mechanical alignment expected performances and software validation with MPM

Before aligning this system, two possible methods can be used to estimate the maximum reachable accuracy. The first one consists in the use of the software presented in chapter 3 and can be rapidly performed before the definition of the mechanical design. The second one is called repositioning method and requires that the whole system is mounted and that the alignment procedure is well defined. In this case, the results are obtained repeating the optical element measurements in different conditions and evaluating the variations between them.

6.3.1 Software simulation

The system has been simulated considering the barycentre of the three reference spheres as the origin (0, 0, 0) and the uncertainty of the 3 spheres locations as negligible with respect to the optical elements ones (see chapter 2).

The optical parameters and the geometrical dimensions used are the ones provided by the manufacturer while the acquisition points where 32 for each surface of the lens and 24 for the mirrors.

To estimate the acquisition time is has been considered that the reference points are acquired at the beginning of the alignment. The measurement and the alignment of each optical surface, then, requires approximately 5 minutes and, based on preliminary operational tests, a good alignment is reached within five repetitions. With those input the whole procedure is expected to last about 2.5 hours.

The results obtained by the simulation software are shown in Figure 6.3, Figure 6.4, Figure 6.5, and Figure 6.6. Due to the low alignment time, the temperature drift has a negligible effect. Moreover, the relatively small volume of the system leads to small volumetric errors. For this reason, the measurement accuracy of most of the elements is expected to improve increasing the sampling points. The values for each element have been summarized in Table 6.2.

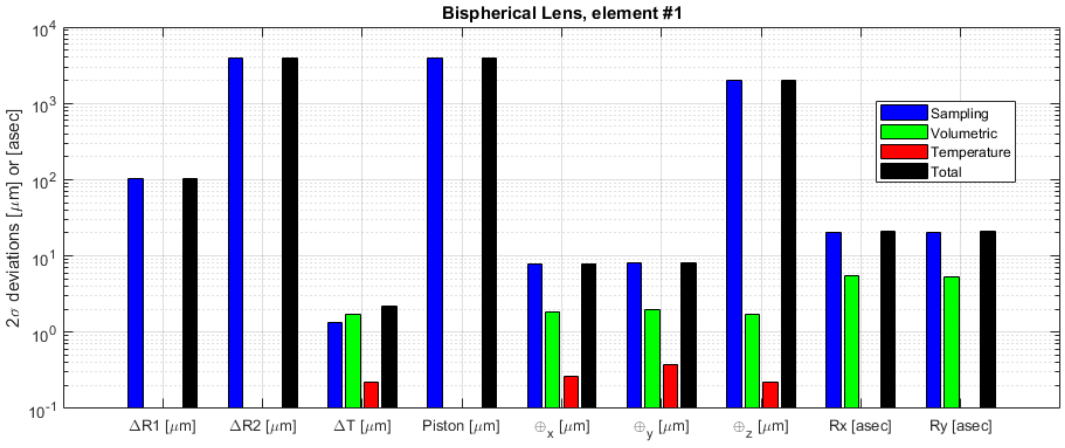

Figure 6.3. Expected deviations of the first lens (bispherical) by simulation software.

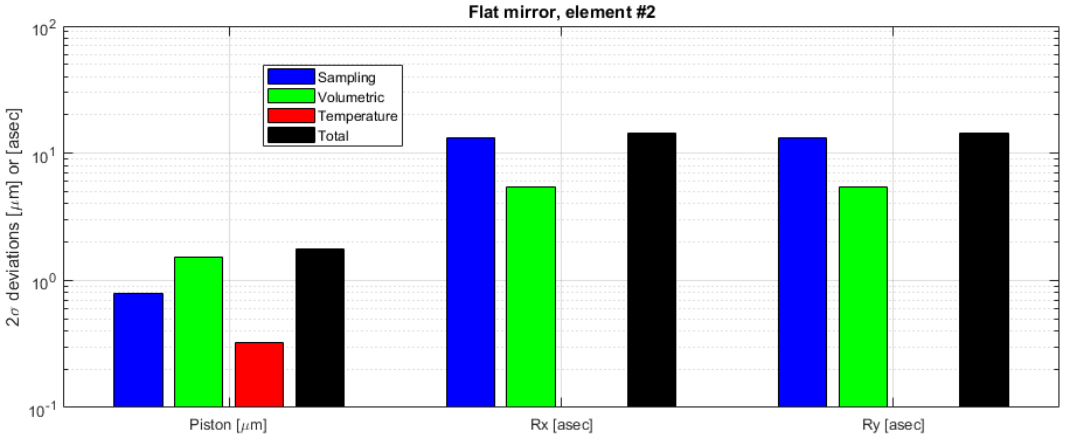

Figure 6.4. Expected deviations of the first mirror by simulation software.

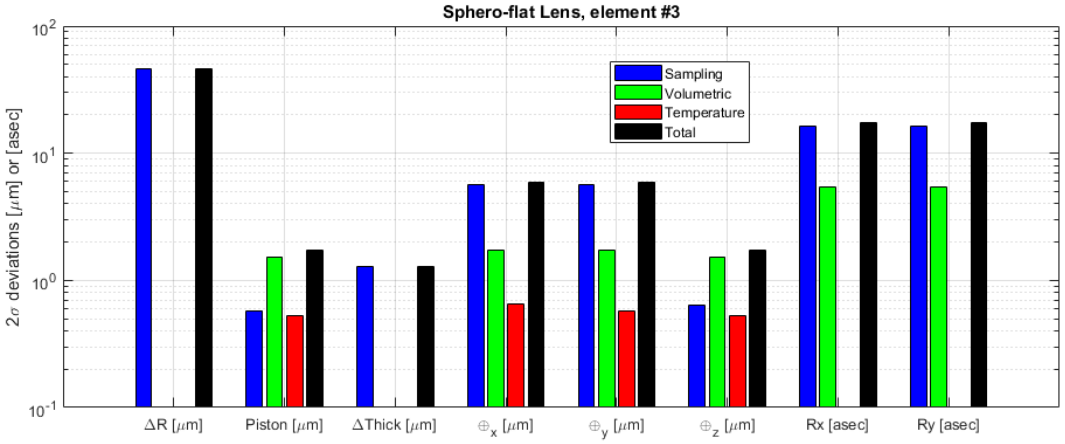

Figure 6.5. Expected deviations of the second lens (plano-spherical) by simulation software.

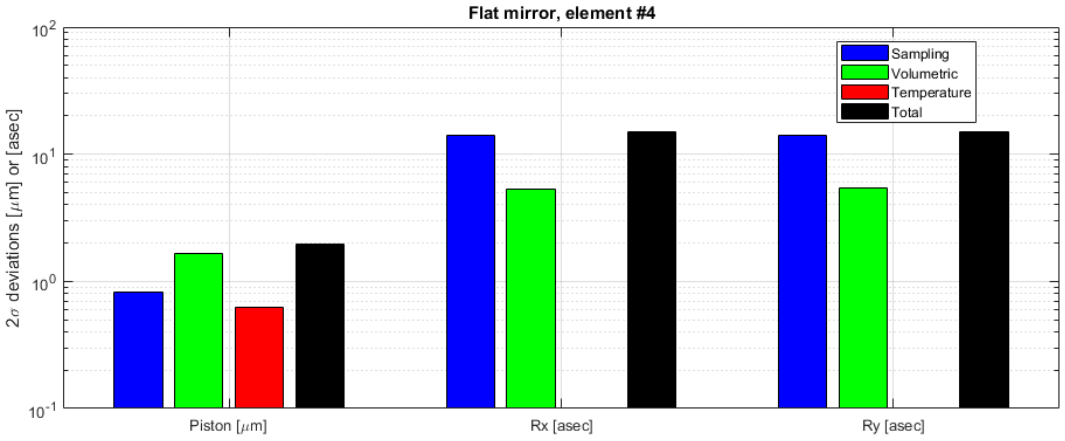

Figure 6.6. Expected deviations of the second mirror by simulation software.

Table 6.2. 2σ values obtained by the simulation software. The coloured background marks the main error source and the bold numbers are the total values.

		RoC [µm]		Thickness	Piston	Position [µm]			Rotation [arcsec]	
		Surf1	Surf2	[µm]	[µm]	X	Y	Z	Rx	Ry
L1	Samp.	104.6	3982	1.3	3988	7.7	8.0	1994	20.5	20.1
	Volum.	-	-	1.7	-	1.9	2.0	1.7	5.4	5.4
	Temp.	-	-	0.2	-	0.3	0.4	0.2	-	-
	TOT	**104.6**	**3982**	**2.4**	**3988**	**8.0**	**8.2**	**1994**	**21.2**	**20.9**
M1	Samp.	-	-	-	0.8	-	-	-	13.3	13.2
	Volum.	-	-	-	1.5	-	-	-	5.4	5.4
	Temp.	-	-	-	0.3	-	-	-	-	-
	TOT	**-**	**-**	**-**	**1.7**	**-**	**-**	**-**	**14.3**	**14.3**
L2	Samp.	46.0	-	1.3	0.6	5.6	5.7	0.6	16.5	16.5
	Volum.	-	-	-	1.5	1.7	1.7	1.5	5.4	5.4
	Temp.	-	-	-	0.5	0.6	0.6	0.5	-	-
	TOT	**46.0**	**-**	**1.3**	**1.7**	**5.9**	**5.9**	**1.7**	**17.4**	**17.4**
M2	Samp.	-	-	-	0.8	-	-	-	14.1	14.0
	Volum.	-	-	-	1.7	-	-	-	5.3	5.4
	Temp.	-	-	-	0.6	-	-	-	-	-
	TOT	**-**	**-**	**-**	**2.0**	**-**	**-**	**-**	**15.1**	**15.0**

6.3.2 Multi positioning method (MPM)

Due to the large number of uncertainty sources in a CMM, different methods have been developed in order to have an estimation of the overall uncertainty of a certain measurement process (task specific uncertainty, see [6.3], [6.4], and chapter 3). One of the methods consists in the repeated measurement of the workpiece in different conditions and can be used both to reduce the uncertainty while measuring a specific part or to estimate the uncertainty of a part in case a similar element is planned to be measured only once in the future (see [6.5]). An example of the first instance can be seen in [6.6] while in our case it will be used to compare the uncertainties obtained by the simulation software.

The procedure consists in the measurement of the dummy system in a basic position (noted ad j=1, left in Figure 6.7) for five times (i=1:5). The same measurements are then carried out in three other orientations (varying also the location on the CMM volume) rotating the system around each of the three reference

system axes from the basic position (j=1:4). Note that the mechanical design has been developed in order to have negligible deformations due to gravity in the different orientations.

For each useful geometrical or dimensional characteristic (y), the standard deviation is calculated as following

$$ {}^{j}S = \sqrt{\frac{1}{n_1 - 1}\sum_{i=1}^{n_1}\left({}^{ij}y - \frac{1}{n_1}\sum_{i=1}^{n_1}{}^{ij}y\right)^2} \tag{6.1} $$

Where n_1=5 is the number of cycles and n_2=4 is the number of orientations.

The standard uncertainty is then calculated as the quadratic average on those standard deviations.

$$ u_{rep} = \sqrt{\frac{1}{n_2}\sum_{j=1}^{n_2}({}^{j}S)^2} \tag{6.2} $$

This uncertainty estimation can be related in general to the repeatability of the CMM, to the sampling strategy, and to the form error of the workpiece. Due to the high quality of the optical surfaces, the third contribution can be ignored.

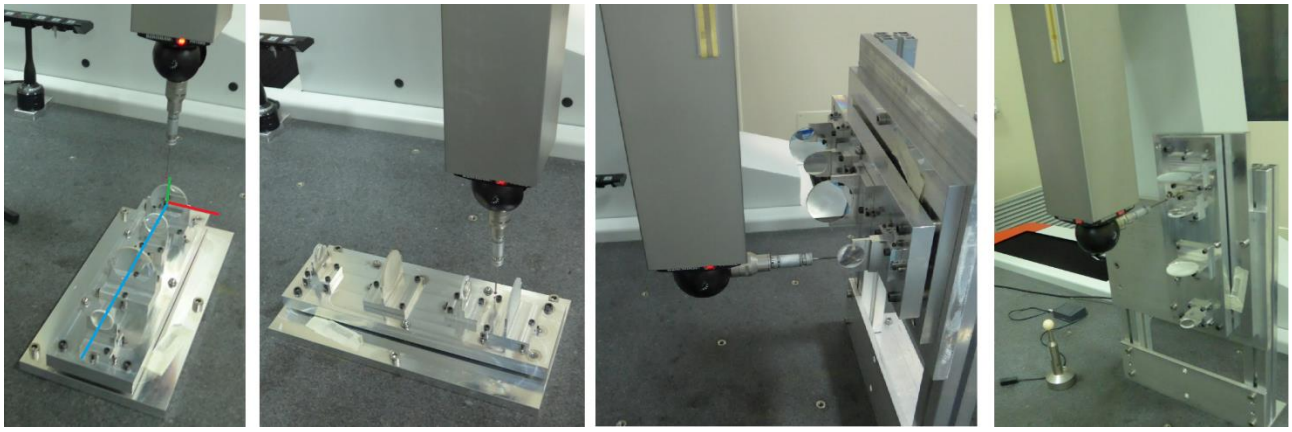

Figure 6.7. Four directions used for the measurement. From left to right: basic (Z oriented as the –X axis of the CMM), -90° rotation around the Y axis, 90° rotation around the Z axis, 90° rotation around the X axis. In the first picture, the reference system used is shown.

The second component of the uncertainty is called u_{geo} and takes into account the CMM geometrical errors. In addition to them, also all the effects related to the repositioning of the element, including the deformations due to the gravity, are captured by it.

It can be calculated as

$$ u_{geo} = \sqrt{\frac{1}{n_2(n_2 - 1)}\sum_{j=1}^{n_2}\left({}^{j}y - \frac{1}{n_1 n_2}\sum_{i=1}^{n_1}\sum_{j=1}^{n_2}{}^{ij}y\right)^2} \tag{6.3} $$

The overall expanded uncertainty (95%) can then be calculated as

$$U = k\sqrt{u_{rep}^2 + u_{geo}^2} \tag{6.4}$$

Where k has been found to be equal to 2.18 using the Welch-Satterthwaite formula and considering $\nu = (n_1 - 1)n_2$ as the number of degrees of freedom.

The overall expanded uncertainty of the average value found during this process, can be calculated instead as

$$U = 2.18\sqrt{\frac{u_{rep}^2}{n_1} + \frac{u_{geo}^2}{n_2}} \tag{6.5}$$

It is important to notice that this method does not consider the geometrical errors that are isotropic into the CMM measuring volume. This value is the -0.56 µm at 50 mm distance considered in chapter 3.5.2.

In case this correction is needed, mainly for CMM without thermal compensation of located in environment characterized by low thermal stability, a series of measurements (n_3) of a gauge blocks as long as the longest distance to be measured must be performed and the average value of must be used to correct the obtained distances as following

$${}^{ij}y_{corr} = {}^{ij}y - \frac{{}^{ij}y}{n_3}\sum_{i=1}^{n_3}\frac{{}^{i}L_{measstd} - L_{calstd}}{L_{calstd}} \tag{6.6}$$

where $L_{emasstd}$-L_{calstd} is the difference between the measured length and the calibrated length of the gauge block.

Its uncertainty (u_{corr}) will also have to be considered including the uncertainty of the gauge block (u_{calstd}) and the standard deviation of the length measurements performed ($u_{measstd}$).

$$u_{corr} = \frac{y_{nominal}}{L_{calstd}}\sqrt{u_{calstd}^2 + \frac{u_{measstd}^2}{n_3}} \tag{6.7}$$

The obtained value will be added to the other uncertainty sources in equation (6.4) and (6.5).

The obtained results are shown in Table 6.3. The repeatability and the geometrical contributions are usually comparable and only the radiuses of curvature estimations are always dominated by the repeatability.

Table 6.3. Uncertainty values obtained by the multi positioning method. The coloured background marks the main error source and the bold numbers are the total expanded uncertainties.

		RoC [µm]		Thickness	Piston	Position [µm]			Rotation [arcsec]	
		Surf1	Surf2	[µm]	[µm]	X	Y	Z	Rx	Ry
L1	u_{rep} 68%	24.1	703	0.4	-	1.3	2.1	1.0	4.0	3.2
	u_{geo} 68%	13.5	622	0.4	-	1.0	1.5	25.5	5.4	4.0
	U 68%	27.6	939	0.6	-	1.7	2.6	25.5	6.8	5.3
	U 95%	**60.1**	**2046**	**1.2**	**-**	**3.6**	**5.6**	**55.6**	**14.8**	**11.5**
M1	u_{rep} 68%	-	-	-	0.5	-	-	-	2.9	1.4
	u_{geo} 68%	-	-	-	0.7	-	-	-	3.2	2.9
	U 68%	-	-	-	0.9	-	-	-	4.4	3.0
	U 95%	**-**	**-**	**-**	**1.9**	**-**	**-**	**-**	**9.6**	**6.6**
L2	u_{rep} 68%	10.1	-	0.2	-	2.0	1.1	0.4	2.9	4.3
	u_{geo} 68%	4.9	-	0.3	-	0.3	0.9	9.3	2.9	3.6
	U 68%	11.2	-	0.4	-	2.1	1.4	9.4	4.2	5.6
	U 95%	**24.4**	**-**	**0.8**	**-**	**4.5**	**3.1**	**20.4**	**9.2**	**12.3**
M2	u_{rep} 68%	-	-	-	0.4	-	-	-	2.2	1.1
	u_{geo} 68%	-	-	-	1.5	-	-	-	4.5	2.7
	U 68%	-	-	-	1.5	-	-	-	5.0	2.9
	U 95%	**-**	**-**	**-**	**3.3**	**-**	**-**	**-**	**10.8**	**6.4**

The comparison between the results obtained by the simulation software and the MPM is shown in Table 6.4. In none of the results, the volumetric isotropic contribution has been considered. However, in almost every value the simulation software overestimates the expected measurement uncertainty, mainly due to the sampling contribution. The main reason for this behaviour could be found in the sampling uncertainty calculation by the simulation software (see Figure 3.25 in chapter 3): the anisotropy of the stylus while measuring one whole hemisphere of the calibration ball plays an important contribution to the standard deviation obtained.

While measuring the optical surfaces, instead, a small solid angle of the probe measuring directions is used, as the radius of curvature is usually larger with respect to the geometrical diameter of the lens. This condition decreases the anisotropy of the probing system and, therefore, reduces its uncertainty.

Table 6.4. 2σ values obtained by the simulation software (SS) and the Multi Positioning method (MPM). Δ shows the percentage overestimation of the SS with respect to the MPM.

		L1			M1			L2			M2		
		SS	MPM	Δ [%]	SS	MPM	Δ [%]	SS	MPM	Δ [%]	SS	MPM	Δ [%]
RoC1 [µm]		104.6	60.1	+74%	-	-		46.3	24.4	+90%	-	-	
RoC2 [µm]		3982	2046	+95%	-	-		-	-		-	-	
Thickness [µm]		2.4	1.2	+100%	-	-		1.3	0.8	+63%	-	-	
Piston [µm]		3988	-		1.7	1.9	-11%	1.7	-		2.0	3.3	-39%
Position [µm]	X	8.0	3.6	+122%	-	-		5.9	4.5	+31%	-	-	
	Y	8.2	5.6	+46%	-	-		5.9	3.1	+90%	-	-	
	Z	1994	55.6		-	-		1.7	20.4		-	-	
Rotation [arcsec]	X	21.2	14.8	+43%	14.3	9.6	+49%	17.4	9.2	+89%	15.0	10.8	+39%
	Y	20.9	11.5	+82%	14.3	6.6	+117%	17.4	12.3	+41%	15.0	6.4	+134%

The deviation from the nominal value can also be estimated starting from the MPM data. While some of the data provided by the manufacturer has no influence in this analysis, the focal length of the optical elements can be more critical to estimate.

In case of reflective spherical elements, the focal length is equal to

$$f = R - \frac{R}{2}\cos\left(\sin\frac{D}{2R}\right) \tag{6.8}$$

where R is the RoC and D is the diameter of the beam. Calculating it as

$$f = \frac{R}{2} \tag{6.9}$$

however, does not introduce any error in the calculation. Considering this second equation, the uncertainty on the focal length definition comes straightforward from the uncertainty of the RoC.

Considering refractive elements, instead, the focal length is calculated with the Lens-maker's equation

$$f = \frac{n\,R_1\,R_2}{(n-1)n(R_2 - R_1) + (n-1)^2\,t} \tag{6.10}$$

where R1 and R2 are the ROCs, n is the index of refraction and t the central thickness of the lens. In case of thin lenses, the equation can be simplified and becomes

$$f = \frac{R_1\,R_2}{(n-1)(R_2 - R_1)} \tag{6.10}$$

its uncertainty is then equal to

$$u_f = \sqrt{\frac{\partial f}{\partial R_1}^2 u_{R1}^2 + \frac{\partial f}{\partial R_2}^2 u_{R2}^2 + \frac{\partial f}{\partial n}^2 u_n^2} \tag{6.11}$$

where

$$\frac{\partial f}{\partial R_1} = \frac{R_2^2}{(R_1 - R_2)^2(n-1)} \tag{6.12}$$

$$\frac{\partial f}{\partial R_2} = \frac{-R_1^2}{(R_1 - R_2)^2(n-1)} \tag{6.13}$$

$$\frac{\partial f}{\partial n} = \frac{R_1 R_2}{(R_1 - R_2)(n-1)^2} \tag{6.14}$$

If a plano-spherical lens has to be considered, f is equal to

$$f = \frac{-R_2}{n-1} \tag{6.15}$$

and the uncertainty

$$u_f = \sqrt{\frac{u_{R2}^2}{(n-1)^2} + \frac{R_2^2\,u_n^2}{(n-1)^4}} \tag{6.16}$$

In Table 6.5 the nominal value of the focal length and their deviations are shown. The manufacturer provides information about the focal length (in a ±1% range), the RoCs and the central thickness (in a ±0.1 mm range). Retrieving the focal length of the element starting from the geometrical data, however, strongly reduce the uncertainty of the focal lengths and values of 99.875±0.027 mm and 100.369±0.011 mm have been found.

Those ones and the uncertainties presented in the previous tables take in consideration only the variation of thickness and radius of curvature for the actual focal length calculation and relays on the refractive index provided by the manufacturer (n=1.5167).

According to [6.7], this value is included in a range of ±0.0005 (grade 3). Considering a standard deviation of 0.00029 and applying the formula (6.11) it is clear that the refractive index is the most critical uncertainty source while evaluating the focal length of a lens.

Table 6.5. Nominal value and standard deviation of the two lenses. All the values are calculated at a wavelength of 632.8nm.

	[mm]	L1	L2
Manufacturer datasheet	focal length	100.3±0.6	100.3±0.6
	from geometry	99.3±0.6	100.0±0.6
MPM	Deviation from datasheet (f)	100.9±0.6	100.8±0.6
	from geometry	99.875	100.369
	Average uncertainty	±0.027	±0.011
	Average uncertainty – with u_n	±0.061	±0.057
	Measurement uncertainty	±0.057	±0.023
	Measurement uncertainty – with u_n	±0.078	±0.060

Building astronomical optical systems, however, demands higher quality of the glasses and requirement of ±0.0002 or even ±0.0001 are common. With those values, the focal length uncertainty is strongly reduced and the lens can be aligned in the axial direction with an accuracy of tens of microns.

In Table 6.6 the expected uncertainties obtained by the MPM have been compared to the resolution of the metallic shims that will be used during the alignment. As it can be noticed, only the focal plane position is clearly limited by the CMM accuracy. On the opposite side, the resolution of the metallic shims divided by the distances between their mounting locations is clearly the limiting factor when aligning the optomechanical elements in tip-tilt.

Table 6.6. Alignment limiting factors (orange background) for all the meaningful degrees of freedom.

	L1		**M1**		**L2**		**M2**	
	MPM	Shim	MPM	Shim	MPM	Shim	MPM	Shim
Decentre X [µm]	3.6	5	-	-	4.5	5	-	-
Decentre Y [µm]	5.6	5	-	-	3.1	5	-	-
Focal plane position [µm]	55.8	5	1.9	5	20.5	5	3.3	5
Rotation Rx [arcsec]	14.8	34	9.6	23	9.2	34	10.8	23
Rotation Ry [arcsec]	11.5	34	6.6	23	12.3	34	6.4	23

6.4 Alignment procedure and results

The first operation to perform during an alignment is to define a reliable reference system. In this case, three planes on the optical bench have been used: the large plane where the optomechanical components will sit as the primary, the long side as secondary, and the front one as tertiary. The origin has been defined, therefore, as the intersection of the three.

The repeatability of the reference system will be limited by the flatness of the planes; however, this operation is needed in order to maintain a similar value of shims below the optomechanical elements and to be able to install the instrument in a quasi-nominal position.

The internal references, in this case the three steel spheres, then, must be measured and their location defined with respect to the reference system. The obtained substitute geometries will be used as the references to align the optical elements and a final reference system will be located in a chosen location roto-translating the original one.

The operation is depicted in Figure 6.8 with the 3-planes reference system on the top left of the image, the final one at the centre of the mirror with the Z-axis along the optical beam direction and the 3 spheres (A, B and C). The optic mounts have been installed to verify the alignment range. In this way if a problem is spotted it is still possible to modify the supports of insert an offset to the final reference system.

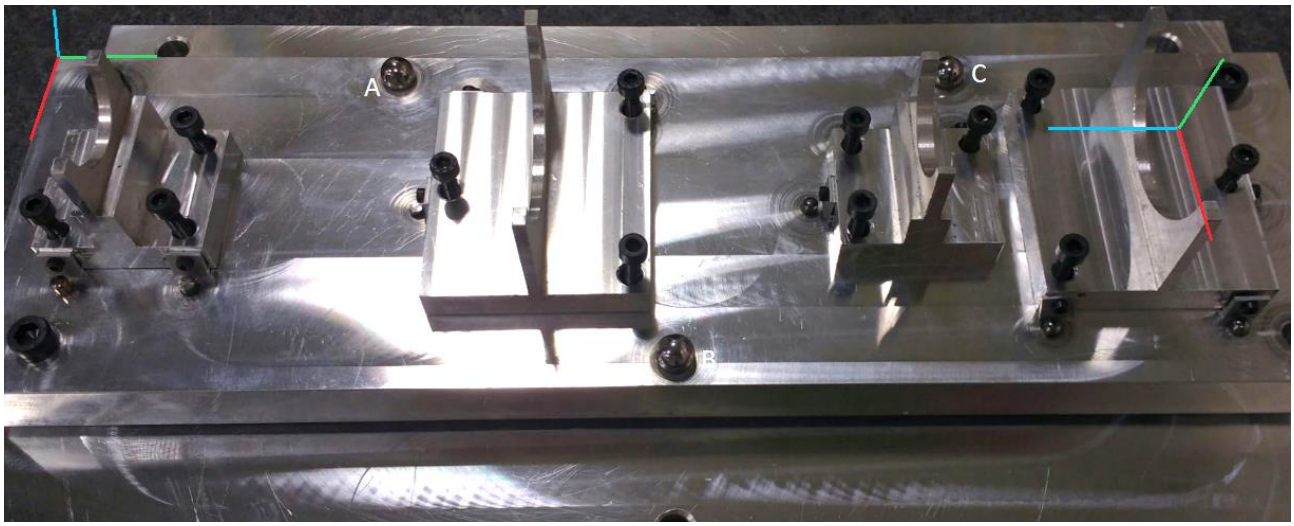

Figure 6.8. Original reference system (top left), final reference system (right) and reference spheres (A-B-C) before the installation of the optical elements.

Every time the system must be re-aligned to the measuring machine in the alignment phase or to the telescope in the installation phase, the spheres will be remeasured and a best-fit operation will be performed between the measured spheres and the nominal ones. The repeatability of this method has been studied in section 2.6.4, showing values at the micrometre level. Using reference spheres with better roundness and increasing the number of spheres can increase the robustness of this method.

After a correction on the nominal Z positions of the elements based on the actual focal lengths, each element has been repeatedly measured and its position corrected. As soon as the alignment of the element was considered satisfactory, the CMM was moved to the next optical element and the operation repeated.

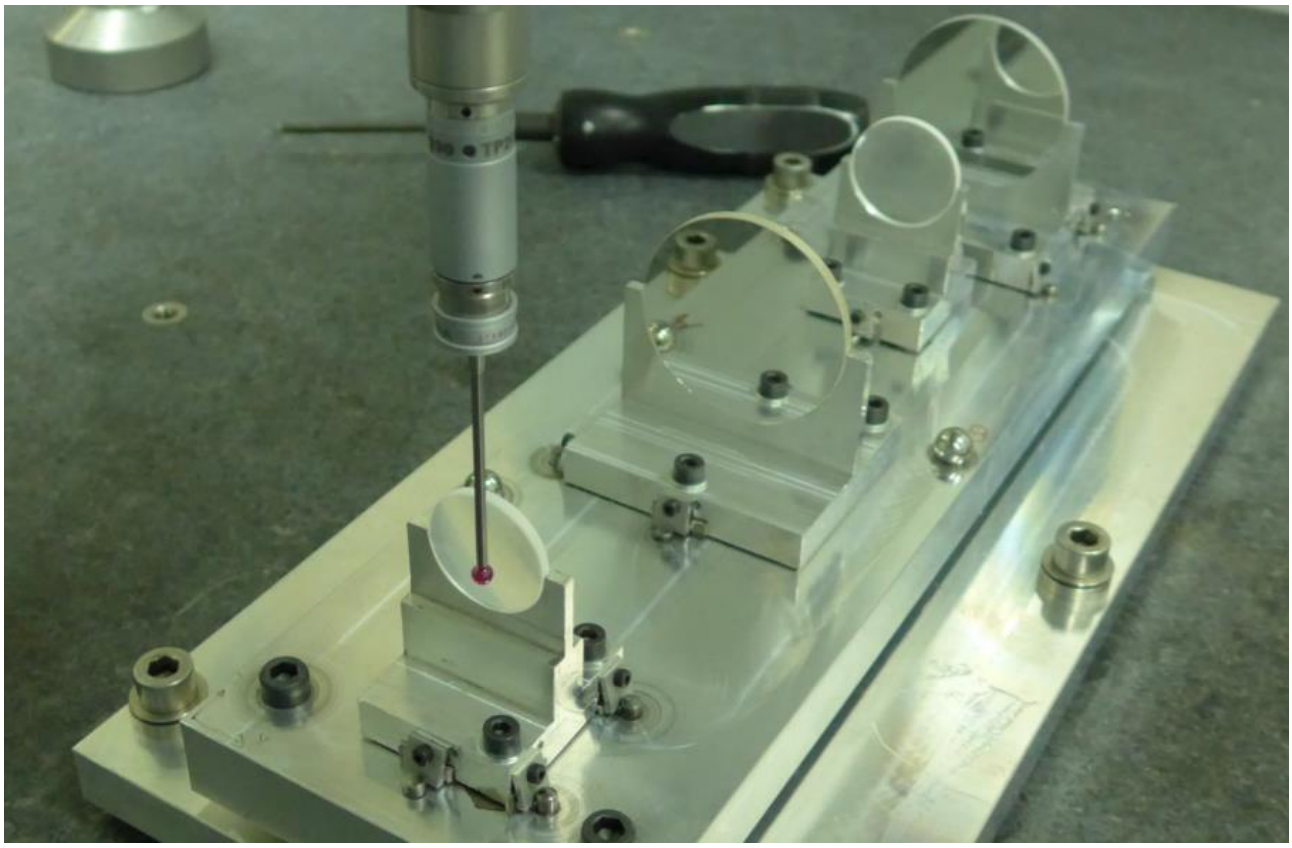

Figure 6.9. Alignment of the first element of the dummy system. Some correction has been already applied, as can be seen by the shims fixed below the screws and the L elements.

The results obtained for the four elements are shown in Figure 6.10, Figure 6.11, Figure 6.12, and Figure 6.13. After each measurement run of an element, the numbers obtained by the CMM software have been used to calculate the modifications to perform on the 6 shims stacks. On the right side of the figure, the results have been plotted together with the limits obtained in Table 6.6, used as a reference.

Even if the alignment quality could have been slightly improved, it was decided to perform it in a fixed amount of time (maximum 30 minutes per element). This timing was foreseen to be sufficient to perform about six repetitions and to reduce the shim errors below the 10-µm level.

This goal was reached in 10 out of the 15 significant degrees of freedom and the limiting factor was the large number of shims inserted at the end of the process and their accuracy.

In every location up to 10 shims with various thickness was placed during the process and this leaded to a difficult positioning of the thinner shims like the 5 µm ones. The most critical situation, however, appeared when the replacement of a shim was needed. This situation was quite common as it was necessary to keep the number of shims under control or to reduce the overall thickness. Due to the thickness uncertainty of the shims (see Table 2.7 in section 2.8.1), the substitution of some of them introduces a random variation of up to tens of microns.

A workaround used consisted in a slight under-shimming of all the degrees of freedom in order to be able to insert the 5 and 10 micrometre shims without removing any other shim.

Lens 1

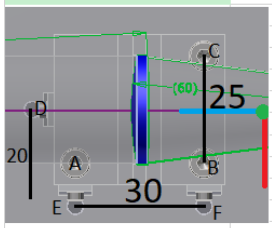

		Nom	Act	Unc 2σ	Res	
Surface 1	X	0	*0.0348*			mm
	Y	0	*-0.0775*			mm
	Z	191.706	*192.1243*			mm
Surface 2	X	0	*-0.1228*			mm
	Y	0	*-0.0018*			mm
	Z	601.006	*608.3875*			mm
Tilt Rx+		0	-0.010	0.002	0.019	°
Tilt Ry+		0	-0.022	0.002	0.019	°
Decenter X		0	0.013	0.002	0.005	mm
Decenter Y		0	-0.067	0.003	0.005	mm
Focus actual lens		250.5680	250.415	0.029	0.005	mm

To add

Shims [mum]	Tilt Rx+	Tilt Ry+	Dec X	Dec Y	Focus	TOTAL
A	-3			67		-11
B	3			67		-5
C	3			67		-5
D					-153	-13
E		-6	13			1
F		6	13			12

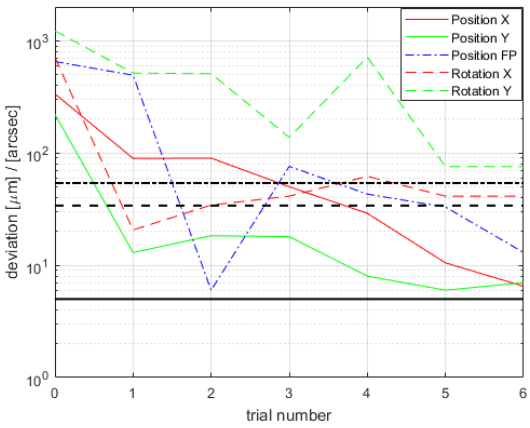

Figure 6.10. Alignment results of the first lens. Left: conversion between measured data and shim correction. Right: approximate misalignment values obtained during the alignment. The black lines show the lower limits defined in Table 6.6 (continuous for X and Y positions, dash-dot for axial position and dashed for rotation).

Mirror 1

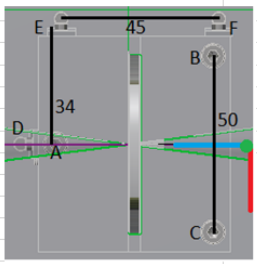

		Nom	Act	Unc 2σ	Res	
Mirror 1	Ang xp	90	*90.0215*			°
	Ang yp	90	*89.992*			°
	Z	151.657	*151.5138*			mm
Tilt Rx+		0	0.008	0.001	0.013	°
Tilt Ry+		0	0.022	0.001	0.013	°
Focus actual lens		151.6570	151.514	0.001	0.005	mm

Shims [mum]	Tilt Rx+	Tilt Ry+	Dec X	Dec Y	Focus	TOTAL
A	3					-72
B	-3					-78
C	-3					-78
D					-143	-3
E		-8				-2
F		8				14

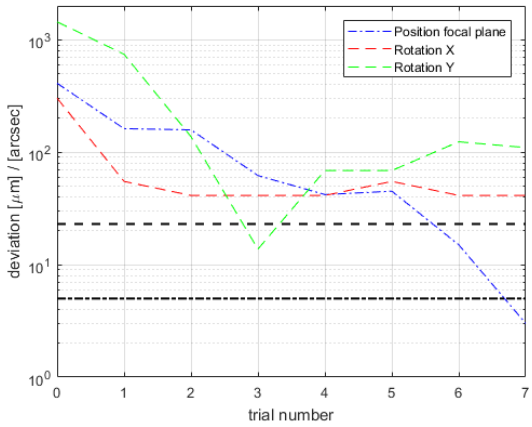

Figure 6.11. Alignment results of the first mirror. Left: conversion between measured data and shim correction. Right: approximate misalignment values obtained during the alignment. The black lines show the lower limits defined in Table 6.6 (dash-dot for axial position and dashed for rotation).

Lens 2

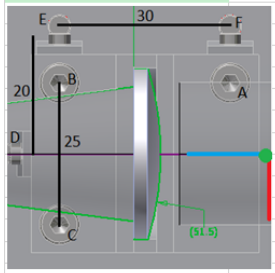

		Nom	Act	Unc 2σ	Res	
Surface 1	Ang xp	90	*90.0014*			°
	Ang yp	90	*90*			°
	Z	58.9774	*59.2663*			mm
Surface 2	X	0	*-0.0048*			mm
	Y	0	*-0.0849*			mm
	Z	105.747	*106.377*			mm
Tilt Rx+		0	0.000	0.001	0.019	°
Tilt Ry+		0	0.001	0.002	0.019	°
Decenter X		0	-0.006	0.002	0.005	mm
Decenter Y		0	-0.085	0.002	0.005	mm
Focus actual lens		56.2557	56.129	0.011	0.005	mm

To add

Shims [mum]	Tilt Rx+	Tilt Ry+	Dec X	Dec Y	Focus	TOTAL
A	0			85		10
B	0			85		10
C	0			85		10
D					-127	13
E		0	6			12
F		0	6			12

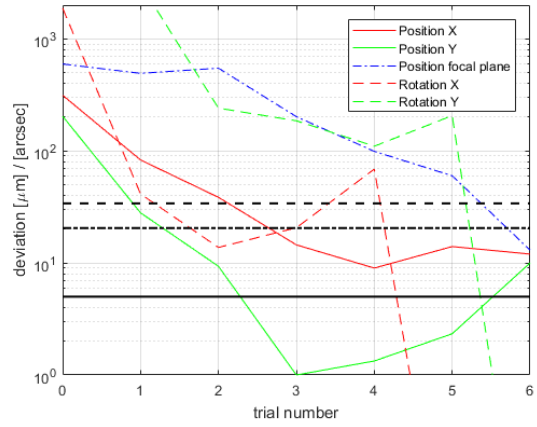

Figure 6.12. Alignment results of the second lens. Left: conversion between measured data and shim correction. Right: approximate misalignment values obtained during the alignment. The black lines show the lower limits defined in Table 6.6 (continuous for X and Y positions, dash-dot for axial position and dashed for rotation).

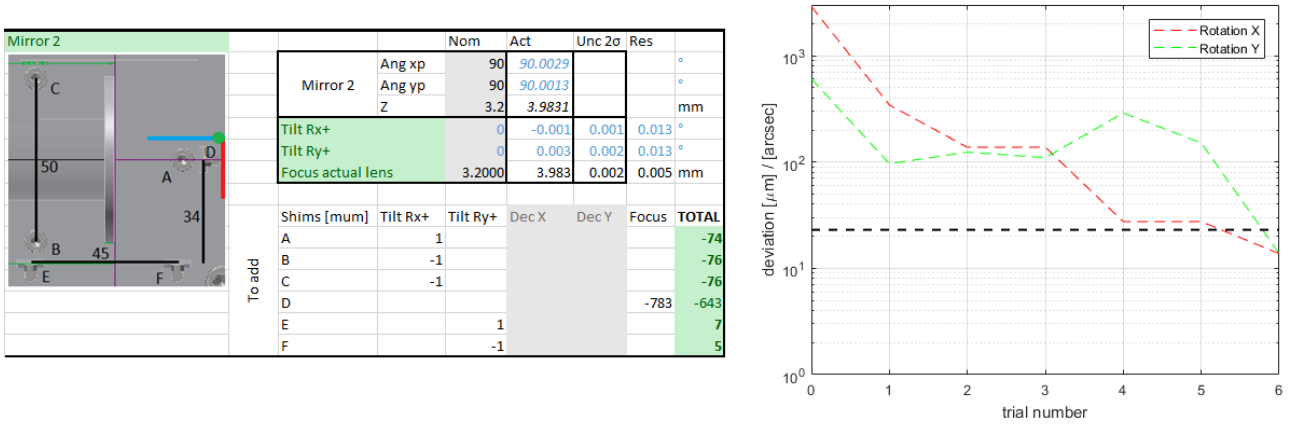

			Nom	Act	Unc 2σ	Res	
Mirror 2		Ang xp	90	*90.0029*			°
		Ang yp	90	*90.0013*			°
		Z	3.2	*3.9831*			mm
Tilt Rx+			0	-0.001	0.001	0.013	°
Tilt Ry+			0	0.003	0.002	0.013	°
Focus actual lens			3.2000	3.983	0.002	0.005	mm

To add	Shims [mum]	Tilt Rx+	Tilt Ry+	Dec X	Dec Y	Focus	TOTAL
	A	1					-74
	B	-1					-76
	C	-1					-76
	D					-783	-643
	E		1				7
	F		-1				5

Figure 6.13. Alignment results of the second mirror. Left: conversion between measured data and shim correction. Right: approximate misalignment values obtained during the alignment. The black line shows the lower limits defined in Table 6.6 (dashed for rotation).

6.5 Alignment validation with interferometer

In order to have an optical feedback of the alignment a measurement of the aligned system has been performed with an interferometer. The interferometer has been equipped with a transmission flat and the system has been optically aligned in order to have M1 perpendicular to the incoming collimated beam.

Two interferograms have been acquired with two different layouts: the first one has the M1 mirror mounted (Figure 6.14, top) while the second one is acquired after removing it (Figure 6.14, bottom). The obtained data is shown on the left in Figure 6.15 for the first case and on the centre and right for the second configuration.

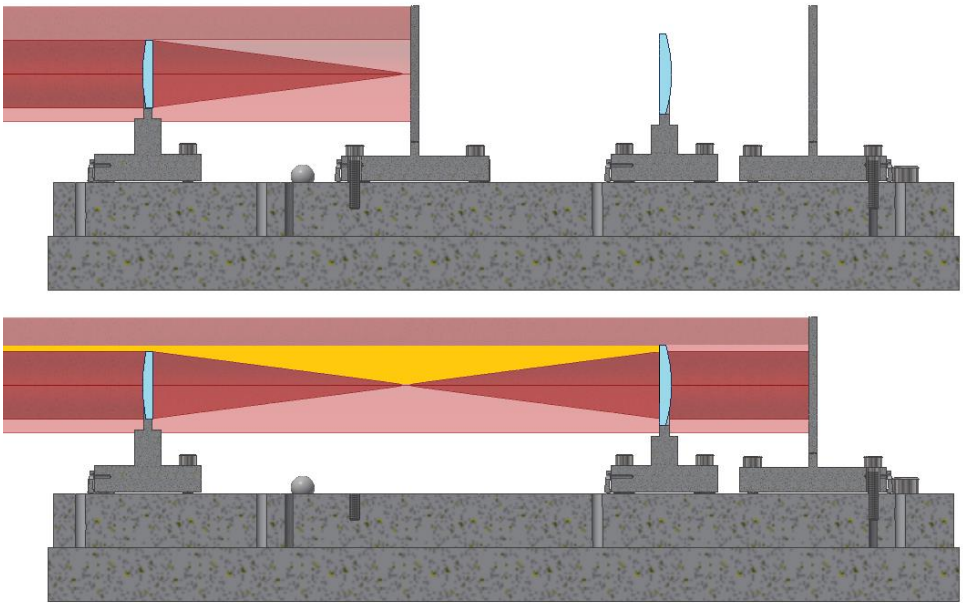

Figure 6.14. Schematic representation of the two configurations measured with the interferometer. Top: first configuration. Light red for M1 collimated beam autoreflection and dark red for M1 central retroreflection. Bottom: second configuration. Light red for M2 collimated beam autoreflection, orange for L2 collimated beam autoreflection and dark red for central autoreflection.

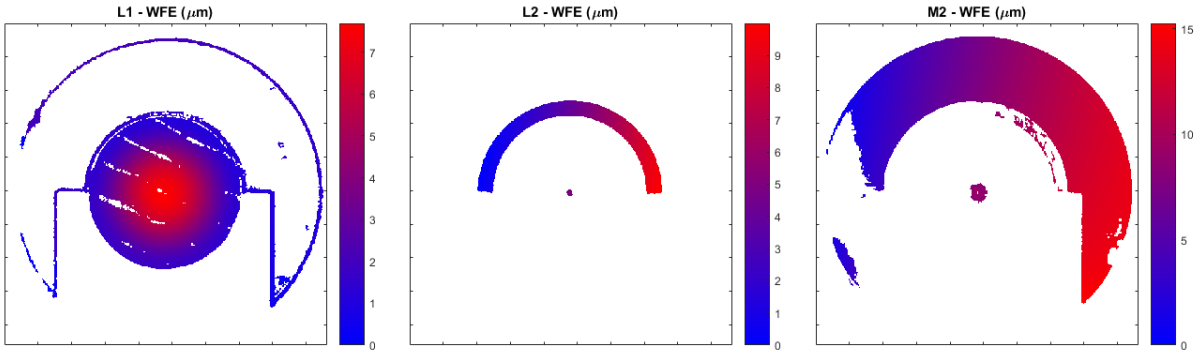

Figure 6.15. Original wavefront error of the optical elements. Left: L1 with the noise coming from M1 (first layout). Centre: L2 (second layout). Right: M2 with the central part disturbed by L2 (second layout).

To see the tip-tilt of the flat surfaces, the images have been processed and cleaned from the disturbances coming from the other optical elements and the obtained results have been fitted with the first Zernike polynomials. The results are shown in Figure 6.16 for L2 and Figure 6.17 for M2. The residuals shapes from the flat mirror seem to be composed by astigmatism (see Figure 1.7 for comparison) while the one from L2 appears to be mainly power even if, due to the limited sampling area, it is difficult to provide a definitive answer.

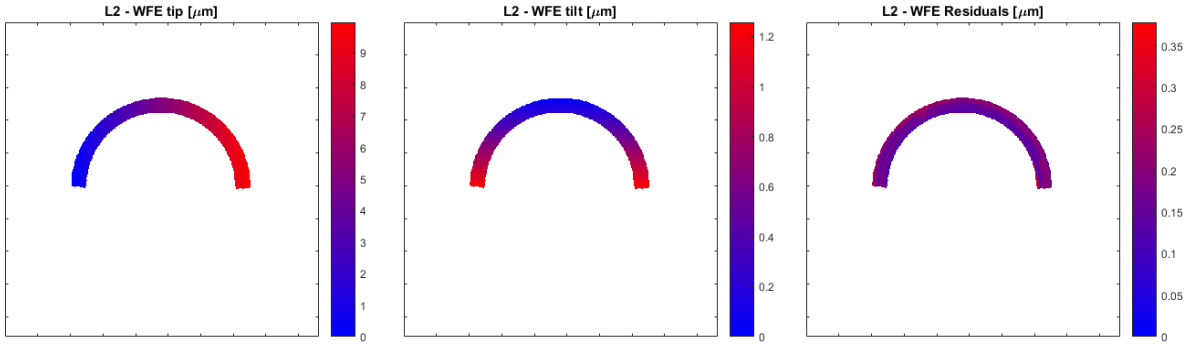

Figure 6.16 L2 wavefront error in tip (left) and tilt (centre). The residuals are shown on the right.

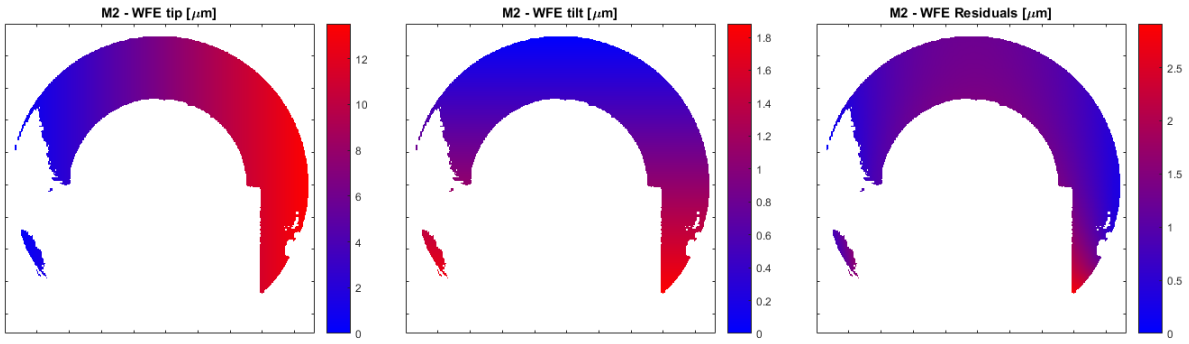

Figure 6.17 M2 wavefront error in tip (left) and tilt (centre). The residuals are shown on the right.

The obtained results have been compared to the ones expected from the CMM alignment and are shown in Table 6.7. The average value for the CMM results is the one obtained from the last measurement and the

expanded uncertainties comes from the Simulation Software and the Multi Positioning Method. On the interferometric side, the average values have been calculated from the Zernike coefficients and the uncertainties are based on the form error provided by the manufacturer. An uncertainty evaluation done starting from the residuals provided similar results.

Table 6.7 Measures of tip-tilt respectively corresponding to rotations aroud Y and X in the dummy reference system.

	Tilt - R_x [arcsec]			Tip - R_y [arcsec]		
	CMM alignment		Interferometer	CMM alignment		Interferometer
	$U_{95\%}$ SS	$U_{95\%}$ MPM	$U_{95\%}$	$U_{95\%}$ SS	$U_{95\%}$ MPM	$U_{95\%}$
M1	Reference					
L2	-29±23	-29±13	-17±11	-72±23	-72±14	-68±11
M2	-33±20	-33± 9	-9±11	-67±20	-67±14	-56±11

The results can be also seen in the plot in Figure 6.18. All the measurements coming from the CMM alignment and the simulation software are compatible to the interferometric ones. In one of the four results obtained by the MPM, the results are not compatible by a few arcseconds. The MPM appears to be slightly too optimistic on the uncertainty calculation. However, it is important to notice that, in order to measure the system under the interferometer, it has been moved in a different location where no temperature stabilization was implemented and it has been installed on a different interface. A different tightening of the screws fixing the dummy system bench has, as a primary effect, a rotation of the M2 mirror around the X axis.

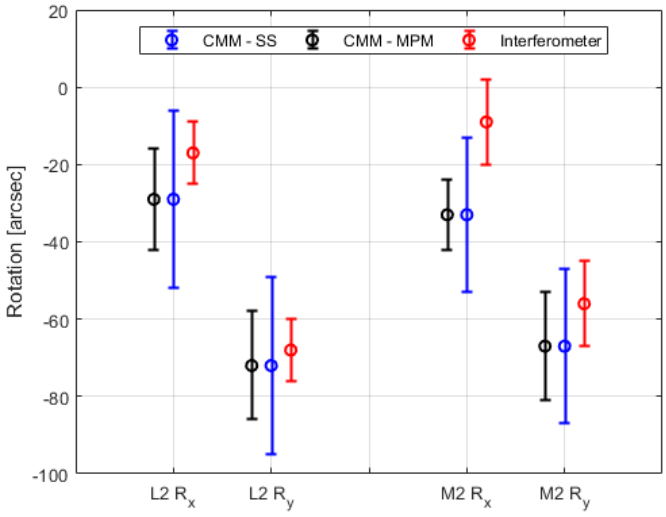

Figure 6.18 Graphical representation of the residuals. The bands represents the 2σ uncertainties.

The original plan foresaw the evaluation of tilt and defocus of L1 and a subsequent evaluation of the L2 results. The obtained L1 rotation obtained during the CMM alignment resulted almost one order of magnitude better than the ones detectable by the interferometer using tip-tilt and coma polynomials.

For the first lens, the Zernike defocus term is shown as wavefront error in Figure 6.19. In the same picture, it is possible to see the residuals heavily dominated by the primary spherical term.

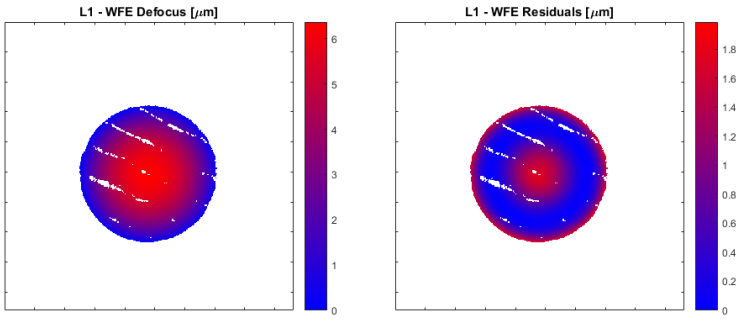

Figure 6.19 Left: L1 wavefront error in defocus. Right: L1 fitting residuals.

Due to the loose specifications on the focal length of the lens it was not possible to directly compare it to the one obtained by the CMM alignment. A verification of the focal position of L1 with respect to M1 updating the optical design with the data obtained from the CMM MPM measurements and the simulated interferogram has been compared to the measured one.

The obtained results, considering the nominal refractive index of the glass, showed a deviation between the optical and the CMM results in the focus direction of +60 µm, well inside the ±114 µm (2σ) predicted by the software. Considering instead that the elements are in the exact position a deviation of the refractive index of the glass of 0.00032 (again, inside the manufacturer specifications of ±0.0005) could explain the variations.

A graphical representation is shown in Figure 6.20. The line shows all the possible combinations of focus position and refractive index. Assuming that the specification of the refractive index provided by the manufacturer is correct, the red part of the line represents the possible non-compatibility combinations (of 16.5% or 21%, considering respectively a Gaussian or a rectangular distribution of the refractive index).

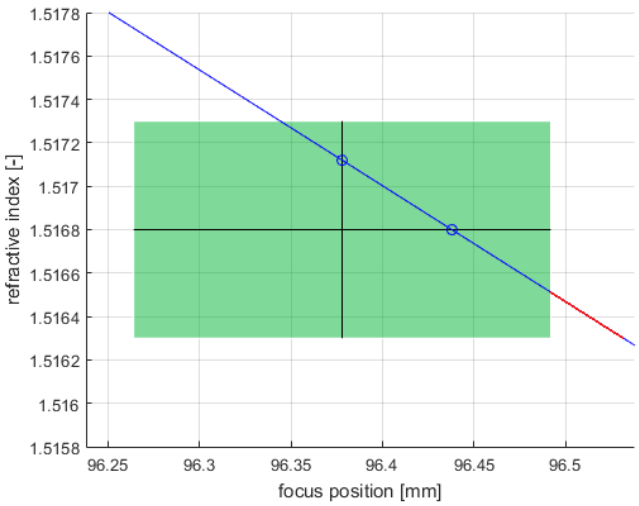

Figure 6.20 Focus analysis. The green rectangle shows all the possible combinations of refractive index (manufacturer value) and focus position (simulation software). The line shows all the possible combinations of focus position and refractive index leading to the condition shown in Figure 6.19 (left).

6.6 Conclusions and future improvements

In this chapter, the alignment process of a dummy optical system has been presented. In the first part the simulation software developed in chapter 3 has been compared to the values obtained by the MPM. The use of the software during the optical design phase of an optical system gives a conservative estimation of the uncertainties, useful to define the mechanical design and the alignment workflow.

Depending on the results obtained by the simulation software, the MPM can still be foreseen to decrease the uncertainty in the estimation on the geometrical characteristics of the single optical elements or, as a final step, to validate the overall alignment of the system.

The tilts of the flat surfaces have been measured with an interferometer and the obtained results were compatible with the ones obtained with the alignment and expected by the simulation software.

As the focal length uncertainty of the optical elements selected for the dummy system is quite high, a different verification methodology is needed to verify the remaining degrees of freedom (e.g. using a mechanically characterized CMOS sensor).

6.7 References

[6.1] W Thompson KP. Aberration fields in tilted and decentered optical systems.

[6.2] Greivenkamp JE. Field guide to geometrical optics. Bellingham, WA: SPIE Press; 2004 Jan 20.

[6.3] ISO/TS 15530-1:2013. Geometrical product specifications (GPS) — Coordinate measuring machines (CMM): Technique for determining the uncertainty of measurement Part 1: Overview and metrological characteristics

[6.4] Wilhelm RG, Hocken R, Schwenke H. Task specific uncertainty in coordinate measurement. CIRP Annals-Manufacturing Technology. 2001 Dec 31;50(2):553-63.

[6.5] ISO/DTS 15530-2:2003. Geometrical Product Specifications (GPS) - Coordinate measuring machines (CMMs): Techniques for evaluation of the uncertainty of measurement - Part 2: Use of multiple measurement strategies

[6.6] Osawa S, Busch K, Franke M, Schwenke H. Multiple orientation technique for the calibration of cylindrical workpieces on CMMs. Precision Engineering. 2005 Jan 1;29(1):56-64.

[6.7] ISO 12123:2010. Optics and photonics — Specification of raw optical glass

[6.8] Aliverti M, Pariani G, Moschetti M, Riva M. Integration and alignment through mechanical measurements: the example of the ESPRESSO front-end units. In SPIE Astronomical Telescopes+ Instrumentation 2016 Aug 9 (pp. 99087C-99087C). International Society for Optics and Photonics.

7 Conclusions

The alignment procedure and its limitations are sometimes understudied during the design on an astronomical instrument. This usually leads to long and iterative modifications until the machine is able to fulfil the scientific and technological requirements.

This thesis originated from the need of a stable spectrograph for the research of extrasolar planets. In such a system, the use of stiff and stable optomechanical elements is one of the basic requirements to achieve high RV stability and, therefore, being able to observe earth-like exoplanets.

Aligning such a system with the classical optical methods can be extremely complicated and different alternative methods have been studied finding the pure mechanical one as the most promising.

Three main risks were identified with this procedure: the capability to place the elements in the desired position, the uncertainty of the measurement machine, and the damages provoked on the optical surfaces.

The first one has been tackled testing different references and different alignment systems. The references must be stable and with a good repeatability as they must reliably define the location of each element to the main reference system and vice-versa and different solutions have been found with the best one having a repeatability of about 200 nm. An accuracy of 5 µm has been found for the best support made with L-shaped fixing system and custom shims having different thickness down to 5 µm.

Aligning all the elements measuring their geometry makes the alignment uncertainty directly related to the measurement uncertainty of the machine used. The research focused on the use of a CMM for the measures and all the uncertainty sources of this machine have been studied. The obtained results have been used to develop a software able to give a prediction of the uncertainty depending on the CMM configuration, the alignment strategy used, and the optical elements involved. In order to validate the software and the alignment procedure, a dummy optical system has been designed, aligned and verified using an interferometer and all the measurable components (tilts and focus) proved to be compatible to the expected ones. It is important to point out that, even if the software is dedicated to a specific CMM, the same results can be derived for similar CMM with little measurement effort.

The risk of damaging the optical elements and, consequently, reducing the performances of the optical system has always been a prime concern when touching the optical surface is a required operation. To dissipate this concern, the contact between the surface and the machine has been deeply studied. The forces involved during the contact have been measured with different CMM configurations and values ranging between 15 mN and more than 4000 mN have been found with the main factors being the stylus length, the measurement speed and the module selected. Some of those parameters could conflict with the accuracy requirement or the mechanical and optical design of the instrument and, therefore, a trade-off between them will be required. Another software has been developed to estimate the contact force in the configuration proposed for the alignment and, even if it is dedicated to the CMM used, it can be easily modified for different CMMs with an extremely limited number of measurements.

The obtained forces have finally been used to estimate the damage on the optical surfaces using a theoretical approach when possible and defining a procedure based on the worst possible conditions in the more complex cases. Different results have been obtained for uncoated surfaces, coated soft substrates, and coated hard substrates. Nevertheless, due to the high variability of the results depending on the materials and manufacturing processes involved, a preliminary test on the surface will always be required to ensure that the damage is below the desired limit.

The overall alignment process proposed is shown in Figure 7.1. An evaluation of the accuracy will be performed considering all the possible uncertainty sources and a preliminary alignment strategy satisfying the alignment requirements will be proposed. This strategy will be verified and eventually modified considering the expected damages on the optics and the scratch/dig and scattering requirements. Finally, the mechanical design will be finalized to allow for the proposed alignment strategy.

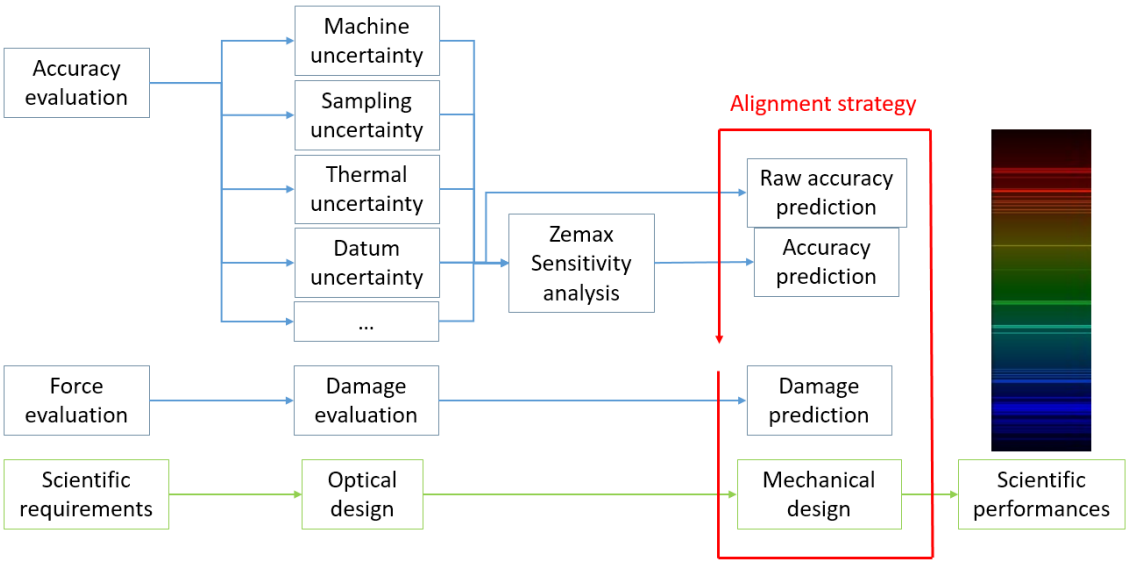

Figure 7.1 Overall view of the alignment process proposed.

This full procedure is currently being considered in the design of SOXS (see Figure 7.2), a spectrograph to be installed at NTT in 2020. The two parts involved are the common path and the infrared (IR) subsystem. The first one is a relay system used to feed the spectrograph and mainly composed by dielectric coated mirrors. In the IR subsystem, different soft material will be used, including aluminium mirrors and soft glass lenses. In both the cases, the density of the optical elements makes them the perfect candidates for the application of this method.

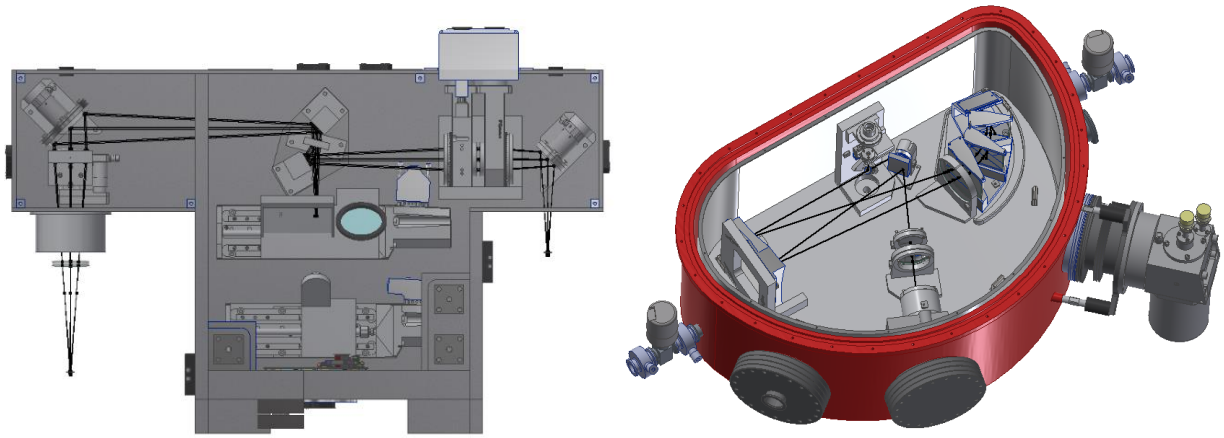

Figure 7.2 Two of the SOXS subsystem where the alignment strategy is currently being applied. Left: common path. Right: cryogenic IR subsystem.

Looking farther in the future this method or, hopefully, an improved version of this method will be applied to the HIRES Front End (Figure 7.3). It is meant to be an extended version of the ESPRESSO Front End with

different modular subsystems working ad different temperature and wavelength ranges and will be characterized by even more stringent stability requirements.

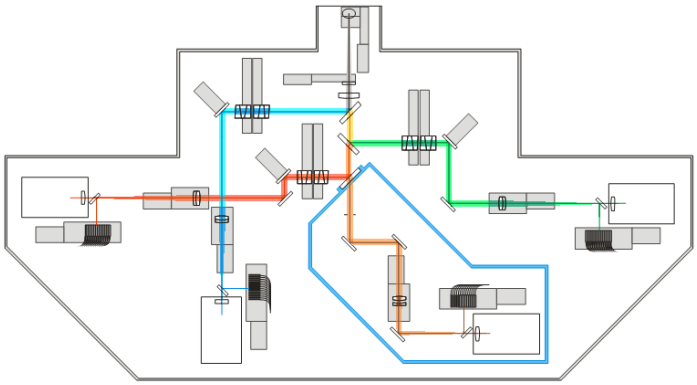

Figure 7.3 Sketch of the HIRES Front End for ELT. The external envelope is about 2.6 m x 1.4 m.

One of the technical challenges of this system is related to the definition of the optical axis of cemented multiple lenses. Different solutions are possible and they include the mechanical characterization of the individual elements or the use of a calibrated CMOS sensor to characterize the complete optical element. The study of those techniques certainly is an interesting evolution of the proposed method.